Fluid-Structure Interaction in Viscous Dominated Flows

by
Longhua Zhao

A dissertation submitted to the faculty of the University of North Carolina at Chapel Hill in partial fulfillment of the requirements for the degree of Doctor of Philosophy in the Department of Computer Science.

Chapel Hill
2010

Approved by:

Roberto Camassa, Advisor

Richard M. McLaughlin, Advisor

M. Gregory Forest, Committee Member

Laura Miller, Committee Member

Richard Superfine, Committee Member

Leandra Vicci, Committee Member

<div align="center">**ABSTRACT**</div>

<div align="center">**LONGHUA ZHAO: Fluid-Structure Interaction in Viscous Dominated Flows.**</div>

<div align="center">**(Under the direction of Roberto Camassa and Richard M. McLaughlin.)**</div>

Theoretical, numerical and experimental studies for several flows in the Low Reynolds number regime are reported in this thesis. It includes the flow structure and blocking phenomena in linear shear or rotation flow past an embedded rigid body, and flows induced by a slender rod precessing a cone to imitate the motion of nodal cilia are studied with the singularity method.

The first subject is to explore interesting phenomena emerging in the fundamental problem of shear flow past rigid obstacles. An analytical and computational study of Lagrangian trajectories for linear shear flow past a sphere or spheroid at low Reynolds numbers is presented. Using the exact solutions available for the fluid flow in this geometry, we explore and analyze blocking phenomena, local bifurcation structures and their influences on dynamical effects arising in the fluid particle paths. In particular, based on the work by Chwang and Wu who established a blocking phenomenon in two-dimensional flows, whereby a cylinder placed in a linear shear prevents an unbounded region of upstream fluid from passing the body, we show that a similar blocking exists in three-dimensional flows. For the special case when the sphere is centered on the zero-velocity plane of the background shear, the separatrix streamline surfaces which bound the blocked region are computable in closed form by quadrature. With such analytical results, we study the foliation of the physical material streamline surfaces, identify the separation in the flow, and measure the blocked flow. When the sphere's center is out of the zero-velocity plane of the background shear, closed form expressions appear unavailable due to the broken up-down mirror symmetry. In this case, computations provide evidences for the persistence of the blocking region. Furthermore, a complex bifurcation structure in the particle trajectories is documented. We compute analytically the emergence of different critical points in the flow and characterize the global streamline topology associated with these critical points, which includes the

emergence of a three-dimensional bounded eddy. Additionally, we study the case of a sphere embedded at a generic position in a rotating background flow, with its own prescribed rotation including fixed and freely rotating. Exact closed form solutions for fluid particle trajectories, stagnation points on the sphere, and critical points in the interior of the flow are derived.

We extend our results further to spheroids as well, where similar blocking results are documented. The broken symmetry offered by a tilted spheroid geometry induces new three-dimensional effects on the streamline deflection, which can be viewed as effective positive or negative suction in the horizontal direction orthogonal to the background flow depending on the tilt orientation. We close this study with results of a spheroid embedded in a rotating background flow, with its own prescribed tilt orientation. Net fluid transport is observed in this flow, where the direction of transport depends on the direction of the background rotation and the tilt orientation of the spheroid.

The study in the second part of this thesis is motivated by the intriguing properties of airway surface liquids in ciliated tissues, and in particular we aim at detailed understanding and theoretical prediction of certain aspects of the fluid dynamics arising in developing embryos. The fluid motion induced by spinning cilia is fundamental to many living organisms. Under some circumstances it is appropriate to approximate cilia as slender rigid rods. We study the effects of shape and orientation of these idealized cilia upon flow structures in a Stokes fluid. In this topic, we model the cilia-induced flow with the slender body theory and imitate the rotary motion of an isolated cilium by spinning a slender rod in highly viscous fluids. By utilizing the slender body theory and the image method, an asymptotic solution is constructed for a slender body attached to a no-slip plane and rotating about its base to sweep out a cone. With fully 3D stereoscopic images for the table-top experiment, 3D experimental particle tracking is constructed. We explore the complex flow structures and present quantified comparisons with the theoretical predictions. Intriguing short, intermediate and long time phenomena of particle trajectories are documented, and the intricacies of their theoretical modeling reported.

ACKNOWLEDGMENTS

and his effort to track RMX videos. I thank David Holz, whom we met at the right time and brought us the ideal tools, for his program to track the pin in the experiments and all the discussions we have had.

This thesis has been greatly improved with helpful comments and suggestions from my advisors and other committee members. I sincerely appreciate their time and efforts.

I also would like to thank the staff in the Mathematics Department, specially Brenda Bethea for her assistance throughout my graduate years.

My friends at the Department of Mathematics have always offered a friendly atmosphere and I am really happy for those years of study. A special acknowledgement goes to all my officemates at UNC. I wish them the best in their future.

I will be grateful to CIIAM at UNC and the National Science Foundation. Specifically, credits are due to the NSF DMS-0509423, NSF NIRT 0507151, and NSF RTG DMS-0502266 grants that provided the equipment and manpower for this research work.

Finally, I acknowledge, appreciate, and return the love of my family, without whom I would be lost. They have been my emotional anchors through not only the vagaries of graduate school, but my entire life. I thank my parents and sisters for their continuous and unconditional support of all my undertakings. And I want to thank my husband, Lingxing, for his untiring encouragement, great care, and support, for cheering me on throughout, commiserating with my frustrations, and sharing in my excitements.

Contents

x

List of Figures

List of Tables

Chapter 1

Introduction: basic concepts, methodology and organization

Studies of highly viscous flows past rigid obstacles and fluid flows induced by rigid bodies with small spatial scales are fundamental in fluid mechanics. These flows play an important role in particle entrainment, sediment transport, micro-fluidic mixing, micro-organism locomotion and many other areas of geophysical and biophysical interests. In these studies, an important class of problems concerns scales where inertia plays a subdominant role to viscous forces, which is the case for many biophysical applications. The Stokes approximation becomes relevant in such cases, despite its limitations in governing fluid motion far from the body. Numerous studies have addressed these Stokes problems in the literature.

The simplest Stokes flows with objects embedded are uniform flow and linear shear flow past an infinite cylinder, a sphere, or an ellipsoid. For 2D uniform flow past a cylinder with its axis perpendicular to the stream, there is no solution in the Stokes regime, which is well-known as the Stokes paradox. For 3D uniform flow past a sphere, the first order approximation of the velocity is obtained to satisfy the no-slip boundary condition on the surface of the sphere and asymptotic to the uniform background flow at infinity. However, a second approximation Stokes solution for uniform flow past

a sphere does not exist, known as Whitehead's paradox [24]. Another version of the Stokes paradox of this 3D flow is reflected on the energy carried by the sphere or the drifting volume if we consider the flow at rest and the sphere is moving with a constant velocity. Oseen correction of uniform flow past a cylinder or sphere has already been well studied [24]. Using the matched asymptotic expansions, uniform flow past an elliptic cylinder has also been studied by Shintani et al. [68].

For a linear shear flow past an infinite cylinder, the velocity field and stream function can be found in Robertson & Acrivos [65], Poe & Acrivos [62], Kossack & Acrivos [42], and Chwang & Wu [19], and the Oseen correction for this 2D flow is derived by Bretherton [11]. In three-dimension, a general solution, the velocity field of an ellipsoid immersed in a linear Stokes flow, can be found back to Jefferey [36]. For a linear shear flow past a sphere, Saffman [66] worked out the Oseen correction for the force acting on the sphere instead of the usual stream functions. The force is governed by one ODE for this 3D flow. A good review is referred to Leal [45]. For most studies about these Stokes flow past a rigid obstacle [44, 22, 47, 41], the focus is the velocity field, the force acting on the flow [66], and sometimes the motion of the suspension in the fluid [36].

Despite the long history of research in Stokes flows, considerable attention to the Stokes flow is continually drawn due to its medical, micro-biological and geological applications. Studies of these applications can lead to better medical approaches for many aliments, better strategies of environmental issues, and deep understanding of the nature of life in the low Reynolds number regime [55], [26] [34]. For these applications, not only the flow motion but also the structure of the flow plays important roles to completely understand the properties of the flow. Understanding of the flow patterns for the fundamental problems will help to predict the streamlines of flow in more complicated geometries.

However, few studies have presented or discussed the flow patterns. Even less has

investigated the flow from Lagrangian viewpoint, which is effective to show the flow structure. Therefore, this thesis focuses on the structure and interaction of the flow in the Lagrangian viewpoint. If the flow is 2D, a single valued continuous stream function can be assumed to find the streamlines. For uniform flow past a sphere in 3D, due to the axis symmetry, the flow can reduce to a 2D flow in the spherical coordinates. Jeffrey & Sherwood [37] have studied the streamline pattern for 2D Stokes shear flow around a rotating cylinder, where the flow is governed by one stream function. For a linear shear flow or rotating flow past a sphere or spheroid, the flow is fully 3D, which is much more complicated and 3D Oseen correction is extremely difficult. Acrivos' group [1, 65, 42, 62] has studied the shear flow past a sphere experimentally and numerically. Cox, Zia & Mason [23] reported the streamline functions in integral form with a freely rotating sphere in a linear shear background flow. Beyond the Stokes regime, a few papers [72] [57] studied the flow structure numerically, considering the inertial effect for this flow. As we know, there is no report about the stream functions of a linear shear flow past a fixed sphere in the literature.

We study the flow problems with the singularity method seen in Chwang & Wu [19], Kim & Karrila [41], Pozrikidis [63], and Leal [47]. This method has been used widely in research and is especially suitable for these Stokes' problems with regular or complicated boundary geometries. The pioneering work about the singularity method can be tracked back to Lorentz [51], Oseen [60], and Burges [13] as Chwang & Wu cited [19] (see a review [50]). The vital components for this method are to identify the type of singularities, determine the distribution and strength of the singularity, and construct the velocity eventually. The singularities are usually distributed inside the obstacle, so that the resulted velocity field is regular.

Based on Chwang and Wu's work [19], we study the shear flow or rotating flow past a sphere or spheroid in the first part of this thesis. Using the velocity field, we

integrate and obtain the trajectory equation of fluid particles. An interesting blocking phenomenon, which is reported by Poe & Acrivos [62], Chwang & Wu [19] and Jeffery & Sherwood [37] in 2D, is observed with fully 3D shear flow past a sphere or spheroid. Through careful study, new phenomena of Stokes flow are documented.

Inside the framework of the singularity method, the slender body theory is a methodology used to take advantage of the slenderness of the body to obtain an approximation to a field surrounding it. The slender body theory has been refined by numerous authors from Batchelor [3], Cox [21] to Johnson [38]. With higher order singularities, Johnson [38] has improved the velocity to an error term of $O(\epsilon^2)$ by matching asymptotics (ϵ is the slenderness parameter). Also, Blake [5] introduced the image system to handle the no-slip boundary condition on a flat plane.

By applying both the slender body theory and the image method, the second part of this thesis reports the study of the flow induced by a slender body sweeping out a cone. This study is motivated by the campus-wide Virtual Lung Project [55, 48] at the University of North Carolina at Chapel Hill, and other biological applications, for example, the flow induced by nodal cilia [12]. Motion of nodal cilia has been found playing an important role in the left-right symmetry breaking at the early stage of the mammal embryos [58, 69, 16]. We model the cilia-induced flow in the Stokes regime with the slender-body theory and imitate the rotary motion of an isolated cilium by spinning a slender bent rod in highly viscous fluid. With the help of modern visualization tools, we also perform stereoscopic fully three-dimensional experiments and reconstruct 3D Lagrangian trajectories to compare with our theoretical predictions.

This thesis is divided into two parts, which are closely related to each other but focus on different Stokes flows. The first part includes Chapter 2, 3 and 4. In Chapter 2, we first introduce the fluid problem and the exact velocity of the flow [19] for a linear shear Stokes flow past a sphere. Then, we integrate by quadratures the fluid particle

equations when the sphere's center is in the zero-velocity plane (see the first case in Figure 2.1). In particular, we study in detail the stagnation points with their associated surfaces, as these provide the framework for the blocked region geometry, and the mode of divergence of the blocked regions' cross-sectional area is calculated. Then, we turn to the second case shown in Figure 2.1, when the center of the sphere is out of the zero-velocity plane of the primary shear. Numerical results demonstrate the persistence of the blocked regions. Complicated global bifurcations are found analytically in the flow field with special ratios related to the shear rate, the radius of the sphere, and the distance from the zero velocity plane of the primary shear to the sphere's center. Furthermore, we show information about the linear shear flow past a freely rotating sphere. Analytical particle trajectory formulas are obtained similarly. There are closed orbits in the flow and the height of the closed orbit near the sphere is convergent.

In Chapter 3, we report the primary results about linear shear flow past a spheroid with the analytical velocity field in the Stokes regime. Numerical results illustrate the blocking phenomenon. Using the explicit formula of the stagnation points, we show the impact of the eccentricity of the spheroid on the positions of stagnation points. When the spheroid is tilted in the symmetry plane, we construct the velocity and find the explicit condition for the stagnation points. In this case, the blocking phenomenon shows new features with respect to the spherical case, including deformation of fluid particle trajectories in a positive and negative suction pattern. The positive or negative suction depends on the orientation of the spheroid with respect to the background shear.

In Chapter 4, we continue to complete the information about a sphere or spheroid embedded in a rotating flow. From the velocity field, we find the explicit fluid particle trajectory equations for either a fixed or self-rotating sphere embedded in a rotating background flow. Similarly, analytical formula for stagnation points on the sphere and critical points in the interior of the flow are derived. With prescribed self-rotating rate

of the sphere, new phenomena appear in the structure of the flow. The analytical and numerical results for rotating flow past a spheroid are presented at the end of this chapter. When a spheroid is tilted in a direction tangential to the rotation background flow, fluid transport is observed.

The second part of this thesis includes Chapter 5, 6, 7 and 8, whose main objects are flows induced by a slender rod. We study the flow using experimental, theoretical and numerical tools. In Chapter 5, the experimental setup and various tools involved in the experiment are introduced. In Chapter 6, we study the flow induced by a rotating straight rod above a no-slip plane. When a straight rod sweeps out an upright cone, the flow has been studied by Leiterman [48] and Bouzarth et al.[9]. When the straight rod sweeps out a tilted cone, new phenomena are introduced. The fluid particles no longer only move along periodic trajectories as in the upright cone case. As the tilt angle increases, the trajectories deform more and open trajectories are observed numerically. There is net transport based on the flux through a vertical plane. The far field of the flow has been checked for better understanding of the flow structure. In Chapter 7, we study the flow induced by a bent rod sweeping out a cone above a no-slip plane. When the slender rod is bent, there are rich structures of the fluid particle trajectories. One appealing phenomenon is the toroidal structure of the trajectories introduced by the bending. Using Poincaré map, we show how the well-ordered nested tori are influenced by the configuration of the rod. With fully 3D experimental abilities, we carefully go through experimental and theoretical comparison. For the straight rod case, our model shows excellent agreements with the experimental data. For the bent rod, qualitatively, both the model and the experiments capture the toroidal structure. Quantitatively, the predictions of the model show good agreement with many, but not all, observations from experimental studies. The discrepancy especially shows up in long-time comparison. Possible contributions to the discrepancies in both the model and the experiments are

discussed. In Chapter 8, a swimming related application of slender body theory is documented. We focus on the flow induced by a periodic motion of a slender body.

Supplemental information of this thesis is provided in the appendices. In Appendix A, we briefly summarize the fundamental singularities applied in this thesis without derivation and the slender body theory with the canonical results of a uniform flow past a slender body. These have been well documented in Chwang & Wu [19], Pozrikidis [63], and Leiterman [48]. The purpose of the repetition is to make the thesis self-contained. In Appendix B, the error analysis is reported if the flow past or induced by a prolate spheroid is studied with the slender body theory, i.e., the spheroid is approximated by a slender body in the flow. In the Stokes regime, the exact velocity field exists for a uniform or linear shear flow past a spheroid. Improved slender body theory results for several basic flows and the exact solution of a prolate spheroid sweeping out a single cone are reported in Appendix C. In Appendix D, the leading order slender body results for uniform flow past a partial torus are documented. In Appendix E, the details about the non-dimensionalization of the farfield velocity field for the flow in Chapter 8 are supplied. Matlab scripts for a straight rod sweeping out a tilted cone and a bent rod sweeping a cone above a no-slip plane are provided. Appendix G summarizes the terminal velocity for one rigid body or two spheres falling in Stokes flow .

Part I

Theoretical studies of linear shear or rotation Stokes flow past a sphere or spheroid

Chapter 2

Lagrangian blocking in highly viscous shear flows past a sphere

Fluid flow over a rigid body in the Stokes' regime is a fundamental problem and has received attention over more than a century. While the case of uniform flows and its ensuing far-field paradoxes in two and three dimensions are well known, features associated with (spatially) non-uniform fluid flows at the far field have received comparatively less attention in the literature.

For far-field linear flows, some experimental and analytical results have been presented in [36, 23, 65, 42, 62, 19]. In particular, Jeffery [36] provided the solutions for both fluid and body motion for the case of an ellipsoid free to move under the fluid-body forces in an imposed far-field linear flow. Even when the velocity field is analytically available, the Lagrangian viewpoint of the fluid particle motion is seldom studied and general solutions are naturally not available. Interestingly, for a freely rotating sphere with its center fixed at the zero-velocity (horizontal, say) plane of a background linear shear, Cox, Zia & Mason [23] computed fluid particle trajectories in closed form by quadratures. For a fixed body, there are even fewer results for particle trajectories. Bretherton [11], and later Chwang & Wu [19], presented an expression for the stream-function for the 2D flow around a fixed disk with its center on the zero-velocity line in a

linear shear. (In this thesis, we use the terminology "disk" to refer to an infinitely long cylinder whose axis is perpendicular to the background stream, i.e. an inherently two-dimensional setup). These authors noted an interesting blocking phenomenon which was observed numerically and experimentally by Acrivos' group [65, 62]. This blocking behaviour is a strong modification of the particle trajectories from situations without and with a fixed disk: in the absence of the body, particles are swept by the shear flow on straight horizontal lines, never crossing the zero-velocity horizontal line. When the disk is placed into the flow, two regions of fluid emerge in which particles cross the zero-velocity line as they approach the disc in either forward or backward time. Particles initially within these regions are confined to them, and will never pass through the vertical line through the disk's center orthogonal to the background shear flow. One of the focuses of this chapter is to analyse this kind of phenomenon in more general 3D flows associated with a sphere or spheroid.

Generally, the regions where blockage occurs are bounded by separation 'stream-surfaces'. In the 2D case involving linear shear flow past a disk, the height of these separation streamlines becomes infinite far from the disk, an effect which was observed by Bretherton [11] and Chwang & Wu [19] and was conjectured not to persist in 3D shear flow past a fixed sphere. This case appears to not have been studied in detail, although particle trajectories are sketched in the symmetry plane by Robertson & Acrivos [65] and Leal [47].

Most of the existing literature seems to concentrate on the flow velocity field and on the forces acting on the sphere, see for example, [36], [66], [19], [63], [57] and [41]. Here we demonstrate that the blocking phenomenon persists in the 3D flows for the simple linear shear flow past a fixed sphere, and obtain explicit expressions for the blocking regions, such as the bounding stream-surfaces and asymptotic estimates for the blocked regions in the far field.
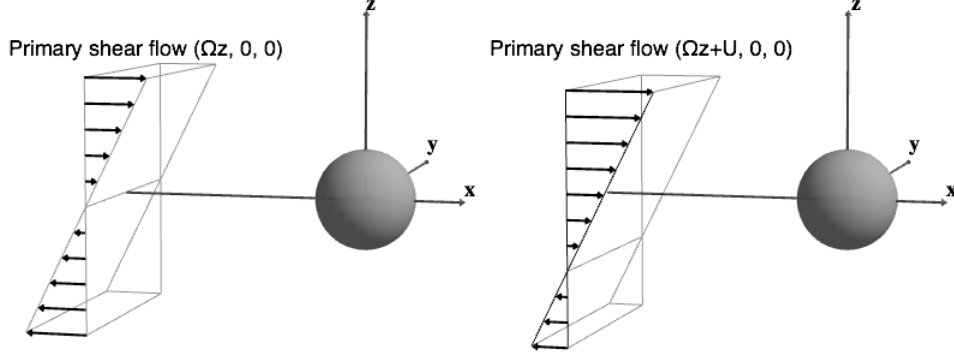
Figure 2.1: Flow past a fixed sphere $x^2 + y^2 + z^2 = a^2$. Without lost of generality, assume $\Omega \geq 0$ and $U \geq 0$.

In this chapter, we thoroughly study the blocking phenomenon for shear flow past a fixed, rigid sphere and document related results. In section 2.1, we introduce the problem and the exact velocity of the flow [19]. In section 2.2, we deduct the trajectory equations of fluid particles, in the closed integral form, for an unbound linear shear flow past a fixed sphere, when the sphere's center is in the zero-velocity plane of the shear flow (see the first case in Figure 2.1). We illustrate the blocking phenomenon in the flow using streamlines in the symmetry plane and separation streamlines. To study the geometry of the blocked flow, we discuss the stagnation lines in detail and compute the area of the cross section of the blocked flow. In section 2.3, we examine the second case shown in Figure 2.1, when the center of the sphere is out the zero-velocity plane of the primary shear. Numerical results indicate the existence of the blocked flow. Complicated bifurcations are found analytically in the flow field with special ratios related to the shear rate, the radius of the sphere, and the distance from the zero velocity plane of the primary shear to the center of the sphere.

2.1 Formulation of problem

We study the motion of an unbounded linear shear flow $\mathbf{U} = \Omega z \mathbf{e}_x + U \mathbf{e}_x$ of constant density ρ and dynamic viscosity μ, past a fixed sphere

$$x^2 + y^2 + z^2 = a^2. \tag{2.1}$$

Since the fluid is incompressible, the continuity equation is

$$\text{div } \mathbf{u} = 0, \tag{2.2}$$

where $\mathbf{u}$ is the fluid velocity. In this thesis, we assume that the inertial terms in the Navier-Stokes equations can be neglected. Thus, the equations of motion are

$$\mu \nabla^2 \mathbf{u} = \nabla p, \tag{2.3}$$

where p denotes the fluid pressure. The condition for (2.3) to hold is that $Re = \Omega a^2 \rho / \mu \ll 1$. The boundary conditions are that $\mathbf{u} = 0$ on the solid boundary, and $\mathbf{u}$ is asymptotic to the basic shear flow at large distances from the rigid body.

Schematics of the problems are shown in Figure 2.1. Case 1 on the left is the shear flow $\Omega z \mathbf{e}_x$ past a fixed sphere at the origin. Case 2 on the right is the shear $\Omega z \mathbf{e}_x + U \mathbf{e}_x$ past the sphere, where the sphere's center is out of the zero-velocity plane of the background shear.

The exact velocity field is constructed by employing Stokes doublets associated with the base vector $\mathbf{e}_x$ and $\mathbf{e}_y$ and potential quadrupole. More details about fundamental singularities can be found in [19]. The velocity field $\mathbf{u}$ for a fixed sphere in the linear

shear is

$$
\begin{aligned}
\mathbf{u} \;=\;& \Omega \left(z\mathbf{e}_x - \frac{5a^3}{6}\frac{3xz\mathbf{x}}{r^5} + \frac{a^3}{2}\frac{\mathbf{e}_y \times \mathbf{x}}{r^3} - \frac{a^5}{6}\nabla\frac{\partial^2}{\partial x \partial z}\frac{1}{r} \right) \\
&+ U\left\{ \mathbf{e}_x - \frac{3a}{4}\left[\frac{\mathbf{e}_x}{r} + \frac{(\mathbf{e}_x \cdot \mathbf{x})\mathbf{x}}{r^3} \right] + \frac{a^3}{4}\nabla\frac{\partial}{\partial x}\frac{1}{r} \right\},
\end{aligned}
\tag{2.4}
$$

where $\mathbf{x} = (x,y,z)$, $r = |\mathbf{x}| = \sqrt{x^2 + y^2 + z^2}$, $\mathbf{e}_x$, $\mathbf{e}_y$ and $\mathbf{e}_y$ are unit vectors along x, y, and z direction, respectively. The force acting on the fixed sphere is $\mathbf{F} = 6\pi\mu\,U\mathbf{e}_x$ and the torque at the origin is $\mathbf{T} = -4\pi\mu\,\Omega\,a^3\mathbf{e}_z$ [19].

Let $\mathbf{x}' = \frac{\mathbf{x}}{a}$, $\mathbf{u}' = \frac{\mathbf{u}}{a\Omega}$ and $U' = \frac{U}{a\Omega}$, nondimensionalizing the equations (dropping the primes), the non-dimensional velocity field is

$$
\begin{aligned}
\mathbf{u} \;=\;& z\mathbf{e}_x - \frac{5}{2}\frac{xz\mathbf{x}}{r^5} + \frac{\mathbf{e}_y \times \mathbf{x}}{2r^3} - \frac{1}{6}\nabla\frac{\partial^2}{\partial x \partial z}\frac{1}{r} \\
&+ U\left[\mathbf{e}_x - \frac{3}{4}\left(\frac{\mathbf{e}_x}{r} + \frac{(\mathbf{e}_x \cdot \mathbf{x})\mathbf{x}}{r^3} \right) + \frac{1}{4}\nabla\frac{\partial}{\partial x}\frac{1}{r} \right].
\end{aligned}
\tag{2.5}
$$

From now on, we use the non-dimensional variables unless stated otherwise.

2.2 Linear shear flow past a sphere whose center is in the zero-velocity plane of the background flow

In this section, we first derive closed formulae for the fluid particle trajectories in the case of an unbounded linear shear past a fixed unit sphere, whose center lies in the zero-velocity plane of the background shear flow. Then, we investigate the blocking phenomena based on the trajectory equations. We report results about the flow's structure on the $y = 0$ symmetry plane followed by results out of this symmetry plane, and compare these results with the 2D flow around an infinitely long cylinder. We

analytically calculate the stagnation points, the 3D separatrix, and the measurement of blocking regions. Additionally, we analyze the structure of the flow near the sphere. For this case, the center of the sphere is in the zero-velocity plane of the background, and the velocity field is a simplified form of equation (2.5)

$$\mathbf{u} = z\mathbf{e}_x - \frac{5}{2}\frac{xz\,\mathbf{x}}{r^5} + \frac{\mathbf{e}_y \times \mathbf{x}}{2r^3} - \frac{1}{6}\nabla\frac{\partial^2}{\partial x \partial z}\frac{1}{r}. \tag{2.6}$$

2.2.1 Exact quadrature formulae for the fluid particle trajectories

Here, streamlines may be constructed as the intersection of two stream surfaces for a 3D flow. Of course, it is not always possible to find explicit formulas of streamlines for a flow field, and we show how particle trajectories may be computed in closed form for the complex flow under study in this chapter.

Based on the special geometry of this problem, we change the coordinates from rectangular coordinates to spherical coordinates (r, ϕ, θ). Using the explicit fluid flow, we may immediately write the particle trajectory equations in spherical coordinates as:

$$\begin{cases} \frac{dr}{dt} &= \cos(\theta)\sin(2\phi)\frac{3-5r^2+2r^5}{4r^4}, \\ \frac{d\theta}{dt} &= \sin(\theta)\cot(\phi)\frac{1+r^2-2r^5}{2r^5}, \\ \frac{d\phi}{dt} &= \cos(\theta)\frac{\cos(2\phi)(r^5-1)+r^5-r^2}{2r^5}, \end{cases} \tag{2.7}$$

where $r = \sqrt{x^2+y^2+z^2}$ $(1 \leq r < \infty)$, $\phi = \arccos\left(\frac{z}{r}\right)$ $(0 \leq \phi \leq \pi)$, and $\theta = \arctan\left(\frac{y}{x}\right)$ $(0 \leq \theta \leq 2\pi)$.

Since ODE system (2.7) is an autonomous system, we eliminate time t and use the

radius r as a new independent variable giving a system for $\frac{d\phi}{dr}$ and $\frac{d\theta}{dr}$:

$$\frac{d\theta}{dr} = \frac{(1 + r^2 - 2r^5)\tan(\theta)}{(3r - 5r^3 + 2r^6)\sin^2(\phi)},$$
$$\frac{d\phi}{dr} = \frac{-r^2 + r^5 + (r^5 - 1)\cos(2\phi)}{r(3 - 5r^2 + 2r^5)\cos(\phi)\sin(\phi)}.$$

Next, changing the variable $y = r\sin(\theta)\sin(\phi)$ and taking the derivative of y with respect to r, yields:

$$\frac{dy}{dr} = \sin(\theta)\sin(\phi) + r\cos(\theta)\sin(\phi)\frac{d\theta}{dr} + r\sin(\theta)\cos(\phi)\frac{d\phi}{dr}.$$

Substituting $\frac{d\theta}{dr}$ and $\frac{d\phi}{dr}$ into the above equation and replacing $\sin(\theta)\sin(\phi)$ with $\frac{y}{r}$, we get

$$\frac{dy}{dr} = \frac{-5(1+r)\sin(\theta)\sin(\phi)}{(r-1)(3 + 6r + 4r^2 + 2r^3)} = \frac{-5(1+r)y}{r(r-1)(3 + 6r + 4r^2 + 2r^3)}. \tag{2.8}$$

Similarly, take derivative of $z = r\cos(\phi)$ with respect to r and substitute $\frac{d\phi}{dr}$ into the resulting formula,

$$\frac{dz}{dr} = \cos(\phi) - r\sin(\phi)\frac{d\phi}{dr} = \frac{(1+r)(3 + 5(2\cos^2(\phi) - 1))}{(6 + 6r - 4r^2 - 4r^3 - 4r^4)\cos(\phi)}.$$

Replacing $\cos(\phi)$ with z/r, the above equation becomes

$$\frac{dz}{dr} = \frac{(r+1)(r^2 - 5z^2)}{r(r-1)(3 + 6r + 4r^2 + 2r^3)z}. \tag{2.9}$$

The obtained ODEs $\frac{dy}{dr}$ and $\frac{dz}{dr}$ decouple.

Using separation of variables, ODE (2.8) can be solved analytically. The analytic

15

solution is,

$$y^3 = C_1 \frac{r^5}{(r-1)^2 (3 + 6r + 4r^2 + 2r^3)}.$$ (2.10)

The ODE in equation (2.9) is not exact, and hence not immediately separable, nonetheless an integrating factor may be found. We rewrite it as

$$\frac{(1+r)(r^2 - 5z^2)}{(r-1)r(3 + 6r + 4r^2 + 2r^3)} dr - z dz = 0.$$

Notice that multiplying this equations by the integrating factor $\frac{(3 - 5r^2 + 2r^5)^{\frac{2}{3}}}{r^{\frac{10}{3}}}$ yields an exact equation which is solved in closed integral form:

$$\int^{\frac{1}{r}} \frac{(1+s)(1-s)^{\frac{1}{3}}}{(2 + 4s + 6s^2 + 3s^3)^{\frac{1}{3}}} ds - \frac{(3 - 5r^2 + 2r^5)^{\frac{2}{3}}}{2 \, r^{\frac{10}{3}}} z^2 = C_2.$$ (2.11)

Here C_1 and C_2 are constants determined by the initial values r_0, y_0, and z_0.

Equations (2.10) and (2.11) describe the fluid particle trajectories. If $r_0 \neq 1$, (2.11) can be rewritten to read:

$$z^2 = \frac{2 \, r^{\frac{10}{3}}}{(3 - 5r^2 + 2r^5)^{\frac{2}{3}}} \int_{\frac{1}{r}}^{\frac{1}{r_0}} \frac{(1+s)(1-s)}{(2 - 5s^3 + 3s^5)^{\frac{1}{3}}} ds + z_0^2 \left(\frac{r}{r_0}\right)^{\frac{10}{3}} \left(\frac{3 - 5r_0^2 + 2r_0^5}{3 - 5r^2 + 2r^5}\right)^{\frac{2}{3}}.$$ (2.12)

This equation expresses the height, z, of the fluid particle trajectory in terms of r. These trajectory equations provide rigorous tools to study the blocking phenomenon.

2.2.2 Blocking phenomenon

Here we analyze the blocking phenomena which occurs in this flow. This blocking behavior is a strong modification of the particle trajectories from situations without and with a fixed solid sphere present in the flow: In the absence of a solid sphere,

16

particles released in the shear flow (starting, say, above the $z = 0$ plane) will be swept from large negative x values, to large positive x values as time progresses. However, when the fixed, solid sphere is introduced into the flow, a large measure of particle trajectories lose this streaming property. Namely, blocked particles starting with large negative x values do not pass the sphere as time progresses, but rather, limit back to large negative x values as time progresses. The regions where this behavior occurs in three dimensional space are defined to be the "blocked regions" of the flow. See Figure 2 which depicts this blocking region when the flow is restricted to the two dimensional symmetry plane. We note that this type of behavior has been observed for the case of an infinitely long cylinder immersed in a linear shear flow by Chwang & Wu [19]; however, they conjectured that this behavior would not persist for situations involving a sphere (instead of a cylinder). Here, we show that in fact for the case of the sphere, the blocking region persists, and moreover, we analytically compute the geometry of this region, and show that it has infinite cross-sectional area. With the exact, closed form expressions for the particle trajectories given in equations (2.10) and (2.12), we may proceed directly to computing the geometry of the blocked regions.

Blocking phenomenon in the $y = 0$ symmetry plane

In the $y = 0$ plane, the velocity field is

$$
\begin{aligned}
u(x, 0, z) &= z\left(1 - \frac{1}{2r^3} - \frac{5x^2}{2r^5} - \frac{z^2 - 4x^2}{2r^7}\right), \\
v(x, 0, z) &= 0, \\
w(x, 0, z) &= x\left(\frac{1}{2r^3} - \frac{5z^2}{2r^5} - \frac{x^2 - 4z^2}{2r^7}\right),
\end{aligned}
$$

and $r = \sqrt{x^2 + y^2 + z^2} = \sqrt{x^2 + z^2}$. Notice that one velocity component v vanishes. Particles initially on this plane never leave this plane, i.e. $y = 0$ for the particle
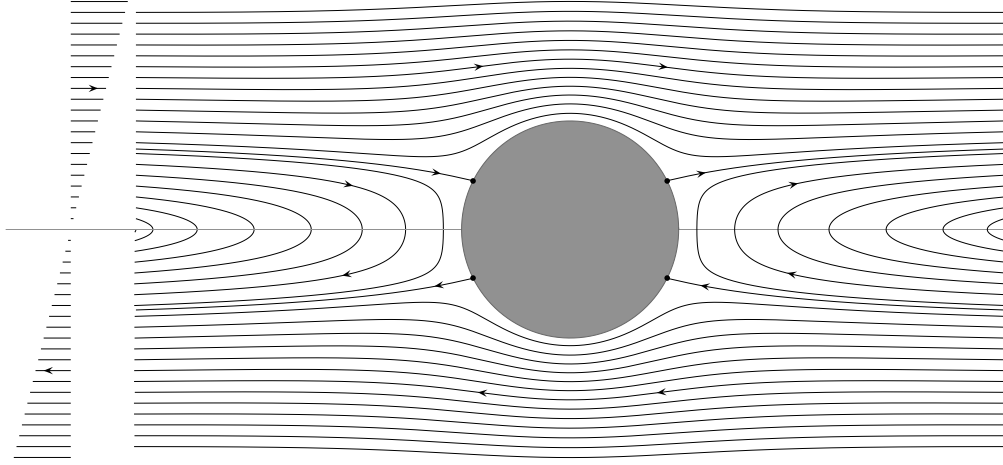
Figure 2.2: Streamlines in the $y = 0$ plane with the linear shear flow $z\mathbf{e}_x$ past a fixed sphere. The four black points on the sphere are stagnation points in this symmetry plane. Note that the separatrix height limits to approximately 0.88207 and is rigorously less than unity.

trajectory. Fluid particles in this plane are thus described by the closed integral formula equation (2.12) with $r_0^2 = x_0^2 + z_0^2$ and $r^2 = x^2 + z^2$. The streamlines in the $y = 0$ symmetry plane shown in Figure 2.2 explicitly depict the blocking region. The fully 3D structure of the blocking region will be described below.

The four dots on the sphere in Figure 2.2 are stagnation points. They are $(x, y, z) = (\pm\frac{2}{\sqrt{5}}, 0, \pm\frac{1}{\sqrt{5}})$ in rectangular coordinates. Two other stagnation points on the sphere are located at $(0, \pm1, 0)$, which are out of this symmetry plane. Stagnation points are special among the fixed points that comprise a no-slip boundary. We define a point on such boundaries to be stagnation points if, for any neighborhood of one such point, there exists a subset of material fluid points of the neighborhood that never leave the neighborhood in backward (for a repelling stagnation point) or forward (for an attracting stagnation point) infinite time. We remark that this definition is in fact valid for classifying any fixed point in the flow, not necessarily those on the boundary. The calculation of these fixed points, as well as the explicit calculation of the separatrices will be presented in the following two subsections.

18

From figure 2.2, it is clear that there are blocking regions. For example, the flow is separated by the stagnation line in the second quadrant. Below that stagnation line the flow is trapped on the left side of the sphere.

It is worth comparing this case with that of the analogous 2D flow: For the 2D flow in the case of an infinitely long cylinder immersed in a linear shear flow with the cylinder axis perpendicular to the lines of constant shear [37], the stream function is

$$\phi(x, z) = \frac{1}{2}z^2 \left(1 - \frac{1}{r^2}\right)^2 + \frac{1}{4}\left(1 - \frac{1}{r^2}\right) - \frac{1}{2}\log r$$

see Chwang & Wu [19] for more details. Here $r^2 = x^2 + z^2$, and the radius of the cylinder is unity. The stagnation points on the cylinder are $(\pm\frac{\sqrt{3}}{2}, \pm\frac{1}{2})$. Notice that the separatrix is totally explicit in this case. Moreover, as $x \to \pm\infty$, the height $|z|$ of separatrix goes to ∞. This peculiar behavior is in some sense similar to the well-known Stokes Paradox in 2D uniform flow past a cylinder. Our results below show that the limiting height of the separatrix is finite in the case involving a fixed, rigid sphere, in sharp contrast with the 2D case.

Blocking phenomenon off the $y = 0$ plane

By continuity, it is expected that the blocking phenomenon extends outside the $y = 0$ symmetry plane. Our analytic results not only show the existence of this 3D blocking region, but further establish that the height of the blocking region is bounded by a constant less than the sphere radius, and dependent upon the distance off the symmetry plane. (We will compute explicitly the 3D geometry of the blocked region in subsection 2.2.5 and 2.2.6.)
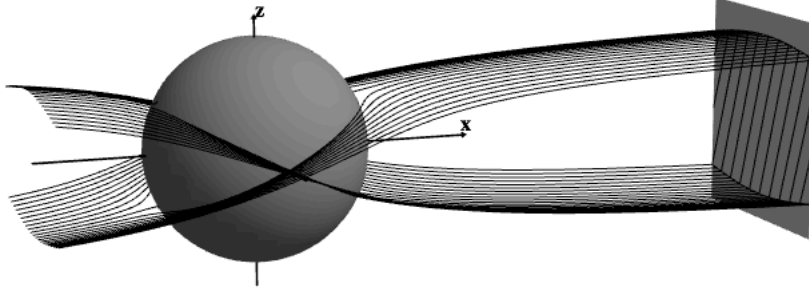
Figure 2.3: Separation surfaces generated by separatrix lines in the flow.

Recall equations (2.10) and (2.12) with initial value (x_0, y_0, z_0):

$$y = y_0 \frac{r^{\frac{5}{3}} (r_0 - 1)^{\frac{2}{3}} (3 + 6r_0 + 4r_0^2 + 2r_0^3)^{\frac{1}{3}}}{r_0^{\frac{5}{3}} (r - 1)^{\frac{2}{3}} (3 + 6r + 4r^2 + 2r^3)^{\frac{1}{3}}},$$

$$z^2 = \frac{2\, r^{\frac{10}{3}}}{(3 - 5r^2 + 2r^5)^{\frac{2}{3}}} \int_{\frac{1}{r}}^{\frac{1}{r_0}} \frac{(1+s)(1-s)^{\frac{1}{3}}}{(2 + 4s + 6s^2 + 3s^3)^{\frac{1}{3}}} ds + z_0^2 \frac{r^{\frac{10}{3}}}{r_0^{\frac{10}{3}}} \left(\frac{3 - 5r_0^2 + 2r_0^5}{3 - 5r^2 + 2r^5} \right)^{\frac{2}{3}},$$

where $r_0 = \sqrt{x_0^2 + y_0^2 + z_0^2}$. Particle trajectories are determined by simultaneously solving (intersecting these surfaces) these equations to obtain a curve relating (x, y, z).

Figure 2.3 shows the separation surfaces in the flow. As shown in this figure, there is a region off the x-z plane between the separation surfaces, where the flow is blocked. The vertical plane in this figure shows the cross section of the blocking region. The cross-sectional area in the limit of $x \to \pm\infty$ will be discussed in subsection 2.2.6.

Figure 2.4a and 2.4b show the stagnation lines close to the sphere and how they connect to the critical points in the flow off the sphere. In this case, the critical points, i.e. fixed points in the flow, are the y-axis outside of the sphere. This line of fixed points is a subset of the original $z = 0$ plane of fixed points present in the absence of

(a) Streamlines close to the sphere.   (b) Zoom in the cube near the y-axis.
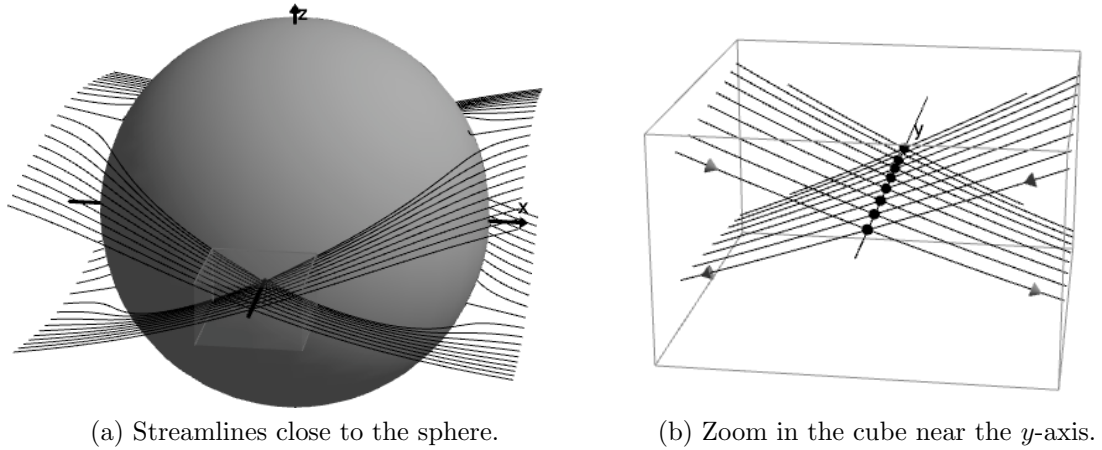
Figure 2.4: Streamlines on separation surfaces close to the sphere.

the rigid sphere. From Figure 2.4b, it is easy to see that they are hyperbolic critical points.

2.2.3   Stagnation points on the sphere

Since all points on a solid boundary are fixed points of the flow, special care is needed to define stagnation points which reside on a solid boundary. This degeneracy on solid boundaries may be split by computing those points on the boundary for which the linearization of the velocity vector field vanishes. These will define the stagnation points on the rigid boundary. Streamlines in the fluid which end at any stagnation point (whether in the fluid or on the boundary) are referred to as stagnation lines. Stagnation lines ending on the boundary are not necessarily perpendicular to the no-slip, rigid boundary. For 2D flow, the angle between the stagnation line and the rigid surface can be computed, as seen in Pozrikidis [63].

To find the stagnation points on the sphere, we linearize and rescale the velocity equation near the surface of the sphere. When the velocity field in spherical coordinates

are linearized with respect to radius r at 1, the expansions are

$$
\begin{aligned}
\frac{dr}{dt} &= O((r-1)^2), \\
\frac{d\theta}{dt} &= -4\cot(\phi)\sin(\theta)(r-1) + O((r-1)^2), \\
\frac{d\phi}{dt} &= \frac{3+5\cos(2\phi)}{2}\cos(\theta)(r-1) + O((r-1)^2).
\end{aligned}
$$

After rescaling time $\tau = t(r-1)$ and neglecting the higher order, we reduce the ODE system to

$$
\begin{aligned}
\frac{dr}{d\tau} &= 0, \\
\frac{d\theta}{d\tau} &= -4\cot(\phi)\sin(\theta), \\
\frac{d\phi}{d\tau} &= \frac{3+5\cos(2\phi)}{2}\cos(\theta).
\end{aligned}
\tag{2.13}
$$

The steady state of the above ODE system provides the stagnation points, yielding the following conditions:

$$
\cot(\phi)\sin(\theta) = 0, \qquad 2\cos(\theta)(5\cos^2(\phi) - 1) = 0.
$$

Since $1 \leq r \leq \infty$, $0 \leq \phi \leq \pi$, $0 \leq \theta < 2\pi$, six stagnation points on the sphere are

$$
r = 1, \quad
\begin{cases}
\theta = 0, \pi, \\
\phi = \arccos\left(\frac{1}{\sqrt{5}}\right), \arccos\left(-\frac{1}{\sqrt{5}}\right);
\end{cases}
\quad \text{and} \quad
\begin{cases}
\theta = \frac{\pi}{2}, \frac{3\pi}{2}; \\
\phi = \frac{\pi}{2}
\end{cases}.
$$

Rewritten in rectangular coordinates, these points are located at

$$
(0, \pm 1, 0), \qquad \left(\pm\frac{2}{\sqrt{5}}, 0, \pm\frac{1}{\sqrt{5}}\right)
\tag{2.14}
$$

(the last ones in the $y = 0$ symmetry plane are plotted in Figure 2.2).

The rescaled velocity field provides an imprint of the particle trajectory pattern just off the sphere surface which mathematically reduces to heteroclinic connections between the stagnation points. These connections can be found from the ODE system (2.13),

$$\frac{d\theta}{d\phi} = -\frac{8\cot(\phi)\tan(\theta)}{3 + 5\cos(2\phi)},$$

and the solution is

$$\sin(\theta)^2 = C\frac{4\cos^2(\phi) - \sin^2(\phi)}{\sin^2(\phi)} = C\frac{5\cos^2(\phi) - 1}{\sin^2(\phi)}, \tag{2.15}$$

where C is a constant depending on the initial value of r, θ, and ϕ. When $r = 1$, using the stagnation points as initial conditions, we get the equation of the trajectories on the sphere in rectangular coordinates:

$$(x, y, z) = \left(\pm 2\cos(\phi), \pm\sqrt{1 - 5\cos^2(\phi)}, \pm\cos(\phi)\right), \quad \left(\arccos\left(1/\sqrt{5}\right) < \phi < \pi/2\right).$$

Or, $r = 1$ and $\cos(\theta) = \pm 2\cot(\phi)$ in the spherical coordinates. These trajectories connect the stagnation points in the rescaled flow field, and demonstrate the topological structure on the sphere (see Figure 2.5). From these trajectories, in the rescaled coordinates, we classify these stagnation points on the sphere as four nodal points (in the symmetry plane) and two hyperbolic points (on the y-axis). We emphasize that the rescaled flows are a projection onto the sphere, and all of these fixed points in the rescaled system correspond to higher order (quadratic) hyperbolic points in the original system.

23
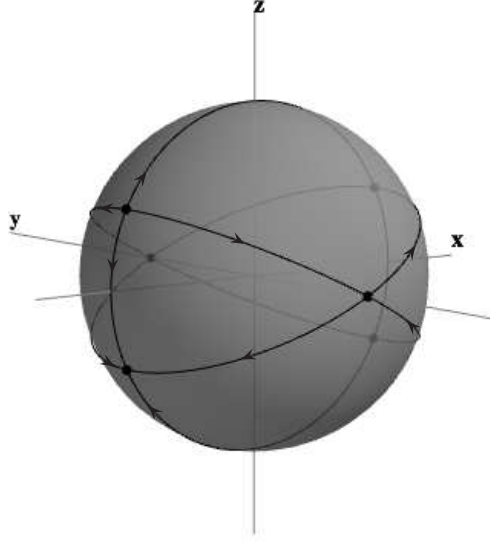
Figure 2.5: "Footprint" of stagnation surfaces on the sphere.

2.2.4 Critical points on the y-axis

Beside the stationary points on the surface of the sphere, we further remark that the entire y-axis exterior to the sphere is a line of fixed points. For finite y values along this line, they are hyperbolic points (in the x-z plane) with orientation depending upon the distance from the sphere. Infinitely far from the sphere along the y-axis, these fixed points lose their hyperbolic structure, with the flow becoming a simple shear flow (the background flow). In this limit, the orientation angle tends to zero. In the opposite limit, approaching the sphere, this line of hyperbolic points tend to the higher order hyperbolic fixed point on the sphere, with the orientation angle depicted by the geodesic curves in Figure 2.5, with tangent value 4/3, which can also be verified by the local analysis near the critical points on the y-axis.

Without loss of generality, we assume $y_0 > 1$ (the radius of the unit sphere). Near

24
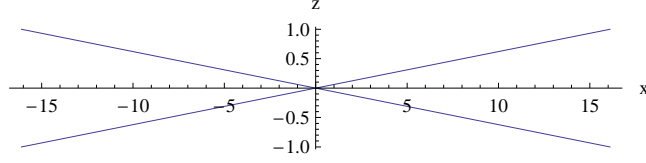
Figure 2.6: Eigenvectors of matrix A at $x = 0$, $y_0 = 5$, $z = 0$.

a point on the y-axis $(0, y_0, 0)$, the linearized velocity field is

$$
\begin{pmatrix} \frac{dx}{dt} \\ \frac{dy}{dt} \\ \frac{dz}{dt} \end{pmatrix} = \begin{pmatrix} 0 & 0 & \frac{2y_0^5 - y_0^2 - 1}{2y_0^5} \\ 0 & 0 & 0 \\ \frac{y_0^2 - 1}{2y_0^5} & 0 & 0 \end{pmatrix} \begin{pmatrix} x \\ y \\ z \end{pmatrix}.
$$

This shows that the flow near $(0, y_0, 0)$ can be reviewed as 2D flow in the x-z plane,

$$
\begin{pmatrix} \frac{dx}{dt} \\ \frac{dz}{dt} \end{pmatrix} = \begin{pmatrix} 0 & \frac{2y_0^5 - y_0^2 - 1}{2y_0^5} \\ \frac{y_0^2 - 1}{2y_0^5} & 0 \end{pmatrix} \begin{pmatrix} x \\ z \end{pmatrix} \equiv A \begin{pmatrix} x \\ z \end{pmatrix}.
$$

Eigenvalues of matrix A are $\pm \frac{(y_0 - 1)\sqrt{(1 + y_0)\left(1 + y_0 + 2y_0^2 + 2y_0^3 + 2y_0^4\right)}}{2y_0^5}$, and the corresponding eigenvectors are

$$
\left(\pm \sqrt{\frac{1 + y_0 + 2y_0^2 + 2y_0^3 + 2y_0^4}{1 + y_0}}, 1 \right).
$$

Figure 2.6 shows the eigenvectors at the point $(0, 5, 0)$. As $y_0 \to \infty$, the angle between the eigenvectors goes to zero. When $y_0 \to 1$, the eigenvectors are $(\pm 2, 1)$, i.e., the tangent value of the angle between these two eigenvectors is $4/3$.

25

2.2.5 Stagnation lines

The precise mathematical definition of the blocking region requires some care to set up. Clearly, the unblocking and blocking regions are divided by the separation surfaces created by stagnation lines in the interior of the fluid as depicted in Figures 2.2 and 2.3. These regions may be succinctly defined as follows: We define the set of unblocked trajectories to be the set of initial points whose particle trajectories intersect the $x = 0$ plane off of the y-axis in finite or infinite time. This set of points is topologically open. The complement of this set (thus closed), we define to be the blocking region. Notice that the boundary of this set defines the separation surface. This connected surface contains the separating surface in the fluid, the y-axis, and the sphere surface.

To calculate this separation surface, we first identify the stagnation lines using the explicit formulae for the trajectory equations given in (2.10) and (2.12), then study their properties on and off the $y = 0$ symmetry plane. Through this analysis, we will prove that the height $|z|$ of stagnation lines is finite as $x \to \pm\infty$ and y fixed.

Stagnation lines in the $y = 0$ symmetry plane

Since one velocity component vanishes in this plane, streamlines are only governed by equation (2.12)

$$z^2 = \frac{1}{\left(\frac{3}{2r^5} - \frac{5}{2r^3} + 1\right)^{\frac{2}{3}}} \left(\int^{\frac{1}{r}} \frac{(1+s)(1-s)^{\frac{1}{3}}}{\left(1 + 2s + 3s^2 + \frac{3}{2}s^3\right)^{\frac{1}{3}}} \, ds + C \right),$$

where C is determined by the initial value $(x_0, 0, z_0)$.

As we know from the previous subsection, four stagnation points on the sphere in this symmetry plane are $(\pm\frac{2}{\sqrt{5}}, 0, \pm\frac{1}{\sqrt{5}})$. We use these points as the initial value and

26

get the equation of the stagnation line in this plane

$$z^2 = \frac{1}{\left(\frac{3}{2r^5} - \frac{5}{2r^3} + 1\right)^{\frac{2}{3}}} \int_{\frac{1}{r}}^{1} \frac{(1+s)(1-s)^{\frac{1}{3}}}{\left(1 + 2s + 3s^2 + \frac{3}{2}s^3\right)^{\frac{1}{3}}} \, ds.$$

A few remarks regarding this stagnation line may be made. First, the height of the stagnation line, $|z|$, is bounded. This is easily seen by replacing the denominator in the integrand by unity, and evaluating the integral. This gives a constant slightly bigger than the unit sphere radius. Second, this bound may be improved substantially through dividing the integral into subintervals and further integrand estimates. In fact, this ultimately establishes very tight upper and lower bounds for the limiting height value of the stagnation line in the limit $x \to \infty$. This upper bound is less than unity, with value 0.8831, and the lower bound is 0.8811. Numerically, we find

$$|z_{max}| \approx 0.88207 \quad \text{as } r \to \infty.$$

Integral estimates for the height of the stagnation line

In the $y = 0$ symmetry plane, the height of the stagnation lines $|z|$ satisfies the following equation

$$z^2 = \frac{1}{\left(\frac{3}{2r^5} - \frac{5}{2r^3} + 1\right)^{2/3}} \int_{\frac{1}{r}}^{1} \frac{(1+s)(1-s)^{1/3}}{\left(1 + 2s + 3s^2 + \frac{3}{2}s^3\right)^{1/3}} \, ds.$$

Let $\epsilon = \frac{1}{r}$, then

$$z^2 = \frac{1}{\left(\frac{3}{2}\epsilon^5 - \frac{5}{2}\epsilon^3 + 1\right)^{2/3}} \int_{\epsilon}^{1} \frac{(1+s)(1-s)^{1/3}}{\left(1 + 2s + 3s^2 + \frac{3}{2}s^3\right)^{1/3}} ds.$$

As the stagnation line is far from the sphere, $\epsilon \to 0$ in the above equation.

When $\epsilon < \frac{1}{10}$,

$$\int_\epsilon^1 \frac{(1+s)(1-s)^{1/3}}{\left(1+2s+3s^2+\frac{3}{2}s^3\right)^{1/3}}\, ds < z^2 < \left(1+\frac{5\epsilon^3}{3}\right)\int_\epsilon^1 \frac{(1+s)(1-s)^{1/3}}{\left(1+2s+3s^2+\frac{3}{2}s^3\right)^{1/3}}\, ds \ <$$
$$\frac{601}{600}\int_\epsilon^1 \frac{(1+s)(1-s)^{1/3}}{\left(1+2s+3s^2+\frac{3}{2}s^3\right)^{1/3}}\, ds < \frac{601}{600}\int_0^1 \frac{(1+s)(1-s)^{1/3}}{\left(1+2s+3s^2+\frac{3}{2}s^3\right)^{1/3}}\, ds, \qquad (2.16)$$

since $1 < \frac{1}{\left(\frac{3}{2}\epsilon^5 - \frac{5}{2}\epsilon^3 + 1\right)^{2/3}} < 1 + \frac{5\epsilon^3}{3} < \frac{601}{600}$.

When $\epsilon < \frac{1}{1000}$,

$$\int_\epsilon^1 \frac{(1+s)(1-s)^{1/3}}{\left(1+2s+3s^2+\frac{3}{2}s^3\right)^{1/3}}\, ds > \int_0^1 \frac{(1+s)(1-s)^{1/3}}{\left(1+2s+3s^2+\frac{3}{2}s^3\right)^{1/3}}\, ds - \epsilon$$
$$> \int_0^1 \frac{(1+s)(1-s)^{1/3}}{\left(1+2s+3s^2+\frac{3}{2}s^3\right)^{1/3}}\, ds - \frac{1}{1000}.$$

Substitute the above lower bound into (2.16), the height of the stagnation line $|z|$ is bounded as

$$\int_0^1 \frac{(1+s)(1-s)^{1/3}}{\left(1+2s+3s^2+\frac{3}{2}s^3\right)^{1/3}}\, ds - \frac{1}{1000} < z^2 < \frac{601}{600}\int_0^1 \frac{(1+s)(1-s)^{1/3}}{\left(1+2s+3s^2+\frac{3}{2}s^3\right)^{1/3}}\, ds. \qquad (2.17)$$

Next, we break the integral interval into two subintervals $[0, \frac{1}{2}]$ and $[\frac{1}{2}, 1]$ and estimate the integrand on each subintervals.

When $0 \le s \le \frac{1}{2}$,

$$L_1 \equiv \left(1 - s^2 + \frac{5s^3}{6} - \frac{4s^5}{3} + \frac{25s^6}{18} + \frac{s^7}{2} - \frac{55s^8}{18}\right) < \frac{(1+s)(1-s)^{1/3}}{\left(1+2s+3s^2+\frac{3}{2}s^3\right)^{1/3}} \qquad (2.18)$$
$$< \left(1 - s^2 + \frac{5s^3}{6} - \frac{4s^5}{3} + \frac{25s^6}{18} + \frac{s^7}{2}\right) \equiv H_1, \qquad (2.19)$$

and when $\frac{1}{2} \leq s \leq 1$,

$$L_2 = \left(\tfrac{2}{15}\right)^{1/3} (1-s)^{1/3} \left[2 + \tfrac{1}{10}(1-s)\right] < \frac{(1+s)(1-s)^{1/3}}{\left(1+2s+3s^2+\frac{3}{2}s^3\right)^{1/3}} \tag{2.20}$$

$$< \left(\tfrac{2}{15}\right)^{1/3} (1-s)^{1/3} \left[2 + \tfrac{(1-s)}{9} + \tfrac{(1-s)^2}{81} - \tfrac{347(1-s)^3}{10935} - \tfrac{4261(1-s)^4}{98415}\right] = H_2. \tag{2.21}$$

Evaluate the integrals with the lower or upper bounds in (2.18)-(2.21),

$$\int_0^{\frac{1}{2}} L_1 \, ds = \frac{1089251}{2322432}, \qquad \int_0^{\frac{1}{2}} H_1 \, ds = \frac{121199}{258048}, \qquad \int_{\frac{1}{2}}^1 L_2 \, ds = \frac{713^{2/3}}{2805^{1/3}},$$

and

$$\int_{\frac{1}{2}}^1 H_2 \, ds = \frac{1164154073}{1528450560015^{1/3}}.$$

Keep four decimal places and substitute these estimations into (2.17), the estimates for z^2 are $0.7764 < z^2 < 0.7799$. Eventually, the bounds for the height of the stagnation lines far from sphere $r \to \infty$ are

$$0.8811 < |z| < 0.8831 .$$

Stagnation lines off the $y = 0$ symmetry plane

We next calculate the stagnation surface out of the symmetry plane. As shown in subsection 2.2.4, the set of critical points which are detached from the sphere is the y-axis. Thus any stagnation line not in the symmetry plane must contain a unique point on the y-axis (as shown in Figure 2.3 and Figure 2.4 which demonstrate this fact). We use these critical points as the initial conditions $r_0 = y_0 > 1$, $z_0 = 0$, and substitute them into the parametric equations for the fluid particle trajectory to obtain

29

stagnation lines lying outside of the symmetry plane

$$y = y_0 \frac{r^{\frac{5}{3}} (y_0 - 1)^{\frac{2}{3}} (3 + 6y_0 + 4y_0^2 + 2y_0^3)^{\frac{1}{3}}}{y_0^{\frac{5}{3}} (r - 1)^{\frac{2}{3}} (3 + 6r + 4r^2 + 2r^3)^{\frac{1}{3}}}, \tag{2.22}$$

$$z^2 = \frac{2\, r^{\frac{10}{3}}}{(3 - 5r^2 + 2r^5)^{\frac{2}{3}}} \int_{\frac{1}{r}}^{\frac{1}{y_0}} \frac{(1+s)(1-s)^{\frac{1}{3}}}{(2 + 4s + 6s^2 + 3s^3)^{\frac{1}{3}}} ds. \tag{2.23}$$

This provides the equations for the stagnation lines out the symmetry plane.

Notice that the stagnation line in the symmetry plane terminates on the sphere at a point which is not on the y-axis. So next we investigate how the points on the separation surface close to the symmetry plane topologically connect stagnation lines intersecting the y-axis with the stagnation line in the symmetry plane. (Due to the symmetry of the flow, we only consider the case of y_0 close to $+1$.)

Using the y coordinate of the stagnation lines crossing the y-axis given in equation (2.22), with initial condition $(0, 1 + \delta, 0)$ ($\delta \ll 1$), we have

$$y = \left(\frac{\delta^2 (15 + 20\delta + 10\delta^2 + 2\delta^3)}{2(1+\delta)^2} \right)^{\frac{1}{3}} \left(1 - \frac{1}{r} \right)^{-\frac{2}{3}} \left(1 + \frac{2}{r} + \frac{3}{r^2} + \frac{3}{2r^3} \right)^{-\frac{1}{3}}.$$

The initial condition specifies a point close to $(0, 1, 0)$. In the limit of $r \to \infty$, this limits to

$$\left(\frac{15}{2} \right)^{\frac{1}{3}} \delta^{\frac{2}{3}} \frac{\left(1 + \frac{4\delta}{3} + \frac{2}{3}\delta^2 + \frac{2}{15}\delta^3 \right)^{\frac{1}{3}}}{(1+\delta)^{\frac{2}{3}}},$$

and as $\delta \to 0$, the leading order approximation is $\left(\frac{15}{2} \right)^{\frac{1}{3}} \delta^{\frac{2}{3}}$. This shows that the out of the symmetry plane stagnation line crossing the critical point $(0, y_0, 0)$, which is sufficiently close to the stagnation point $(0, 1, 0)$ on the sphere, asymptotically approaches the stagnation line in the $y = 0$ plane as $r \to \infty$ (we note that the z value given in equation (2.23) trivially converges in this limit to the limiting height computed above). This property guarantees that the blocking region at $x = \infty$ is completely characterized by the separation lines which intersect the y-axis. This will be very useful in measuring
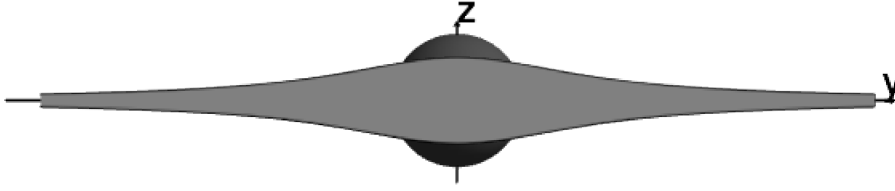
Figure 2.7: Light gray area is the front view of the cross section of the bounded blocking region at $x = \infty$.

the cross-sectional area of the blocking region.

2.2.6 Cross-sectional area of the blocking region

We next study the geometry of this blocking region far from the sphere. We do this by examining its cross-sectional structure (as in Figure 2.3 and Figure 2.7).

Unfortunately, at finite distances from the body, this cross-sectional region of intersecting the plane $x = L$ with the stagnation surface is not readily provided by the equations in (2.22) and (2.23) as they are parametrized by the spherical radius. Fortunately, we can overcome this difficulty by working with $L \to \infty$ since $r \sim x$ in this limit. In this limit, the formulae in equations (2.22) and (2.23) provide (y, z) coordinates for the curves bounding the blocking region, shown for large, but finite L, in Figure 2.7). While from this figure it is clear that the height $z = z(y)$ will decay to zero as $y \to \infty$, the limiting procedure yields a parametric representation (with parameter y_0) for this curve. To obtain the decay rate of $z(y)$ as $y \to \infty$ (which is critical to determine if the cross-sectional area is infinite) requires further analysis.

From the equations of the stagnation lines (2.22) and (2.23), we get

$$y \sim y_0 \left(1 - \frac{1}{y_0}\right)^{\frac{2}{3}} \left(1 + \frac{2}{y_0} + \frac{3}{y_0^2} + \frac{3}{2y_0^3}\right)^{\frac{1}{3}}, \tag{2.24}$$

$$z^2 \sim \int_0^{\frac{1}{y_0}} \frac{(1+s)(1-s)^{\frac{1}{3}}}{\left(1 + 2s + 3s^2 + \frac{3}{2}s^3\right)^{\frac{1}{3}}} ds = (z_\infty)^2, \tag{2.25}$$

as $r \to \infty$ by taking $x \to \infty$, where $z_\infty > 0$. Here y_0, a point on the y-axis, is the initial value in the trajectory equations for y, and z. This parametric representation for the curve $z = z(y)$ may be viewed as an image of the y axis under the flow after infinite time, which we may use to derive an explicit expression for the cross-sectional area. To whit, the Jacobian matrix for this mapping is

$$\frac{dy}{dy_0} = \left(1 + \frac{3}{2y_0^5} - \frac{5}{2y_0^3}\right)^{\frac{1}{3}} + \frac{5(1+y_0)}{2y_0^4 \left(1 - \frac{1}{y_0}\right)^{\frac{1}{3}} \left(2 + \frac{4}{y_0} + \frac{6}{y_0^2} + \frac{3}{y_0^3}\right)^{\frac{2}{3}}}.$$

The area of the blocking flow is noted as A,

$$\frac{A}{4} = \int_0^\infty z(y)\, dy = \int_1^\infty z_\infty (y_0) \frac{dy}{dy_0} dy_0$$

$$= \int_1^\infty z_\infty \left(1 + \frac{3}{2y_0^5} - \frac{5}{2y_0^3}\right)^{\frac{1}{3}} dy_0 + \int_1^\infty z_\infty \frac{5(1+y_0)}{2y_0^4 \left(1 - \frac{1}{y_0}\right)^{\frac{1}{3}} \left(2 + \frac{4}{y_0} + \frac{6}{y_0^2} + \frac{3}{y_0^3}\right)^{\frac{2}{3}}} dy_0$$

$$= \text{Part1} + \text{Part2}.$$

For integral Part2, the leading order of the integrand $\dfrac{5(1+y_0)}{2y_0^4 \left(1 - \frac{1}{y_0}\right)^{\frac{1}{3}} \left(2 + \frac{4}{y_0} + \frac{6}{y_0^2} + \frac{3}{y_0^3}\right)^{\frac{2}{3}}}$ is $\dfrac{5}{2(2)^{\frac{2}{3}} y_0^3}$ as $y_0 \to \infty$. Notice that integrand in equation (2.25) is bounded. Consequently, an upper bound for the decay of z_∞ is $\sqrt{\frac{1}{y_0}}$ as $y_0 \to \infty$. Thus, the integral Part2 is bounded.

We next show that integral Part1 diverges:

$$\text{Part1} = \int_1^\infty z_\infty \left(1 - \frac{5}{2y_0^3} + \frac{3}{2y_0^5}\right)^{\frac{1}{3}} dy_0 \ .$$

Substitute $z_\infty(y_0)$ in equation (2.25) into the integrand

$$\text{Part1} = \int_1^\infty \left(\int_0^{\frac{1}{y_0}} \frac{(1+s)(1-s)^{\frac{1}{3}}}{\left(1 + 2s + 3s^2 + \frac{3}{2}s^3\right)^{\frac{1}{3}}} ds \right)^{\frac{1}{2}} \left(1 - \frac{5}{2y_0^3} + \frac{3}{2y_0^5}\right)^{\frac{1}{3}} dy_0,$$

As $y_0 \to \infty$,

$$\left(1 - \frac{5}{2y_0^3} + \frac{3}{2y_0^5}\right)^{\frac{1}{3}} \to 1.$$

Using the following result to estimate the integral in the kernel (which follows directly through straightforward Taylor expansion),

$$\int_0^\eta \frac{(1+s)(1-s)^{\frac{1}{3}}}{\left(1 + 2s + 3s^2 + \frac{3}{2}s^3\right)^{\frac{1}{3}}} ds = \eta - \frac{\eta^3}{3} + O\left(\eta^4\right),$$

This establishes the following asymptotic expansion:

$$\int_0^{\frac{1}{y_0}} \frac{(1+s)(1-s)^{\frac{1}{3}}}{\left(1 + 2s + 3s^2 + \frac{3}{2}s^3\right)^{\frac{1}{3}}} ds \sim \frac{1}{y_0} \quad \text{as} \ y_0 \to \infty.$$

So, the integrand of Part1 is asymptotic to $\sqrt{\frac{1}{y_0}}$ as $y_0 \to \infty$. With such a decay rate the integral $\int_1^\infty \sqrt{\frac{1}{y_0}} dy_0 = \infty$ is divergent. Since the integrand is sign definite, this result shows that Part1 is divergent. Consequently, the total **area of the cross-section of the blocking region is infinite** when the plane $x = x_0 \to \infty$.

In the y-z plane (i.e. $x = 0$), the blocking region is the y-axis , i.e. the area of the cross section is zero. This is in sharp contrast with the calculation just presented above,

where it was shown that at $x = \infty$, the cross section of the blocking region is infinite. Since the explicit, closed form formula for the area at an arbitrary distance from the sphere is not available, we study its behavior by analyzing the integrand involved here under different asymptotic limits. We will see a continuous connection between zero cross-sectional blocking area at $x = 0$, to diverging cross-sectional blocking area as $x \to \infty$.

The separation surface is generated by the stagnation lines cross the critical points $(0, y_0, 0)$ on the y-axis, where $|y_0| > 1$. If we take the cross section of the blocking region at x_0, then $y^2 + z^2 = r^2 - x_0^2$. Based on the trajectory equation (2.22) and (2.23),

$$\left(\frac{3}{2}\frac{1}{r^5} - \frac{5}{2}\frac{1}{r^3} + 1\right)^{2/3} \left(r^2 - x_0^2\right) = \int_{\frac{1}{r}}^{\frac{1}{y_0}} \frac{(s+1)(1-s)^{1/3}}{\left(\frac{3}{2}s^3 + 3s^2 + 2s + 1\right)^{1/3}} ds \tag{2.26}$$
$$+ y_0^2 \left(\frac{3}{2}\frac{1}{y_0^5} - \frac{5}{2}\frac{1}{y_0^3} + 1\right)^{\frac{2}{3}}.$$

From the above equation, we find the mapping from r to y_0 with x_0 fixed. With such a mapping, the boundary of the cross section of the blocking area can be written as parametric functions

$$\begin{cases} y &= y\left(r\left(y_0\right), y_0\right) \\ z &= z\left(r\left(y_0\right), y_0\right) \end{cases} \tag{2.27}$$

at $x = x_0$ fixed. The leading order asymptotic solution to (2.26) is

$$r \sim \sqrt{y_0^2 + x_0^2} \quad \text{as } y_0 \to \infty \quad \text{and } x_0 \text{ fixed.} \tag{2.28}$$

If $\vec{a} = (0, z)$ and $\vec{n}$ is the outer normal direction of the cross section,

$$\vec{a}.\vec{n} = \frac{z(y_0)\frac{dy}{dy_0}}{\left|\frac{dy}{dy_0}\right|}.$$

34

By the Divergence theorem or Gauss' theorem, the cross section of the blocking area I is an explicit integral:

$$\frac{I}{4} = \int_\Omega dA = \int_\Omega \text{div}\vec{a}\ dA = \int_{\partial\Omega} \vec{a}.\vec{n}\ ds = \int_1^\infty \left(z(y_0)\frac{dy}{dy_0} \right) dy_0 . \qquad (2.29)$$

From the asymptotic result (2.28) and several applications of the implicit function theorem to obtain derivative asymptotics (we relegate these technical details to the next subsection), we find that for finite x_0, the integrand decays as $\frac{x_0}{\sqrt{2}y_0^{3/2}}$ when $y_0 \to \infty$, which yields a finite cross-sectional blocking area.

To study the behavior for the blocking area as x_0 increases, we take the cross section at $x_0 = y_0^\epsilon$, where $\epsilon > 0$ is a constant.

- When $0 < \epsilon < 1$, from equation (2.26), we find $r \sim \sqrt{y_0^2 + y_0^{2\epsilon}}$ as $y_0 \to \infty$. Substitute this into the integrand for the blocking area, the integrand for the blocking area is asymptotic to $\frac{1}{\sqrt{2}}\frac{1}{y_0^{3/2-\epsilon}}$. When $0 < \epsilon < \frac{1}{2}$, the integral is convergent. Otherwise, $\frac{1}{2} < \epsilon < 1$, the integral is divergent.

- If the cross section is taken at $x_0 = y_0^\epsilon$ ($\epsilon \geq 1$), then $r \sim \sqrt{y_0^{2\epsilon} + y_0^2}$ as $y_0 \to \infty$. In this case, the integrand of equation (2.29) for the blocking area decays as $\frac{3}{2\sqrt{y_0}}$ with $y_0 \to \infty$.

This illustrates an unreported property about the solution of the Stokes flow but physically not observed. Since, at large distances, the characteristic length used in the Reynolds number need to be redefined, the inertia terms ignored in Navier-Stokes equation are not negligible.

If $\vec{a} = \frac{1}{2}(y, z)$, similar results are hold. Then,

$$\vec{a}.\vec{n} = \frac{1}{2}\frac{z(y_0)\frac{dy}{dy_0} - y(y_0)\frac{dz}{dy_0}}{\sqrt{\left(\frac{dz}{dy_0}\right)^2 + \left(\frac{dy}{dy_0}\right)^2}}.$$

Similarly, by the Divergence theorem or Gauss' theorem, the cross section of the block-ing area I is an explicit integral:

$$\frac{I}{4} \;=\; \int_\Omega dA = \int_\Omega \mathrm{div}\,\vec{a}\; dA = \int_{\partial\Omega} \vec{a}.\vec{n}\; ds = \frac{1}{2}\int_1^\infty \left(z(y_0)\frac{dy}{dy_0} - y(y_0)\frac{dz}{dy_0} \right) dy_0.$$

We find that for finite x_0, the integrand decays as $\frac{x_0}{\sqrt{2}y_0^{3/2}}$ when $y_0 \to \infty$, and

- When $0 < \epsilon < 1$, from equation (2.26), the integrand for the blocking area is asymptotic to $\frac{1}{8\sqrt{2}}\frac{1}{y_0^{3/2-\epsilon}}$. When $0 < \epsilon < \frac{1}{2}$, the integral is convergent. Otherwise, $\frac{1}{2} < \epsilon < 1$, the integral is divergent.

- If the cross section is taken at $x_0 = y_0^\epsilon$ ($\epsilon \geq 1$), the integrand of equation (2.30) for the blocking area decays like $\frac{3}{2\sqrt{y_0}}$ as $y_0 \to \infty$, which leads to the divergence of the integral.

Details of asymptotics of the integrand for the cross-sectional area

In this subsection, we provides the details about the decay rate of the integrand used to compute the cross-sectional area of the blocking region. When the integrand decays fast enough, the integral is convergent, which implies that the cross section of the blocking area is finite. Otherwise, the integral is divergent and the cross-sectional area of the blocking region is infinite.

The closed integral form trajectory equations (2.22) and (2.23) of the fluid particles are

$$y \;=\; y_0 \left(\frac{\left(1-\frac{1}{y_0}\right)^2 \left(\frac{3}{2}\frac{1}{y_0^3} + 3\frac{1}{y_0^2} + 2\frac{1}{y_0} + 1\right)}{\left(1-\frac{1}{r}\right)^2 \left(\frac{3}{2}\frac{1}{r^3} + 3\frac{1}{r^2} + 2\frac{1}{r} + 1\right)} \right)^{1/3}, \tag{2.30}$$

$$z^2 \;=\; \frac{1}{\left(1+\frac{3}{2r^5} - \frac{5}{2r^3}\right)^{2/3}} \int_{\frac{1}{r}}^{\frac{1}{y_0}} \frac{(s+1)(1-s)^{1/3}}{\left(\frac{3}{2}s^3 + 3s^2 + 2s + 1\right)^{1/3}} ds. \tag{2.31}$$

36

Substituting y and z in the originally ODE system used to derive the trajectory equations, we have

$$
\begin{aligned}
\frac{dy}{dr} &= \frac{5\left(\frac{1}{r}+1\right)y}{(1-r)\left(3+6r+4r^2+2r^3\right)} \\
&= \frac{5y_0\left(\frac{1}{r}+1\right)}{(1-r)\left(3+6r+4r^2+2r^3\right)}\left[\frac{\left(1-\frac{1}{y_0}\right)^2\left(\frac{3}{2}\frac{1}{y_0^3}+3\frac{1}{y_0^2}+2\frac{1}{y_0}+1\right)}{\left(1-\frac{1}{r}\right)^2\left(\frac{3}{2}\frac{1}{r^3}+3\frac{1}{r^2}+2\frac{1}{r}+1\right)}\right]^{\frac{1}{3}} \quad (2.32)
\end{aligned}
$$

$$
\begin{aligned}
\frac{dz}{dr} &= \frac{(1+r)\left(\frac{5}{r^2}z^2-1\right)}{3+3r-2r^2-2r^3-2r^4}\frac{r}{z} \\
&= \frac{(1+r)r\left(\frac{5}{r^2\left(\frac{3}{2}\frac{1}{r^5}-\frac{5}{2}\frac{1}{r^3}+1\right)^{\frac{2}{3}}}\int_{\frac{1}{r}}^{\frac{1}{y_0}}\frac{(s+1)(1-s)^{\frac{1}{3}}}{\left(\frac{3}{2}s^3+3s^2+2s+1\right)^{\frac{1}{3}}}ds-1\right)}{(3+3r-2r^2-2r^3-2r^4)\left\{\frac{1}{\left(\frac{3}{2}\frac{1}{r^5}-\frac{5}{2}\frac{1}{r^3}+1\right)^{\frac{2}{3}}}\int_{\frac{1}{r}}^{\frac{1}{y_0}}\frac{(s+1)(1-s)^{\frac{1}{3}}}{\left(\frac{3}{2}s^3+3s^2+2s+1\right)^{\frac{1}{3}}}ds\right\}^{\frac{1}{2}}} \quad (2.33)
\end{aligned}
$$

All these four equations are in terms of r and y_0.

If $x = x_0$, from $x^2 = r^2 - y^2 - z^2$, we derive the following constraint

$$
\left(1-\frac{5}{2r^3}+\frac{3}{2r^5}\right)^{\frac{2}{3}}\left(r^2-x_0^2\right)=\int_{\frac{1}{r}}^{\frac{1}{y_0}}\frac{(s+1)(1-s)^{\frac{1}{3}}}{\left(\frac{3}{2}s^3+3s^2+2s+1\right)^{\frac{1}{3}}}ds+y_0^2\left(1-\frac{5}{2y_0^3}+\frac{3}{2y_0^5}\right)^{\frac{2}{3}}.
$$

Taking implicit differentiation, we have

$$
\begin{aligned}
\frac{dr}{dy_0} &= \frac{2y_0^5-y_0^2-1}{y_0^4(1-\frac{5}{2r^3}+\frac{3}{2r^5})^{2/3}(1-\frac{5}{2y_0^3}+\frac{3}{2y_0^5})^{1/3}} \Bigg/ \\
&\quad \left\{\frac{\left(1-\frac{1}{r}\right)\left(1+\frac{1}{r}\right)}{r^2\left(1-\frac{5}{2r^3}+\frac{3}{2r^5}\right)}+\frac{10y_0^2(1+r)}{r(r-1)(3+6r+4r^2+2r^3)}\left(\frac{1+\frac{3}{2y_0^5}-\frac{5}{2y_0^3}}{1-\frac{5}{2r^3}+\frac{3}{2r^5}}\right)^{\frac{2}{3}}\right. \\
&\quad \left.+2r-\frac{5\left(1-r^2\right)}{r^6\left(1-\frac{5}{2r^3}+\frac{3}{2r^5}\right)^{\frac{5}{3}}}\int_{\frac{1}{r}}^{\frac{1}{y_0}}\frac{(s+1)(1-s)^{\frac{1}{3}}}{\left(\frac{3}{2}s^3+3s^2+2s+1\right)^{1/3}}ds\right\}.
\end{aligned}
$$

Also, from the trajectory equation, we get

$$\frac{\partial y\,(r, y_0)}{\partial y_0} = -\frac{(y_0^5 - 1)}{y_0^5 \left(1 - \frac{5}{2r^3} + \frac{3}{2r^5}\right)^{1/3} \left(1 - \frac{5}{2y_0^3} + \frac{3}{2y_0^5}\right)^{2/3}}, \tag{2.34}$$

$$\frac{\partial z\,(r, y_0)}{\partial y_0} = -\frac{\left(1 - \frac{1}{y_0}\right)\left(1 + \frac{1}{y_0}\right)}{2y_0^2 \left(\int_{\frac{1}{r}}^{\frac{1}{y_0}} \frac{(s+1)(1-s)^{1/3}}{\left(\frac{3}{2}s^3 + 3s^2 + 2s + 1\right)^{1/3}}\,ds\right)^{1/2}} \frac{\left(1 - \frac{5}{2r^3} + \frac{3}{2r^5}\right)^{-1/3}}{\left(1 + \frac{3}{2y_0^5} - \frac{5}{2y_0^3}\right)^{1/3}}. \tag{2.35}$$

Now all the components involved in the integrals for the cross-sectional area are pre-pared in terms of r and y_0.

If $\vec{a} = (0, z)$, then

$$\vec{a} \cdot \vec{n} = \frac{z\frac{dy}{dr}}{\sqrt{\left(\frac{dz}{dr}\right)^2 + \left(\frac{dy}{dr}\right)^2}}, \quad ds = \sqrt{\left(\frac{dz}{dr}\right)^2 + \left(\frac{dy}{dr}\right)^2}\,dr,$$

or

$$\vec{a} \cdot \vec{n} = \frac{z\frac{dy}{dy_0}}{\sqrt{\left(\frac{dz}{dy_0}\right)^2 + \left(\frac{dy}{dy_0}\right)^2}}, \quad ds = \sqrt{\left(\frac{dz}{dy_0}\right)^2 + \left(\frac{dy}{dy_0}\right)^2}\,dy_0.$$

Note the area of the 2D cross section as I. By the divergence theorem, the area of the 2D cross section of the blocked region is

$$\frac{I}{4} = \int_\Omega dA = \int_\Omega \mathrm{div}\,\vec{a}\,dA = \int_{\partial\Omega} \vec{a}.\vec{n}ds = \int_1^\infty z\frac{dy}{dr}\frac{dr}{dy_0}dy_0 = \int_1^\infty z\left(\frac{\partial y}{\partial r}\frac{\partial r}{\partial y_0} + \frac{\partial y}{\partial y_0}\right)dy_0.$$

We will analyze the integrand involved in the cross-sectional area of the blocked region

$$z\left(\frac{\partial y}{\partial r}\frac{\partial r}{\partial y_0} + \frac{\partial y}{\partial y_0}\right),$$

38

to study the property the cross-sectional area of the blocking region.

Substitute all the components (2.30)-(2.35) into the integrand, we write the integrand as function of r and y_0,

$$
\begin{aligned}
z \left(\frac{\partial y}{\partial r} \frac{\partial r}{\partial y_0} + \frac{\partial y}{\partial y_0} \right) &= \frac{1}{\left(1 - \frac{5}{2r^3} + \frac{3}{2r^5}\right)^{\frac{2}{3}}} \left(\int_{\frac{1}{r}}^{\frac{1}{y_0}} \frac{(1+s)(1-s)^{1/3}}{\left(\frac{3}{2}s^3 + 3s^2 + 2s + 1\right)^{1/3}} ds \right)^{\frac{1}{2}} \\
&\left\{ \frac{\left(1 - \frac{1}{y_0^5}\right)}{\left(1 - \frac{5}{2y_0^3} + \frac{3}{2y_0^5}\right)^{\frac{2}{3}}} - \frac{5\left(1 + \frac{1}{r}\right)\left(1 + \frac{1}{y_0^2} - 2y_0^3\right)}{y_0(1-r)\left(3 + 6r + 4r^2 + 2r^3\right)\left(1 - \frac{5}{2r^3} + \frac{3}{2r^5}\right)^{\frac{2}{3}}} \right/ \\
&\left(2r - \frac{102^{2/3}y_0^2\left(1 + \frac{3}{2y_0^5} - \frac{5}{2y_0^3}\right)^{2/3}}{r(1-r)\left(3 + 6r + 4r^2 + 2r^3\right)} + \frac{1 - \frac{1}{r^2}}{r^2\left(1 - \frac{5}{2r^3} + \frac{3}{2r^5}\right)} \right. \\
&\left. - \frac{5\left(1 - r^2\right)}{r^6\left(1 - \frac{5}{2r^3} + \frac{3}{2r^5}\right)^{5/3}} \int_{\frac{1}{r}}^{\frac{1}{y_0}} \frac{(s+1)(1-s)^{1/3}}{\left(\frac{3}{2}s^3 + 3s^2 + 2s + 1\right)^{1/3}} ds \right) \right\}. \quad (2.36)
\end{aligned}
$$

If x_0 is a fixed finite number, from the constraint (2.34), we get the asymptotic solution $r \sim \sqrt{y_0^2 + x_0^2}$. Substitute this solution to the above equation (2.36). The asymptotic result of the integrand is

$$
z \left(\frac{\partial y}{\partial r} \frac{\partial r}{\partial y_0} + \frac{\partial y}{\partial y_0} \right) \sim \frac{x_0}{\sqrt{2} y_0^{3/2}} \quad \text{as } y_0 \to \infty.
$$

At a finite distance $|x_0|$ from the sphere, the cross-sectional area of the blocked region depends on x_0 and is finite.

If the cross section is taken at infinite $x_0 = \infty$, then

$$
y \sim y_0 \left(\left(1 - \frac{1}{y_0}\right)^2 \left(1 + \frac{3}{2y_0^3} + \frac{3}{y_0^2} + \frac{2}{y_0}\right) \right)^{1/3},
$$

$$
z^2 \sim \int_0^{\frac{1}{y_0}} \frac{(s+1)(1-s)^{1/3}}{\left(\frac{3}{2}s^3 + 3s^2 + 2s + 1\right)^{1/3}} ds.
$$

39

The cross-sectional area I is computed as

$$\frac{I}{4} = \int_\Omega dA = \int_\Omega \operatorname{div}\vec{a}\, dA = \int_{\partial\Omega} \vec{a}.\vec{n}\, ds = \int_1^\infty z\frac{dy}{dy_0}\, dy_0.$$

The integrand decays as

$$z\frac{dy}{dy_0} \sim \left(\int_0^{\frac{1}{y_0}} \frac{(s+1)(1-s)^{1/3}}{\left(\frac{3}{2}s^3 + 3s^2 + 2s + 1\right)^{1/3}}\, ds \right)^{1/2} \left(\frac{2^{2/3}\left(-1 + y_0^5\right)\left(\frac{y_0^5}{3 - 5y_0^2 + 2y_0^5}\right)^{2/3}}{y_0^5} \right)$$

$$\sim \frac{1}{\sqrt{y_0}} + \frac{5}{3}\left(\frac{1}{y_0}\right)^{7/2} \qquad \text{when } y_0 \to \infty.$$

With such a decay rate, the integral is divergent. This demonstrates that far enough from the sphere the cross-sectional area is infinite .

To understand the growth of the area, we assume $x_0 = y_0^\epsilon$ ($\epsilon > 0$). Then, from the constraint (2.34), we get the asymptotic solution $r \sim \sqrt{y_0^2 + y_0^{2\epsilon}}$. Substituting this solution into the integrand (2.36) and computing the asymptotic as $y_0 \to \infty$, we have:

- when $0 < \epsilon < 1$, as $y_0 \to \infty$, the leading order of the integrand (2.36) is

$$z\left(\frac{\partial y}{\partial r}\frac{\partial r}{\partial y_0} + \frac{\partial y}{\partial y_0} \right) \sim -\frac{y_0^{-\frac{3}{2} + \epsilon}}{\sqrt{2}} \qquad \text{as } y_0 \to \infty.$$

  As $y_0 \to \infty$, the integrand decays like $y_0^{-\frac{3}{2} + \epsilon}$. Consequently, when $0 < \epsilon < \frac{1}{2}$, the integral is convergent. When $\epsilon \geq \frac{1}{2}$, the integral is divergent.

- when $\epsilon \geq 1$, as $y_0 \to \infty$, the leading order of the integrand (2.36) is

$$z\left(\frac{\partial y}{\partial r}\frac{\partial r}{\partial y_0} + \frac{\partial y}{\partial y_0} \right) \sim -\frac{3}{2\sqrt{y_0}} \qquad \text{as } y_0 \to \infty.$$

  In this case, the cross-sectional area of the blocking region is infinite.

40

2.3 Linear shear flow past a sphere whose center off the zero-velocity plane of the primary shear flow

When the center of the unit sphere $x^2+y^2+z^2=1$ is out of the zero-velocity plane of the background shear flow illustrated in Figure 2.1, the non-dimensional primary linear shear flow can be written as $\mathbf{U}=z\mathbf{e}_x+U\mathbf{e}_x$, in which the uniform flow rate U is related to the shear rate and the distance between the sphere's center and the zero-velocity plane of the shear flow. Without loss the generality, we can assume $U>0$. While a closed form explicit solution in these off-center cases is not available, we explicitly compute the stagnation points on the sphere and the fixed points in the interior of the fluid.

The exact velocity field for the flow is given in equation (2.5). We rewrite the velocity field as an ODE system in spherical coordinates:

$$\begin{cases} \dfrac{dr}{dt} &= \dfrac{Ur(1+2r)+(3+6r+4r^2+2r^3)\cos(\phi)}{2r^4}(r-1)^2\cos(\theta)\sin(\phi), \\ \dfrac{d\theta}{dt} &= \dfrac{Ur\left(1+3r^2-4r^3\right)+2\left(1+r^2-2r^5\right)\cos(\phi)}{4r^5\sin(\phi)}\sin(\theta), \\ \dfrac{d\phi}{dt} &= -\dfrac{Ur\left(1+3r^2-4r^3\right)\cos(\phi)+4\left(1-r^5\right)\cos^2(\phi)+2\left(r^2-1\right)}{4r^5}\cos(\theta), \end{cases} \qquad (2.37)$$

where $1 \le r < \infty$, $0 \le \phi \le \pi$, and $0 \le \theta < 2\pi$. From the above ODE system (2.37), we apply the same approach as we have used in the previous section to attain the ODEs $\frac{dy}{dr}$ and $\frac{dz}{dr}$. Skipping the detail of changing variables and taking derivatives, we get $\frac{dy}{dr}$

and $\frac{dz}{dr}$ with the radius r as a new independent variable:

$$\frac{dy}{dr} = \frac{(1+r)\left(3r^2 U + 10z\right)y}{2(1-r)r\left[r^2(1+2r)U + (3+6r+4r^2+2r^3)z\right]}, \tag{2.38}$$

$$\frac{dz}{dr} = \frac{(1+r)\left(3Uz + 10\frac{z^2}{r^2} - 2\right)}{2(1-r)\left[r(1+2r)U + (3+6r+4r^2+2r^3)\frac{z}{r}\right]}, \tag{2.39}$$

and $x = \sqrt{r^2 - y^2 - z^2}$. Here, $\frac{dy}{dr}$ and $\frac{dz}{dr}$ are no longer decoupled as in the first case, though $\frac{dz}{dr}$ is independent of y. For this case, we have not found the fluid particle trajectories explicitly, but equations (2.38)-(2.39) are crucial to determine the bifurcation diagrams of the flow.

To demonstrate the flow structures, we plot trajectories of fluid particles with different uniform flow rates U. Figure 2.8a and 2.8b show the trajectories of fluid particles in 3D when the sphere's center is in the zero-velocity plane of the background shear flow $(U = 0)$, the case in the previous section; Figure 2.8c and 2.8d show the trajectories with a different background flow $(U = 1)$; and Figure 2.9 is for $U = 3$ in the background shear flow.

2.3.1 Bifurcation of streamlines and stagnation points on the sphere

From the equations (2.37), we find the analytical formulae of the stagnation points on the sphere and the critical points in the interior of the flow. As U varies, the curves of critical points in the interior of the flow deform and the location of the stagnation points on the sphere changes. The curves of the critical points are always in the y-z plane. Figure 2.10 demonstrates bifurcation diagrams in the trajectories for four canonical stages and the transitions between them in the $y = 0$ symmetry plane close to the sphere, as U increases. Critical uniform flow rates $U^\star$ and $U^{\star\star}$ are provided in

(a) $U = 0$ (b) $U = 0$

(c) $U = 1$ (d) $U = 1$
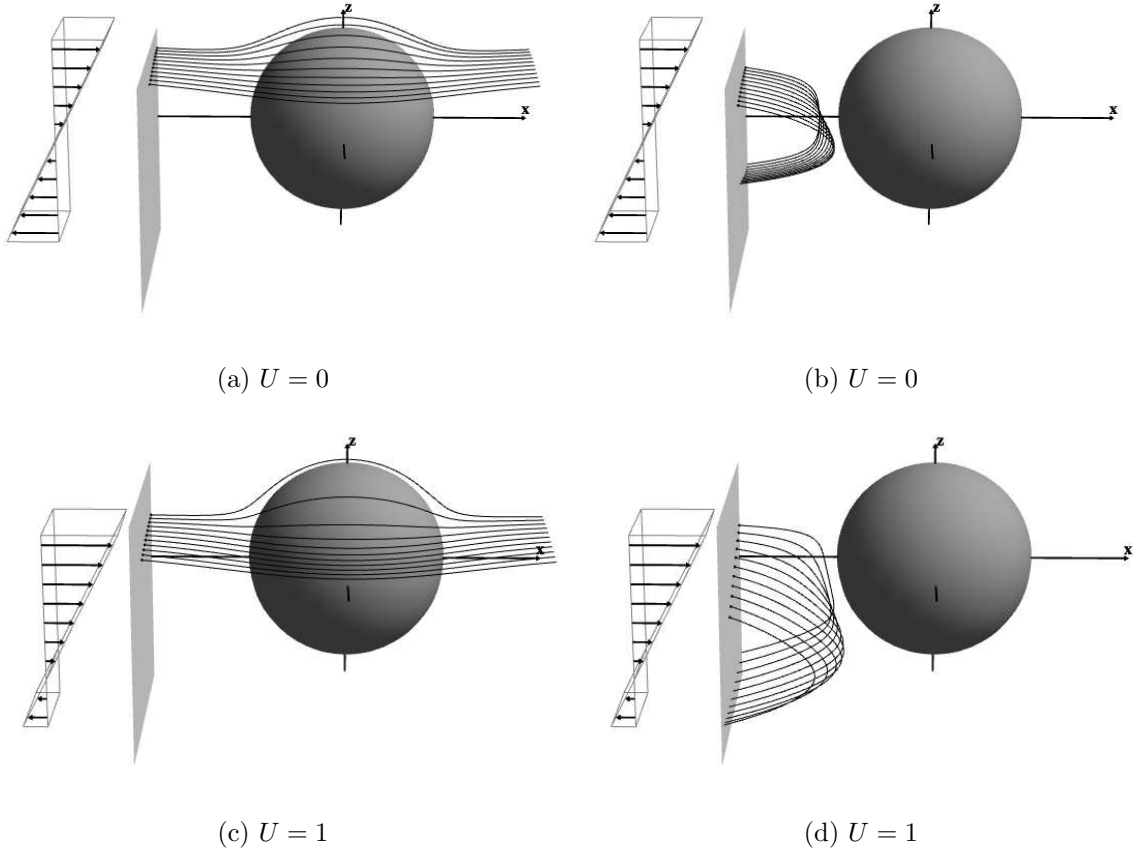
Figure 2.8: 3D fluid particle trajectories passing the sphere or blocked with different U in the background shear flow.
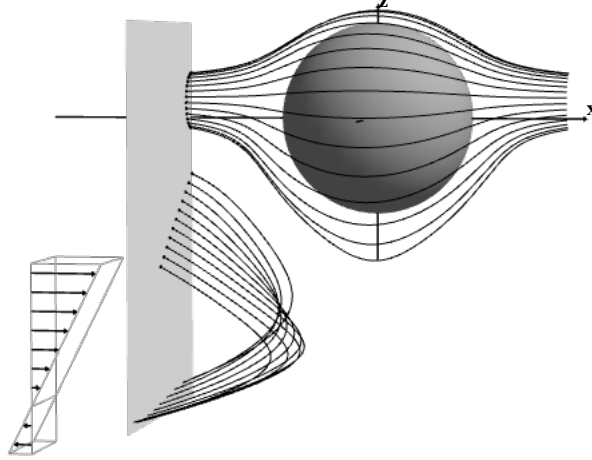
Figure 2.9: Trajectories of fluid particles starting from those black dots when $U = 3$.

the next subsection, after the general formula of critical points are derived.

For Stage 1, Figure 2.10a shows the diagram of streamlines in the symmetry plane below the sphere when $U < U^\star$. The stagnation line bounding the blocking region moves downward with the stagnation points on the sphere, as the center of the sphere moves upwards from the zero-velocity plane of the background shear. There is no critical point in the interior of the flow in this symmetry plane for this stage. The critical points in the interior of the flow are on two curves in the y-z plane.

The transition from stage 1 to stage 2 appears when $U = U^\star$, when a cubic parabolic critical point (a cusp point) emerges in the symmetry plane (Figure 2.10b). In stage 2 ($U^\star < U < U^{\star\star}$), this cubic parabolic critical point deforms into a pair of critical points, one elliptical critical point and one hyperbolic critical point, in the symmetry plane. Surrounding the elliptical critical point, there are closed orbits in the symmetry plane plotted in Figure 2.10c.

The transition from stage 2 to stage 3 occurs when $U = U^{\star\star}$. With this critical value, the stagnation lines separating the blocking region also form a separatrix distinguishing

44

the open trajectories from the closed trajectories below the sphere. These stagnation lines cross the hyperbolic critical point and end on the stagnation point on the sphere. Above the hyperbolic critical point, streamlines are closed; below it, the streamlines are open and fluid particles pass the sphere from the right to the left. There is no flow past the sphere from the left to the right below the sphere in this symmetry plane.

In stage 3 ($U^{\star\star} < U < \frac{8}{3}$) as Figure 2.10e, the elliptical critical point moves toward the sphere. The stagnation lines ending on the hyperbolic critical points are no longer separation lines of the elliptical critical points. The closed orbits around the elliptical critical point are above the blocking region in this symmetry plane. There are open streamlines between the elliptical critical point and the hyperbolic point. Fluid particles along the open streamlines pass the sphere from the left to the right above the hyperbolic critical points.

Stage 4 begins at $U = \frac{8}{3}$, when the elliptic critical point, the two stagnation points in the symmetry plane on the sphere, and two stagnation points out of the symmetry plane vanish or collapse simultaneously at the open dot shown in the Figure 2.10f. After these four stagnation points on the sphere and the elliptical critical point in the interior of the flow collapse, the flow structure remains the same as shown in Figure 2.10f, with only two stagnation points on the sphere.

A brief discussion regarding dynamical system theory is merited. For example, there is a criterion (Poincaré-Bendixson) which states that a 2D non-divergence free vector field may posses periodic particle trajectories only if the divergence of the flow changes sign. In the symmetry plane, we have a 2D compressible flow for all values of the parameter U. For some values of this parameter, we just document the existence of closed orbits in the symmetry plane. A quick inspection of the divergence of the

(a) Stage 1 ($U < U^\star$)

(b) Stage 1-2 ($U = U^\star$)

(c) Stage 2 ($U^\star < U < U^{\star\star}$)

(d) Stage 2-3 ($U = U^{\star\star}$)

(e) Stage 3 ($U^{\star\star} < U < \frac{8}{3}$)

(f) Stage 4 ($U \geq \frac{8}{3}$)
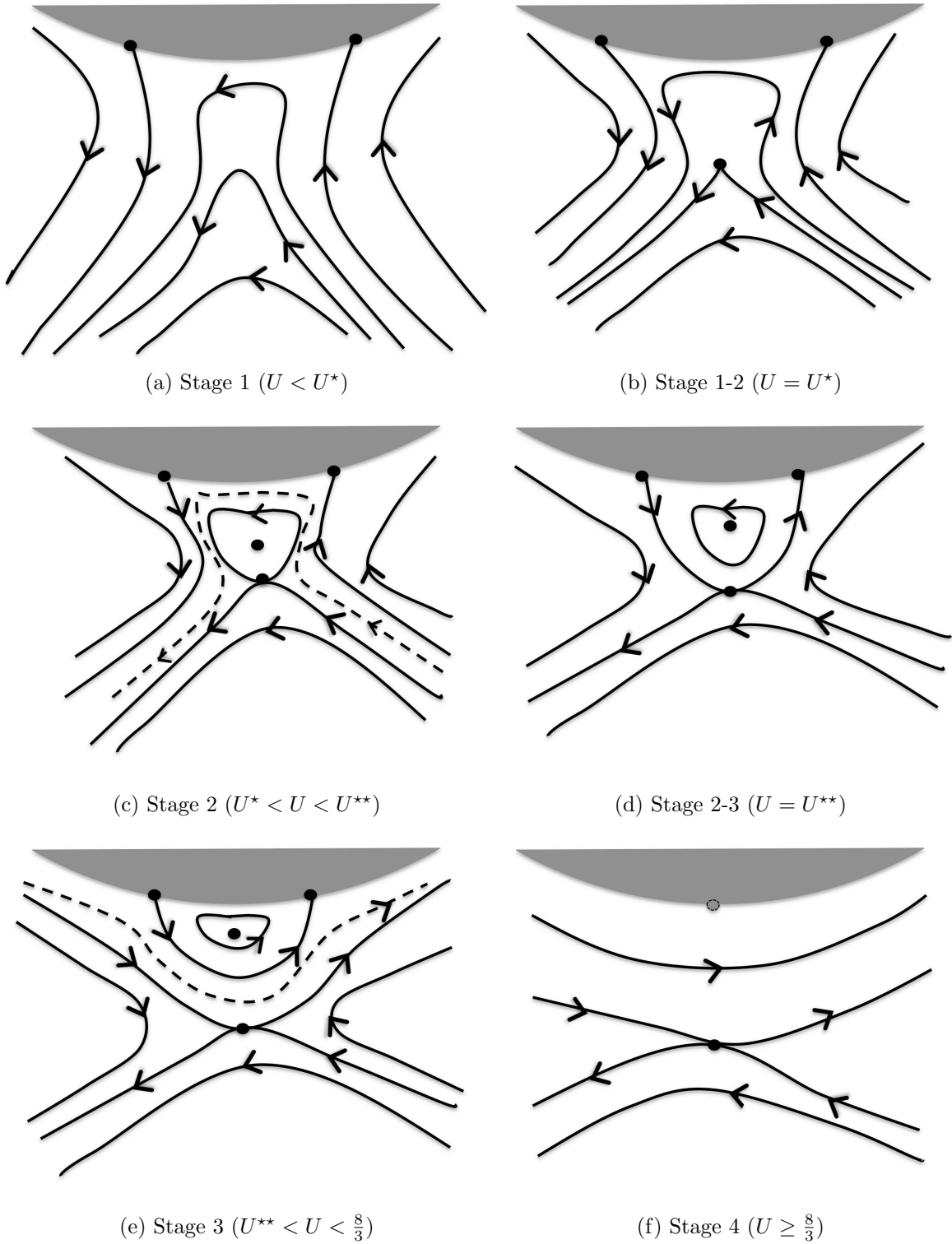
Figure 2.10: Bifurcation diagram below the sphere in the $y = 0$ symmetry plane as the uniform flow rate U increases. The gray regions are portions of the sphere. Black dots indicate stagnation points on the sphere or critical points in the interior of the flow. Arrows show the direction of the flow along the trajectories.

46

velocity field

$$(u(x, 0, z), w(x, 0, z)) = \frac{x(x^2 + z^2 - 1)\left[3U(x^2 + z^2) + 10z\right]}{4(x^2 + z^2)^{\frac{7}{2}}}$$

shows that indeed it does change sign, in the agreement with the Poincaré-Bendixson's criterion. Moreover, using the generalized Poincaré-Hopf index definition by Ma & Wang [52], the index of the flow is also shown to be preserved, with the caveat that fixed points on the boundary are indexed with selected weight one half.

2.3.2 Stagnation points and critical points in the interior of the flow

Next, we provide the explicit formula for the stagnation points on the sphere when its center is out of the zero-velocity plane of the primary background shear flow. After linearizing, rescaling $\tau = t(r - 1)$ and neglecting the higher order terms in the ODE system (2.37), we get

$$\begin{aligned}
\frac{dr}{d\tau} &= 0, \\
\frac{d\theta}{d\tau} &= -\frac{3U\csc(\phi) + 8\cot(\phi)}{2}\sin(\theta), \\
\frac{d\phi}{d\tau} &= \frac{3U\cos(\phi) + (3 + 5\cos(2\phi))}{2}\cos(\theta).
\end{aligned}$$

Based on the conditions for stagnation points on the sphere,

$$\frac{d\theta}{d\tau} = 0 \quad \text{and} \quad \frac{d\phi}{d\tau} = 0, \tag{2.40}$$

the explicit formula for stagnation points on the sphere are obtained as:

47

- When $0 \leq U < \frac{8}{3}$, there are six solutions of (2.40) $\begin{cases} \theta = 0, \pi; \\ \phi = \arccos\left(\frac{-3U \pm \sqrt{9U^2 + 80}}{20}\right), \end{cases}$

and $\begin{cases} \theta = \frac{\pi}{2}, \frac{3\pi}{2}; \\ \phi = \arccos\left(-\frac{3U}{8}\right) \end{cases}$. In rectangular coordinates, these six points are :

$\left(\pm\left(1 - (\frac{\sqrt{9U^2+80}-3U}{20})^2\right)^{\frac{1}{2}}, 0, \frac{\pm\sqrt{9U^2+80}-3U}{20} \right)$, and $\left(0, \pm\sqrt{1 - \left(\frac{3U}{8}\right)^2}, -\frac{3U}{8} \right)$.

As $U \to \frac{8}{3}$, four of the stagnation points at the lower part of the sphere approach each other; at $U = \frac{8}{3}$, they collapse and disappear, and there are two stagnation points $\left(\pm\frac{2\sqrt{6}}{5}, 0, \frac{1}{5} \right)$ left on the sphere.

- When $U \geq \frac{8}{3}$, there are only two solutions of (2.40) $\begin{cases} \theta = 0, \pi; \\ \phi = \arccos\left(\frac{\sqrt{9U^2+80}-3U}{20}\right) \end{cases}$

representing two stagnation points $\left(\pm\left(\frac{4}{5} + \frac{3U\left(\sqrt{9U^2+80}-3U\right)}{200}\right)^{\frac{1}{2}}, 0, \frac{\sqrt{9U^2+80}-3U}{20} \right)$

on the sphere in rectangular coordinates.

Besides the stagnation points on the sphere, we find the explicit formula for all the critical points in the interior of the flow. In the spherical case where the center of the sphere is in the zero-velocity plane of the primary shear flow, i.e. $U = 0$ in the primary flow, the critical points are on the y-axis. When $U \neq 0$, the curves for critical points still only appear in the y-z plane but are no longer restricted to the y-axis. The critical points in the interior of the flow are found as functions of r and U from equations (2.38) and (2.39)

$$\begin{cases} x(r, U) &= 0, \\ z(r, U) &= -\frac{Ur^2\left(1+3r^2-4r^3\right)}{2(1+r^2-2r^5)}, \\ y(r, U) &= \pm\sqrt{r^2 - z^2(r, U)} = \pm\sqrt{r^2 - \left(\frac{Ur^2}{2}\frac{(1+3r^2-4r^3)}{(1+r^2-2r^5)}\right)^2}. \end{cases} \quad (2.41)$$

If $0 < U < U^\star$, the critical points are on two curves. Each of them ends on one of the stagnation points $\left(\pm \left(1 - \frac{\left(3U + \sqrt{9U^2 + 80}\right)^2}{400} \right)^{1/2}, 0, -\frac{\sqrt{9U^2 + 80} + 3U}{20} \right)$ on the sphere. Far away from the sphere, these two curves are asymptotic to line $(0, y, -U)$, which is in the zero-velocity plane of the background linear shear. On the other hand, closer to the sphere, as U increases, these two distinct curves of fixed points deform and intersect at a critical value of $U = U^\star$, as shown in the second column and row in Table 2.1. Before this critical value a few other transitions in the graph of these curves are noteworthy. When $U \leq \frac{16}{9}\sqrt{2}$, the curves of critical points in the y-z plane can be written as functions of y. When $U = \frac{16}{9}\sqrt{2} < U^\star$, the curve $(y(r, U), z(r, U))$ has a vertical tangent line at the stagnation point on the sphere.

The critical ratio $U^\star$ equals to $\frac{2\left(1 + s^2 - 2s^5\right)}{s\left(1 + 3s^2 - 4s^3\right)}$, in which s is the smallest positive real root of the following polynomial

$$8s^6 + 4s^5 - 4s^3 - 11s^2 - 2s - 1 = 0. \tag{2.42}$$

derived from the equation (2.41). At this critical ratio $U^\star$, the two pieces of curves join at a cusp critical point in the symmetry plane.

As $U(U^\star \leq U < \frac{8}{3})$ increases further, these two curves of critical points bifurcate into two new curves. One of the new curves has no end point on the sphere, and all points on this curve are hyperbolic critical points. The other curve is a finite length curve whose end points are two stagnation points on the sphere. Along this finite length curve, the critical points change properties as they move away from the stagnation points on the sphere: near the two stagnation points on the sphere, i.e. near the two end points of the curve of critical points, the curve consists of hyperbolic critical points; a bit further down the curve, at a critical position these points become two degenerate critical points with three vanishing eigenvalues; finally, moving still further away from the sphere and close to the $y = 0$ symmetry plane, the points on this curve become

49

elliptical critical points and no further transition is observed through the symmetry plane. These properties are determined by the sign of the following function

$$
\begin{aligned}
F(r,U) \ = \ & 2\left[1 + r + 2r^2(1 + r + r^2)\right]^3 \\
& + U^2 r^4\left(5 + 3r + 24r^2 - 48r^3 - 84r^4 - 60r^5 - 44r^6 + 36r^7 + 24r^8\right)
\end{aligned}
\tag{2.43}
$$

and the equation (2.41). This function, $F(r,U)$, is derived through a standard eigen-analysis. For given U and r, if $F(r,U) > 0$, the corresponding point (x,y,z) from the equation (2.41) is a hyperbolic critical point. If $F(r,U) < 0$, and the point (x,y,z) satisfying (2.41) is an elliptical critical point. Otherwise, when $F(r,U) = 0$, the point of (2.41) is a higher order critical point with all three eigenvalues being zero.

When $U = \frac{8}{3}$, the finite curve shrinks into a point and collapses with the four stagnation points on the sphere, and all the critical points in the interior of the flow are now on the infinite length curve. After $U \geq \frac{8}{3}$, critical points in the interior of the flow are always on such a curve.

The quantified streamline plots shown in Table 2.1 document the qualitative bifurcation diagram sketched in Figure 2.10. In Table 2.1, we show critical point curves in the flow and the flow structure in the x-z symmetry plane with given U. Notice that the critical points are plotted in the y-z plane, since the critical points in the flow are only in the y-z plane. In the table, the first column shows the different values of U studied, and in the second column are plots for curves of critical points from equation (2.41) (the gray area indicates the sphere). The third column are streamlines patterns obtained numerically in the x-z symmetry plane, i.e., the lateral view.

The first value $U = \frac{16}{9}\sqrt{2} < U^{\star}$ is picked corresponding to stage 1 in the bifurcation diagram Figure 2.10. In this case, as shown in the second column, critical points are on two infinite length curves, each of whose end point is a stagnation point on the sphere.

50

With this special value, the curves of critical points in the y-z plane have infinite slopes at the stagnation point. With the second value $U = 2.64837 \approx U^\star$, a cubic parabolic (cusp) critical point appears. In the third row $U^\star < U = 2.64912 < U^{\star\star}$, the critical points in the flow are on two new curves. Both end points of the finite length curve are stagnation points on the sphere, and the curve with infinite length is asymptotic to a line in the zero-velocity plane of the background shear flow. With the fourth value $U = 2.65059 \approx U^{\star\star}$, the critical points in the flow are still on two curves. The stagnation lines in the streamline plot in the symmetry plane connect the hyperbolic critical point in the flow with the stagnation points on the sphere, and separate the closed orbits around the elliptical critical point from the open trajectories. For $U^{\star\star}$, we do not have an explicit formula for this value and use the numerical approximation 2.65059. For the fifth $U^{\star\star} < U = 2.65287 < \frac{8}{3}$, the elliptical critical points moves up as U increases, and there are fluid particles which pass the sphere from the left to the right between the elliptical critical point and the hyperbolic critical point. The last case $U = \frac{8}{3}$ shows that critical points are on one curve in the flow.

These numerical results clearly show the existence of the blocking regions when the sphere is out of the zero-velocity plane of the primary shear flow. The streamlines plots in the $y = 0$ plane show the interesting bifurcation appearing in the fluid particle trajectories.

When $U^\star < U < \frac{8}{3}$, streamlines show a 3D eddy near the elliptical critical points below the sphere. Figure 2.11 shows the circulation near the elliptical critical points below the sphere when $U = 2.6514$. Figure 2.11a is the front view of fluid particles' trajectories, and Figure 2.11b is the lateral view of the same trajectories. From Figure 2.11b, it is clear that these are closed trajectories circulating around the elliptical critical points on the finite length critical point curve in the symmetry plane and out of the symmetry plane. From the front view Figure 2.11a and Figure 2.12a, we see the
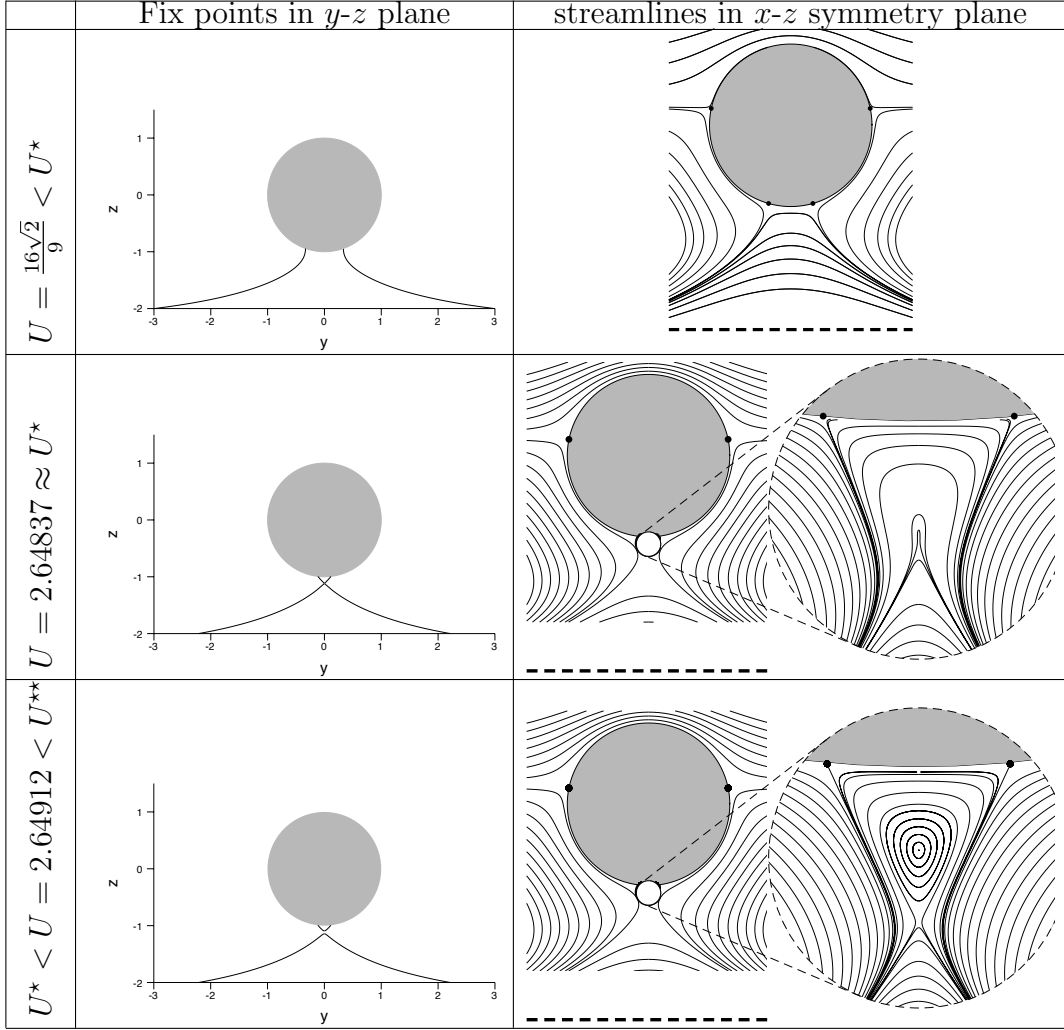
Table 2.1: Critical points in the interior of the flow in the $x = 0$ plane and streamlines in the $y = 0$ symmetry plane for different U. The thick dash lines in the streamline patterns indicate the zero-velocity plane of the primary background shear flow. The gray area is the sphere.
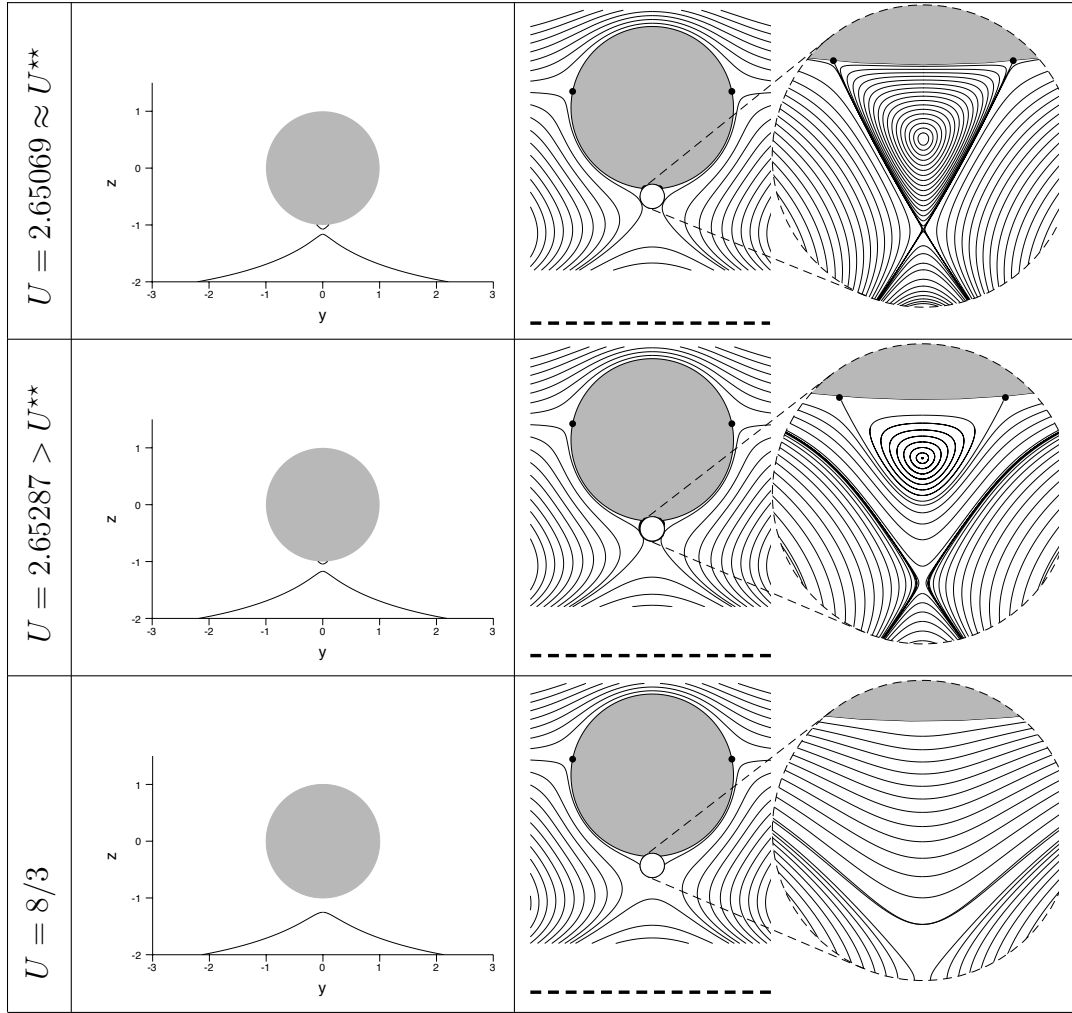
Table 2.2: Continue of Table 2.1.

53

(a) Front view   (b) Lateral view
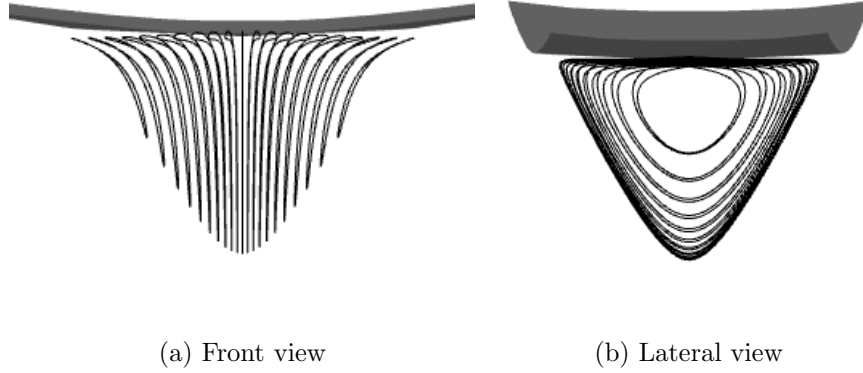
Figure 2.11: Circulation near the elliptical and hyperbolic critical points below the sphere. The gray surface is a portion of the surface of the sphere.

trajectories are further deformed when they are close to the surface of the sphere and approaching the hyperbolic fixed point on the finite length critical point curve.

Figure 2.12 and Figure 2.13 show streamlines in the $y < 0$ half space below the sphere. In Figure 2.12, the streamlines are only closed orbits near the critical points on the finite length curve (here, we take $U = 2.6514$). Figure 2.12a is the front view, Figure 2.12b is the lateral view, and Figure 2.12c is the 3D view. These orbits are selected so that they are around the elliptical points, but near the sphere they are close to the hyperbolic critical points on the finite length critical point curve. Figure 2.13 shows both closed and open streamlines near the critical points.

2.4   Linear shear flow past a freely rotating sphere

When non-dimensional shear flow $U = z\mathbf{e}_x$ past a freely rotating sphere [62], the governing equations are Stokes equations

$$\nabla^2 \mathbf{u} = \nabla p, \tag{2.44}$$

$$\text{div } \mathbf{u} = 0. \tag{2.45}$$

(a) Front view

(b) Lateral view

(c) 3D view
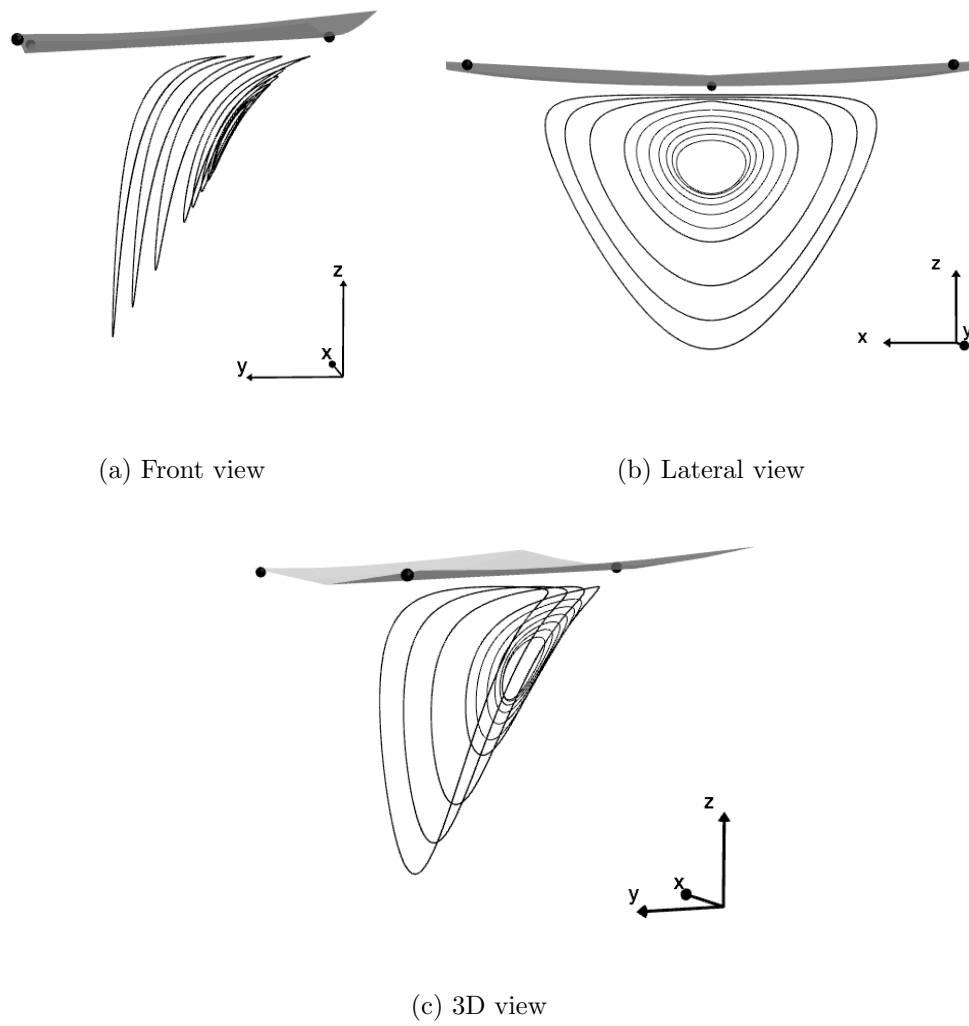
Figure 2.12: Circulation near the elliptical and hyperbolic critical points below the sphere.

(a)

(b)
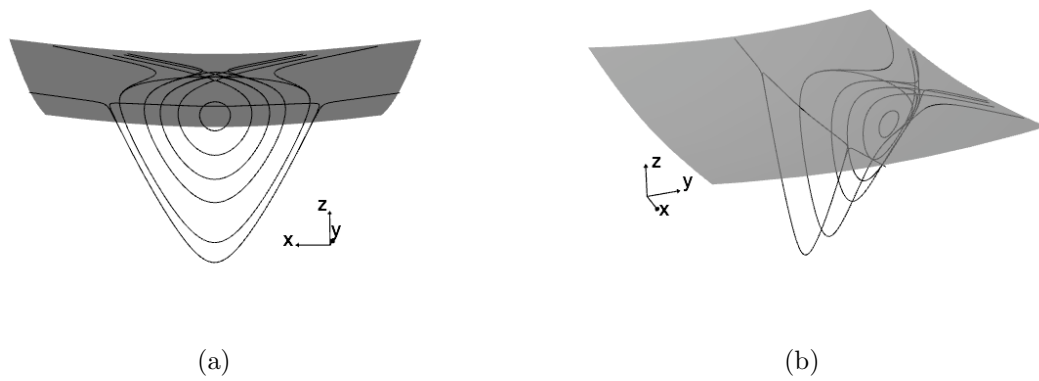
Figure 2.13: Closed and open streamlines below the sphere.

The boundary conditions are changed to

$$u = (0, \omega, 0) \times \mathbf{x} \text{ at } |\mathbf{x}| = 1 \text{ on the surface of the sphere,}$$

$$u \sim U = z\mathbf{e}_x \text{ as } |r| \to \infty,$$

where ω is the angular velocity of the sphere. Since the background shear flow is prescribed, the direction of the sphere rotation has been specified. When the sphere is freely rotating, $\omega = \frac{1}{2}$ is determined by the condition of no force or torque on the sphere.

The velocity of the flow is

$$\mathbf{u} = z\mathbf{e}_x - \frac{5}{6}\mathbf{U}_{SS}(\mathbf{x}, \mathbf{e}_z, \mathbf{e}_x) - \frac{1}{6}\frac{\partial}{\partial x}\mathbf{U}_D(\mathbf{x}, \mathbf{e}_z). \tag{2.46}$$

The pressure is

$$p(\mathbf{x}) = -\frac{5xy}{(x^2 + y^2 + z^2)^{\frac{5}{2}}}.$$

This velocity field is adopted from the velocity formula from Chwang & Wu [19]. In detail, it is

$$
\begin{aligned}
u(\mathbf{x}) &= z\left[1 - \frac{1}{2(x^2+y^2+z^2)^{\frac{5}{2}}} - \frac{5x^2}{2(x^2+y^2+z^2)^{\frac{5}{2}}}\left(1 - \frac{1}{x^2+y^2+z^2}\right)\right], \\
v(\mathbf{x}) &= -\frac{5xyz}{2(x^2+y^2+z^2)^{\frac{5}{2}}}\left(1 - \frac{1}{x^2+y^2+z^2}\right), \\
w(\mathbf{x}) &= x\left[-\frac{1}{2(x^2+y^2+z^2)^{\frac{5}{2}}} - \frac{5z^2}{2(x^2+y^2+z^2)^{\frac{5}{2}}}\left(1 - \frac{1}{x^2+y^2+z^2}\right)\right].
\end{aligned}
$$

From the velocity, the critical points in the interior of the flow is the y-axis out of the sphere.

With the same techniques we use for the fixed sphere embedded in a linear shear,
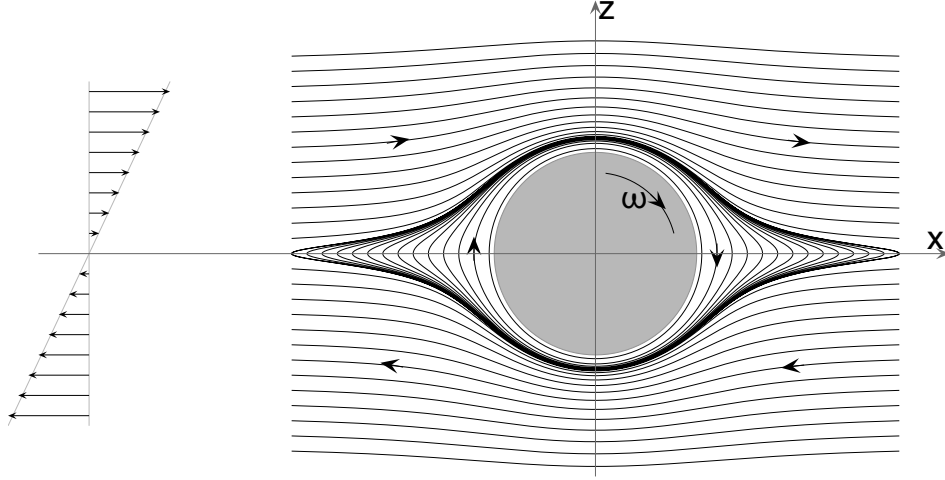
Figure 2.14: Streamlines in the $y = 0$ plane when shear flow past a center fixed but freely rotating sphere. The angular velocity of the sphere rotation is $\omega = \frac{1}{2}$. Two classes of orbits are drawn here: closed orbits and open orbits. Initial points of closed orbits are evenly distributed when $z = 0$. Initial points of open orbits are evenly distributed with height z as x values are fixed.

fluid particle's trajectory equations are found in closed integral form

$$y = y_0 \frac{r^{5/3}}{(r-1)^{2/3} \left(3 + 6r + 4r^2 + 2r^3\right)^{1/3}} \left(\frac{r_0^{5/3}}{(r_0 - 1)^{2/3} \left(3 + 6r_0 + 4r_0^2 + 2r_0^3\right)^{1/3}}\right)^{-1},$$

$$\int^r \frac{dr}{(s-1)^{2/3} s^{7/3} \left(3 + 6s + 4s^2 + 2s^3\right)^{1/3}} + \frac{(r-1)^{4/3} \left(3 + 6r + 4r^2 + 2r^3\right)^{2/3}}{r^{10/3}} \frac{z^2}{2} = C_2,$$

where $r_0 = \sqrt{x_0^2 + y_0^2 + z_0^2}$, and C_2 is a constant depending on the initial value (x_0, y_0, z_0).

This system is autonomous. The fluid particle's trajectory is equivalent to the stream-line.

Near the sphere, there are closed streamlines [23, 1, 42, 62]. Figure 2.14 shows the streamlines in the $y = 0$ symmetry plane. At a certain distance above or be-low the sphere, there is a separation line that divides the closed streamline from the open streamlines. This separation streamline is asymptotic to the x-axis, the center of background shear flow.

In the $y = 0$ symmetry plane, the height of the separation streamline is determined

by the following integral equation

$$\int_1^r \frac{1}{(s-1)^{2/3}s^{7/3}(3+6s+4s^2+2s^3)^{1/3}}ds + \frac{(r-1)^{4/3}(3+6r+4r^2+2r^3)^{2/3}}{r^{10/3}}\frac{z^2}{2} = 0.$$

It is independent of the shear rate. Numerically, we find the critical height is $|z| \approx$ 1.155645 for the unit sphere.

Chapter 3

Linear shear flow past a fixed spheroid

When a linear shear flow past a fixed sphere, complicated flow structures and interesting blocking phenomenon are explored. The simple modification of a sphere in the flow is a spheroid. We study the flow structure and blocking phenomena for a prolate spheroid embedded in a linear shear flow in this chapter. With respect to the spherical case, the spheroid orientation relative to the background shear enriches the phenomena, some of which will be examined here. The literature on this setup has concentrated mostly on forces and torques [7], while some experimental investigations of three-dimensional separation structures for flows past spheroids can be found in the high Reynolds regime [76].

3.1   Linear shear flow past an upright spheroid

First, we report results about the shear flow $\Omega z \mathbf{e}_x$ past an upright spheroid. The spheroid sits with its center on the zero-velocity plane with its major axis upright (as shown in Figure 3.1),

$$\frac{x^2 + y^2}{b^2} + \frac{z^2}{a^2} = 1 \,,$$

Primary shear flow (Ωz, 0, 0)
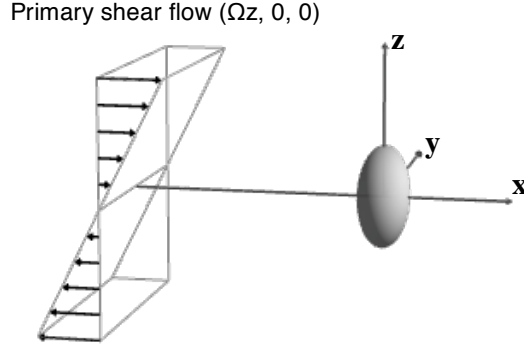
Figure 3.1: A linear shear flow past a fixed prolate spheroid. The major axis of the spheroid is perpendicular to the direction of the shear flow (an upright spheroid).

where $a > b$ are the major and minor semi-axis, respectively, and the half focal length c and the eccentricity e are defined as $c = (a^2 - b^2)^{1/2} = e\,a$. From [19], the exact velocity field in this case is

$$
\begin{aligned}
\mathbf{u}(x) \;=\;& \Omega z \mathbf{e}_x - \int_{-c}^{c} \left(c^2 - \xi^2\right) \left(\alpha \mathbf{U}_{\mathrm{SS}}\left(\mathbf{x} - \boldsymbol{\xi}; \mathbf{e}_z, \mathbf{e}_x\right) + \gamma \mathbf{U}_{\mathrm{R}}\left(\mathbf{x} - \boldsymbol{\xi}; \mathbf{e}_y\right)\right) d\xi \\
& - \beta \int_{-c}^{c} \left(c^2 - \xi^2\right)^2 \partial_z \mathbf{U}_{\mathrm{D}}\left(\mathbf{x} - \boldsymbol{\xi}; \mathbf{e}_x\right) d\xi,
\end{aligned}
\tag{3.1}
$$

where $\mathbf{U}_{\mathrm{SS}}$, $\mathbf{U}_{\mathrm{R}}$ and $\mathbf{U}_{\mathrm{D}}$ are the fundamental singularities of stresslet, rotlet and doublelet, located at $\boldsymbol{\xi}$,

$$
\begin{aligned}
U_{\mathrm{SS}}\left(\mathbf{x} - \boldsymbol{\xi}; \mathbf{e}_z, \mathbf{e}_x\right) \;&=\; \frac{3\left((\mathbf{x} - \boldsymbol{\xi}) \cdot \mathbf{e}_z\right)\left((\mathbf{x} - \boldsymbol{\xi}) \cdot \mathbf{e}_x\right)}{R^5}(\mathbf{x} - \boldsymbol{\xi}), \\
U_{\mathrm{R}}\left(\mathbf{x} - \boldsymbol{\xi}, \mathbf{e}_y\right) \;&=\; \frac{(\mathbf{x} - \boldsymbol{\xi}) \times \mathbf{e}_y}{R^3}, \\
U_{\mathrm{D}}\left(\mathbf{x} - \boldsymbol{\xi}, \mathbf{e}_x\right) \;&=\; -\frac{\mathbf{e}_x}{R^3} + \frac{3(\mathbf{x} - \boldsymbol{\xi}) \cdot \mathbf{e}_x}{R^5}(\mathbf{x} - \boldsymbol{\xi}),
\end{aligned}
$$

with $R = \sqrt{x^2 + y^2 + (z - \xi)^2}$, and $\boldsymbol{\xi} = \xi \mathbf{e}_z$. Here, α, β and γ are known constants,

$$
\alpha = \beta \frac{4e^2}{1 - e^2} = \gamma\, e^2 \frac{-2e + \left(1 - e^2\right) L_e}{2e\left(2e^2 - 3\right) + 3\left(1 - e^2\right) L_e}, \qquad \gamma = \frac{\Omega}{-2e + \left(1 + e^2\right) L_e},
$$

60

and $L_e = \log\left(\frac{1+e}{1-e}\right)$. Numerical results show the existence of blocking regions in the flow as Figure 3.2, where the streamlines are plotted in the $y = 0$ symmetry plane.

3.2 Stagnation points on the spheroid

From the velocity field (3.1), we find the stagnation points on the spheroid. Similar to the spherical case, we first rewrite the velocity field in the prolate spherical coordinates

$$
\begin{cases}
x &= a\,e\sinh(\mu)\sin(\nu)\cos(\phi) \\
y &= a\,e\sinh(\mu)\sin(\nu)\sin(\phi) \\
z &= a\,e\cosh(\mu)\cos(\nu)\,,
\end{cases}
$$

where $\mathrm{acosh}(\frac{1}{e}) \leq \mu \leq \infty$, $0 \leq \nu \leq \pi$, and $0 \leq \phi \leq 2\pi$. Next, we rescale time $\tau = \left(\mu - \mathrm{acosh}(\frac{1}{e})\right)t$, and expand the velocity field near the no-slip boundary of the spheroid where $\mu = \mathrm{arccosh}(\frac{1}{e})$, ignoring higher order terms of order $\left(\mu - \mathrm{arccosh}(\frac{1}{e})\right)^2$. The linearized ODE system for the trajectory of fluid particle near the surface of the spheroid reduces to

$$
\begin{cases}
\dfrac{d\mu}{d\tau} &= 0, \\[2mm]
\dfrac{d\nu}{d\tau} &= 4\,\omega\,e^3\,\dfrac{\cos(\phi)}{e^2 + e^2\cos(2\nu) - 2}\dfrac{k(e)}{d(e)}, \\[2mm]
\dfrac{d\phi}{d\tau} &= 4\,\omega\,e^3\,\dfrac{\left[2e\left(3 - e^2\right) + \left(e^4 + 2e^2 - 3\right)L_e\right]}{d(e)}\dfrac{\cot(\nu)\sin(\phi)}{1 - e^2},
\end{cases}
\tag{3.2}
$$

where

$$
d(e) \equiv 12e^2 - 8e^4 + 4e\left(e^4 + e^2 - 3\right)L_e - 3\left(e^4 - 1\right)L_e^2\,,
$$

61

and

$$k(e) \equiv 2e \left(6 - e^2\right) + \left(e^4 + 3e^2 - 6\right) L_e + e^2 \cos(2\nu) \left(\left(1 + e^2\right) L_e - 2e\right) .$$

The conditions for stagnation points on the boundary

$$\frac{d\mu}{d\tau} = 0, \quad \frac{d\nu}{d\tau} = 0, \quad \text{and} \quad \frac{d\phi}{d\tau} = 0, \tag{3.3}$$

define six stagnation points on the upright prolate spheroid in the prolate spherical coordinates

$$a\left(\operatorname{arccosh}(1/e), \frac{\pi}{2}, \frac{\pi}{2}\right) , \quad a\left(\operatorname{arccosh}(1/e), \frac{3\pi}{2}, \frac{\pi}{2}\right) ,$$

$$a\left(\operatorname{arccosh}(1/e), 0, \arccos\left(\pm\left(\frac{6e - \left(3 - e^2\right) L_e}{2e^3 - e^2 \left(1 + e^2\right) L_e}\right)^{1/2}\right)\right) ,$$

and

$$a\left(\operatorname{arccosh}(1/e), \pi, \arccos\left(\pm\left(\frac{6e - \left(3 - e^2\right) L_e}{2e^3 - e^2 \left(1 + e^2\right) L_e}\right)^{1/2}\right)\right) .$$

In the original rectangular coordinates, the latter stagnation points lie in the $y = 0$ symmetry plane

$$a\left(\pm\sqrt{1 - e^2}\left(1 - \frac{6e - \left(3 - e^2\right) L_e}{2e^3 - e^2 \left(1 + e^2\right) L_e}\right)^{1/2}, 0, \pm\left(\frac{6e - \left(3 - e^2\right) L_e}{2e^3 - e^2 \left(1 + e^2\right) L_e}\right)^{1/2}\right) ,$$

while the other two are on the y-axis at $(0, \pm a\sqrt{1 - e^2}, 0)$.

The location of the stagnation points in the $y = 0$ symmetry plane migrate towards the spheroid's "tips" with increasing eccentricity e at fixed a. The four points merge into two at the tips in the "needle" limit of eccentricity $e \to 1$, while for the opposite limit of a sphere $(e \to 0)$ we retrieve the spherical result (2.14). Like for the spherical case, the zero-velocity plane of the background shear flow collapses to the y-axis for

62
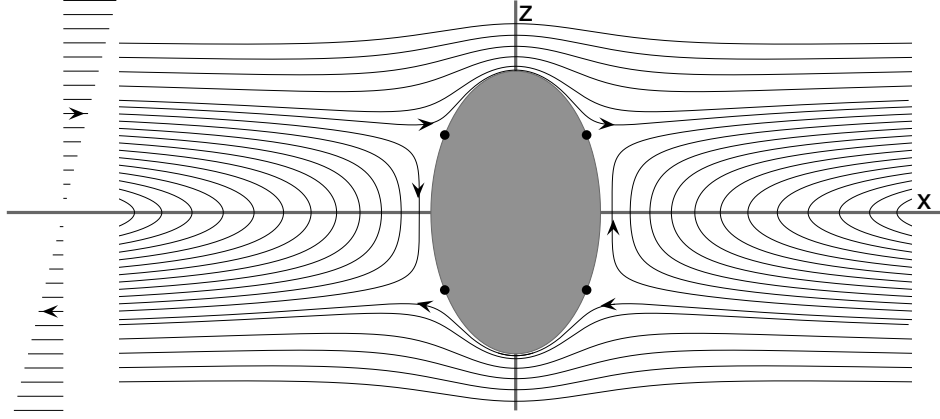
Figure 3.2: Streamlines in the $y = 0$ symmetry plane for a linear shear past a fixed upright spheroid. The four points mark the stagnation points on the spheroid.

the upright spheroid whose center is on this zero-velocity plane.

3.3 Characterization of stagnation stream lines on the surface of the spheroid

As for the case of the sphere, the rescaled velocity field provides an imprint of the particle trajectory pattern just off the spheroid surface which mathematically reduces to heteroclinic connections between the stagnation points, see Figure 3.3.

From the rescaled velocity field ODE (3.2), we obtain the governing equation of the fluid particle imprint on the spheroid

$$\frac{d\nu}{d\phi} = \frac{\left(1 - e^2\right)\cot(\phi)\tan(\nu)k(e)}{\left(e^2\cos(2\nu) + e^2 - 2\right)\left[2e\left(3 - e^2\right) + \left(e^4 + 2e^2 - 3\right)L_e\right]} \, .$$

The solution for the above equation is

$$\sin(\phi)\sin(\nu) = C\left(k(e)\right)^{p(e)} , \qquad (3.4)$$
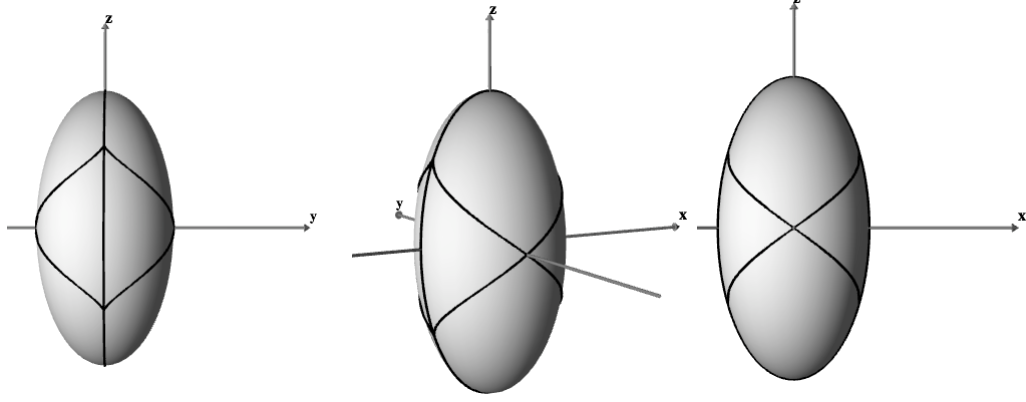
Figure 3.3: "Footprint" of stagnation surfaces on the spheroid surface from different viewpoints.

where the constant C is determined by the initial conditions, and the constant $p(e)$ is

$$p(e) \equiv \frac{2e + (e^2 - 1) L_e}{(1 - e^2)\left((1 + e^2) L_e - 2e\right)}. \tag{3.5}$$

Substituting the stagnation points into (3.4) yields the trajectories

$$
\begin{aligned}
x^2 &= \left(1 - e^2\right)\left(a^2 - z^2\right) - y^2 = a^2 \left(1 - e^2\right) \sin^2(\nu) - y^2, \\
y &= a\sqrt{1 - e^2} \sin(\nu) \sin(\phi) = a\sqrt{1 - e^2} \, C \left(k(e)\right)^{p(e)}, \\
z &= a\cos(\nu).
\end{aligned}
$$

in the first octant $(x, y, z$ positive), which can be extended by the symmetry of the flow to the whole space.

3.4   Linear shear flow past a tilted spheroid

When the major axis of the spheroid is tilted with an angle κ, defined as the angle between the positive z-axis and the major axis of the spheroid in the x-z plane (see

Figure 3.4a and Figure 3.5a), the $y = 0$ plane is still a symmetry plane of the flow. However, the up-down symmetry of the fluid-body setup is broken. The tilted prolate spheroid is

$$\frac{(x\cos(\kappa) - z\sin(\kappa))^2 + y^2}{b^2} + \frac{(x\sin(\kappa) + z\cos(\kappa))^2}{a^2} = 1 \quad (a > b > 0). \qquad (3.6)$$

(The upright spheroid case is recovered with $\kappa = 0$.)

The solution of Stokes equations for this tilted case can be efficiently obtained from the general results of Chwang & Wu [19] and Jeffery [36] in the body frame. In this frame, the spheroid's major axis is on the x-axis, and the background flow can be decomposed into two simple shear flows $x\mathbf{e}_y$ and $y\mathbf{e}_x$, and an elongational flow $x\mathbf{e}_x - y\mathbf{e}_y$. The velocity field $\mathbf{u}_L(\mathbf{x}_L)$ in the laboratory frame can be obtained from the velocity field $\mathbf{u}(\mathbf{x})$ in the body frame with the transformation between these two reference frames

$$\mathbf{u}_L(\mathbf{x}_L) = R\mathbf{u}(R^T\mathbf{x}),$$

where the transformation matrix

$$R = \begin{pmatrix} \cos(\kappa) & 0 & \sin(\kappa) \\ 0 & 1 & 0 \\ -\sin(\kappa) & 0 & \cos(\kappa) \end{pmatrix}.$$

For two shear background flows, the velocity field in the body frame for the shear flow $x\mathbf{e}_y$ is given by changing coordinates of (3.1), and the velocity field in the body

frame for the shear flow $y\mathbf{e}_x$ is

$$
\begin{aligned}
\mathbf{u}(\mathbf{x}) \;=\;& y\mathbf{e}_x + \int_{-c}^{c} \left(c^2 - \xi^2\right) \left(\alpha_3 \mathbf{U}_{\mathrm{SS}}\left(\mathbf{x} - \boldsymbol{\xi}; \mathbf{e}_x, \mathbf{e}_y\right) + \gamma_3 \mathbf{U}_{\mathrm{R}}\left(\mathbf{x} - \boldsymbol{\xi}; \mathbf{e}_z\right)\right) d\xi \\
&+ \beta_3 \int_{-c}^{c} \left(c^2 - \xi^2\right)^2 \partial_y \mathbf{U}_{\mathrm{D}}\left(\mathbf{x} - \boldsymbol{\xi}; \mathbf{e}_x\right) d\xi\,,
\end{aligned}
\tag{3.7}
$$

where

$$
\gamma_3 = \frac{1 - e^2}{-2e + (1 + e^2)L_e}\,,\quad \beta_3 = \frac{(1 - e^2)(L_e - 2e)}{4e(2e^2 - 3) + 6(1 - e^2)L_e}\gamma_3\,,\ \text{and}\quad \alpha_3 = \frac{4e^2}{1 - e^2}\beta_3\,.
$$

3.4.1 The velocity field for an extensional flow past a spheroid

The velocity field for linear shears past a prolate spheroid $\frac{x^2}{a^2} + \frac{y^2 + z^2}{b^2} = 1$ along the x-axis is reported in Chwang & Wu [19], while the velocity field of the extension flow $x\mathbf{e}_x - y\mathbf{e}_y$ past a spheroid is not available explicitly. The velocity field could be constructed using the singularity method. Here, we provide the details about the velocity field of an extensional flow $(\Omega x, -\Omega y, 0)$ past a spheroid from the general velocity field in Jeffery [36]. Adopted from Jeffery's results, the velocity field of the extensional flow past a prolate spheroid is,

$$
\begin{aligned}
u \;=\;& x\{\Omega + \beta'(W - V) - 2(\alpha + 2\beta)A\} \\
&- \frac{2xP^2}{(a^2 + \lambda)\,\triangle}\left[\{W - 2(a^2 + \lambda)A + 2(b^2 + \lambda)B\}y^2\right. \\
&\qquad\qquad\qquad \left. -\{V - 2(b^2 + \lambda)C + 2(a^2 + \lambda)A\}z^2\right],
\end{aligned}
$$

$$
\begin{aligned}
v \;=\;& y\{-\Omega + \alpha'U - \beta'W - 2(\alpha + 2\beta)B\} \\
&- \frac{2yP^2}{(b^2 + \lambda)\,\triangle}\left[\{U - 2(b^2 + \lambda)B + 2(b^2 + \lambda)C\}z^2/(b^2 + \lambda)^2\right. \\
&\qquad\qquad\qquad \left. -\{W - 2(a^2 + \lambda)A + 2(b^2 + \lambda)B\}x^2/(a^2 + \lambda)^2\right],
\end{aligned}
$$

66

$$w = z\{\beta'V - \alpha'U - 2(\alpha + 2\beta)C\}$$
$$-\frac{2zP^2}{(b^2 + \lambda)\triangle}\left[\{V - 2(b^2 + \lambda)C + 2(a^2 + \lambda)A\}x^2/(a^2 + \lambda)^2\right.$$
$$\left.-\{U - 2(b^2 + \lambda)B + 2(b^2 + \lambda)C\}y^2/(b^2 + \lambda)^2\right].$$

Next, all the variables used in the above equation are provided in detail.

First, $\triangle = (a^2 + \lambda)^{\frac{1}{2}}(b^2 + \lambda)$, so the velocity field can be rewritten as

$$u = x\{\Omega + \beta'(W - V) - 2(\alpha + 2\beta)A\}$$
$$-\frac{2xP^2}{(a^2 + \lambda)^{\frac{3}{2}}(b^2 + \lambda)^3}\left[\{W - 2(a^2 + \lambda)A + 2(b^2 + \lambda)B\}y^2\right.$$
$$\left.-\{V - 2(b^2 + \lambda)C + 2(a^2 + \lambda)A\}z^2\right],$$

$$v = y\{-\Omega + \alpha'U - \beta'W - 2(\alpha + 2\beta)B\}$$
$$-\frac{2yP^2}{(a^2 + \lambda)^{\frac{1}{2}}(b^2 + \lambda)^2}\left[\{U - 2(b^2 + \lambda)B + 2(b^2 + \lambda)C\}z^2/(b^2 + \lambda)^2\right.$$
$$\left.-\{W - 2(a^2 + \lambda)A + 2(b^2 + \lambda)B\}x^2/(a^2 + \lambda)^2\right],$$

$$w = z\{\beta'V - \alpha'U - 2(\alpha + 2\beta)C\}$$
$$-\frac{2zP^2}{(a^2 + \lambda)^{\frac{1}{2}}(b^2 + \lambda)^2}\left[\{V - 2(b^2 + \lambda)C + 2(a^2 + \lambda)A\}x^2/(a^2 + \lambda)^2\right.$$
$$\left.-\{U - 2(b^2 + \lambda)B + 2(b^2 + \lambda)C\}y^2/(b^2 + \lambda)^2\right].$$

Here, λ is the positive root of $\frac{x^2}{a^2+\lambda} + \frac{y^2+z^2}{b^2+\lambda} = 1$, i.e.

$$\lambda = \frac{1}{2}\left(x^2 + y^2 + z^2 - a^2 - b^2\right.$$
$$\left.+\sqrt{(x^2 + y^2 + z^2 - a^2 - b^2)^2 + 4\{a^2(y^2 + z^2 - b^2) + b^2x^2\}}\right),$$

and

$$P^2 = \left(\frac{x^2}{(a^2 + \lambda^2)^2} + \frac{y^2 + z^2}{(b^2 + \lambda)^2} \right)^{-1}.$$

The explicit harmonic functions included in the velocity field are

$$\alpha = \int_\lambda^\infty \frac{1}{(a^2 + \lambda)^{\frac{3}{2}} (b^2 + \lambda)} \, d\lambda = -\frac{2}{(a^2 - b^2) \sqrt{a^2 + \lambda}} - \frac{\log \left(\frac{\sqrt{a^2+\lambda} - \sqrt{a^2-b^2}}{\sqrt{a^2+\lambda} + \sqrt{a^2-b^2}} \right)}{(a^2 - b^2)^{3/2}},$$

$$\beta = \int_\lambda^\infty \frac{1}{(b^2 + \lambda)^2 \sqrt{(a^2 + \lambda)}} \, d\lambda = \frac{\sqrt{a^2 + \lambda}}{(a^2 - b^2)(b^2 + \lambda)} + \frac{\log \left(\frac{\sqrt{a^2+\lambda} - \sqrt{a^2-b^2}}{\sqrt{a^2+\lambda} + \sqrt{a^2-b^2}} \right)}{2(a^2 - b^2)^{3/2}},$$

$$\alpha' = \int_\lambda^\infty \frac{1}{(b^2 + \lambda)^3 \sqrt{(a^2 + \lambda)}} \, d\lambda$$

$$= \frac{\sqrt{a^2 + \lambda} \, (2a^2 - 5b^2 - 3\lambda)}{4(a^2 - b^2)^2 (b^2 + \lambda)^2} - \frac{3 \log \left(\frac{\sqrt{a^2+\lambda} - \sqrt{a^2-b^2}}{\sqrt{a^2+\lambda} + \sqrt{a^2-b^2}} \right)}{8(a^2 - b^2)^{5/2}},$$

$$\beta' = \int_\lambda^\infty \frac{1}{(a^2 + \lambda)^{\frac{3}{2}} (b^2 + \lambda)^2} \, d\lambda$$

$$= \frac{a^2 + 2b^2 + 3\lambda}{(a^2 - b^2)^2 \sqrt{a^2 + \lambda} \, (b^2 + \lambda)} + \frac{3 \log \left(\frac{\sqrt{a^2+\lambda} - \sqrt{a^2-b^2}}{\sqrt{a^2+\lambda} + \sqrt{a^2-b^2}} \right)}{2(a^2 - b^2)^{5/2}},$$

$$\alpha'' = \int_\lambda^\infty \frac{\lambda}{(b^2 + \lambda)^3 \sqrt{(a^2 + \lambda)}} \, d\lambda = \beta - b^2 \alpha' = \frac{\sqrt{a^2 + \lambda}}{(a^2 - b^2)(b^2 + \lambda)}$$

$$- \frac{b^2 (2a^2 - 5b^2 - 3\lambda) \sqrt{a^2 + \lambda}}{4(a^2 - b^2)^2 (b^2 + \lambda)^2} + \frac{(4a^2 - b^2) \log \left(\frac{\sqrt{a^2+\lambda} - \sqrt{a^2-b^2}}{\sqrt{a^2+\lambda} + \sqrt{a^2-b^2}} \right)}{8(a^2 - b^2)^{5/2}},$$

and

$$\beta'' = \int_\lambda^\infty \frac{\lambda}{(a^2 + \lambda)^{\frac{3}{2}} (b^2 + \lambda)^2} \, d\lambda = \alpha - b^2 \beta'$$

$$= -\frac{(b^2 \lambda + a^2 (3b^2 + 2\lambda))}{(a^2 - b^2)^2 \sqrt{a^2 + \lambda} \, (b^2 + \lambda)} - \frac{(2a^2 + b^2) \log \left(\frac{\sqrt{a^2+\lambda} - \sqrt{a^2-b^2}}{\sqrt{a^2+\lambda} + \sqrt{a^2-b^2}} \right)}{2(a^2 - b^2)^{5/2}}.$$

The constants A through W are

$$A = \frac{\Omega}{6\beta_0''}, \qquad B = \Omega\frac{-2\beta_0'' - \alpha_0''}{6\beta_0''(\beta_0'' + 2\alpha_0'')}, \qquad C = \Omega\frac{-\alpha_0'' + \beta_0''}{6\beta_0''(\beta_0'' + 2\alpha_0'')},$$

$$U = -\frac{\Omega b^2}{2\alpha_0'' + \beta_0''}, \qquad V = \frac{\Omega b^2(\beta_0'' - \alpha_0'')}{3\beta_0''(\beta_0'' + 2\alpha_0'')} - \frac{\Omega a^2}{3\beta_0''}, \qquad W = \frac{\Omega a^2}{3\beta_0''} + \frac{\Omega b^2(2\beta_0'' + \alpha_0'')}{3\beta_0''(\beta_0'' + 2\alpha_0'')},$$

where $\alpha_0'' = \frac{3-e^2}{4a^3e^4(1-e^2)} - \frac{(e^2+3)L_e}{8a^3e^5}$ and $\beta_0'' = \frac{-6e+(3-e^2)L_e}{2a^3e^5}$ are α'' and β'' evaluated at $\lambda = 0$, respectively.

3.4.2   Stagnation points on the tilted spheroid

As for the other cases we have discussed, six stagnation points on the tilted spheroid are obtained by rescaling the velocity field in prolate spherical coordinates and linearizing it near the surface of the spheroid. Two of the stagnation points are located at $(0, \pm b, 0)$, while the location of the other four are defined by the solutions of the following equation in prolate spheroid coordinates

$$\frac{\cos(2\kappa)\cos(2\nu)}{3(1-e^2)L_e + 2e(2e^2 - 3)}$$
$$- \frac{\{22e^3 - 18e + (9 - 14e^2 + 5e^4)L_e\}\sin(2\kappa)\sin(2\nu)}{2\sqrt{1-e^2}\left(6e + (e^2 - 3)L_e\right)\left(2e(5e^2 - 3) + 3(e^2 - 1)^2 L_e\right)} \tag{3.8}$$
$$+ \frac{12e - 8e^3 - 6(1-e^2)L_e + (6e + (e^2 - 3)L_e)e^2\cos(2\kappa)}{e^2\left(3(1-e^2)L_e + 2e(2e^2 - 3)\right)\left((1+e^2)L_e - 2e\right)} = 0 \ .$$

Use notation $T = \tan(\nu)$, then

$$\frac{e^2\cos(2\kappa)\left(1 - T^2\right)}{3(1-e^2)L_e + 2e(2e^2 - 3)} - \frac{e^2\left(5e^4 L_e + 22e^3 - 14e^2 L_e - 18e + 9L_e\right)\sin(2\kappa)T}{\sqrt{1-e^2}\left(6e + (e^2 - 3)L_e\right)\left(2e(5e^2 - 3) + 3(e^2 - 1)^2 L_e\right)}$$
$$+ \frac{(-6L_e + 2e(6 - 4e^2 + 3eL_e) + e^2(6e + (e^2 - 3)L_e)\cos(2\kappa))}{(3L_e + e(4e^2 - 3eL_e - 6))(L_e + e(eL_e - 2))}\left(1 + T^2\right) = 0.$$

(a) Configuration   (b) Streamlines
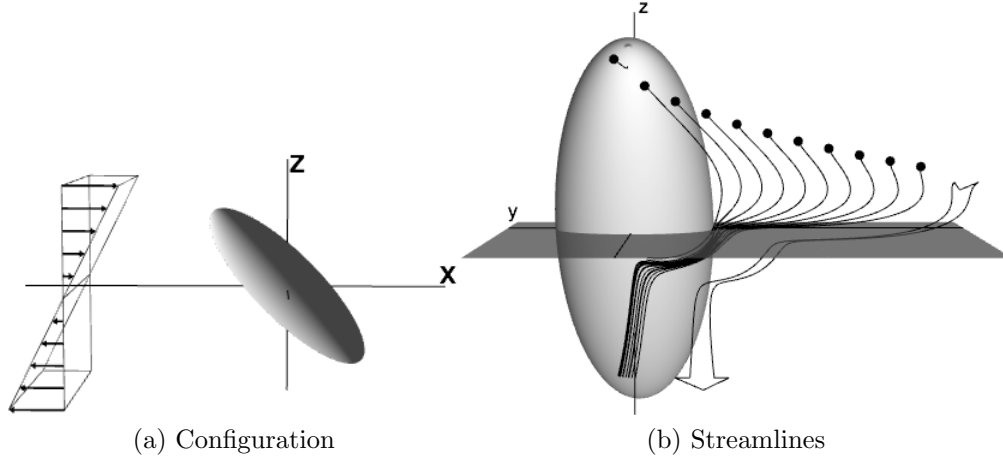
Figure 3.4: Blocked streamlines near the separation surface in the $y < 0$ half space when the spheroid is tilted toward the shear with $\kappa = -\frac{\pi}{4}$. Particles initially distributed on a curve within the blocked region move downwards while being attracted toward the body as indicated by the perspective arrow to the right.

This equation yields two values of the angle ν between 0 and π, corresponding to two stagnation points on the spheroid in the $y = 0$ symmetry plane. In the original rectangular coordinates, where the spheroid is tilted in the shear flow, these two stagnation points are defined by substituting such solutions ν into

$$
\begin{pmatrix} x_s \\ y_s \\ z_s \end{pmatrix} = a \begin{pmatrix} -\sin(\kappa)\cos(\nu) - \sqrt{1-e^2}\cos(\kappa)\sin(\nu) \\ 0 \\ \cos(\kappa)\cos(\nu) - \sqrt{1-e^2}\sin(\kappa)\sin(\nu) \end{pmatrix}. \tag{3.9}
$$

Using the specular symmetry of the setup with respect to the origin in the $y = 0$ plane locates the other two stagnation points.

Figure 3.4 and 3.5 are plots of numerically evaluated streamlines from the above exact velocity field in the laboratory frame which illustrate the main features of the flow. When the spheroid is tilted in the x-z plane, the portion of the y-axis in the fluid turns into a stagnation streamline, as opposed to a line of fixed points for the upright case, i.e., points on the y-axis move in the y-direction. However, the y-axis keeps its

70
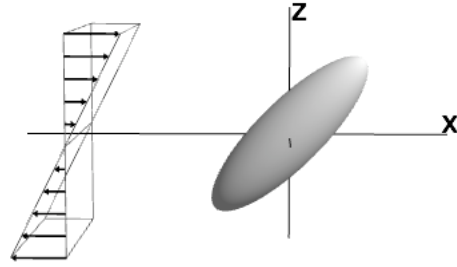
(a) Configuration
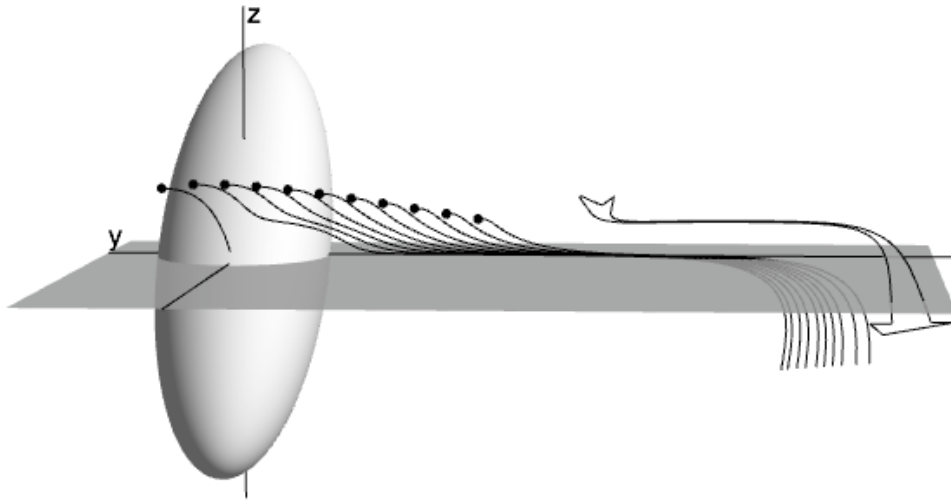
(b) Streamlines

Figure 3.5: Similar to Figure 3.4, blocked streamlines near the separation surface in the $y < 0$ half space, when the spheroid is tilted along the shear with $\kappa = \frac{\pi}{4}$.

feature of being the intersection of separation surfaces bounding the blocked region of fluid. For a given spheroid, the maximum speed on the y-axis streamline is achieved at a certain finite location on this axis for the tilt corresponding to the angle $\kappa = \pm\frac{\pi}{4}$. The speed along the y-axis is zero on the body and at infinity.

- When the spheroid is tilted toward the background linear shear ($\kappa < 0$), on the y-axis, the flow pushes the fluid particles toward to the spheroid. Figure 3.4a shows the configuration of the linear shear and the tilted spheroid with $\kappa = -\frac{\pi}{4}$, and Figure 3.4b shows the positive suction of the fluid particles when the particle trajectories are close to the separation surface.

- When the spheroid is tilted along the background linear shear ($\kappa > 0$), on the y-axis, the flow pushes the fluid particles away from the spheroid. The configuration of the linear shear and the tilted spheroid with $\kappa = \frac{\pi}{4}$ is shown in Figure 3.5a, and the negative suction of the fluid particles is illustrated with the blocked fluid particles trajectories close to the separation surface in Figure 3.5b.

3.4.3 Cross sections of the blocked regions

For the cross section of the blocked region, when the spheroid is upright or horizontal, i.e. when its major axis is aligned along the z or x axis, respectively, the up-down symmetry (reflections with respect to the x-y plane) of the setup is preserved; in this case, the cross section is symmetric as shown in Figure 3.6a. This is similar to the spherical case in Figure 2.7, but notice that corners develop on the bounding surfaces along the $y = 0$ plane. The cross section height is a decreasing function of y. When the spheroid is tilted in the x-z plane, the up-down symmetry of the cross section is also broken: when the spheroid is tilted against the background stream ($\kappa < 0$), both boundaries of the cross section are concave upward near $y = 0$; when the spheroid is tilted along the background linear shear ($\kappa > 0$), both boundaries of the cross section

(a) Upright spheroid ($\kappa = 0$)

(b) $\kappa = -\frac{\pi}{4}$

(c) $\kappa = \frac{\pi}{4}$
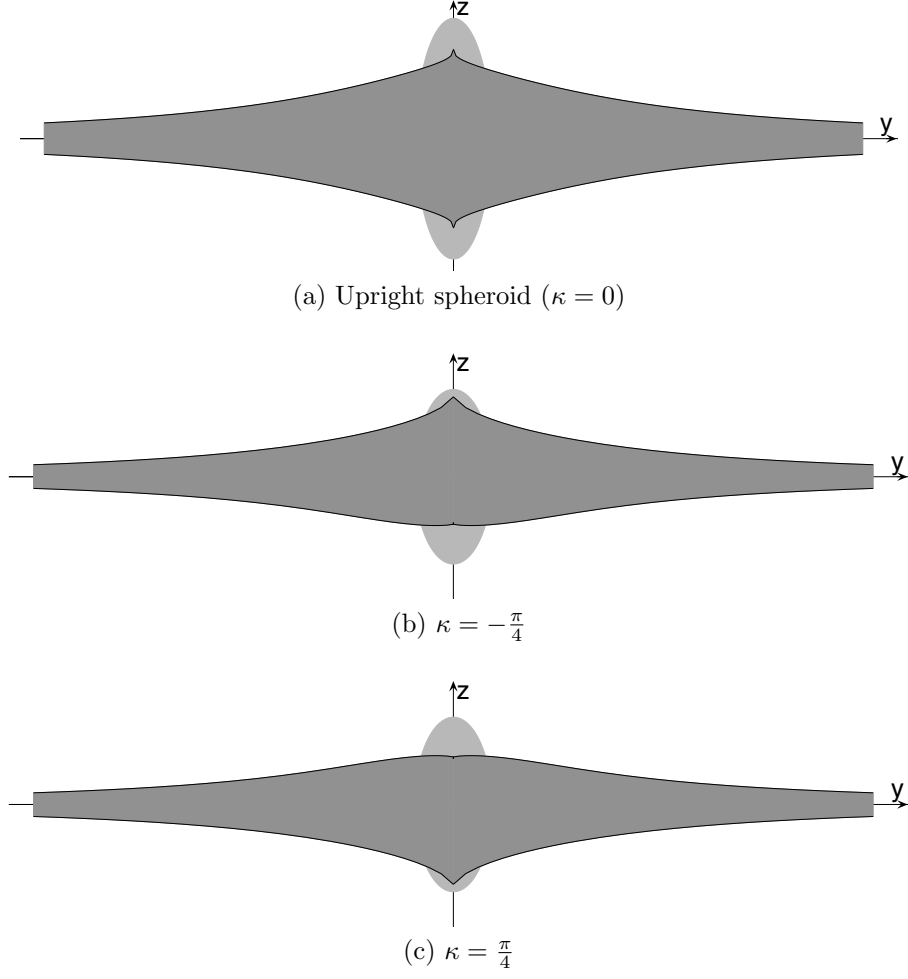
Figure 3.6: Cross sections of the blocked region at $x = -5$ fixed.

are concave downward near $y = 0$. Figure 3.6b and Figure 3.6c are cross sections of the blocked region with $\kappa = -\frac{\pi}{4}$ and $\kappa = \frac{\pi}{4}$, respectively.

Near the corners, the concavity of the boundaries of the blocked region depends on the spheroid's eccentricity e and the tilt angle κ. From the local analysis near the stagnation points 3.9 in the symmetry plane, the eigenvectors of the matrix of the linearized velocity in the general body frame, where the spheroid is along the x-axis, are $(0, 0, a)$ and $a\left(0, \sqrt{1 - e^2}\sin(\nu), \cos(\nu)\right)$. When these two vectors are perpendicular

to each other, i. e. the eccentricity e and the tilt angle κ satisfy

$$\frac{12e - 8e^3 - 6(1 - e^2)L_e + \left(6e + \left(e^2 - 3\right) L_e\right) e^2 \cos(2\kappa)}{e^2 \left(3(1 - e^2)L_e + 2e \left(2e^2 - 3\right)\right) \left((1 + e^2)L_e - 2e\right)}$$
$$- \frac{\cos(2\kappa)}{3(1 - e^2)L_e + 2e \left(2e^2 - 3\right)} = 0,$$

the concavity of the blocked region changes.

Chapter 4

A sphere or spheroid embedded in a rotation flow

To further explore the flow past a rigid obstacle, we consider the flow with a sphere or spheroid embedded in rotating flows in this chapter.

4.1   A sphere embedded in a rotating flow

First, we consider the flow with a sphere embedded in rotating flows. The center of the sphere is set at the origin of the coordinate system. The background flow is a rigid body rotation in the x-y plane with the rotation axis parallel to the z-axis and translated a fixed distance L from the origin. In this case, the x-y plane is the symmetry plane of the flow. The planar linear shear case with the sphere's center at some distance off the zero-velocity plane may be viewed as an extreme case of this rotating background flow in that at large distances L, the curvature of rigid body rotation streamlines over regions of sphere radius scales becomes negligible. However, there are important differences with respect to the planar case in the interpretation of blocking regions for the case of rotating background flow past a sphere, as in this case the definition of blocking itself becomes fundamentally different. We will study

the case when the sphere is fixed in the rotating flow first and then allow the sphere to additionally self-rotate. For a sphere self-rotating in the rotating background flow, we report results about the flow in the cases when the sphere may freely self-rotate and the cases when the sphere self rotates with a prescribed angular velocity. The rotation axis of the self-rotation of the sphere is always the z-axis. For a sphere embedded in such rotating flows, we will find the explicit fluid particle trajectories from the exact velocity field and document the analytical formula for stagnation points on the sphere and the critical points in the interior of the flow.

4.1.1 A fixed sphere in the rotating flow

When the unit sphere is embedded in purely rotating flows, the background flow can be decomposed into a uniform flow plus two linear shear flows in the rectangular coordinates, whose origin is the center of the sphere. Assuming the non-dimensional angular velocity of the rotation is $(0, 0, 1)$ and the distance between the rotation axis and the origin is $L \geq 0$, the background flow is $y\mathbf{e}_x - (x + L)\mathbf{e}_y$. When the sphere is fixed, with the no-slip boundary condition on the surface of the sphere, the velocity of the flow can be obtained from (2.4),

$$
\begin{aligned}
u(x, y, z) &= \left(y - \frac{y}{(x^2 + y^2 + z^2)^{3/2}} + \frac{3Lxy}{4(x^2 + y^2 + z^2)^{3/2}} - \frac{3Lxy}{4(x^2 + y^2 + z^2)^{5/2}} \right), \\
v(x, y, z) &= -L - x + \frac{x}{(x^2 + y^2 + z^2)^{3/2}} + \\
&\quad \frac{L}{4} \left(\frac{3}{\sqrt{x^2 + y^2 + z^2}} + \frac{1 + 3y^2}{(x^2 + y^2 + z^2)^{3/2}} - \frac{3y^2}{(x^2 + y^2 + z^2)^{5/2}} \right), \quad (4.1) \\
w(x, y, z) &= -\frac{3Lyz}{4(x^2 + y^2 + z^2)^{5/2}} + \frac{3Lyz}{4(x^2 + y^2 + z^2)^{3/2}}.
\end{aligned}
$$

Similar to the planar shear past a sphere, we calculate the fluid particle trajectories

for this velocity field and obtain the explicit formulae in terms of r,

$$
\begin{aligned}
x &= \frac{r^2(5+4r)}{8L(1-r)} + \frac{r^2\left(27\sqrt{2}\log(2\sqrt{r}+\sqrt{2(1+2r)})-8C_1\right)}{16L(1-r)\sqrt{r(1+2r)}}, \\
z^2 &= \frac{C_2 r^3}{(r-1)^2(1+2r)}, \\
y^2 &= r^2 - x^2 - z^2,
\end{aligned}
$$

where C_1 and C_2 are constant determined by the initial condition of the fluid particle.

To present the structure of the flow, we plot fluid particle trajectories with different L in the x-y symmetry plane.

- When $L = 0$, trajectories are shown as in Figure 4.1a. In this case, it is easy to verify from the velocity field (4.1) that there is no motion in the z-direction and all velocity components vanish along the z-axis ($x = y = 0$).

- When $0 < L < 2$, trajectories are illustrated in Figure 4.1b with a specified value $L = 1$. There are two stagnation points on the sphere and they are in the x-z plane, shown in Figure 4.3b when we show the stagnation points on the sphere.

- When $L = 2$, trajectories are shown in Figure 4.1c. There is one stagnation point on the sphere at $(-1, 0, 0)$.

- When $L > 2$, trajectories are plotted as Figure 4.1d with $L = 3$. There are two stagnation points on the sphere. Figure 4.2 is the 3D view of Figure 4.1d.

As Figure 4.1 and 4.2 show, the stagnation points on the sphere depend on the distance L. For a unit sphere, there are two stagnation points $(-\frac{L}{2}, 0, \frac{\sqrt{4-L^2}}{2})$ and $(-\frac{L}{2}, 0, \frac{\sqrt{4-L^2}}{2})$ on the sphere if $0 \leq L < 2$. When $L = 2$, there is only one stagnation point $(-1, 0, 0)$ on the sphere. When $L > 2$, there are two stagnation points on the

(a) L=0

(b) L=1

(c) L=2

(d) L=3
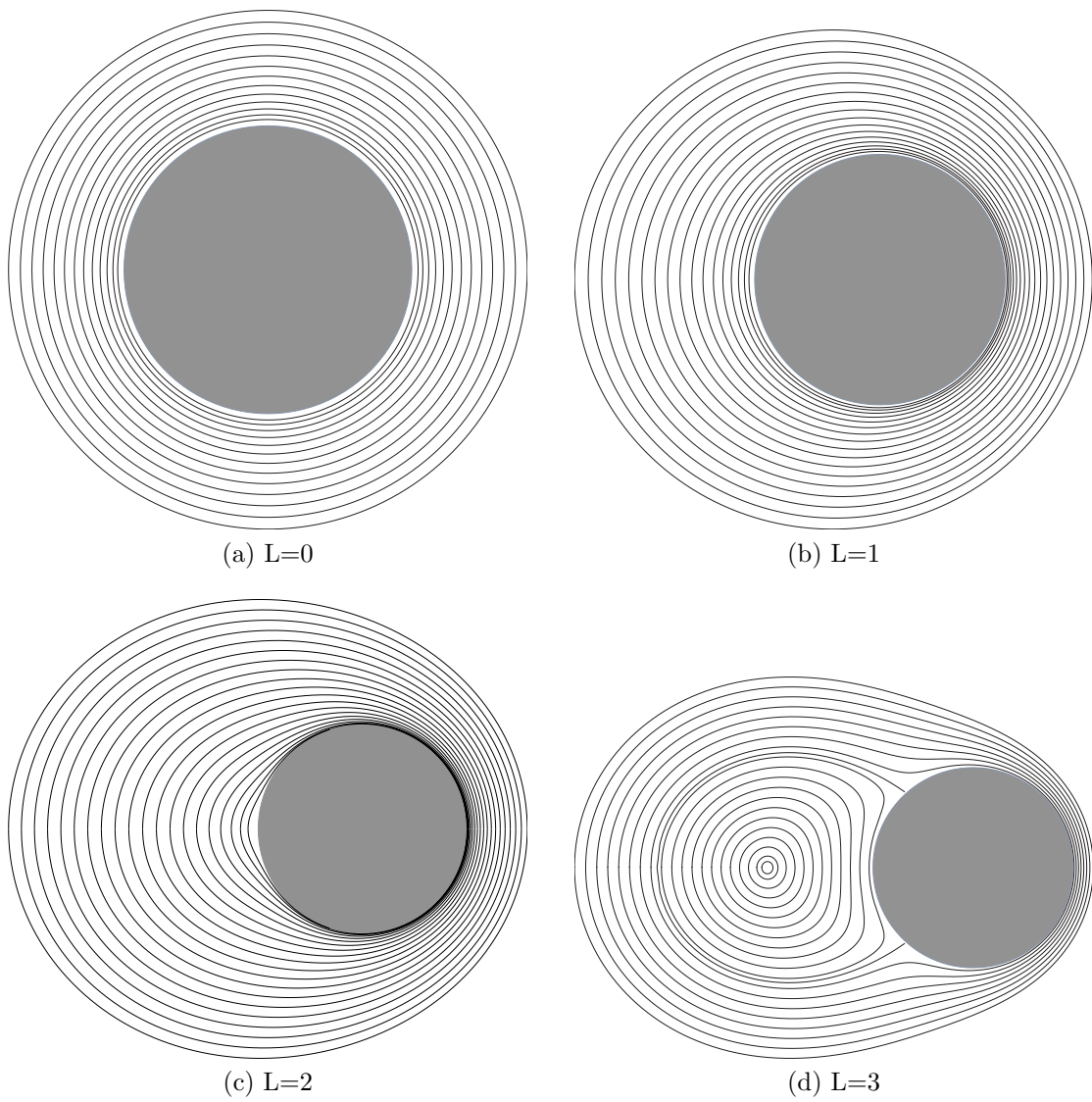
Figure 4.1: Trajectories in the x-y symmetry plane.
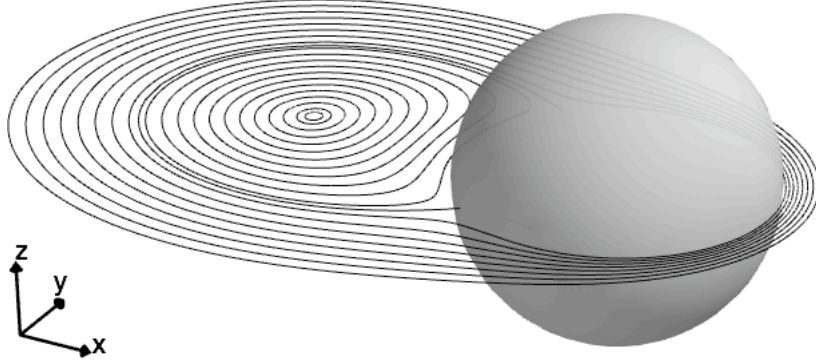
Figure 4.2: 3D view o f trajectories in the x-y symmetry plane when $L > 2$.

sphere at $(-\frac{2}{L}, \frac{\sqrt{L^2-4}}{L}, 0)$ and $(-\frac{2}{L}, -\frac{\sqrt{L^2-4}}{L}, 0)$, but they are in the x-y symmetry plane instead of the x-z plane for the $L < 2$ cases.

Furthermore, we get the formula for critical points in the interior of the flow, which are always in the x-z plane. The implicit formula for critical points in the flow is

$$\frac{L + 4x}{4\left(x^2 + z^2\right)^{3/2}} = L + x - \frac{3L}{4\sqrt{x^2 + z^2}}.$$

In parametric formulae, they are

$$x = -\frac{L}{4}\frac{1 + s + 4s^2}{1 + s + s^2},$$
$$z = \pm\sqrt{s^2 - x^2} = \pm\frac{\sqrt{16s^2(1 + s + s^2)^2 + L^2(1 + s + 4s^2)^2}}{4(1 + s + s^2)},$$

where $|s| \geq 1$. When $L \leq 2$, critical points in the interior of the flow connect to the two stagnation points $(-\frac{L}{2}, 0, \frac{\sqrt{4-L^2}}{2})$ and $(-\frac{L}{2}, 0, \frac{\sqrt{4-L^2}}{2})$ on the sphere as shown in Figure 4.3a and Figure 4.3b. Black dots on the sphere are stagnation points in Figure

4.3. Since critical points in the flow are only in the x-z plane, plots in Figure 4.3 are restricted in the x-z plane. The black curve in Figure 4.3a shows where critical points are when $L = 0$. Figure 4.3b shows the location of critical points when $L = 1$. For the special case $L = 2$ shown in Figure 4.3c, the curve connects to the unique stagnation point $(-1, 0, 0)$ on the sphere. Otherwise, for $L > 2$, as in Figure4.3d $(L = 3)$, critical points are on a curve that is still in the x-z plane but is away from the sphere. All the curves are asymptotic to the rotation axis of the background flow as $|z| \to \infty$. Notice the analogy of these curves of fixed points with those identified off the x-z plane by the analysis of the linear planar shear case in Table 2.1 in Chapter 2. The force acting on the fixed sphere is $\mathbf{F} = -6\pi\mu L\mathbf{e}_y$ and the torque at the origin is $\mathbf{T} = -8\pi\mu\mathbf{e}_y$ in dimensionless formulae.

4.1.2 A self-rotating sphere in the rotating flow

If the sphere self-rotates in the rotating background flow, imposing the no-slip boundary condition on the rotating sphere requires the velocity on the surface of the sphere to be $\mathbf{U}' = -\gamma y\mathbf{e}_x + \gamma x\mathbf{e}_y$. Here, γ is the angular velocity of the sphere's self-rotation in the z direction. For the special torque free case involving a sphere freely self-rotating at the origin, the angular velocity of the self-rotation is set to $\gamma = -1$, as the calculation shows. The exact velocity field is

$$
\begin{aligned}
u(x,y,z) &= y + \frac{3Lxy}{4\left(x^2 + y^2 + z^2\right)^{3/2}} - \frac{3Lxy}{4\left(x^2 + y^2 + z^2\right)^{5/2}} - \frac{(\gamma+1)y}{\left(x^2 + y^2 + z^2\right)^{3/2}}, \\
v(x,y,z) &= -L - x + \frac{3L}{4\sqrt{x^2 + y^2 + z^2}} + \frac{4x(\gamma+1) + L(1 + 3y^2)}{4\left(x^2 + y^2 + z^2\right)^{3/2}} \\
&\quad - \frac{3Ly^2}{4\left(x^2 + y^2 + z^2\right)^{5/2}}, \\
w(x,y,z) &= \frac{3Lyz}{4\left(x^2 + y^2 + z^2\right)^{3/2}} - \frac{3Lyz}{4\left(x^2 + y^2 + z^2\right)^{5/2}}.
\end{aligned}
$$

(a) $L = 0$

(b) $L = 1$

(c) $L = 2$

(d) $L = 3$
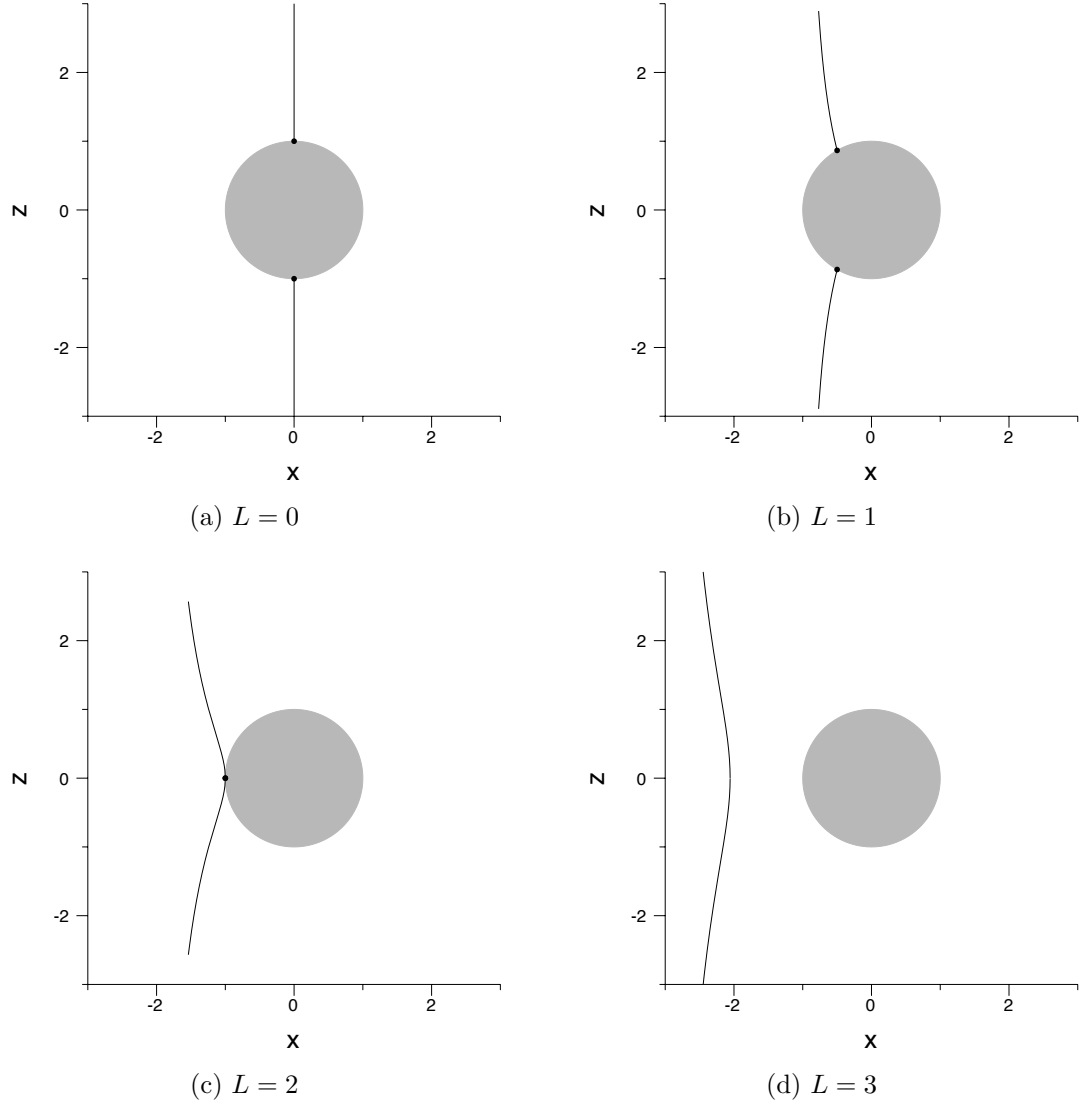
Figure 4.3: Critical points in the flow when a fixed sphere is embedded in a rotating background flow. L is the distance from the rotation center of the background flow to the center of the unit sphere.

And the equation of fluid particles is the following parametric system

$$
\begin{aligned}
x &= \frac{r^3}{2L\sqrt{(r-1)^2 r^3(1+2r)}} \left\{ -\frac{1}{24\sqrt{(1+2r)}} \left[64\gamma\sqrt{3(1+2r)}\operatorname{arctanh}\left(\sqrt{\frac{3r}{1+2r}}\right) \right.\right. \\
&\quad \left.\left. +3\left(2\sqrt{r}\left(5+14r+8r^2\right)+27\sqrt{2(1+2r)}\log\left(2\sqrt{r}+\sqrt{2(1+2r)}\right)\right)\right] - C_1 \right\}, \\
z^2 &= \frac{r^3}{C_2(r-1)^2(1+2r)}, \\
y^2 &= r^2 - x^2 - z^2,
\end{aligned}
$$

where constants C_1 and C_2 depend on initial values.

   Critical points in the interior of the flow are

$$
\begin{cases}
x &= \frac{L}{4(\gamma+1-r^3)}(4r^3 - 3r^2 - 1), \\
z^2 &= r^2 - x^2.
\end{cases}
\tag{4.2}
$$

The slope of the critical-point curve as depicted in Figure 4.4 is $\frac{2\gamma}{3L}$ at the top of the sphere $(0,0,1)$. For the degenerate cases $L = 0$ and $\gamma > -1$, the velocity does not only vanish on the curve prescribed by (4.2) in the x-z plane but also on the shell $x^2 + y^2 + z^2 = (1+\gamma)^{\frac{2}{3}}$. For the special case $\gamma = 0$ (with the fixed sphere), the location of stagnation points on the sphere depends on L as shown in Figure 4.3. Figure 4.4 shows the critical points in the x-z plane for different L when the sphere is freely self-rotating in the rotating background flow.

   Figure 4.5 shows the freely self-rotating case's fluid particle trajectories in the x-y symmetry plane for different L. Figure 4.6 shows trajectories of fluid particles out of the x-y symmetry plane, when $L = 4$ and the sphere is freely rotating.

   When the orientation of the sphere's self-rotation is opposite and equal to that of the background flow, Figure 4.7 shows critical points in the x-z plane and Figure 4.8 shows the trajectories of fluid particles in the x-y symmetry plane with different values of L and $\gamma = 1$. Figure 4.9 show the structure of the fluid particle trajectories out of

(a) $L = 0$

(b) $L = 2$

(c) $L = 3.330407$

(d) $L = 4$
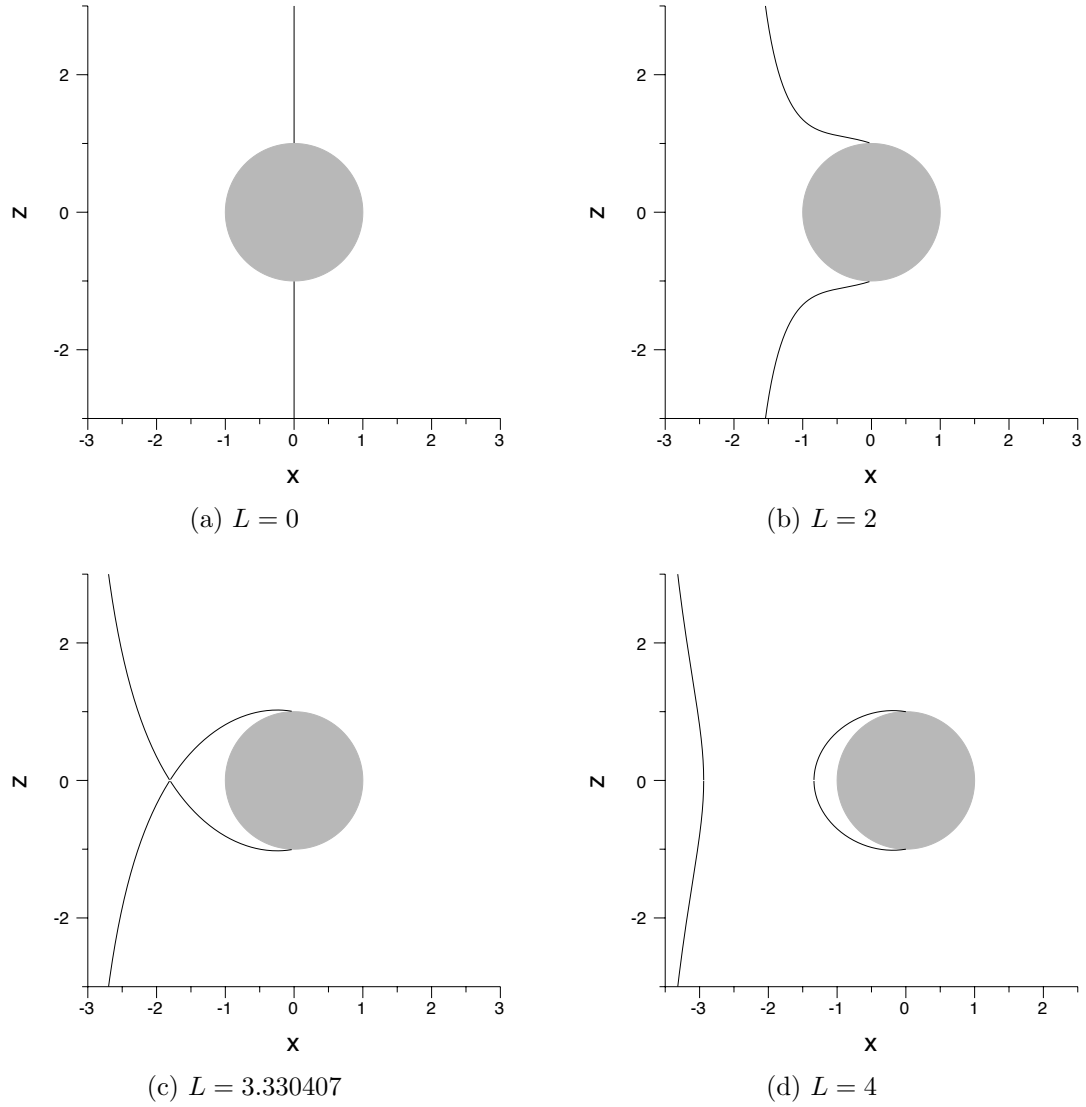
Figure 4.4: Same as Figure 4.3 but for the case of the sphere freely self-rotating in a rotating background flow ($\gamma = -1$).

(a) L=0

(b) L=2
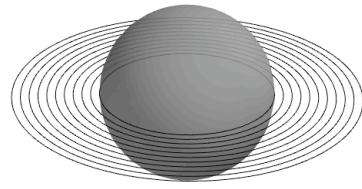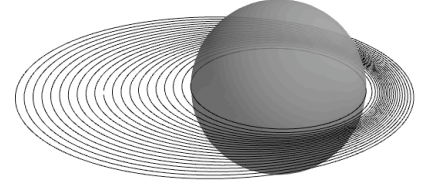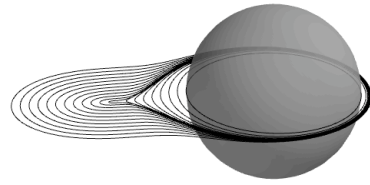
(c) L=3.330407
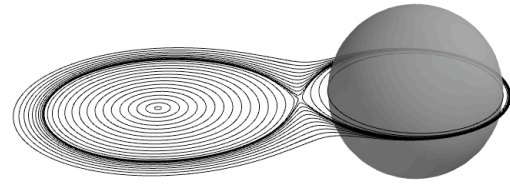
(d) L=4

Figure 4.5: Trajectories in the x-y symmetry plane with a freely-rotating sphere.
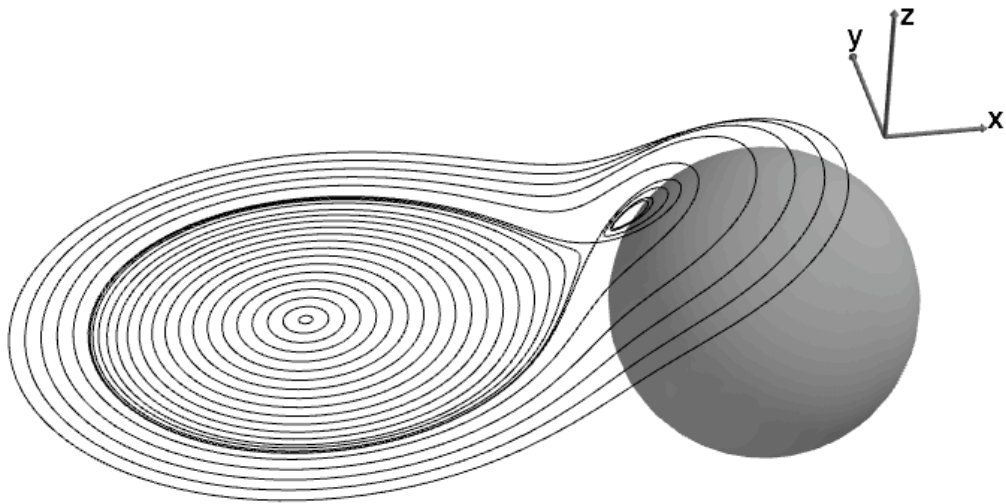
Figure 4.6: Trajectories out of the x-y symmetry plane when the sphere is freely rotating and $L = 4$.

the symmetry plane when $L = 3$.

Comparisons between Figures 4.4-4.6 and Figures 4.7-4.9 show locations of the hyperbolic fixed points may be at either the left or the right side of the sphere, depending upon parameters L, ω and γ.

4.2   A spheroid embedded in a rotation flow

As for the linear shear flow case, we generate our results to the prolate spheroid embedded in the rotating flow in this section. The major axis of the spheroid could be parallel to the axis of the background rotation, or oriented with a tilt angle $\kappa \neq 0$. The tilt angle $(-\frac{\pi}{2} \leq \kappa < \frac{\pi}{2})$ is defined as the angle between the major axis of the spheroid and the axis of the rotation.

The background flow is purely rotating flow in the x-y plane with a constant angular velocity $(0, 0, -\omega)$. If $\omega > 0$, the flow rotates clockwise, otherwise, the background flow rotates counter-clockwise. The distance between the center of the spheroid to the center of the rotation is noted as L. We specify the center of the spheroid at the origin, and the axis of the rotation of the background flow at $(-L, 0, z)$. In this coordinates, the linear velocity of the background flow is

$$\mathbf{U} = \vec{\omega} \times \vec{r} = y_L\,\omega\,\mathbf{e}_x - (x_L + L)\,\omega\,\mathbf{e}_y = \begin{pmatrix} 0 & \omega & 0 \\ -\omega & 0 & 0 \\ 0 & 0 & 0 \end{pmatrix} \begin{pmatrix} x_L \\ y_L \\ z_L \end{pmatrix} - \begin{pmatrix} 0 \\ \omega L \\ 0 \end{pmatrix}.$$

It is a uniform flow plus shear flows in both x direction and y direction.

If the major axis of the spheroid is parallel or perpendicular to the rotation axis of the background flow, the flow is similar to a sphere embedded in a rotation flow. The exact velocity can be constructed with the components for uniform flows and shear

(a) $L = 0$

(b) $L = 0.02$

(c) $L = 1$

(d) $L = 3$
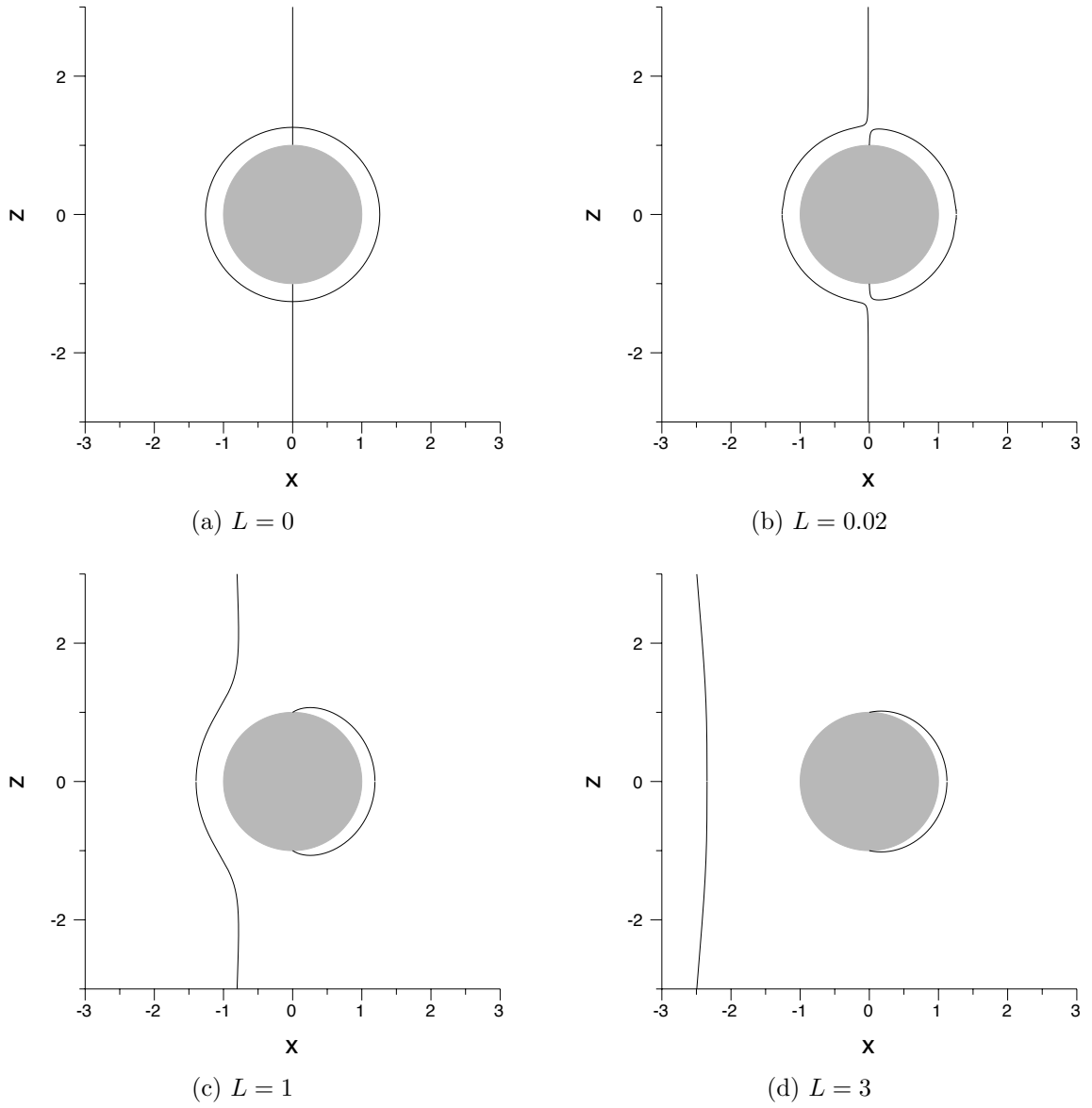
Figure 4.7: Same as Figure 4.3 and 4.4 but with a unit sphere self-rotating in an opposite direction with respect to the background flow ($\gamma = 1$).

(a) L=0

(b) L=0.02

(c) L=1

(d) L=3
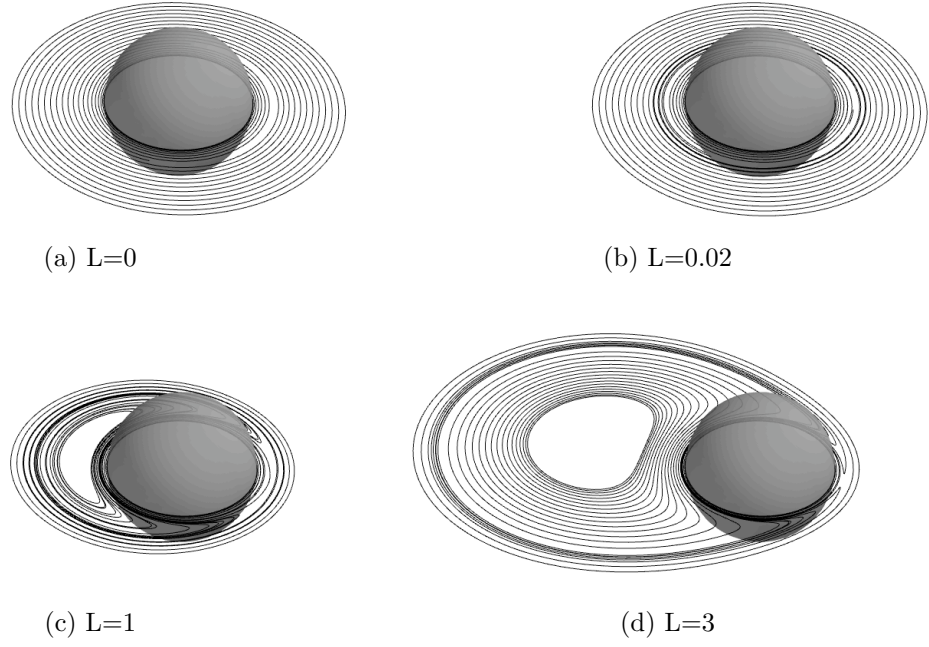
Figure 4.8: Trajectories in the x-y symmetry plane when the sphere is self-rotating in an opposite direction with respect to the background flow.
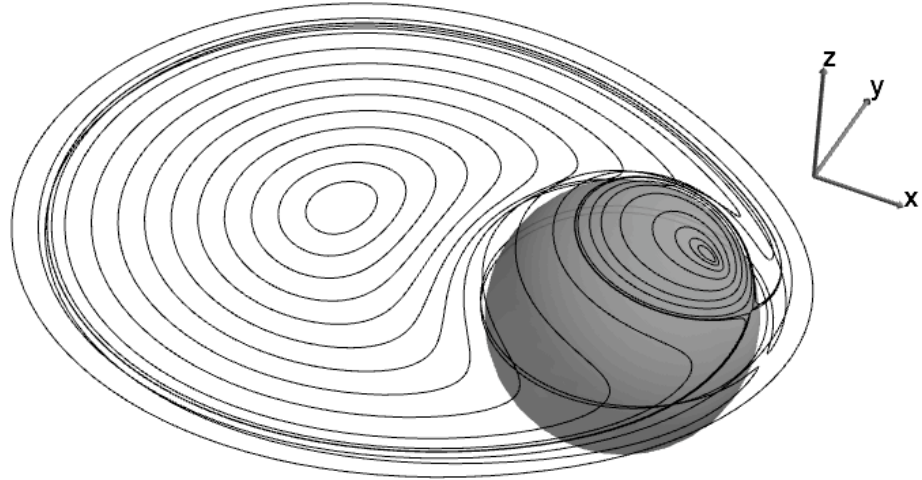
Figure 4.9: Trajectories out of the x-y symmetry plane when the sphere is self-rotating in an opposite direction with respect to the background flow.

flows in Chwang & Wu [19], if their the velocity field is viewed as the velocity field in the body frame. In that body frame, the major axis of the prolate spheroid is along the x-axis and the center of the spheroid is at the origin of the coordinates, which is referred as the "general" body frame in this thesis. When the spheroid is tilted in the radial direction of the rotation ($L = 0$), it is the flow when a spheroid sweeps out an upright cone in one of its body frame as defined in (4.3), which can be similarly obtained from the flow in the general body frame [14].

We consider that the spheroid is tilted in the plane tangential to the rotating background flow, and the angle κ between the major axis of the spheroid and the rotation axis of the background is between $-\frac{\pi}{2}$ and $\frac{\pi}{2}$. Then any tilt direction can be decomposed into radial and tangential directions to the rotation. When $\kappa = 0$, the upright spheroid case is automatically recovered. In the laboratory frame (x_L, y_L, z_L), the tilted prolate spheroid is

$$\frac{x_L^2 + (y_L \cos(\kappa) - z_L \sin(\kappa))^2}{b^2} + \frac{(y_L \sin(\kappa) + z_L \cos(\kappa))^2}{a^2} = 1, \quad (a > b). \qquad (4.3)$$

We construct the velocity field of the flow in the general body frame, where the spheroid is along the x-axis. Then, the equation of the spheroid is $\frac{x_b^2}{a^2} + \frac{y_b^2 + z_b^2}{b^2} = 1$.

The transformation matrix between the laboratory frame (x_L, y_L, z_L) and the general body frame (x_b, y_b, z_b) is

$$R = \begin{pmatrix} 0 & 0 & 1 \\ \sin(\kappa) & -\cos(\kappa) & 0 \\ \cos(\kappa) & \sin(\kappa) & 0 \end{pmatrix}. \qquad (4.4)$$

So,

$$\left(\begin{array}{ccc} x_L & y_L & z_L \end{array} \right)^T = R \left(\begin{array}{ccc} x_b & y_b & z_b \end{array} \right)^T \tag{4.5}$$

The background flow in the general body frame is

$$\mathbf{U}_b(\mathbf{x}_b) = R^T \mathbf{U}(R\mathbf{x}_b) = \omega \left(\begin{array}{c} -\sin(\kappa)z_b \\ \cos(\kappa)z_b \\ \sin(\kappa)x_b - \cos(\kappa)y_b \end{array} \right) + \omega L \left(\begin{array}{c} -\sin(\kappa) \\ \cos(\kappa) \\ 0 \end{array} \right), \tag{4.6}$$

which consists of a uniform flow $-\omega L \sin(\kappa)\mathbf{e}_x + \omega L \cos(\kappa)\mathbf{e}_y$ in x and y directions and four shear flows $-\omega \sin(\kappa)z_b\mathbf{e}_x$, $\omega \cos(\kappa)z_b\mathbf{e}_y$, $\omega \sin(\kappa)x_b\mathbf{e}_z$ and $-\omega \cos(\kappa)y_b\mathbf{e}_z$.

4.2.1 The velocity field

From (4.7), the velocity field for the **uniform flow** $-\omega L \sin(\kappa)\mathbf{e}_x + \omega L \cos(\kappa)\mathbf{e}_y$ past a prolate spheroid $\frac{x_b^2}{a^2} + \frac{y_b^2 + z_b^2}{b^2} = 1$ is

$$\begin{aligned} \mathbf{u}_1(\mathbf{x}_b) = & -\omega L \sin(\kappa)\mathbf{e}_x + \omega L \cos(\kappa)\mathbf{e}_y - \int_{-c}^{c} \left[\alpha_1 \mathbf{u}_S \left(\mathbf{x}_b - \boldsymbol{\xi}; \mathbf{e}_x \right) + \alpha_2 \mathbf{u}_S \left(\mathbf{x}_b - \boldsymbol{\xi}; \mathbf{e}_y \right) \right] d\xi \\ & + \int_{-c}^{c} \left(c^2 - \xi^2 \right) \left[\beta_1 \mathbf{u}_D \left(\mathbf{x}_b - \boldsymbol{\xi}; \mathbf{e}_x \right) + \beta_2 \mathbf{u}_D \left(\mathbf{x}_b - \boldsymbol{\xi}; \mathbf{e}_y \right) \right] d\xi, \end{aligned} \tag{4.7}$$

where $\boldsymbol{\xi} = \xi\mathbf{e}_z$,

$$\alpha_1 = \frac{2e^2}{1 - e^2} \beta_1 = \frac{-\omega L \sin(\kappa)e^2}{-2e + (1 + e^2) L_e}, \quad \alpha_2 = \frac{2e^2}{1 - e^2} \beta_2 = \frac{2\omega L \cos(\kappa)e^2}{2e + (3e^2 - 1) L_e},$$

and $L_e = \log \left(\frac{1+e}{1-e} \right)$.

The velocity field for the **shear flow** $-\omega \sin(\kappa)z_b\mathbf{e}_x$ past the spheroid $\frac{x_b^2}{a^2} + \frac{y_b^2 + z_b^2}{b^2} = 1$ is not provided directly in Chwang & Wu [19]. However, by changing coordinates, the

velocity field is obtained as

$$
\mathbf{u}_2(\mathbf{x}_b) = -\omega \sin(\kappa) z_b \mathbf{e}_x + \int_{-c}^{c} \left(c^2 - \xi^2\right) \left[\alpha_3 \mathbf{u}_{\mathrm{SS}}\left(\mathbf{x}_b - \boldsymbol{\xi}; \mathbf{e}_x, \mathbf{e}_z\right) - \gamma_3 \mathbf{u}_{\mathrm{R}}\left(\mathbf{x}_b - \boldsymbol{\xi}; \mathbf{e}_y\right)\right] d\xi
$$
$$
+ \beta_3 \int_{-c}^{c} \left(c^2 - \xi^2\right)^2 \frac{\partial}{\partial z} \mathbf{u}_{\mathrm{D}}\left(\mathbf{x}_b - \boldsymbol{\xi}; \mathbf{e}_x\right) d\xi \,, \tag{4.8}
$$

where

$$
\gamma_3 = \frac{-\omega \sin(\kappa)(1 - e^2)}{-2e + (1 + e^2) L_e}, \quad \text{and } \alpha_3 = \frac{4e^2}{1 - e^2} \quad \beta_3 = \frac{2e^2(L_e - 2e)}{2e(2e^2 - 3) + 3(1 - e^2) L_e} \gamma_3 \,.
$$

The velocity field for the **shear flow** $\omega \cos(\kappa) z_b \mathbf{e}_y$ past the spheroid $\frac{x_b^2}{a^2} + \frac{y_b^2 + z_b^2}{b^2} = 1$ is provided directly in Chwang & Wu [19]

$$
\mathbf{u}_3(\mathbf{x}_b) = \omega \cos(\kappa) z_b \mathbf{e}_y + \int_{-c}^{c} \left(c^2 - \xi^2\right) \left[\alpha_4 \mathbf{u}_{\mathrm{SS}}\left(\mathbf{x}_b - \boldsymbol{\xi}; \mathbf{e}_y, \mathbf{e}_z\right) + \gamma_4 \mathbf{u}_{\mathrm{R}}\left(\mathbf{x}_b - \boldsymbol{\xi}; \mathbf{e}_x\right)\right] d\xi
$$
$$
+ \beta_4 \int_{-c}^{c} \left(c^2 - \xi^2\right)^2 \frac{\partial}{\partial z} \mathbf{u}_{\mathrm{D}}\left(\mathbf{x}_b - \boldsymbol{\xi}; \mathbf{e}_y\right) d\xi \,, \tag{4.9}
$$

where

$$
\gamma_4 = \frac{\omega \cos(\kappa)(1 - e^2)}{4e - 2(1 - e^2) L_e}, \quad \text{and } \alpha_4 = \frac{4e^2}{1 - e^2} \quad \beta_4 = \frac{2 \omega \cos(\kappa) e^2 (1 - e^2)}{2e(3 - 5e^2) - 3(1 - e^2)^2 L_e} \,.
$$

The velocity field for the **shear flow** $\omega \sin(\kappa) x_b \mathbf{e}_z$ past the spheroid $\frac{x_b^2}{a^2} + \frac{y_b^2 + z_b^2}{b^2} = 1$ can be adopted from the results in Chwang & Wu [19]

$$
\mathbf{u}_4(\mathbf{x}_b) = \omega \sin(\kappa) x_b \mathbf{e}_z - \int_{-c}^{c} \left(c^2 - \xi^2\right) \left[\alpha_5 \mathbf{u}_{\mathrm{SS}}\left(\mathbf{x} - \boldsymbol{\xi}; \mathbf{e}_x, \mathbf{e}_z\right) - \gamma_5 \mathbf{u}_{\mathrm{R}}\left(\mathbf{x} - \boldsymbol{\xi}; \mathbf{e}_y\right)\right] d\xi
$$
$$
- \beta_5 \int_{-c}^{c} \left(c^2 - \xi^2\right)^2 \frac{\partial}{\partial x} \mathbf{u}_{\mathrm{D}}\left(\mathbf{x} - \boldsymbol{\xi}; \mathbf{e}_z\right) d\xi \,, \tag{4.10}
$$

90

where

$$\gamma_5 = \frac{\omega \sin(\kappa)}{-2e + (1 + e^2)L_e} , \quad \text{and } \alpha_5 = \frac{4e^2}{1 - e^2} \, \beta_5 = \frac{-2e + (1 - e^2)L_e}{2e(2e^2 - 3) + 3(1 - e^2)L_e} e^2 \gamma_5 .$$

The velocity field for the **shear flow** $-\omega \cos(\kappa) y_b \mathbf{e}_z$ past a spheroid $\frac{x_b^2}{a^2} + \frac{y_b^2 + z_b^2}{b^2} = 1$ can be obtained from the results in Chwang & Wu [19]

$$\begin{aligned}
\mathbf{u}_5(\mathbf{x}) &= -\omega \cos(\kappa) y_b \mathbf{e}_z + \int_{-c}^{c} \left(c^2 - \xi^2\right) \left[\alpha_6 \mathbf{u}_{\mathrm{SS}} \left(\mathbf{x} - \boldsymbol{\xi}; \mathbf{e}_y, \mathbf{e}_z\right) + \gamma_6 \mathbf{u}_{\mathrm{R}} \left(\mathbf{x} - \boldsymbol{\xi}; \mathbf{e}_x\right)\right] d\xi \\
&+ \beta_6 \int_{-c}^{c} \left(c^2 - \xi^2\right)^2 \frac{\partial}{\partial y} \mathbf{u}_{\mathrm{D}} \left(\mathbf{x} - \boldsymbol{\xi}; \mathbf{e}_z\right) d\xi ,
\end{aligned} \tag{4.11}$$

where

$$\gamma_6 = \frac{-\omega \cos(\kappa)}{-2e + (1 + e^2)L_e} , \quad \text{and } \alpha_6 = \frac{4e^2}{1 - e^2} \, \beta_6 = \frac{-2e + (1 - e^2)L_e}{2e(2e^2 - 3) + 3(1 - e^2)L_e} e^2 \gamma_6 .$$

Totally, the velocity field in the body frame is

$$\mathbf{u}(\mathbf{x}_b) = \mathbf{u}_1(\mathbf{x}_b) + \mathbf{u}_2(\mathbf{x}_b) + \mathbf{u}_3(\mathbf{x}_b) + \mathbf{u}_4(\mathbf{x}_b) + \mathbf{u}_5(\mathbf{x}_b).$$

The singularities involved in the above velocity fields are provided in Appendix A and explicitly integrable. The tedious formulae are curtailed.

4.2.2 Fluid particle trajectories

When an upright prolate spheroid embedded in the rotation flow, as stated at the beginning of this section, the flow structure is similar to a sphere embedded in the rotation flow. Both the $y = 0$ and $z = 0$ planes are the symmetry planes of the flow. In the $z = 0$ plane, the vertical velocity component vanishes. So, the fluid particle will stay in the plane. The separation of the flow depends on the distance of the center of

the sphere to the rotation axis of the background flow.

Figure 4.10 shows the fluid particle trajectories near the spheroid. When $L = 0$, the flow is rotating around the spheroid as Figure 4.10a. As L increases, the fluid particle trajectories deform but are still closed orbits around the spheroid as Figure 4.10b for $L = 0.5$. When L increases more, there are fluid particles trajectories that separate and wrap around the spheroid slowly as shown in Figure 4.10c for $L = 2$. In these plots, the shear rate $\omega = 1$, the semimajor axis $a = 1$, and the semiminor axis $b = 1/2$. On the surface of the spheroid, the no-slip boundary condition is always preserved. Nevertheless, the fluid particle trajectories are closed periodic orbits.

When the spheroid's center is coincident with the center of the rotation ($L = 0$) and tilted with a tilt angle κ, the flow can be viewed as the flow generated by the spheroid sweeping out a double cone in free space in a body frame. Figure 4.11 shows particle trajectories for such a tilted spheroid in the rotating flow. These fluid particles are initialized at same height $z = 0.275$ or $z = -0.275$. When they move close to the spheroid, the particles are separated by the spheroid and wrap the spheroid. Similar trajectories have been reported in Leiterman [48].

When the tilted spheroid is embedded in a purely rotating background flow with a tilt angle $\kappa \neq 0$ and the spheroid's center is away from the rotation axis of the background flow ($L \neq 0$), there is net flow transport as shown in Figure 4.12. Neither $y = 0$ nor $z = 0$ is the symmetry plane of the flow. In Figure 4.12, the fluid particle moves from the upper half space to the lower half space when the spheroid is tilted with $\kappa = \frac{\pi}{6}$. The distance from the center of the rotation background to the spheroid's center is $L = 2$. For a specified rotation of the background flow, the tilt angle determines the direction of the transport. This phenomenon is essentially different from those observed in the spherical cases or the upright spheroid cases.

Further analysis about the stagnation points on the spheroid in the rotation flow
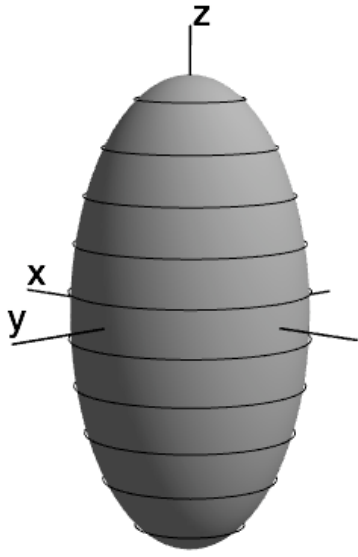
(a) $L = 0$
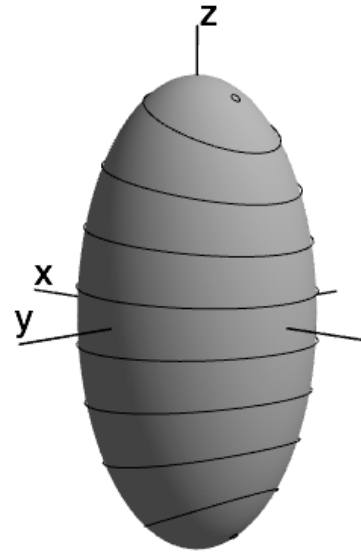
(b) $L = 0.5$
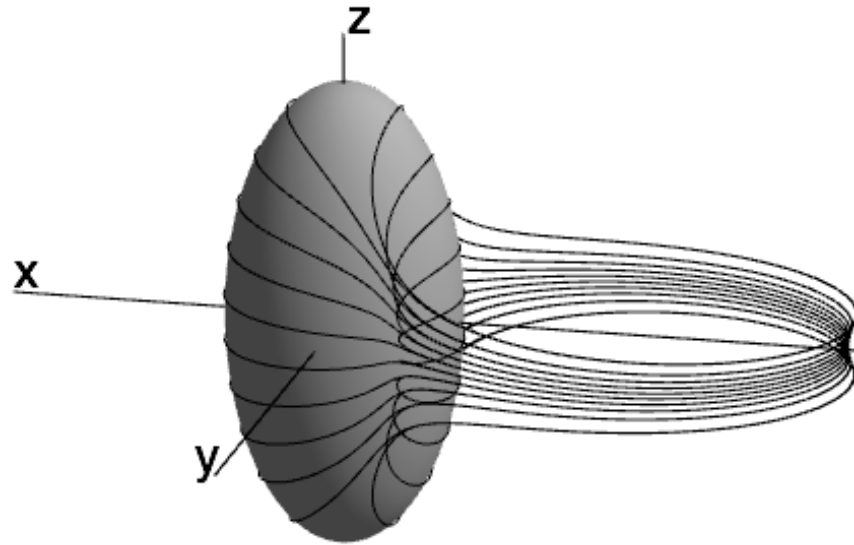
(c) $L = 2$

Figure 4.10: A rotating flow past an upright spheroid $4(x^2 + y^2) + z^2 = 1$ with $\omega = 1$ and different values of L.
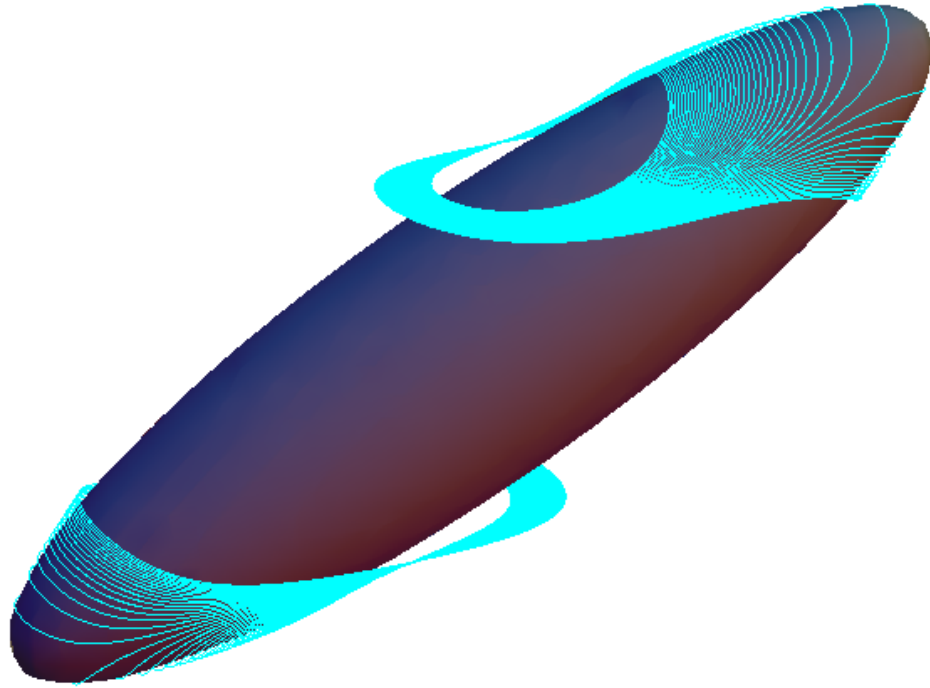
Figure 4.11: Fluid particle trajectories (cyan) in the rotation flow past a tilted spheroid $16x^2 + 16\left(y\cos(\kappa) - z\sin(\kappa)\right)^2 + \left(y\sin(\kappa) + z\cos(\kappa)\right)^2 = 1$ with the tilted angle $\kappa = \frac{\pi}{3}$. The rotation rate of the background flow is $\omega = 1$. The spheroid center is coincidentally on the rotation axis of the background flow, i.e., $L = 0$.

(a) View 1   (b) View 2
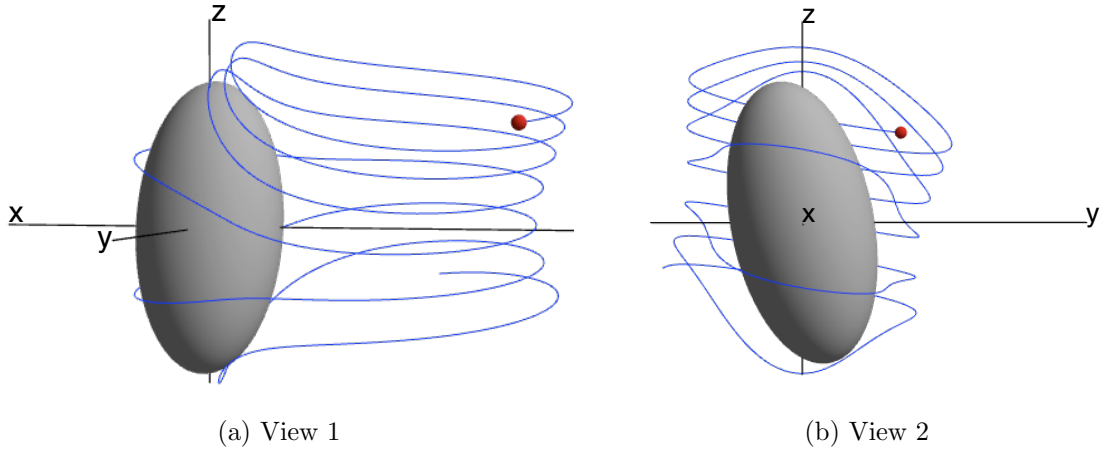
Figure 4.12: Two views of a fluid particle trajectory in the rotation flow past a tilted spheroid $4x^2 + 4\left(y\cos(\kappa) - z\sin(\kappa)\right)^2 + \left(y\sin(\kappa) + z\cos(\kappa)\right)^2 = 1$. Here $\omega = 1$, $L = 2$ and $\kappa = -\frac{\pi}{16}$. The red dots indicate the initial position.

and the "imprint" on the surface will be interested. This information will be pursued in the future study.

Part II

Experimental, theoretical and numerical study of flows induced by a slender body

Chapter 5

Experiments for a rod sweeping out a cone above a no-slip plane

Study of flows induced by nodal cilia in the Stokes regime plays an important role in fluid dynamics. Learning the flow structure will improve understanding of the fluid flow in a ciliated system [9, 25]. For example, numerous left-right asymmetries in the internal organs of the vertebrates are established during embryogenesis. Advanced results about flow generated by nodal cilia on the embryo can help to verify the evidences of the left-right symmetry breaking [58, 16, 32]. A review about the study of left-right symmetry is referred to Hamada [29]. A few studies have been reported from the fluid mechanics view [69]. But, as we know, there is no experimental work compared with the model in the Lagrangian view. Because of its practical significance, experimental and theoretical investigations are carried out on this Stokes problem. For the experimental study, it can validate the mathematical theory and allow for direct comparison of experimental data with theoretical observations.

In this chapter, the table-top experimental work with Rotation and Mixing eXperiment (RMX) is reported. This chapter focuses on the experimental setup and the procedures. Experimental data are reported in Chapter 6 and Chapter 7, when we compare the experimental trajectories with the theoretical predictions.

5.1 Experimental setup

Table-top experiments are conducted in a $30cm$ cubical, clear plexiglass tank filled with approximately $10cm$ height highly viscous fluid. Figure 5.1 shows the tank, lighting and camera setup on a kinematic mount. The two 1024×768 black and white PointGray Dragonfly cameras are put in front of the tank and at the left side of the tank, referring as side camera and front camera. With fiber optical illuminator light source through the diffusers (white glass on the two sides), rods and the tracer in the fluid cast shadows to each camera, in silhouette.

Above the horizontal planar bottom of the tank, a magnetically permeable rod precesses in a cone (as Figure 5.2). The rod is driven by a 3000 G permanent magnet mounted on a motorized turntable underneath the tank. Both straight and bent rods are manufactured with body length $\ell = 1cm$ and cross-sectional radius $r \sim 0.038\pm0.002cm$. The curvature of the bent rod is about $0.40 \pm 0.01cm^{-1}$. Figure 5.3a and 5.3b show a batch of bent pins used in our experiments and an individual one. At least one end of the rod is sharped to provide a well-defined pivot point to precess. Ideally, the pivot point is the rotation axis of a motor driven turnable.

The configuration of the cone is shown in Figure 5.2. For a straight rod, the rod will be the red chord. For a bent rod, the sharp tip at the apex of the cone is bent off the plane of the rod and causes a scooping angle which is defined as the angle between the plane of the rod and the vertical plane through the cone axis and the rod's chord as angle β shown in Figure 5.2. The cone angle κ is defined as the angle between the chord of the rod and the cone axis. It is determined by the offset of the magnet underneath the tank from the rotation center of the turning table.

We use two different fluids, Karo corn syrup and silicone oil. The Karo light corn syrup's density is approximately 1.36 g/cc and its dynamic viscosity is about 32 Poise. A thin layer of baby oil is put on the top of the corn syrup to prevent evaporation. The
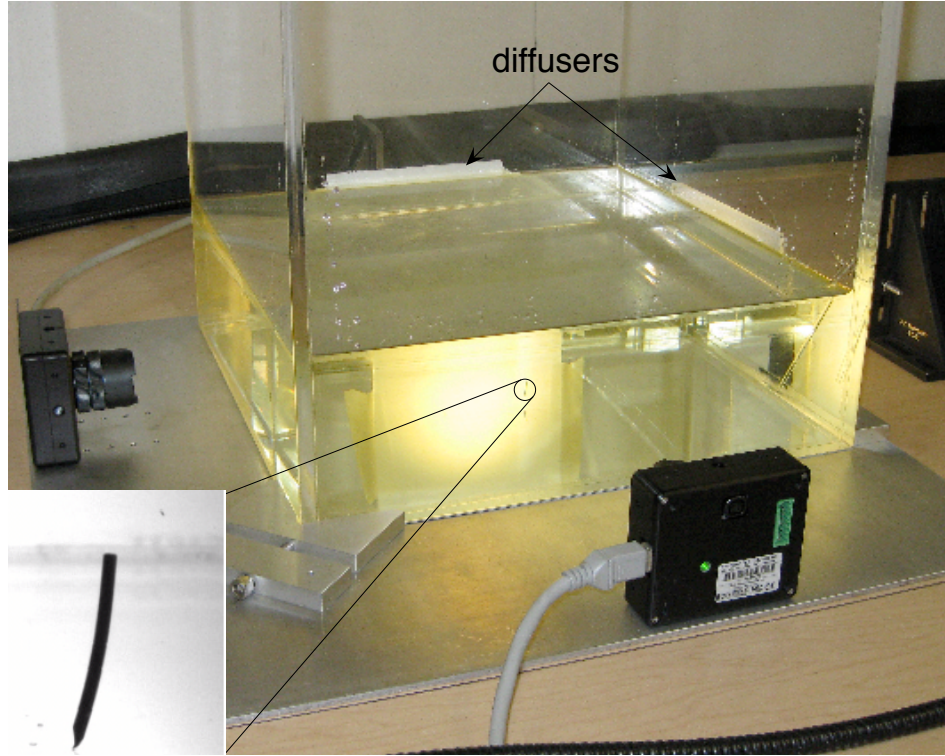
Figure 5.1: Setup of the tank, cameras, diffusers, and lighting.
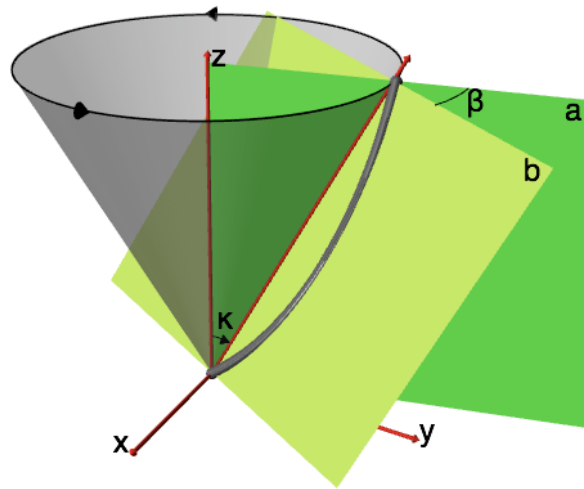
Figure 5.2: Configuration of a bent rod sweeping out an upright cone above a no-slip plane. Cone angle κ is the angle between the rod's chord and the positive z-axis (the cone axis). Scooping angle β is the angle between plane "a" and plane "b" in which the rod lies.

(a) A batch of uniformly bent pin with one sharped tip.

(b) One individual pin

Figure 5.3: Bent pins used in our experiments.

silicone oil is with density 0.92 g/cc and kinematic viscosity 12500 Cst (about 95 Poise for dynamic viscosity). The magnet turntable is engaged and adjusted so that the pin precesses conically at a $\omega = 0.2$ Hz rate.

The fluid viscosities and precession frequencies are selected so that a Reynolds number Re and $SrRe$ of 10^{-3} are not exceeded, where the Reynolds number is $Re=\frac{\rho\,\omega\,\ell^2\,\sin(\kappa)}{\mu}$, the Strouhal number is $Sr=\frac{\omega\,\ell}{U}=\frac{\omega\,\ell}{\omega\,\ell\sin(\kappa)}=\frac{1}{\sin(\kappa)}$ and $U=\omega\,\ell\sin(\kappa)$. So, $SrRe=\frac{\omega\ell^2}{\nu}$. When $Re\ll 1$ and $Sr\,Re\ll 1$, the fluid flow is in the Stokes' regime.

The details of the parameters of the flow are listed in Table 5.1 and Table 5.2. If the cone angle is about 30 degrees and the characteristic length is the radius of the rod, then Re and $Sr\,Re\approx 10^{-3}$ for the corn syrup. If the cone angle is about 30 degree and the characteristic length is the radius of the rod, then $Re\approx 10^{-4}$ and $Sr\,Re\approx 10^{-3}$ for the silicone oil.

From Cartwright et al. [16], the Reynolds number of the cilia flow $Re=\frac{v\,L}{\nu}$ is of order 10^{-3}. Here the characteristic length L is the size of the nodal cilia, v is the flow

Table 5.1: Physical properties of Karo light corn syrup.

length of the pin	$\ell = 1cm$
radius of the pin	$r = 0.036796cm$
spin rate of	$\omega = 12RPM = 0.2s^{-1}$
viscosity of Karo light corn syrup	$\mu = \rho\nu = 3200cP(= 32g\ cm^{-1}s^{-1})$
density of Karo light corn syrup	$\rho = 1.360g\ cm^{-3}$
density of air at 20° and 1 atm (sea level)	$\rho = 1.2kg\ m^{-3}(= 1.2 \cdot 10^{-3}g\ cm^{-3})$
The density of air at room temperature	$\rho = 10^{-3}g\ cm^{-3}$

Table 5.2: Physical properties of Silicone Oil 12500 cst.

length of the pin	$\ell = 1cm$
radius of the pin	$r = 0.036796cm$
spin rate of	$\omega = 12RPM = 0.2s^{-1}$
dynamic (absolute) viscosity of Silicone Oil	$\mu = \rho\nu = 9500cP(= 95g\ cm^{-1}s^{-1})$
density of Silicone Oil	$\rho = 0.975g\ cm^{-3}$
density of air at 20° and 1 atm (sea level)	$\rho = 1.2kg\ m^{-3}(= 1.2 \cdot 10^{-3}g\ cm^{-3})$
The density of air at room temperature	$\rho = 10^{-3}g\ cm^{-3}$

Camera Calibration Toolbox – Standard Version			
Image names	Read images	Extract grid corners	Calibration
Show Extrinsic	Reproject on images	Analyse error	Recomp. corners
Add/Suppress ima...	Save	Load	Exit
Comp. Extrinsic	Undistort image	Export calib data	Show calib results
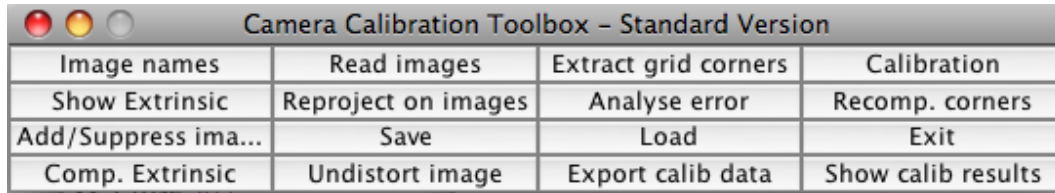
Figure 5.4: The main calibration toolbox window.

velocity, ν is the kinematic viscosity of the extraembryonic fluid.

5.2   3D camera calibration

One important step for the 3D experiments is the camera calibration. The 3D calibration is done with Camera Calibration Toolbox for Matlab from caltech.edu [8]. The main calibration toolbox window is shown in Figure 5.4. Figure 5.5a and 5.5b shows one pair of images of the checkerboard used for our calibration. To pursue the stereo calibration, we choose about 20 corresponding images for both cameras for each run of the calibration. The fundamental calibration for each camera is obtained first. Then, we run the 3D stereo calibration. Figure 5.5c shows one group of calibration images for the front camera.

Figure 5.6a shows the corners picked for an image. Once the origin "O" of the grid on the checkerboard and other three end points (blue circles) are selected, the same order should be kept for the rest of the images. Similarly, the corresponding corners from images of the other camera need to be in exactly the same order. Usually we pick the origin of the checkerboard at the upper-left corner and pick the other extreme corner clockwise. So, on the grid, "Y" is in the horizontal direction and "X" is in the vertical direction. If the orders of the corners are selected differently, the calibration result is still valid, but with a different coordinate mapping on the grid. Picking up the corners consistently is the first necessary step for the calibration.
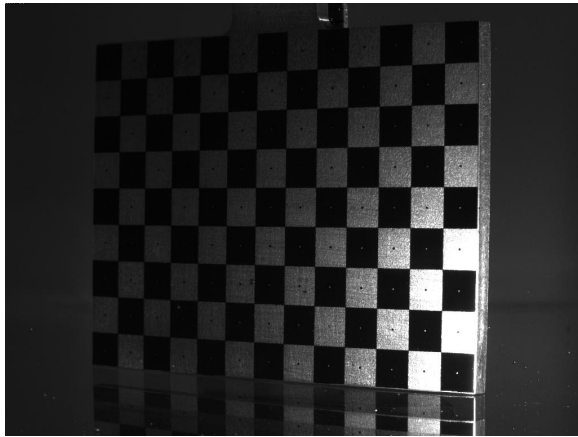
(a) From front camera
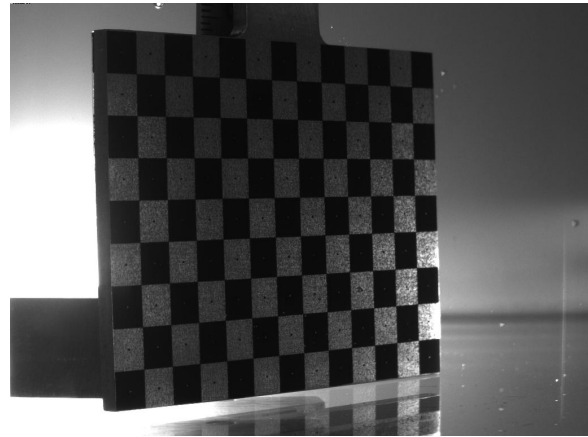
(b) From side camera

Calibration images
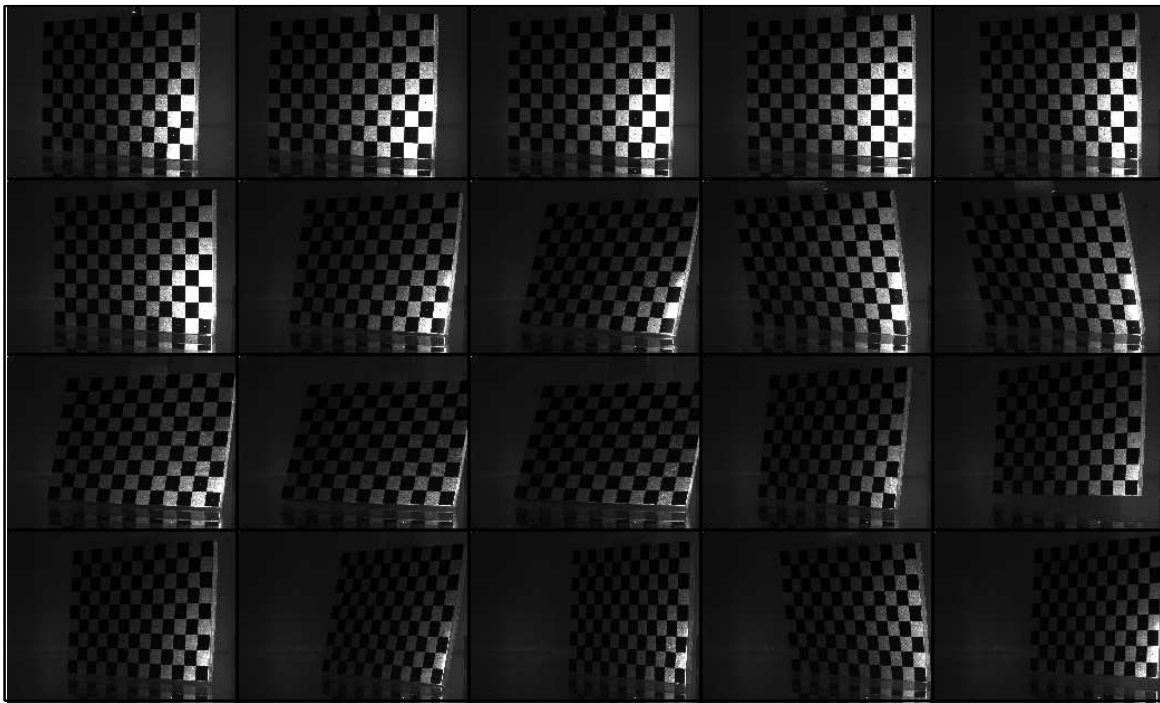
(c) One group images from front camera

Figure 5.5: Images for the calibration.

(a) Extract corners   (b) Reprojected corners
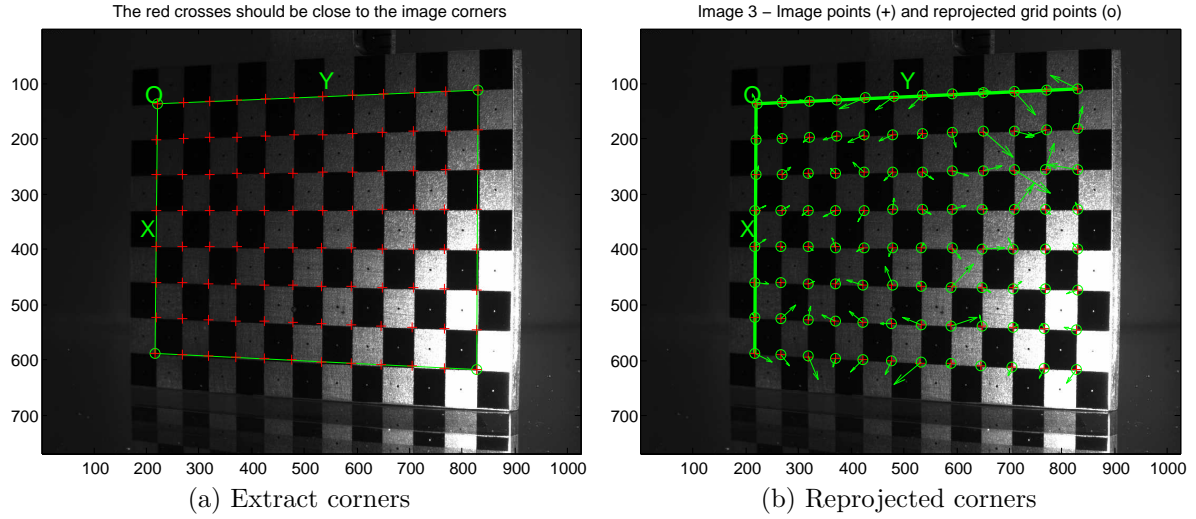
Figure 5.6: Extracted corners on one image and reprojected corners after calibration.

After extracting the corners, click "calibration" to run the calibration with all corners from the images. Figure 5.6b shows the reprojected corners as green circles after calibration, as compared to the extracted corners. The arrows show the magnitude and the direction of the difference. Figure 5.7 shows the reconstructed 3D grid on the checkerboard from the 20 images selected here, with camera-centered view and world-centered view.

Figure 5.8 shows the grids and the position of the camera. Since the camera is placed outside the tank, the distance between the camera and the checkerboard is much larger than the size of the checkerboard. The calibrated data are in the camera-view coordinates. Notice the orientation of the coordinates (X_c, Y_c, Z_c) and the origin "O" are different from the coordinates defined in our model. The coordinate system for our model is the cone-centered view as in Figure 5.2. Rotation and translation must be applied to the experimental data to make the coordinates consistent with each other.

During the calibration, press the button "Analysis error" to check the reprojection error. For example, Figure 5.9 shows the reprojection errors are within 5 pixels for the calibration images showed in Figure 5.5. Reprojection errors within 10 pixels are with
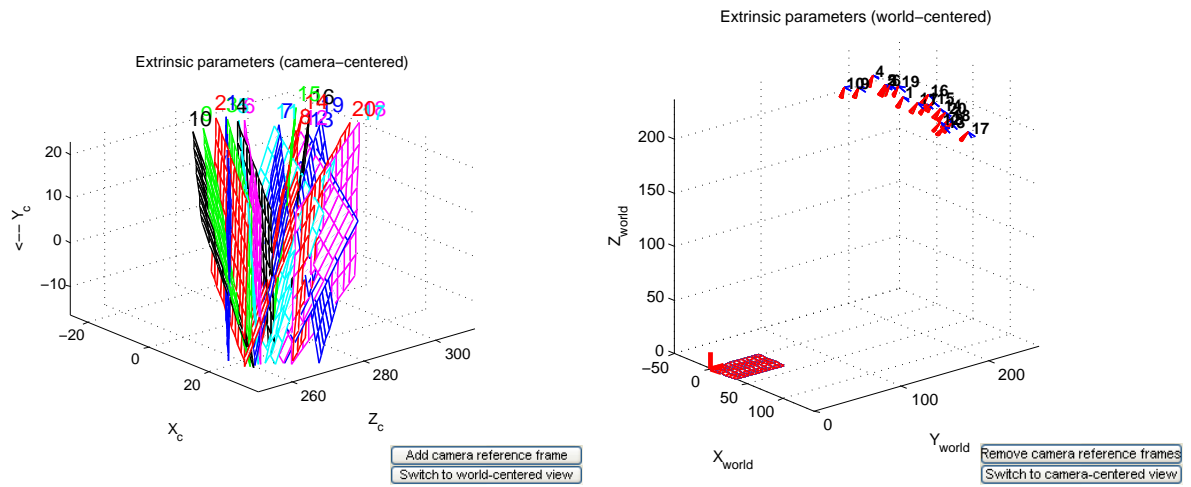
Figure 5.7: Extrinsic parameters.
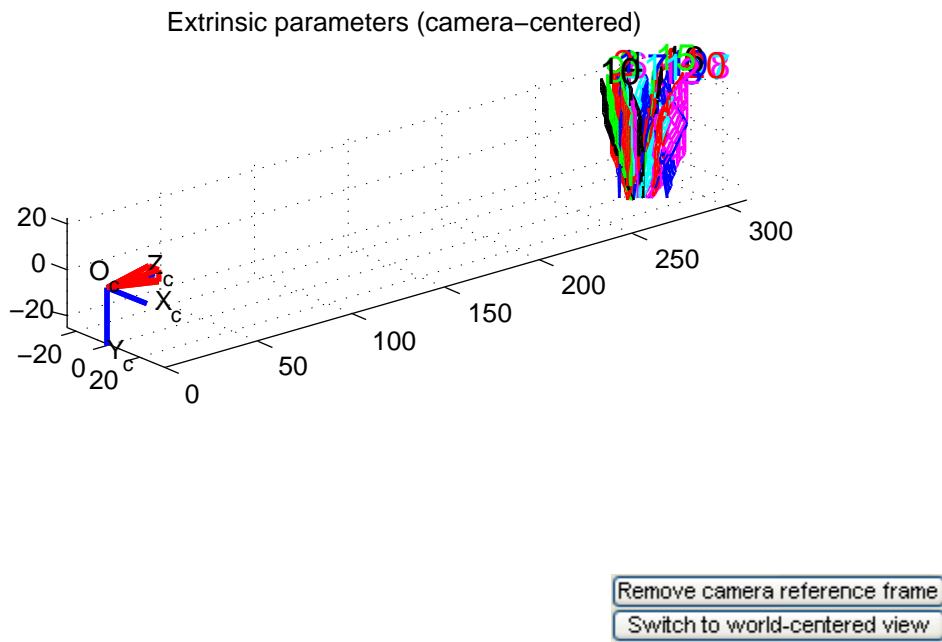
Figure 5.8: Extrinsic parameters with the camera on.

(a) For images from the front camera   (b) For images from the side camera
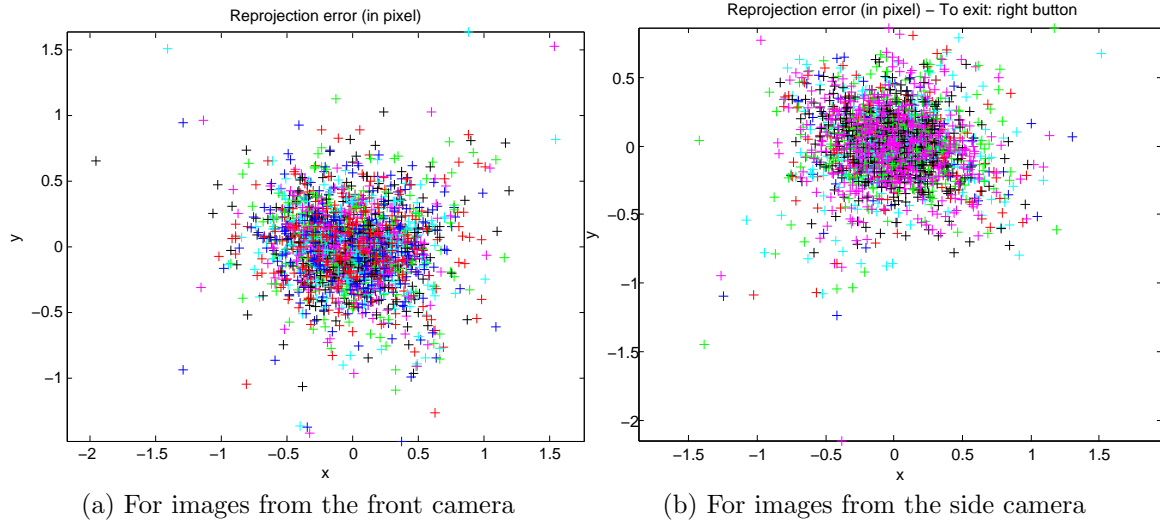
Figure 5.9: Reprojection error.

a reasonable range for our images. Running a few iterations of "Recomp·corners" and "Add/Suppress images" is helpful to reduce the reprojection error.

For details of calibration toolbox, refer to the website of the calibration tool [8]. Here are a few tips to produce a good calibration for our experiments. We should always be aware of the blockage of the corners of the grid by any object, for example, air bubbles in the fluid, tracers or the rod. If this happens, the stereo calibration data may not be produced. Missing a corner sometimes can cause such severe problems that the calibration for that camera itself could fail. Also the images selected for the calibration should not be too close to each other, otherwise, the ill-condition in the data can fail the calibration. Thirdly, when the calibration fails, go to "Analysis error" in the camera calibration tool and click the "+" with a large pixel error to check which image and which corner on that image produces that error. For example, if the error information is following:

Selected image: 1

Selected point index: 8

Pattern coordinates (in units of (dX,dY)): (X,Y)=(7,11)
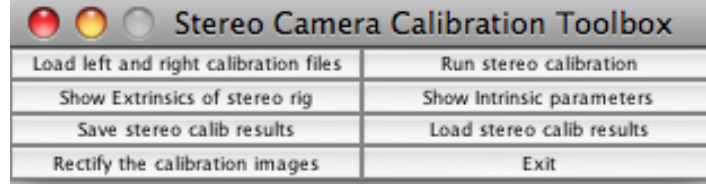
Figure 5.10: The stereo calibration window.

Image coordinates (in pixel): (776.94,627.15)

Pixel error = (2.64628,7.82514)

Window size: (wintx,winty) = (8,8)

It means the clicked pixel error (2.64628,7.82514) is caused by the corner with index 8 on image 1. In the calibration grid, that corner is at $(x, y) = (7, 11)$ in the unit of grid, and (776.94,627.15) in pixel. The window size used to picked up corners is (8,8) pixels. Also, set the camera perpendicular to the wall of the tank to avoid extreme distortions. In this case, a single distortion coefficient automatically selected by the toolbox will be sufficient. Otherwise, call manual_corner_extraction.m after the standard corner extraction and choose the appropriate distortion model with help of isualize_distortions.

When the calibration data for both camera are saved, run "stereo_gui" for 3D stereo calibration. The stereo calibration toolbox window is shown in Figure 5.10. Load the calibration for the two cameras in order and then press "Run stereo calibration" to get the 3D stereo calibration. Figure 5.11 shows the extrinsic parameters for the stereo calibration with the left camera corresponding to the side camera and the right camera corresponding to the front camera for our experiment. Since the scale of the checkerboard is much small compare to dimensions of the tank, the grids are compressed at the center on the figure. However, this figure demonstrates the relative positions of our cameras very well. Finally, save the data for 3D calibration. Based on the stereo calibration data, 3D trajectory is constructed with function stereo_triangulation.
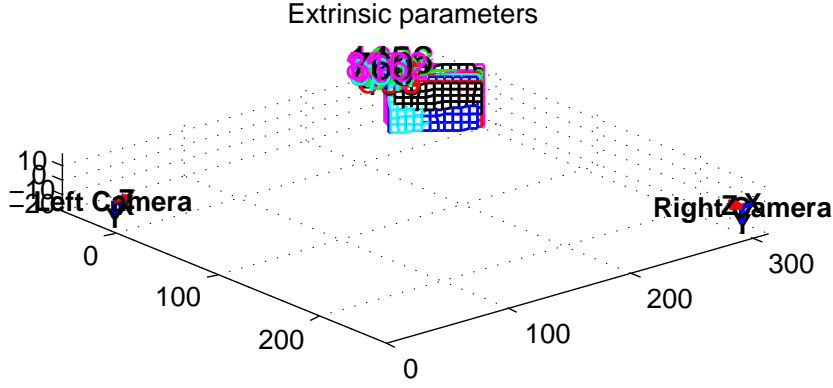
Figure 5.11: Extrinsic parameters for the 3D stereo calibration.

5.3 Image processes and 3D data construction

To visualize the motion of the fluid, visible markers of the order of 100 microns are placed at the desired locations in the fluid with a syringe to enable optical tracking of their Lagrangian trajectories. Two synchronized PointGray Dragonfly digital cameras are set up at the sides of the tank to capture videos with the program Ladybugrecord [20] as shown in Figure 5.1.

Main image analyses involved in the experiments are raw video processes and the 3D calibration, which has been documented in detail in the 3D calibration section. The raw image processes and the 3D data reconstruction are reported in this section.

The captured videos are originally saved as raw data files which can previewed by "rawplayer" and read by "raw2ppm" associated with Ladybugrecord. Each raw file includes 450 frames. At the current 15fps (frame per second) speed for our cameras, each file contains data for a 30-second movie. Every 100 raw files will be written to one folder. The first 100 raw files in folder "dir0", and the second 100 files in folder "dir1", etc. But the frame number is sequentially saved. Run "raw2txt" script to extract the information of these raw files and check if there are fames dropped during the filming.

The raw files are then compressed into an AVI container from Matlab and processed

Figure 5.12: Snapshot of tracking.

with program Video Spot Tracker [73]. Video Spot Tracker program can read AVI video stream or one raw file with current version v06.02. Figure 5.12 is a snapshot of tracking with Video Spot Tracker program. The yellow trajectory is the trace of the marker. The red dot numbered with "0" is the tracker which is overlapped with the maker.

After tracking the marker from both cameras, based on the calibration data, we construct the 3D trajectory with the function "stereo_triangulation" in the calibration toolbox. The parameters of the rod are tracked with the tracking program in Matlab from David Holz [35] with the calibration information.

The units of the output data from the calibration are consistent with the units imputed during the calibration. For the 7×11 checkerboard used in our experiment, the grid size is 5mm$\times$ 5mm. If we enter 5mm for the size of each square, the reconstructed 3D trajectories of our tracer are in the units of mm. The origin of the reconstructed data is in the camera-centered coordinates. Proper rotation and translation are applied

to the experimental trajectories to compare with the theoretical trajectories.

Chapter 6

A straight rod sweeping a tilted cone above a no-slip plane

A prolate spheroid or a straight slender rod sweeping out a cone or double cone in Stokes flow draw scientists' attention due to its biological applications to flows generated by spinning cilia [58, 69, 16]. Such fluid motions are fundamental to many living organisms. One important example is the left-right symmetry breaking in the early development of mammals, where primary nodal cilia exhibit canonical rotatory movement [16, 12]. Effectively, it is appropriate to approximate nodal cilia as rigid slender rods. We build a model to study the flow generated by a slender rod and compare the theoretical prediction to the experimental data. Such direct comparisons have not been found in the literature yet.

In free space, the exact velocity field for a spheroid sweeping out a double cone has been reported in Camassa et al. [14]. (In the appendix, we provide the error analysis of the velocity field if the spheroid is approximated with a slender body.) When the slender body precesses an upright cone above a no-slip plane, the velocity field and the properties of the fluid particle trajectories have been studied with the slender body theory and the image method [48, 9]. The velocity field is constructed in the body frame, where the rod is fixed and there is rotating background flow. In this frame, a

fundamental singularity Stokeslet is distributed along the center-line of the slender rod. Since the slender rod is sweeping out an upright cone, the distance between a point on the rod and the no-slip plane is fixed. So, the center-line of the rod and its image with respect to the no-slip plane have no time dependence in the body frame. Ultimately, the velocity field in the body frame is independent of time and can be constructed with Blakelet [5]. By applying the transformation between the body frame and the laboratory frame, the velocity in the laboratory frame is obtained from the velocity field in the body frame.

When the cone is tilted, the distance from a point on the rod to the no-slip plane varies while the rod sweeps. In such situations, the flow is fully time dependent in both the body frame and the laboratory frame. To construct the velocity field, we have to carry time information either in the body frame (to identify the position of the no-slip plane over time) or in the lab frame. The simplification in the body frame is no longer available, compared to the upright cone case. The tilt of the cone makes the construction of the flow velocity field complicated. The tilted cone is especially interesting, since most cilia sweep out tilted cones or extensive tilted cones in reality and the cilia themselves are bent. Results for bent cilia sweeping out a cone will be reported in the next chapter, which is much more complicated.

This chapter will continue with a brief review of results about the straight rod sweeping out an upright cone, and then focus on the straight rod sweeping a tilted cone above a no-slip plane. For a rod sweeping a tilted cone, we construct the velocity directly in the laboratory frame and show the properties of the flow with fluid particle trajectories. Distinct phenomena for a rod sweeping a tilted cone are deformations of the Lagrangian fluid particle trajectories and directional fluid transport induced by the rod. Since our model is flexible about the configuration of the cone, we run the model with tracked cone angle from the experiment and compare the numerical

trajectories with the experimental trajectories. Our model shows good agreement with the experimental data.

6.1 A straight rod sweeping out an upright cone

For a straight rod sweeping out an upright cone above a no-slip plane, Leiterman [48] has studied the flow in the Lagrangian view point with the slender body theory. To construct the velocity field for the flow, three different types of fundamental singularities are used, i.e. Stokeslet, Stokes doublet, and potential doublet (also known as dipole). The special combination of these three different singularities is Blakelet. It is a Stokeslet with its image system introduced by Blake [5] to satisfy the no-slip boundary condition in the flow. Leiterman [48] has reviewed these singularities and written the formula conveniently applied here. The velocity field satisfying

$$\mu \nabla^2 \mathbf{u}_B + 8\pi\mu\boldsymbol{\alpha}\delta(\mathbf{x} - \mathbf{s}) = \nabla p,$$

$$\nabla \cdot \mathbf{u}_B = 0,$$

$$\mathbf{u}_B|_{z=0} = 0,$$

in the upper half space $\{\mathbf{x} = (x, y, z) \in \mathbf{R}^3 | z \geq 0\}$ is given as the Blakelet $\mathbf{u}_B(\mathbf{x} - \mathbf{s}; \boldsymbol{\alpha})$, which is a collection of singularities

$$\mathbf{u}_B(\mathbf{x} - \mathbf{s}; \boldsymbol{\alpha}) = \mathbf{u}_S(\mathbf{x} - \mathbf{s}; \boldsymbol{\alpha}) + \mathbf{u}_S(\mathbf{x} - \mathbf{s}'; -\boldsymbol{\alpha}) \qquad (6.1)$$

$$+ \mathbf{u}_{SD}(\mathbf{x} - \mathbf{s}'; \mathbf{e}_z, 2h\boldsymbol{\alpha}') + \mathbf{u}_D(\mathbf{x} - \mathbf{s}'; -2h^2\boldsymbol{\alpha}')$$

where $\mathbf{s} = (s_1, s_2, s_3)$ is the location of the Stokeslet, $\mathbf{s}' = (s_1, s_2, -s_3)$ is the location of the image system, $\boldsymbol{\alpha} = (\alpha_1, \alpha_2, \alpha_3)$ is the strength of the Stokeslet, $\boldsymbol{\alpha}' = (\alpha_1, \alpha_2, -\alpha_3)$, and $h = s_3$ is the distance from the point-force (Stokeslets) in the flow field to the

113

no-slip plane.

When a slender rod with radius r and length ℓ sweeps out an upright cone with the cone angle κ defined as the angle between the cone axis and the rod, the angular velocity of the rod is $(0, 0, \omega)$. If $\omega > 0$, then the rod sweeps out a cone counter-clockwise. If $\omega < 0$, then the rod sweeps out a cone clockwise. The introduced velocity by a slender body sweeping out an upright cone in the body frame is

$$
\begin{aligned}
\mathbf{u}(\mathbf{x}) = \mathbf{U}(\mathbf{x}) + &\int_0^\ell \left(\mathbf{u}_{\mathrm{S}}(\mathbf{x} - \mathbf{x}_s; \boldsymbol{\alpha}(s)) + \mathbf{u}_{\mathrm{S}}(\mathbf{x} - \mathbf{x}_s'; -\boldsymbol{\alpha}(s)) \right. \\
&\left. + \mathbf{u}_{\mathrm{SD}}(\mathbf{x} - \mathbf{x}_s'; \mathbf{e}_z, 2z_s\boldsymbol{\alpha}'(s)) + \mathbf{u}_{\mathrm{D}}(\mathbf{x} - \mathbf{x}_s'; -2z_s^2\boldsymbol{\alpha}'(s)) \right) ds \\
= \mathbf{U}(\mathbf{x}) + &\int_0^\ell \left[\frac{\boldsymbol{\alpha}(s)}{|\mathbf{x} - \mathbf{x}_s|} + \frac{(\mathbf{x} - \mathbf{x}_s)\left((\mathbf{x} - \mathbf{x}_s) \cdot \boldsymbol{\alpha}(s)\right)}{|\mathbf{x} - \mathbf{x}_s|^3} \right. \\
&- \left(\frac{\boldsymbol{\alpha}(s)}{|\mathbf{x} - \mathbf{x}_s'|} + \frac{(\mathbf{x} - \mathbf{x}_{\mathrm{S}'}(s))\left((\mathbf{x} - \mathbf{x}_s') \cdot \boldsymbol{\alpha}(s)\right)}{|\mathbf{x} - \mathbf{x}_s'|^3} \right) + \\
&\left. + 2z_s \left(\frac{-z\boldsymbol{\alpha}(s)'}{|\mathbf{x} - \mathbf{x}_s'|^3} + \frac{(\mathbf{x} - \mathbf{x}_s') \times \mathbf{e}_z \times \boldsymbol{\alpha}(s)'}{|\mathbf{x} - \mathbf{x}_s'|^3} + \frac{3z(\mathbf{x} - \mathbf{x}_s')\left((\mathbf{x} - \mathbf{x}_s) \cdot \boldsymbol{\alpha}(s)'\right)}{|\mathbf{x} - \mathbf{x}_s'|^5} \right) \right] ds.
\end{aligned}
\tag{6.2}
$$

Here, $\mathbf{U}(\mathbf{x}) = (\omega y, -\omega x, 0)$ is the background rotating flow in the body frame, $\mathbf{x}_s = (s\sin(\kappa), 0, s\cos(\kappa))$, $\mathbf{x}_s' = (s\sin(\kappa), 0, -s\cos(\kappa))$, and $\boldsymbol{\alpha}(s) = \boldsymbol{\alpha}(s)' = \frac{\omega\epsilon\sin(\kappa)}{2}(0, s, 0)$. The slenderness ϵ is defined as $\epsilon = \log^{-1}(\frac{\ell}{r})$.

6.2   A straight rod sweeping a tilted cone

Similarly, to study the flow induced by a straight rod sweeping out a tilted cone, we utilize the slender body theory and the image method to construct the velocity field. This inquires the information about types of the singularities, locations of singularities, and the strength of the singularities. Stokeslet is distributed along the center-line of the slender rod to achieve the leading order approximation, and the image system is added to satisfy the no-slip boundary condition.

Positions of the singularities

The singularities are distributed along the center-line of the rod. To find the positions of the singularities, it is essential to find the center-line of the slender rod. This requires that we analyse the motion of the rod and configuration of the cone. The slender rod sweeps out a tilted circular cone with a tilt angle λ, which is defined as the angle between the cone axis and the positive z-axis. Without loss of generality, we always choose the coordinate system that the tilt of the cone is in the x-z plane. If the axis is tilted to the positive x-axis, $\lambda > 0$. Otherwise, $\lambda < 0$. When $\lambda = 0$, the cone is upright. The cone angle κ is still the angle from the axis of the cone to the center-line of the slender rod. The rod rotates counter-clockwise with an angular velocity ω in the cone axis direction in the laboratory frame. To find the expression of the center-line, we consider the cone as tilting the rod with angle κ first, then rotate the rod with the angular velocity ω, and finally tilt the cone itself. Following this procedure, we get the center-line of the rod as

$$
\mathbf{x}_s = R_\lambda R_\omega R_\kappa (s,0,0)^T = s \begin{pmatrix} \sin(\kappa)\cos(\omega t)\cos(\lambda) + \cos(\kappa)\sin(\lambda) \\ \sin(\kappa)\sin(\omega t), \\ -\sin(\kappa)\cos(\omega t)\sin(\lambda) + \cos(\kappa)\cos(\lambda) \end{pmatrix}, \qquad (6.3)
$$

where $0 \le s \le \ell$,

$$
R_\kappa = \begin{pmatrix} \sin(\kappa) & 0 & -\cos(\kappa) \\ 0 & 1 & 0 \\ \cos(\kappa) & 0 & \sin(\kappa) \end{pmatrix}, \quad R_\omega = \begin{pmatrix} \cos(\omega t) & -\sin(\omega t) & 0 \\ \sin(\omega t) & \cos(\omega t) & 0 \\ 0 & 0 & 1 \end{pmatrix},
$$

115

and

$$R_\lambda = \begin{pmatrix} \cos(\lambda) & 0 & \sin(\lambda) \\ 0 & 1 & 0 \\ -\sin(\lambda) & 0 & \cos(\lambda) \end{pmatrix}.$$

We obtain the position of the center-line of the rod $\mathbf{x}_s$ as a function of the rod's arc-length s in (6.3), which provides the location of the Stokeslet. The location of the image system is determined accordingly.

Strength of singularities for a tilted cone

The strength of the singularities is obtained by imposing the no-slip boundary condition on the surface of the slender rod. As the canonical slender body theory, the strength of the singularity is in proportion to the velocity. The ratios are different from the tangential direction to the normal and binormal directions of the rod. With the prescribed velocity of the rod and the ratios from the slender body theory, the strength of the Stokeslet is determined as

$$
\begin{aligned}
\alpha_1 &= -\frac{\epsilon\,\omega}{2}\sin(\kappa)\sin(\omega t)\cos(\lambda), \\
\alpha_2 &= \frac{\epsilon\,\omega}{2}\sin(\kappa)\cos(\omega t), \\
\alpha_3 &= \frac{\epsilon\,\omega}{2}\sin(\kappa)\sin(\omega t)\sin(\lambda),
\end{aligned}
\tag{6.4}
$$

where $\epsilon = \log^{-1}(\frac{\ell}{r})$ is the slenderness defined in the previous section.

With the location and strength of the singularity and the relation of the image

system with the Stokeslet, the velocity field is finally found as

$$
\begin{aligned}
\mathbf{u}(\mathbf{x}) &= \int_0^\ell \mathbf{u}_B(\mathbf{x} - \mathbf{x}_s; \boldsymbol{\alpha}) ds \\
&= \int_0^\ell \left[\mathbf{u}_S(\mathbf{x} - \mathbf{x}_s; \boldsymbol{\alpha}) + \mathbf{u}_S(\mathbf{x} - \mathbf{x}_s'; -\boldsymbol{\alpha}) \right. \tag{6.5} \\
&\quad \left. + \mathbf{u}_{SD}(\mathbf{x} - \mathbf{x}_s; \mathbf{e}_z; 2h\boldsymbol{\alpha}') + \mathbf{u}_D\left(\mathbf{x} - \mathbf{x}_s; -2h^2\boldsymbol{\alpha}'\right) \right] ds \\
&= \int_0^\ell \left[\frac{\boldsymbol{\alpha}}{|\mathbf{x} - \mathbf{x}_s|} + \frac{(\mathbf{x} - \mathbf{x}_s)((\mathbf{x} - \mathbf{x}_s) \cdot \boldsymbol{\alpha})}{|\mathbf{x} - \mathbf{x}_s|^3} - \frac{\boldsymbol{\alpha}}{|\mathbf{x} - \mathbf{x}_s'|} - \frac{(\mathbf{x} - \mathbf{x}_s')((\mathbf{x} - \mathbf{x}_s') \cdot \boldsymbol{\alpha})}{|\mathbf{x} - \mathbf{x}_s'|^3} \right. \\
&\quad \left. + 2z_s \left(\frac{-z\boldsymbol{\alpha}'}{|\mathbf{x} - \mathbf{x}_s'|^3} + \frac{(\mathbf{x} - \mathbf{x}_s') \times \mathbf{e}_z \times \boldsymbol{\alpha}'}{|\mathbf{x} - \mathbf{x}_s'|^3} + \frac{3z(\mathbf{x} - \mathbf{x}_s')[\boldsymbol{\alpha}' \cdot (\mathbf{x} - \mathbf{x}_s')]}{|\mathbf{x} - \mathbf{x}_s'|^5} \right) \right] ds.
\end{aligned}
$$

Three components of the velocity field are:

$$
\begin{aligned}
u_1(x,y,z) = \int_0^\ell &\left\{ \frac{\alpha_1}{|\mathbf{x} - \mathbf{x}_s|} + \frac{(x - x_s)\left((x - x_s)\alpha_1 + \alpha_2(y - y_s) + (z - z_s)\alpha_3\right)}{|\mathbf{x} - \mathbf{x}_s|^3} \right. \tag{6.6} \\
&- \frac{\alpha_1}{|\mathbf{x} - \mathbf{x}_s|} - \frac{(x - x_s)\left((x - x_s)\alpha_1 + \alpha_2(y - y_s) + (z + z_s)\alpha_3\right)}{|\mathbf{x} - \mathbf{x}_s'|^3} + 2z_s \left[\frac{-z\alpha_1}{|\mathbf{x} - \mathbf{x}_s'|^3} \right. \\
&\left. \left. + \frac{(x - x_s)\alpha_3}{|\mathbf{x} - \mathbf{x}_s'|^3} + \frac{3z(x - x_s)\left(\alpha_1(x - x_s) + \alpha_2(y - y_s) - \alpha_3(z + z_s)\right)}{|\mathbf{x} - \mathbf{x}_s'|^5} \right] \right\} ds,
\end{aligned}
$$

$$
\begin{aligned}
u_2(x,y,z) = \int_0^\ell &\left\{ \frac{\alpha_2}{|\mathbf{x} - \mathbf{x}_s|} + \frac{(y - y_s)\left((x - x_s)\alpha_1 + \alpha_2(y - y_s) + (z - z_s)\alpha_3\right)}{|\mathbf{x} - \mathbf{x}_s|^3} \right. \tag{6.7} \\
&- \frac{\alpha_2}{|\mathbf{x} - \mathbf{x}_s'|} + \frac{(y - y_s)\left((x - x_s)\alpha_1 - \alpha_2(y - y_s) + (z + z_s)\alpha_3\right)}{|\mathbf{x} - \mathbf{x}_s'|^3} + 2z_s \left[\frac{-z\alpha_2}{|\mathbf{x} - \mathbf{x}_s'|^3} \right. \\
&\left. \left. + \frac{(y - y_s)\alpha_3}{|\mathbf{x} - \mathbf{x}_s'|^3} + \frac{3z(y - y_s)\left(\alpha_1(x - x_s) + \alpha_2(y - y_s) - \alpha_3(z + z_s)\right)}{|\mathbf{x} - \mathbf{x}_s'|^5} \right] \right\} ds,
\end{aligned}
$$

$$u_3(x,y,z) = \int_0^\ell \left\{ \frac{\alpha_3}{|\mathbf{x}-\mathbf{x}_s|} + \frac{(z-z_s)\left((x-x_s)\alpha_1 + \alpha_2(y-y_s) + (z-z_s)\alpha_3\right)}{|\mathbf{x}-\mathbf{x}_s|^3} \right.$$

$$-\frac{\alpha_3}{|\mathbf{x}-\mathbf{x}_s'|} - \frac{(z+z_s)\left((x-x_s)\alpha_1 + \alpha_2(y-y_s) + (z+z_s)\alpha_3\right)}{|\mathbf{x}-\mathbf{x}_s'|^3} \qquad (6.8)$$

$$+2z_s\left[\frac{z\alpha_3}{|\mathbf{x}-\mathbf{x}_s'|^3} + \frac{(y-y_s)\alpha_2 + (x-x_s)\alpha_1}{|\mathbf{x}-\mathbf{x}_s'|^3}\right.$$

$$\left.\left.+\frac{3z(z+z_s)\left(\alpha_1(x-x_s) + \alpha_2(y-y_s) - \alpha_3(z+z_s)\right)}{|\mathbf{x}-\mathbf{x}_s'|^5}\right]\right\} ds,$$

where

$$|\mathbf{x}-\mathbf{x}_s| = \left[(x-x_s)^2 + (y-y_s)^2 + (z-z_s)^2\right]^{1/2}$$

and

$$|\mathbf{x}-\mathbf{x}_s'| = \left[(x-x_s)^2 + (y-y_s)^2 + (z+z_s)^2\right]^{1/2}.$$

As $\mathbf{x}_s$ given by (6.3) and $\boldsymbol{\alpha}$ in (6.4) are dependent of time and the geometry of cone, the velocity field is fully 3D and time dependent. From the analytical velocity field, we study the fluid particle trajectory numerically.

6.3   Fluid particle trajectories

When a straight rod sweeps out a cone above a no-slip plane, the trajectory of the fluid particle is computed numerically from the velocity field equation (6.2) or (6.5). The upright cone case can be recovered from (6.5) by setting the tilt angle $\lambda = 0$.

Since this upright cone case has been studied before [48, 9], we simply provide one fluid particle trajectory with two views in Figure 6.1 to show the main properties of fluid particle trajectories. While the rod rotates, the fluid particle moves along a slow, large, periodic orbit surrounding the cone, and small epicycles with time scale proportional to one revolution of the rod. Except for a periodic fluctuation during each epicycle, the fluid particle stays at a fixed z-level. This property is illustrated clearly from the side

(a) Top view   (b) Side view
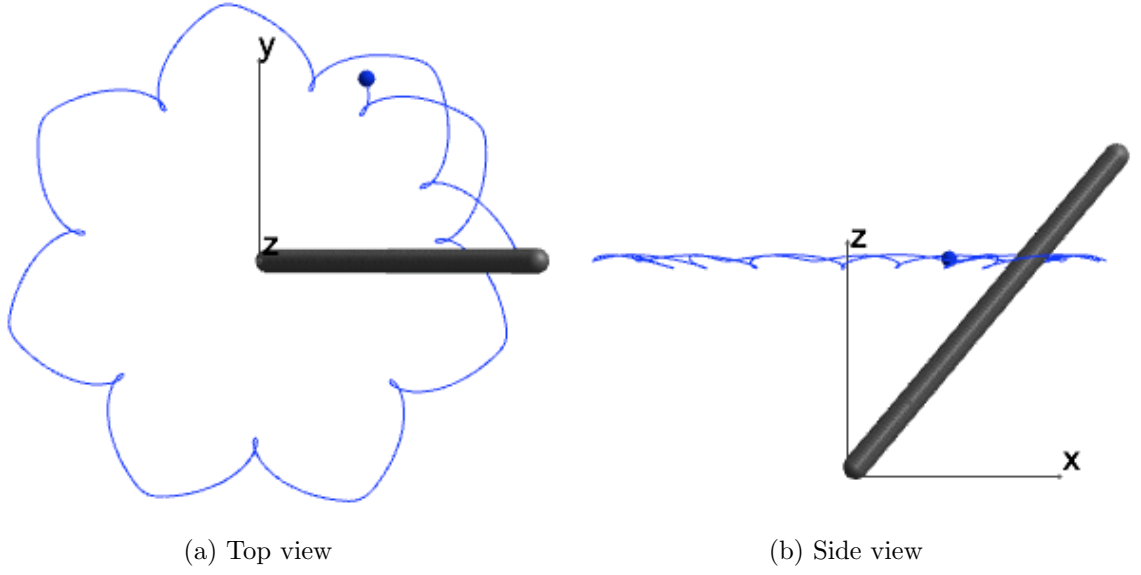
Figure 6.1: A fluid particle trajectory starts at $(0.6, 0, 0.5)$ within 10 revolutions of the straight rod sweeping out an upright cone. The cone angle $\kappa = 40^o$, the length of the rod is $\ell = 1$, and the radius is $r = 0.038$.

view of the trajectory in Figure 6.1b.

When the rod sweeps out a tilted cone, the symmetry of the cone with respect to the no-slip plane is broken, which introduces new phenomena in the flow. Figure 6.2 shows fluid particle trajectories at one fixed initial position with different values of the tilt angle λ, with the other parameters in the model held fixed for these trajectories. The larger the tilted angle is, the more the trajectory is deformed. In Figure 6.2, the fluid particle trajectory seems changed from a closed orbit to an open orbit when $\lambda = \frac{\pi}{4}$ (the cone is always above the no-slip plane).

With the same geometry of the rod, Figure 6.3 and 6.4 show tilt effects with the fluid particle trajectories initially on a line perpendicular to the cone axis. If the cone is upright, such particles will stay at almost the same level. As the tilt angle λ increases, the motion in the cone axis direction is enhanced. Initial positions on the plots are marked with filled green circles. The cone angle for both cases is $\kappa = \frac{\pi}{6}$. The tilt angle λ is $\frac{\pi}{12}$ for Figure 6.3, and λ equals $\frac{\pi}{6}$ for Figure 6.4. The geometry of the rod in Figure

119

(a) Top view

(b) Side view

(c) 3D view
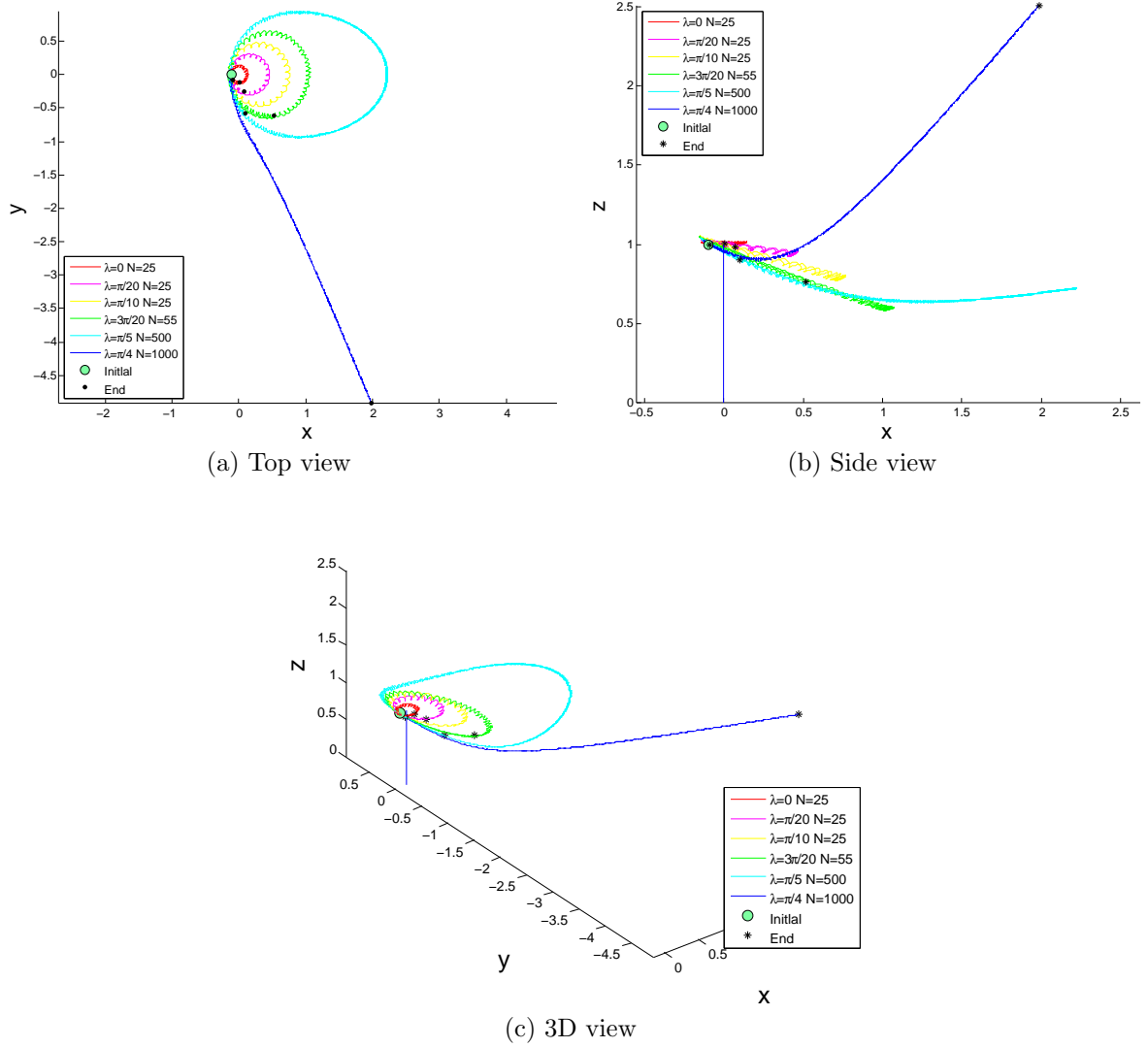
Figure 6.2: Fluid particle trajectories created by the straight rod sweeping out a tilted cone with different values of the tilt angle λ. The cone angle is $\kappa = \frac{\pi}{6}$, the length of the rod is $\ell = 1$, and the radius is $r = 0.02$. Number N in the legend is the number of revolutions of the rod.

6.3 and 6.4 is kept the same as in Figure 6.2.

Figure 6.5 shows another group of fluid particle trajectories within the same number of revolutions N of the rod. The initial positions are at the opposite side of the x-axis compared to the tilted cone axis. In another word, the cone axis is tilted to the $x > 0$ side, but $x < 0$ for the fluid particle initial positions. The cone angle is $\kappa = \frac{\pi}{6}$ and the tilt angle is $\lambda = \frac{\pi}{4}$. The geometry of the rod is the same as in Figure 6.2. These fluid particle trajectories are not closed orbits around the tilted cone. As this figure shows, they are open trajectories. Since these are numerical trajectories, further theoretical study is required to verify this.

As the fluid particle trajectories indicate, the tilted cone creates net transport. The trajectories are periodic closed orbits near the cone, but there are open trajectories away from the cone. Especially, some fluid particle trajectories are similar to the streamlines of flow past a Stokeslet as shown in Figure 6.5. This is a new phenomenon never observed with a straight rod sweeping out an upright cone.

6.4 Far field behaviors

To understand the open trajectories in the flow induced by the straight rod sweeping out a tilted cone, it is worthwhile to check the flow far from the body. In the far field, the flow motion could be captured by the leading order of the non-dimensionalized velocity field.

To examine the velocity field as the observation point x gets far from the force distribution, the non-dimensional formulae are introduced. Let

$$\tilde{x} = x/R, \quad \tilde{s} = s/\ell, \quad \tilde{\alpha}' = \alpha/U, \tag{6.9}$$

where R is a scalar parameter with the dimensions of length assumed to be large and

121

(a) 3D view

(b) Cone axis view

(c) Top view

(d) Side view
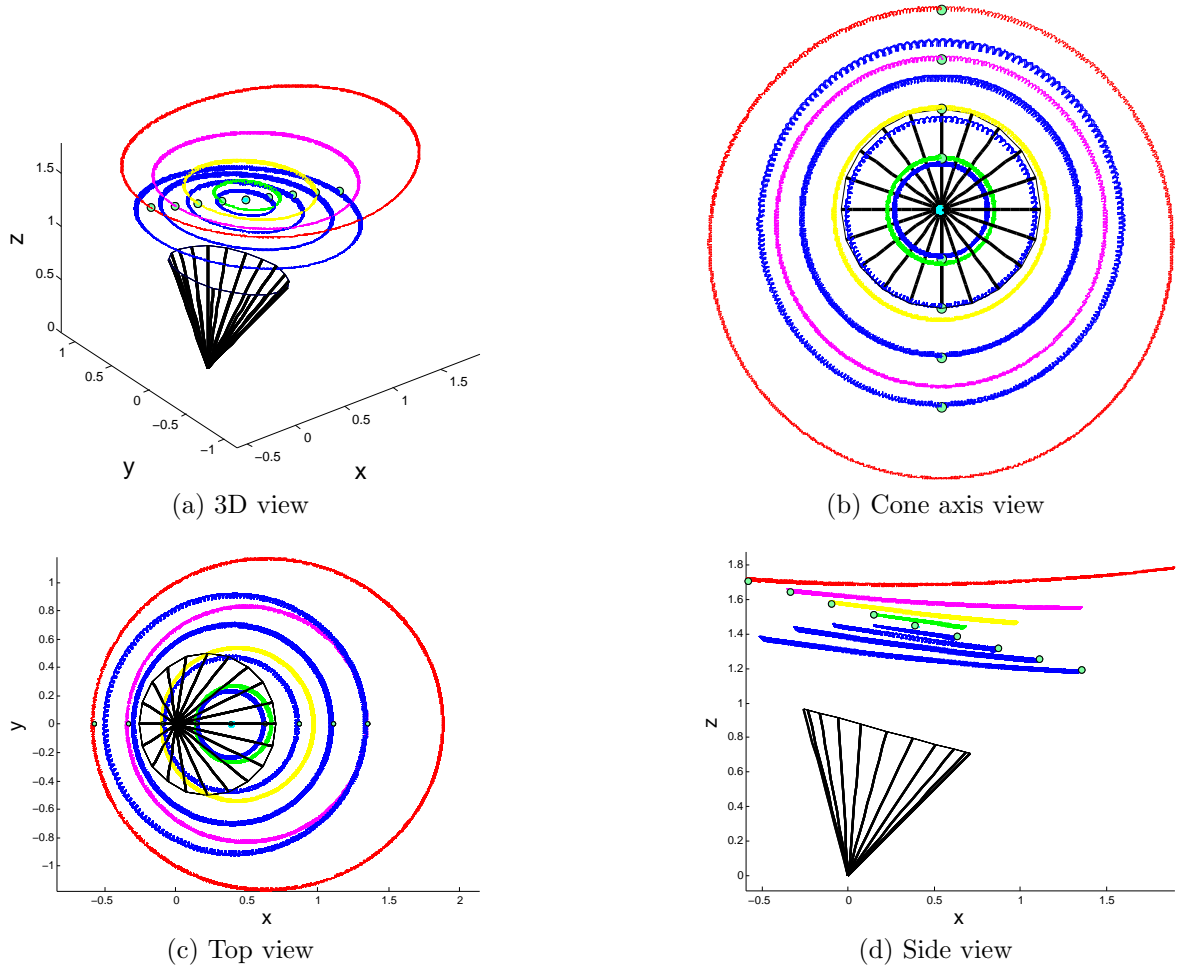
Figure 6.3: Fluid particle trajectories within the same number of revolutions $N = 1000$ of the rod. The initial positions are distributed on a line perpendicular to the cone axis in the x-z plane, indicated by the green points. The cone angle $\kappa = \frac{\pi}{6}$ and the tilt angle $\lambda = \frac{\pi}{12}$. The geometry of the rod is same as in Figure 6.2.

(a) 3D view

(b) Cone axis view

(c) Top view

(d) Side view
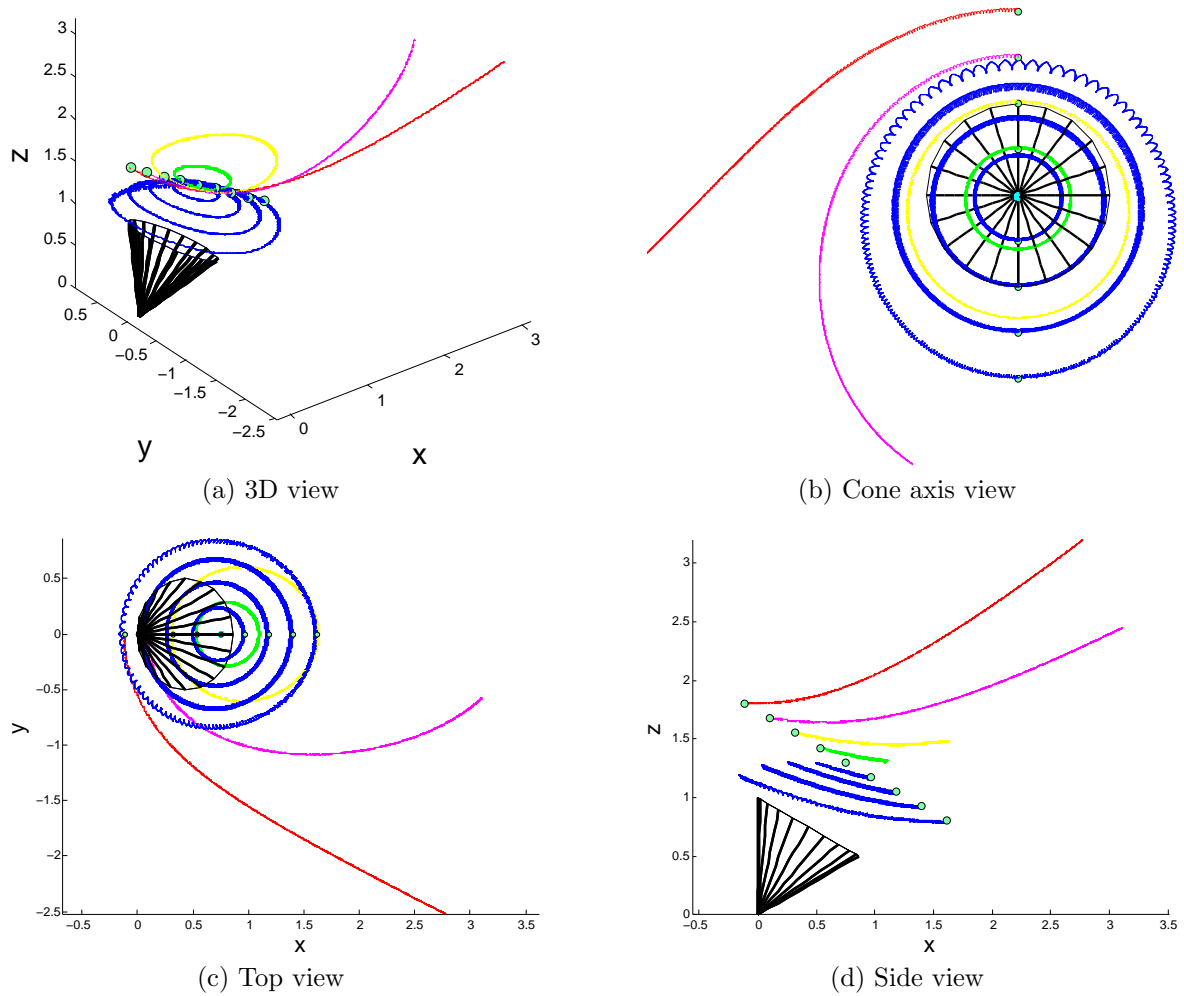
Figure 6.4: Similar to Figure 6.3 but with the tilt angle $\lambda = \frac{\pi}{6}$.

(a) Top view

(b) Side view

$\kappa=\pi/6, \lambda=\pi/4$

(c) 3D view
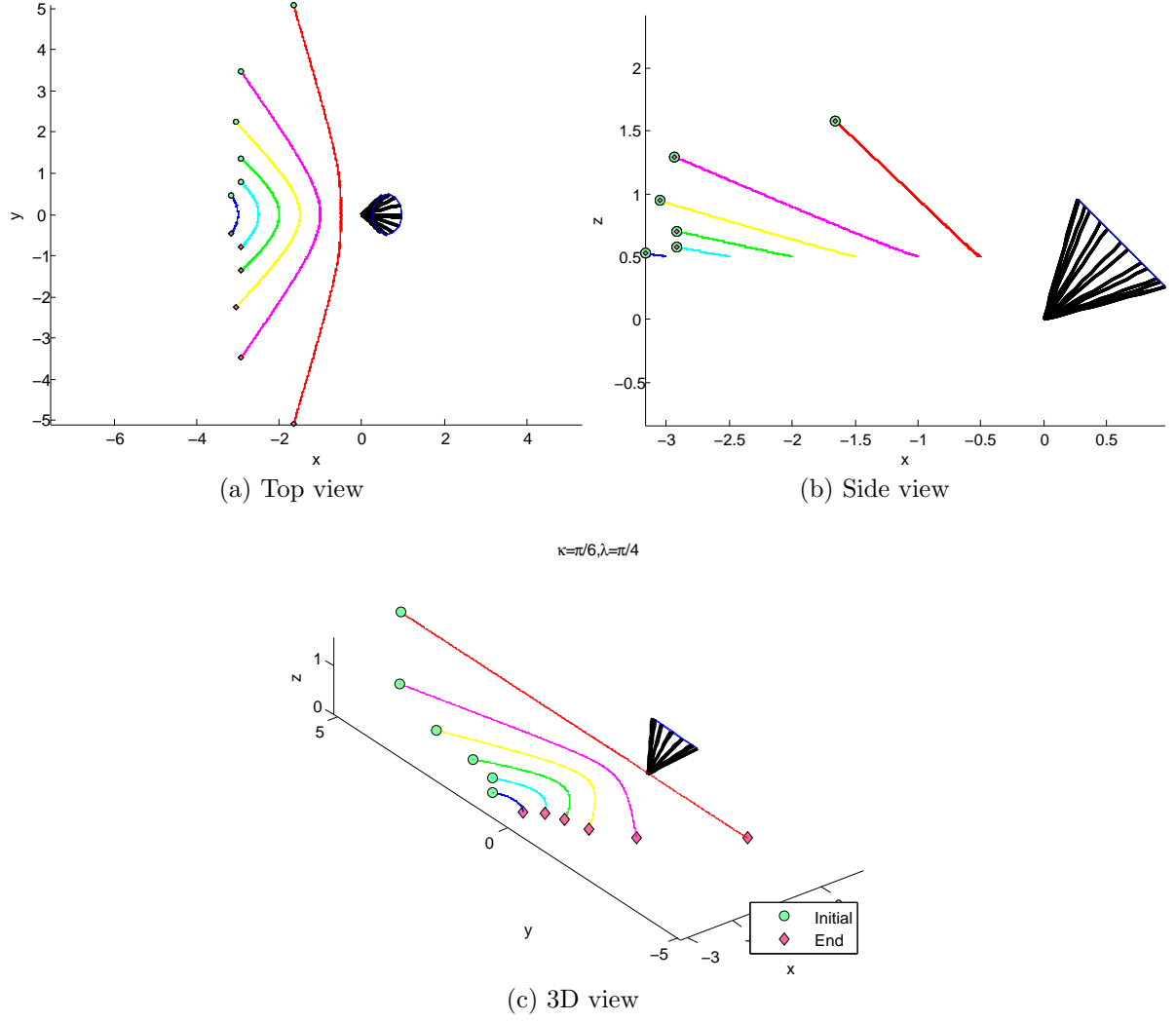
Figure 6.5: Fluid particle trajectories created within the same number of revolutions of the straight rod with $\kappa = \frac{\pi}{6}$ and $\lambda = \frac{\pi}{4}$. The geometry of the rod is kept the same as in Figure 6.2.

$U = \omega\ell$ is a characteristic velocity. The velocity field written as function of the non-dimensional variables in (6.9) becomes

$$
\begin{aligned}
u_1'(\tilde{x}, \tilde{y}, \tilde{z}) = \int_0^\ell &\left[\frac{U\tilde{\alpha}_1}{R\left|\tilde{\mathbf{x}} - \frac{\ell}{R}\tilde{\mathbf{x}}_s\right|} \right. \\
&+ \frac{U(\tilde{x} - \frac{\ell}{R}\tilde{x}_s)\left((\tilde{x} - \frac{\ell}{R}\tilde{x}_s)\tilde{\alpha}_1 + (\tilde{y} - \frac{\ell}{R}\tilde{y}_s)\tilde{\alpha}_2 + (\tilde{z} - \frac{\ell}{R}\tilde{z}_s)\tilde{\alpha}_3\right)}{R\left|\tilde{\mathbf{x}} - \frac{\ell}{R}\tilde{\mathbf{x}}_s\right|^3} \\
&- \frac{U\tilde{\alpha}_1}{R\left|\tilde{\mathbf{x}} - \frac{\ell}{R}\tilde{\mathbf{x}}_s\right|} - \frac{U(\tilde{x} - \frac{\ell}{R}\tilde{x}_s)\left((\tilde{x} - \frac{\ell}{R}\tilde{x}_s)\tilde{\alpha}_1 + \tilde{\alpha}_2(\tilde{y} - \frac{\ell}{R}\tilde{y}_s) + (\tilde{z} + \frac{\ell}{R}\tilde{z}_s)\tilde{\alpha}_3\right)}{R\left|\tilde{\mathbf{x}} - \frac{\ell}{R}\tilde{\mathbf{x}}_s'\right|^3} \\
&+ 2\ell\tilde{z}_s\left(\frac{-\tilde{z}U\tilde{\alpha}_1 U}{R^2\left|\tilde{\mathbf{x}} - \frac{\ell}{R}\tilde{\mathbf{x}}_s'\right|^3} + \frac{(\tilde{x} - \frac{\ell}{R}\tilde{x}_s)U\tilde{\alpha}_3}{R^2\left|\tilde{\mathbf{x}} - \frac{\ell}{R}\tilde{\mathbf{x}}_s'\right|^3} \right. \\
&\left.\left. + \frac{3U\tilde{z}(\tilde{x} - \frac{\ell}{R}\tilde{x}_s)\left(\tilde{\alpha}_1(\tilde{x} - \frac{\ell}{R}\tilde{x}_s) + \tilde{\alpha}_2(\tilde{y} - \frac{\ell}{R}\tilde{y}_s) - \tilde{\alpha}_3(\tilde{z} + \frac{\ell}{R}\tilde{z}_s)\right)}{R^2\left|\tilde{\mathbf{x}} - \frac{\ell}{R}\tilde{\mathbf{x}}_s'\right|^5} \right) \right] ds,
\end{aligned}
$$

$$
\begin{aligned}
u_2'(\tilde{x}, \tilde{y}, \tilde{z}) = \int_0^\ell &\left[\frac{U\tilde{\alpha}_2}{R\left|\tilde{\mathbf{x}} - \frac{\ell}{R}\tilde{\mathbf{x}}_s\right|} \right. \\
&+ \frac{U(\tilde{y} - \frac{\ell}{R}\tilde{y}_s)\left((\tilde{x} - \frac{\ell}{R}\tilde{x}_s)\tilde{\alpha}_1 + (\tilde{y} - \frac{\ell}{R}\tilde{y}_s)\tilde{\alpha}_2 + (\tilde{z} - \frac{\ell}{R}\tilde{z}_s)\tilde{\alpha}_3\right)}{R\left|\tilde{\mathbf{x}} - \frac{\ell}{R}\tilde{\mathbf{x}}_s\right|^3} \\
&- \frac{U\tilde{\alpha}_2}{R\left|\tilde{\mathbf{x}} - \frac{\ell}{R}\tilde{\mathbf{x}}_s'\right|} + \frac{U(\tilde{y} - \frac{\ell}{R}\tilde{y}_s)\left((\tilde{x} - \frac{\ell}{R}\tilde{x}_s)\tilde{\alpha}_1 - \tilde{\alpha}_2(\tilde{y} - \frac{\ell}{R}\tilde{y}_s) + (\tilde{z} + \frac{\ell}{R}\tilde{z}_s)\tilde{\alpha}_3\right)}{R\left|\tilde{\mathbf{x}} - \frac{\ell}{R}\tilde{\mathbf{x}}_s'\right|^3} \\
&+ 2\ell\tilde{z}_s\left(\frac{-\tilde{z}U\tilde{\alpha}_2}{R^2\left|\tilde{\mathbf{x}} - \frac{\ell}{R}\tilde{\mathbf{x}}_s'\right|^3} + \frac{(\tilde{y} - \frac{\ell}{R}\tilde{y}_s)U\tilde{\alpha}_3}{R^2\left|\tilde{\mathbf{x}} - \frac{\ell}{R}\tilde{\mathbf{x}}_s'\right|^3} \right. \\
&\left.\left. + \frac{3U\tilde{z}(\tilde{y} - \frac{\ell}{R}\tilde{y}_s)\left(\tilde{\alpha}_1(\tilde{x} - \frac{\ell}{R}\tilde{x}_s) + \tilde{\alpha}_2(\tilde{y} - \frac{\ell}{R}\tilde{y}_s) - \tilde{\alpha}_3(\tilde{z} + \frac{\ell}{R}\tilde{z}_s)\right)}{R^2\left|\tilde{\mathbf{x}} - \frac{\ell}{R}\tilde{\mathbf{x}}_s'\right|^5} \right) \right] ds,
\end{aligned}
$$

$$u_3'(\tilde{x}, \tilde{y}, \tilde{z}) = \int_0^\ell \left[\frac{U\tilde{\alpha}_3}{R \left| \tilde{\mathbf{x}} - \frac{\ell}{R}\tilde{\mathbf{x}}_s \right|} \right.$$

$$+ \frac{U(\tilde{z} - \frac{\ell}{R}\tilde{z}_s) \left((\tilde{x} - \frac{\ell}{R}\tilde{x}_s)\tilde{\alpha}_1 + \tilde{\alpha}_2(\tilde{y} - \frac{\ell}{R}\tilde{y}_s) + (\tilde{z} - \frac{\ell}{R}\tilde{z}_s)\tilde{\alpha}_3 \right)}{R \left| \tilde{\mathbf{x}} - \frac{\ell}{R}\tilde{\mathbf{x}}_s \right|^3}$$

$$- \frac{U\tilde{\alpha}_3}{R \left| \tilde{\mathbf{x}} - \frac{\ell}{R}\tilde{\mathbf{x}}_s' \right|} - \frac{U(\tilde{z} + \frac{\ell}{R}\tilde{z}_s) \left((\tilde{x} - \frac{\ell}{R}\tilde{x}_s)\tilde{\alpha}_1 + \tilde{\alpha}_2(\tilde{y} - \frac{\ell}{R}\tilde{y}_s) + (\tilde{z} + \frac{\ell}{R}\tilde{z}_s)\tilde{\alpha}_3 \right)}{R \left| \tilde{\mathbf{x}} - \frac{\ell}{R}\tilde{\mathbf{x}}_s' \right|^3}$$

$$+ 2\ell\tilde{z}_s \left(\frac{\tilde{z}U\tilde{\alpha}_3}{R^2 \left| \tilde{\mathbf{x}} - \frac{\ell}{R}\tilde{\mathbf{x}}_s' \right|^3} + U\frac{(\tilde{y} - \frac{\ell}{R}\tilde{y}_s)\tilde{\alpha}_2 + (\tilde{x} - \frac{\ell}{R}\tilde{x}_s)\tilde{\alpha}_1}{R^2 \left| \tilde{\mathbf{x}} - \frac{\ell}{R}\tilde{\mathbf{x}}_s' \right|^3} \right.$$

$$\left. \left. + \frac{3U\tilde{z}(\tilde{z} + \frac{\ell}{R}\tilde{z}_s) \left(\tilde{\alpha}_1(\tilde{x} - \frac{\ell}{R}\tilde{x}_s) + \tilde{\alpha}_2(\tilde{y} - \frac{\ell}{R}\tilde{y}_s) - \tilde{\alpha}_3(\tilde{z} + \frac{\ell}{R}\tilde{z}_s) \right)}{R^2 \left| \tilde{\mathbf{x}} - \frac{\ell}{R}\tilde{\mathbf{x}}_s \right|^5} \right) \right] ds.$$

Let $\epsilon_0 = \frac{\ell}{R}$ and drop all the tilde, we expand the velocity in order of ϵ_0. The leading order of the far-field velocity is

$$\frac{dx}{dt} = \frac{4C\ell xz\epsilon_0^2 (x\alpha_1 + y\alpha_2)}{(x^2 + y^2 + z^2)^{5/2}},$$

$$\frac{dy}{dt} = \frac{4C\ell yz\epsilon_0^2 (x\alpha_1 + y\alpha_2)}{(x^2 + y^2 + z^2)^{5/2}},$$

$$\frac{dz}{dt} = \frac{4C\ell z^2\epsilon_0^2 (x\alpha_1 + y\alpha_2)}{(x^2 + y^2 + z^2)^{5/2}}.$$

For the rod sweeping out a tilted cone,

$$C = \cos(\kappa)\cos(\lambda) - \cos(\omega t)\sin(\kappa)\sin(\lambda)$$

$$\alpha_1 = -\frac{\omega\epsilon}{2}\cos(\lambda)\sin(\kappa)\sin(\omega t),$$

$$\alpha_2 = \frac{\omega\epsilon}{2}\sin(\kappa)\cos(\omega t),$$

$$\alpha_3 = \frac{\omega\epsilon}{2}\sin(\lambda)\sin(\kappa)\sin(\omega t),$$

where ϵ is the slenderness.

Type of singularity

The leading term in the far-field expansion of linear distribution of Blakelet is

$$\mathbf{u} = \frac{2C\ell z(\mathbf{x} \cdot \boldsymbol{\alpha})}{(x^2 + y^2 + z^2)^{5/2}}\mathbf{x} + \frac{2C\ell z(\mathbf{x} \cdot \boldsymbol{\alpha}')}{(x^2 + y^2 + z^2)^{5/2}}\mathbf{x}.$$

So,

$$u(\mathbf{x}) \sim u_{\mathrm{SD}}\left(\mathbf{x}; (\alpha_1, \alpha_2, 0), \frac{4}{3}\epsilon_0^2 C\ell \mathbf{e}_z\right) = 4\epsilon_0^2 C\ell z \frac{\left(\boldsymbol{\alpha}^T \cdot \mathbf{x}^T\right)\mathbf{x}}{|\mathbf{x}|^5}. \tag{6.10}$$

While the leading term in the far-field expansion of a uniform distribution of Stokeslets is a single Stokeslet, the leading term in the farfield expansion of linear distribution of Stokeslet is a Stokeslet doublet as (6.10).

Trajectory

From the far-field velocity (6.10), we rewrite the governing equations of the fluid particle trajectory as

$$\frac{dy}{dx} = \frac{y}{x},$$
$$\frac{dz}{dx} = \frac{z}{x}.$$

Let $\frac{y}{x} = \text{constant} = \eta$ and $\frac{z}{x} = \text{constant} = \zeta$, then $y = \eta x$ and $z = \zeta x$. Fluid particles move along straight lines in the far field.

Computing the mean farfield velocity over one rotation of the rod, we get

$$\overline{u} = \frac{\omega}{2\pi} \int_0^{2\frac{\pi}{\omega}} \mathbf{u}(\mathbf{x}, t)\, dt,$$

which is

$$\frac{d\overline{x}}{dt} = -\frac{\ell\epsilon^3\omega\sin^2(\kappa)\sin(\lambda)}{(\overline{x}^2 + \overline{y}^2 + \overline{z}^2)^{5/2}}\overline{xyz},$$

$$\frac{d\overline{y}}{dt} = -\frac{\ell\epsilon^3\omega\sin^2(\kappa)\sin(\lambda)}{(\overline{x}^2 + \overline{y}^2 + \overline{z}^2)^{5/2}}\overline{y}^2\overline{z},$$

$$\frac{d\overline{z}}{dt} = -\frac{\ell\epsilon^3\omega\sin^2(\kappa)\sin(\lambda)}{(\overline{x}^2 + \overline{y}^2 + \overline{z}^2)^{5/2}}\overline{y}\overline{z}^2.$$

The above mean velocity field also shows the trajectories are straight lines.

6.5   Fluid transport

When a straight rod spins an upright cone, there is no net flux through a plane per-pendicular to the no-slip plane over one rod revolution, due to the symmetry property of the rotation. When the cone is tilted, the symmetry is broken. As the cone axis is tilted in the x-z plane, there is net flux through a semi-infinite plane parallel to the x-z plane. The flux is computed as an integral of velocity component v in the y-direction. The mean flux is computed as a double integral of the velocity over the semi-infinite plane and over one revolution.

From the velocity field (6.7), we first compute the integral over the spacial variables. Then, the integral is over the semi-infinite plane at fixed y, parallel to the x-z plane, and above the $z = 0$ plane. We notice the flux is contributed by the Stokeslet with point force pointing perpendicular to this semi-infinite. In terms of the strength in (6.4), they are velocity components associated with α_2.

We first analyze the flux induced by a Blakelet $\mathbf{u}_\mathrm{B}(\mathbf{x} - Cs\mathbf{e}_z; \alpha_2\mathbf{e}_y)$ through the semi-infinite plane. The flux induced by either one Stokeslet $\mathbf{u}_\mathrm{S}(\mathbf{x} - Cs\mathbf{e}_z; \alpha_2\mathbf{e}_y)$ or a pair of Stokeslets $\mathbf{u}_\mathrm{S}(\mathbf{x} - Cs\mathbf{e}_z; \alpha_2\mathbf{e}_y) + \mathbf{u}_\mathrm{S}(\mathbf{x} + Cs\mathbf{e}_z; -\alpha_2\mathbf{e}_y)$ in the Blakelet is infinite. The Stokes doublet and the point source dipole in the Blakelet are higher order singularities

for the spatial coordinates, compared to the Stokeslet, and their contribution to the velocity field decays faster at inifinity. However, seen from large distances, the pair of Stokeslets contributes at leading order the same rate of decay as that of the Stokes doublet and dipole, and hence there can be a cancellation that makes the flux induced by a Blakelet $\mathbf{u}_B(\mathbf{x} - Cs\mathbf{e}_z; \alpha_2\mathbf{e}_y)$ is finite, as can be easily checked.

Based on the above information, we switch the order of integral to simplify the integrals. The instantaneous flux through the semi-infinite plane perpendicular to the y-axis is

$$\int_0^\infty \int_{-\infty}^\infty v(x,y,z)dxdz = \int_0^\ell \int_0^\infty \int_{-\infty}^\infty v_B(x,y,z)dxdzds \qquad (6.11)$$
$$= \int_0^\ell 8[\cos(\kappa)\cos(\lambda) - \cos(\omega t)\sin(\kappa)\sin(\lambda)]\sin(\kappa)\cos(\omega t)\frac{\omega\epsilon}{2}s^2 ds,$$

where $v_B(x,y,z)$ is the velocity component of a Blakelet in the y-direction. The average flux over one revolution of the rod is

$$
\begin{aligned}
\text{Flux} &= \frac{\omega}{2\pi}\int_0^{\frac{2\pi}{\omega}}\left(\int_0^\infty\int_{-\infty}^\infty v(x,y,z)dxdz\right)dt & (6.12)\\
&= \frac{\omega}{2\pi}\int_0^{\frac{2\pi}{\omega}}dt\int_0^\ell 4\,\omega\,\epsilon(\cos(\kappa)\cos(\lambda) - \cos(\omega t)\sin(\kappa)\sin(\lambda))\sin(\kappa)\cos(\omega t)s^2 ds\\
&= \frac{\omega}{2\pi}\int_0^{\frac{2\pi}{\omega}}\frac{4\ell^3\epsilon\,\omega}{3}\cos(\omega t)\sin(\kappa)[\cos(\kappa)\cos(\lambda) - \cos(\omega t)\sin(\kappa)\sin(\lambda)]dt\\
&= -\frac{2}{3}\ell^3\epsilon\,\omega\sin^2(\kappa)\sin(\lambda).
\end{aligned}
$$

This is consistent with the result from Smith et al. [69], which is in terms of the resistance coefficient and computed with the far-field velocity. The negative sign is due to the prescribed counter-clockwise rotation of the rod and the definition of the tilt angle λ. If the cone is tilt to the positive x-axis direction and the rod is sweeping counter-clockwise with angular velocity ω, then the flux past a plane at $y > 0$ is

(a) Tracked Rod   (b) Top view
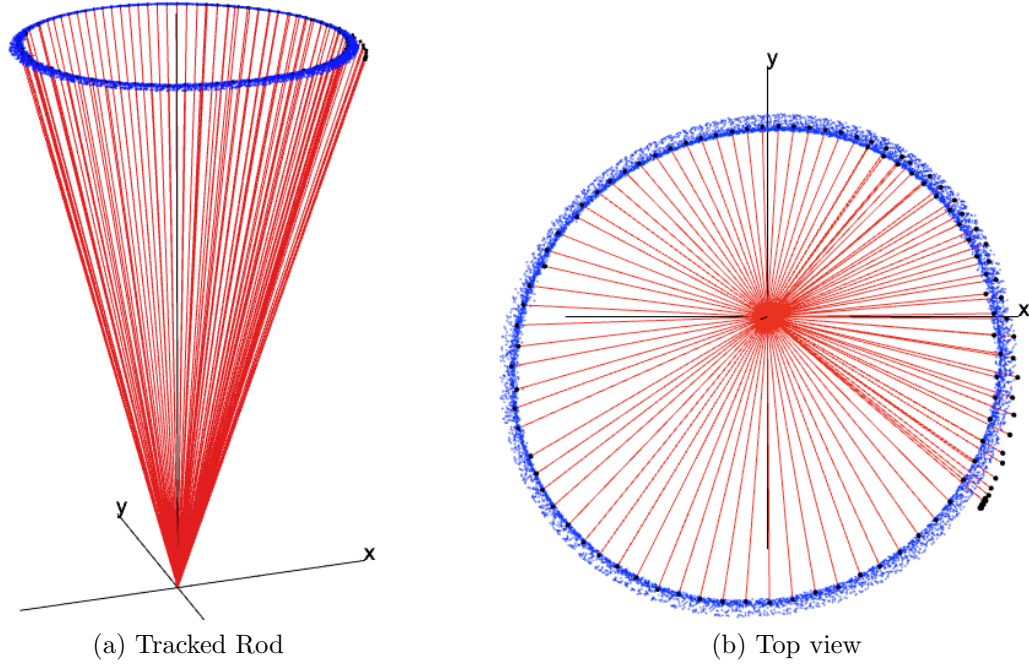
Figure 6.6: Tracked rod tips (blue dots) and the tracked center-line of the straight rod during initial transition and about one full revolution for one experiment.

negative, which means the fluid moves in the negative y-direction.

6.6   Experimental and numerical trajectory

In this section, we report experimental study of a straight rod sweeping out a cone and compare the experimental trajectories with those from the mathematical model. Based on the fully 3D experimental capability, the positions of the marker and the rod are resolved accurately for the experimental data.

Figure 6.6 shows the tracking data for the straight rod sweeping out a cone with its base as the cone's apex. The blue dots are the time sequence of the top tip. Here we only plot the center-line of the rod during the initial transient and one full revolution. The black dots are corresponding tips for these positions. From this plot, the cone generated by the rod in the experiment is not an upright cone.
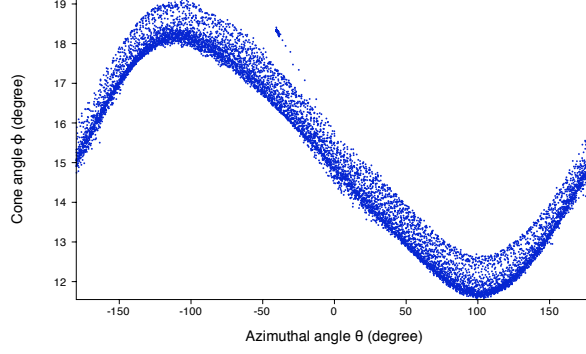
Figure 6.7: Tracked angles for the experiment of Figure 6.6.

Figure 6.7 shows the corresponding tracking angles, the azimuthal angle θ and the "generalized" cone angle ϕ. This is due to the difficulty of defining the cone axis for a dynamic cone. If the cone is upright, $\phi = \kappa$ is the standard cone angle defined in our model. Otherwise, if the cone angle is tilted or dynamic, for example the case shown in Figure 6.7, we use the reference angle ϕ between the vertical axis and the center-line of the rod as the generalized cone angle for simplification. These tracked data are obtained with the tracking program from Holz [35].

Figure 6.8 shows one trajectory of an air bubble in silicone Oil with kinematic viscosity 125000 cst compared with the asymptotic solution. Since the density of the air bubble is smaller than the silicone oil, the buoyancy effect is considered in the model as an external vertical velocity component. The length of the pin is 1cm and the radius is 0.04cm. So, the slenderness $\epsilon = \log^{-1}(\frac{\ell}{r}) \sim 0.31$. (The length unit used here is centimeter.) The black dot indicates the initial position of the air bubble $(-0.4840365, -0.16052, 0.8341694)$. In this case, not only is the cone tilted but also the cone angle varies dynamically as shown in Figure 6.6 and 6.7.

Assume the flow is at rest, then the comparison is shown in Figure 6.8a and 6.8b, where the experimental trajectory is in red and the numerical trajectory is in black. In our lab space, we do not have good control of the temperature and the humidity. Ther-

mal instability is observed in the tank, even though the convection is slow and observed in a very large time scale. In Figure 6.8c and 6.8d, the blue numerical trajectories are obtained with optimized shear background flow $(-1.050^{-4}, -7.283 \times 10^{-4}, 0)z$ cm/s. The optimized background flow is considered on the magnitude and direction of the measured velocity of the air bubble without the motion of the rod for this experiment. The shear flow instead of uniform background flow is input to avoid the invalidation of no-slip boundary condition on the flat plane. These figures show that our model and experiment have good agreement.

One mysterious result is the black trajectory shown in Figure 6.9. It is a numerical trajectory if the background shear flow is directly added to the velocity field generated by the rotating rod. In such a situation, the strength of the Stokeslet distributed along the center-line of the rod should be adjusted properly to satisfy the no-slip boundary condition on the surface. However, this trajectory with shear flow $(5 \times 10^{-6}, 4 \times 10^{-5}, 0)z$ directly added to the flow field has an excellent agreement with the trajectory with the right velocity field, even though at the end of the trajectory very small discrepancy shows up from the side view.
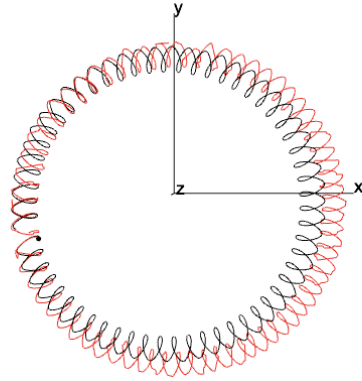
(a) Top view
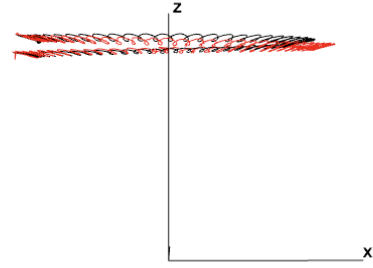
(b) Side view
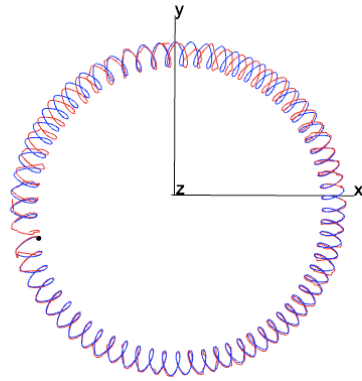
(c) Top view
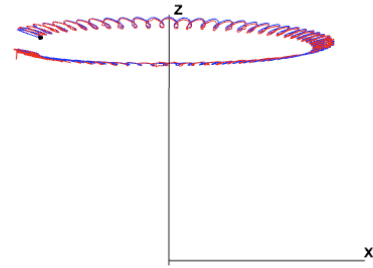
(d) Side view

Figure 6.8: Experimental trajectories compare to numerical trajectories when a straight rod sweeps out a cone. The red trajectory is from experimental data. The black trajectory is from the numerical simulation without considering the convection in the fluid. The blue trajectory is the numerical trajectory with a shear background flow. The velocity of the background flow is based on the convection velocity measured in the tank.
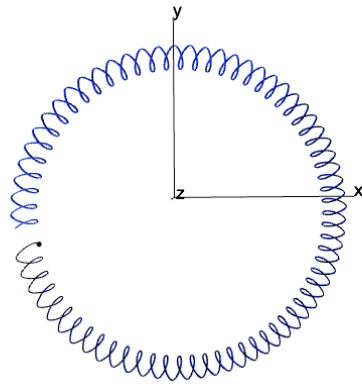
(a) Top view
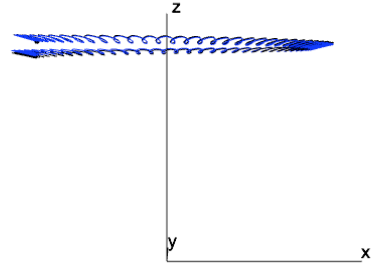
(b) Side view

Figure 6.9: The numerical trajectory with the shear background flow compared with a numerical trajectory with an invalid shear background flow. The blue trajectory is the numerical trajectory in Figure 6.8c by correctly adding the background shear flow in the fluid problem. The black trajectories is the trajectory with the invalid background shear. In the numerical simulation, the background shear is added directly to the flow field generated by spinning a rod in a stationary background flow instead of considering the shear flow as the background flow and justifying the singularities on the rod.

Chapter 7

A bent rod sweeping out a cone above a no-slip plane

Following the study of flows generated by a straight rod sweeping out a cone in the previous chapter, we study the flow induced by a bent rod, which precesses conically above a no-slip plane in a highly viscous fluid. When a straight rod sweeps out an upright cone, the flow preserves symmetry properties. When the rod is bent, symmetry breaking induced by the bend creates new phenomena over a long time scale. A family of nested tori appears in the fluid particle trajectories. Similar to the straight rod case, we use experiment, theory and numerics to investigate and understand the flow generated by a bent rod sweeping out a cone.

7.1   Model

The configuration of the motion of a bent rod is shown in Figure 7.1, which has been briefly discussed in the experiment setup in Chapter 5. The rod stands above a no-slip plane and sweeps out a cone with its lower tip as the pivot point. For the bent rod case, the cone angle is defined as the angle between the chord of the rod and the axis of the cone, and an extra scooping angle β is introduced. As the bent rod is in plane "b" in
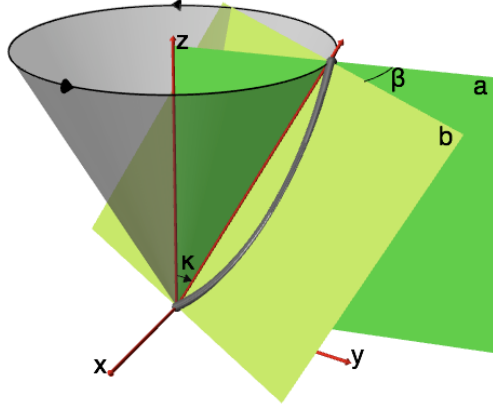
Figure 7.1: Configuration of a bent rod sweeping out an upright cone. Cone angle κ is the angle between the chord of the rod and the positive z-axis. Scooping angle β is the angle between plane "a" and plane "b" where the rod is.

Figure 7.1, the scooping angle β is defined as the angle from plane "a", where the chord and the axis of cone are, to plane "b". To make the scooping angle unique for each rod position, angle β is defined from plane "a" outside the cone to plane "b" clockwise. Figure 7.2 shows four extreme situations of the rod sweeping out a cone. When $\beta = 0$, we call it belly out; when $\beta = \pi$, we call it belly in; $\beta = \frac{\pi}{2}$ and $\beta = \frac{3\pi}{2}$ for scooping and anti-scooping, respectively, when the rotation is counter-clockwise as views from above.

A model based on the slender-body theory is developed to study the induced flow above the infinite no-slip plane. The essence is to express the solutions in terms of a collection of fundamental singular solutions to the Stokes equations, and then to compute the strength of the selected singularities in order to satisfy the far field and no-slip boundary conditions. The image system for the Stokeslet derived by Blake [5] is utilized to handle

(a) Belly out ($\beta = 0$)   (b) Belly in ($\beta = \pi$)

(c) Scoop ($\beta = \frac{\pi}{2}$)   (d) Anti-scoop ($\beta = \frac{3\pi}{2}$)
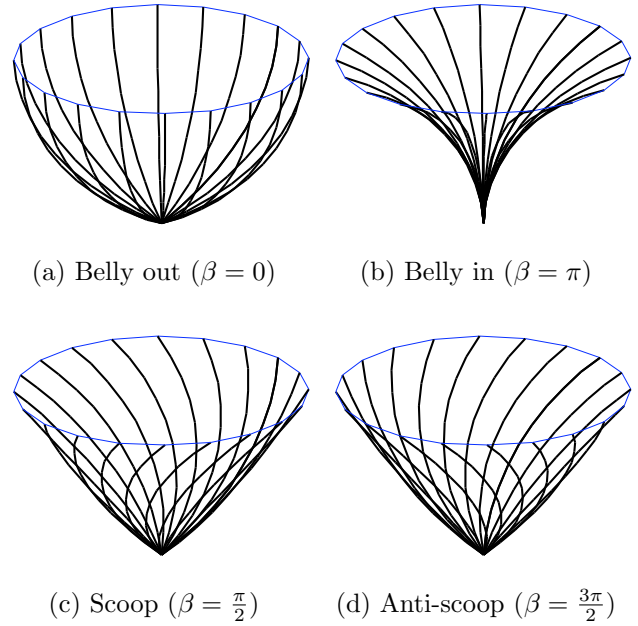
Figure 7.2: Four extreme statuses of the cone.

the no-slip boundary condition on the

flat plane upon which the apex of the cone rests.

The details about the velocity field for a bent rod precessing in an upright cone are provided here. For the experimental verification, we extend our model to the tilted cone case as necessary. Since the tilted cone for the bent rod is similar to the straight rod case in the previous chapter, we skip those details to avoid redundancies.

In the body frame, when the rod sweeps out an upright cone, the rod and the no-slip plane are relatively fixed and there is rotation background flow in the body frame. In this frame, we construct an asymptotic solution in closed form using the slender body theory. As for the straight rod case, Blakelets are distributed along the center-line of the bent rod. In the body frame, the center-line of the bent rod is fixed and can be written as a parametric function of its arc-length s. With prescribed scooping angle β and cone angle κ, the center-line $\mathbf{x}_b = (x_b(s), y_b(s), z_b(s))^T$ is

$$x_b = -2a\cos(\beta)\cos(\kappa)\sin(\frac{\ell-s}{2a})\sin(\frac{s}{2a}) + 2a\sin(\kappa)\cos\left(\frac{\ell-s}{2a}\right)\sin(\frac{s}{2a}), \quad (7.1)$$

$$y_b = -2a\sin(\beta)\sin(\frac{\ell-s}{2a})\sin(\frac{s}{2a}), \quad (7.2)$$

$$z_b = 2a\cos(\kappa)\cos(\frac{\ell-s}{2a})\sin(\frac{s}{2a}) + 2a\cos(\beta)\sin(\kappa)\sin\left(\frac{\ell-s}{2a}\right)\sin(\frac{s}{2a}), \quad (7.3)$$

$(0 \leq s \leq \ell)$, where ℓ is the body length and $K = \frac{1}{a}$ is the local non-dimensional curvature of the body center-line with respect to the body length.

The strength of the Stokeslet in the Blakelet

$$\boldsymbol{\alpha} = R\,diag(\frac{\epsilon}{4}, \frac{\epsilon}{2}, \frac{\epsilon}{2})\,R^{-1}\mathbf{U} \quad (7.4)$$

is determined from the linear background velocity $\mathbf{U}$ in the local coordinates of the bent rod. In the body frame, $\mathbf{U} = \boldsymbol{\omega} \times \mathbf{x}_b = (0, 0, \omega) \times (x_b, y_b, z_b)$ is the rotation background

flow and $\boldsymbol{\omega}$ is the angular velocity of the spinning rod in the laboratory frame. Matrix $R = (e_s,\ e_n\ , e_b)$ is the transformation matrix between the body frame and the rod's local coordinates, where $e_s = \frac{\partial \mathbf{x}_b}{\partial s}$, $e_n = \frac{1}{K}\frac{\partial^2 \mathbf{x}_b}{\partial s^2}$, and $e_b = e_s \times e_n$ are the unit vectors of the local coordinates,

$$
e_s = \frac{\partial \mathbf{x}_b}{\partial s} = \begin{pmatrix} \cos(\frac{\ell-2s}{2a})\sin(\kappa) - \sin(\frac{\ell-2s}{2a})\cos(\beta)\cos(\kappa) \\ -\sin(\frac{\ell-2s}{2a})\sin(\beta) \\ \cos(\frac{\ell-2s}{2a})\cos(\kappa) + \sin(\frac{\ell-2s}{2a})\cos(\beta)\sin(\kappa) \end{pmatrix},
$$

$$
e_n = \frac{1}{K}\frac{\partial^2 \mathbf{x}_b}{\partial s^2} = \begin{pmatrix} \sin(\frac{\ell-2s}{2a})\sin(\kappa) + \cos(\frac{\ell-2s}{2a})\cos(\beta)\cos(\kappa) \\ \cos(\frac{\ell-2s}{2a})\sin(\beta) \\ \sin(\frac{\ell-2s}{2a})\cos(\kappa) - \cos(\frac{\ell-2s}{2a})\cos(\beta)\sin(\kappa) \end{pmatrix},
$$

$$
e_b = \begin{pmatrix} -\sin(\beta)\cos(\kappa), & \cos(\beta), & \sin(\beta)\sin(\kappa) \end{pmatrix}^T.
$$

So, the strength $\boldsymbol{\alpha}$ is

$$
\begin{aligned}
\alpha_1 &= -\frac{a\epsilon\omega}{8}\sin(\frac{s}{2a})\sin(\beta)\left[(7+\cos(2\kappa))\sin(\frac{\ell-s}{2a})\right.\\
&\quad \left. +2\sin(\frac{\ell-3s}{2a})\sin^2(\kappa) + 2\cos(\beta)\sin(\frac{\ell-2s}{2a})\sin(\frac{s}{2a})\sin(2\kappa)\right],\\
\alpha_2 &= \frac{a\epsilon\omega}{8}\sin(\frac{s}{2a})\left\{8\cos(\beta)\cos(\kappa)\sin(\frac{\ell-s}{2a})\right.\\
&\quad \left. -\left[\cos(\frac{\ell-s}{2a})(7+\cos(2\beta)) - 2\cos(\frac{\ell-3s}{2a})\sin^2(\beta)\right]\sin(\kappa)\right\},\\
\alpha_3 &= \frac{a\epsilon\omega}{2}\sin^2(\frac{s}{2a})\sin(\beta)\sin(\kappa)\left[\cos(\frac{\ell-2s}{2a})\cos(\kappa) + \sin(\frac{\ell-2s}{2a})\cos(\beta)\sin(\kappa)\right].
\end{aligned}
$$

When the strength of the Stokeslet along the center-line of the rod is determined, the

138

strength of the singularities for the image system is automatically specified. With the strength and the location of the singularities, the velocity field of the flow is

$$\mathbf{u} = \mathbf{U} - \int_0^\ell \mathbf{u}_B \left(\mathbf{x} - \mathbf{x}_b; \boldsymbol{\alpha} \right) ds, \tag{7.5}$$

where $\mathbf{U} = \boldsymbol{\omega} \times \mathbf{x}_b$ is the rotation background flow and Blakelet $\mathbf{u}_B \left(\mathbf{x} - \mathbf{x}_b; \boldsymbol{\alpha} \right)$ is

$$
\begin{aligned}
\mathbf{u}_B(\mathbf{x} - \mathbf{x}_b; \boldsymbol{\alpha}) &= \mathbf{u}_S(\mathbf{x} - \mathbf{x}_b; \boldsymbol{\alpha}) + \mathbf{u}_S(\mathbf{x} - \mathbf{x}_b'; -\boldsymbol{\alpha}) + \mathbf{u}_{SD}(\mathbf{x} - \mathbf{x}_b; \mathbf{e}_z; 2h\boldsymbol{\alpha}') \\
&\quad + \mathbf{u}_D \left(\mathbf{x} - \mathbf{x}_b; -2h^2\boldsymbol{\alpha}' \right) \\
&= \left(\frac{\boldsymbol{\alpha}}{|\mathbf{x}-\mathbf{x}_b|} + \frac{(\mathbf{x}-\mathbf{x}_b)((\mathbf{x}-\mathbf{x}_b)\cdot\boldsymbol{\alpha})}{|\mathbf{x}-\mathbf{x}_b|^3} \right) - \left(\frac{\boldsymbol{\alpha}}{|\mathbf{x}-\mathbf{x}_b'|} + \frac{(\mathbf{x}-\mathbf{x}_b')((\mathbf{x}-\mathbf{x}_b')\cdot\boldsymbol{\alpha})}{|\mathbf{x}-\mathbf{x}_b'|^3} \right) \\
&\quad + 2z_b \left(\frac{-z\boldsymbol{\alpha}'}{|\mathbf{x}-\mathbf{x}_b'|^3} + \frac{(\mathbf{x}-\mathbf{x}_b')\times\mathbf{e}_z\times\boldsymbol{\alpha}'}{|\mathbf{x}-\mathbf{x}_b'|^3} + \frac{3z(\mathbf{x}-\mathbf{x}_b')[\boldsymbol{\alpha}'\cdot(\mathbf{x}-\mathbf{x}_b')]}{|\mathbf{x}-\mathbf{x}_b'|^5} \right).
\end{aligned}
\tag{7.6}
$$

In the above equation, $\mathbf{x}_b$ is the location of the Stokeslet along the center-line of the rod, $\mathbf{x}_b' = (x_b(s), y_b(s), -z_b(s))^T$ is the location of the image system, $\boldsymbol{\alpha}$ is the strength of Stokeslet, and $\boldsymbol{\alpha}' = (\alpha_1, \alpha_2, -\alpha_3)$. This velocity field is in the body frame. Since singularities are located outside the domain of the flow, the velocity field is regular.

From the velocity field (7.6), the induced fluid motion is time independent in the body frame, if the angular velocity $\boldsymbol{\omega} = (0, 0, \omega)$ is a constant vector. If $\boldsymbol{\omega} = (0, 0, \omega(t))$ depends on time, the bent rod sweeps out an "upright" cone but with time-varying angular velocity. Then, the velocity field in the body frame is still time independent in the sense that the time information only applying to the strength with the angular velocity and the transformation matrix. This conclusion is similar to the straight rod spinning an upright cone case. However, the velocity field in the lab frame is fully three-dimensional and time-varying for any cones.

(a) Top view   (b) Side view
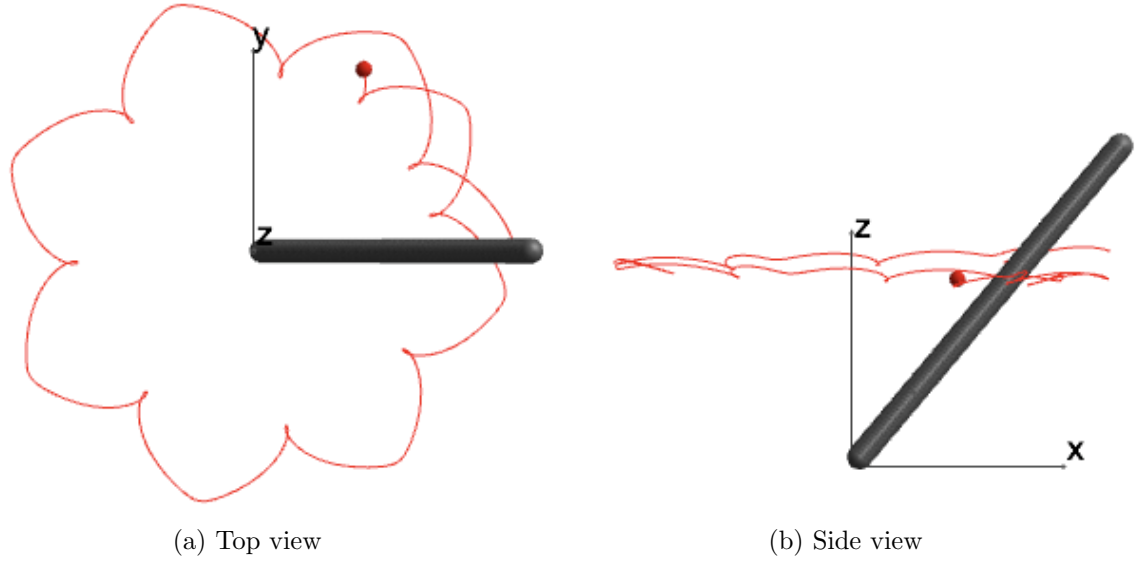
Figure 7.3: A short-time fluid particle trajectory created by a bent rod sweeping out an upright cone above a no-slip plane.

7.2 Fluid particle trajectories

Using the velocity field (7.6), we compute the numerical trajectories with the Runge-Kutta method. We provide theoretical predictions of the fluid particle's behavior as a function of its spatial location, investigate complicated effects of the cilium's geometry on the flow, and compare numerical results with experimental data.

Figure 7.3 shows one fluid particle trajectory when a uniformly bent rod sweeps out an upright cone. The initial position of the fluid particle is $(0.6, 0, 0.5)$. The bent rod's length is 1, its radius is 0.038, and the curvature is 0.395604. The scooping angle of the rod is $\beta = 58^o$ and the cone angle is $\kappa = 40^o$. The lengths here are always in units of cm, unless otherwise specified.

If we keep the rod body length, the cross-sectional radius of the rod, the cone angle, the initial position of the particle the same for both a straight rod case and a bent rod case, Figure 7.4 shows the fluid particle trajectories with the bent rod (in red) and with the straight rod (in blue). If the cylindrical rod is straight, the fluid particle is

(a) Top view   (b) Side view
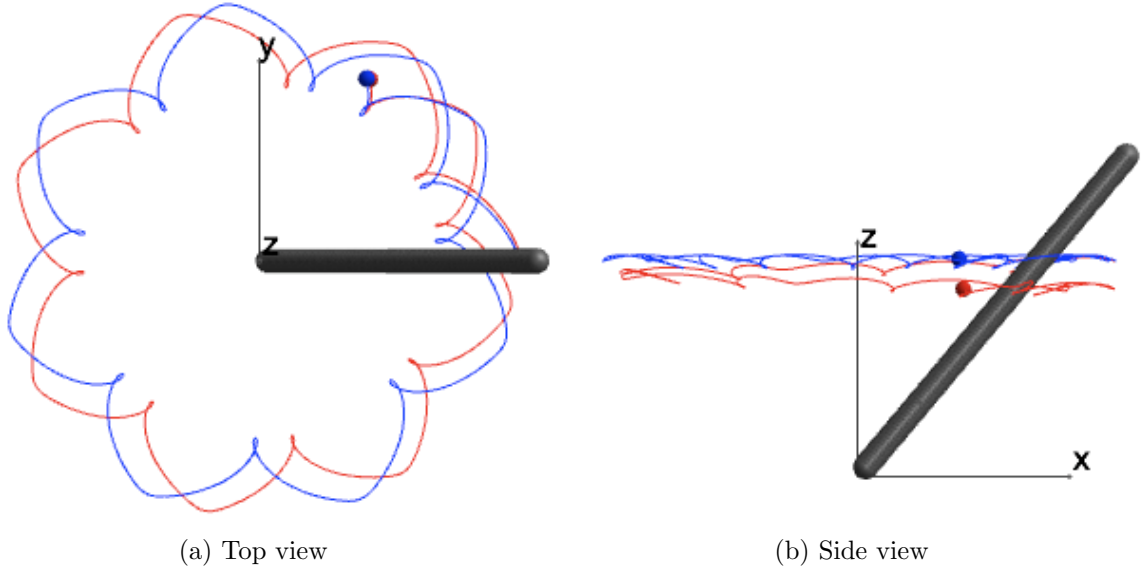
Figure 7.4: Trajectory generated by spinning a bent rod vs a straight rod. The initial position of the fluid particle, the body length, the cross-sectional radius of the rod, the cone angle are the same values for both case. The blue trajectory is corresponding to the straight rod, and the red one is to the bent rod.

observed to follow a fast epicyclic motion with a period roughly commensurate with one rod rotation. Over a longer time scale, it follows a slow orbit around the cone at a fixed height. These properties have been documented in the fluid particle trajectory section in Chapter 6.

From the comparison in the side view in Figure 7.4b, a vertical motion induced by the bend is clearly illustrated. For the straight rod, except the small fluctuation during each epicycle, the particle moves on a periodic trajectory and stays at a relatively fixed height. When the rod is bent, not only the fast epicycles and the slow orbits in Figure 7.4a occurs, but also toroidal flow structures over much longer times are exhibited in the fluid particle trajectory as shown in Figure 7.5. Figure 7.6 is the cross section of this trajectory in the x-z plane.

To visualize the toroidal structure of the fluid particle trajectory, we use Poincaré maps of the fluid particle trajectories in the body frame. A Poincaré map is the
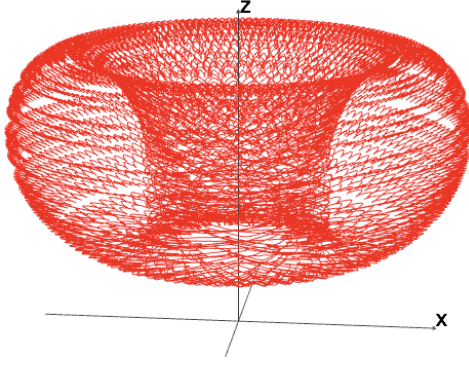
Figure 7.5: A long-time particle trajectory in the lab frame.
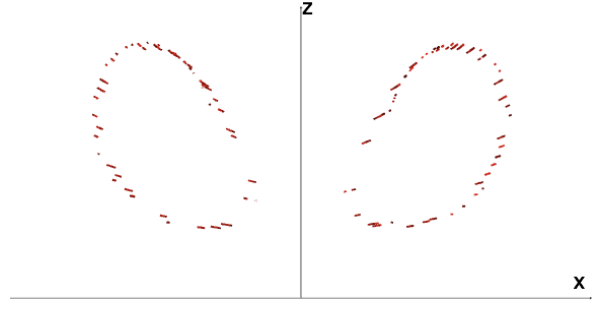
Figure 7.6: The cross section of the trajectory in Figure 7.5 in the x-z plane.

intersection of the trajectory with a fixed plane in the body frame as Figure 7.7. We choose the plane containing the rod's chord and the axis of the cone as the fixed plane. It is orthogonal to the no-slip plane. If the rod is straight, the center-line of the rod is contained in this fixed plane. Otherwise, only two tips of the rod are in this plane. For Poincaré maps included in this chapter, we project the body to this fixed plane for the bent rod. This will show the relative scale of the torus to the body length. Figure 7.8 shows the Poincaré map for hundred fluid particles when a straight rod sweeps out an upright cone. Since the trajectory is a periodic large circle in the body frame, each fluid particle only generates two points on the Poincaré map.

When the rod is bent, the Poincaré map for each fluid particle trajectory describes a torus. Table 7.1 are nine Poincaré maps generated by 100 neutrally buoyant particles initially evenly distributed in the $x > 0$, $y = 0$ plane within the same number of revolutions of the rod. These Poincaré maps show the rich spacial flow structure of the fluid particle trajectories. They are dependent on the scooping angle β and the cone angle κ, and the tori sequencing on the Poincaré map is well ordered. If $\beta = 0$ and π for belly-in and belly-out, the Poincaré maps are scattered dots as Figure 7.8.

In each row of Table 7.1, the cone angle varies. When the cone angle κ increases from left to right, the centers of tori deform apparently. For the smallest cone angle in

142
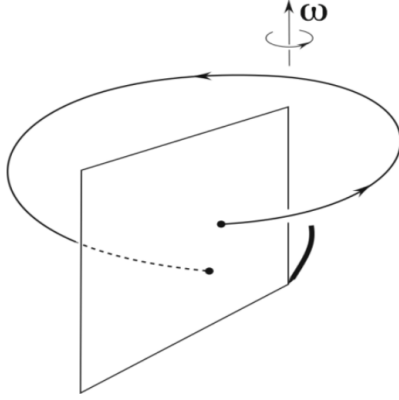
Figure 7.7: Sketch of the Poincaré map in the body frame.
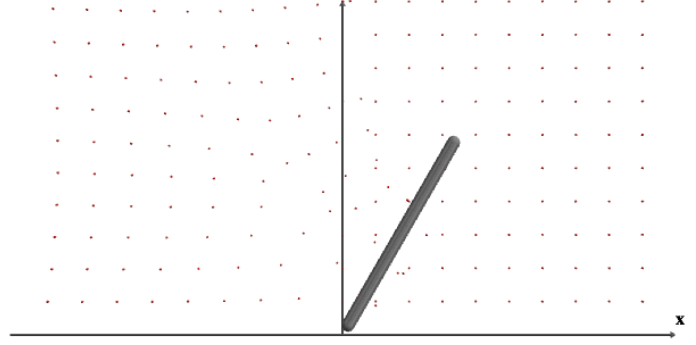
Figure 7.8: Poincaré map of fluid particle trajectories with a straight rod.

this table, the torus centered inside the cone is close to the z-axis. As the cone angle increases, the centers of these tori move away the z-axis. Additionally, the centers of tori, which is outside the cone, are pushed toward the no-slip plane.

In each column, the scooping angle β varies. From these plots, the torus of a fluid particle at the same initial position does not change much as the scooping angle decreases from $\beta = 90^0$ (complete scooping) to $\beta = 5^0$(close to belly out). However, the time for the same particle to create a full torus grows when the scooping angle β decreases. In another word, the time for a fluid particle at a given initial position to complete a torus is highly dependent on the scooping angle if the cone angle is fixed. When the scooping angle β varies from belly out to complete scooping, more of the torus is completed during the same mount of time. Figure 7.9 shows the result about time to complete a torus with fixed initial positions, fixed cone angle κ and fixed angular velocity but varying scooping angle β. The time is presented by the number of rod's revolutions N. The plot on the right side in Figure 7.9 is the loglog plot of the left one to show the growth rate.

As the torus sequencing is well ordered, its orientation depends on the scooping
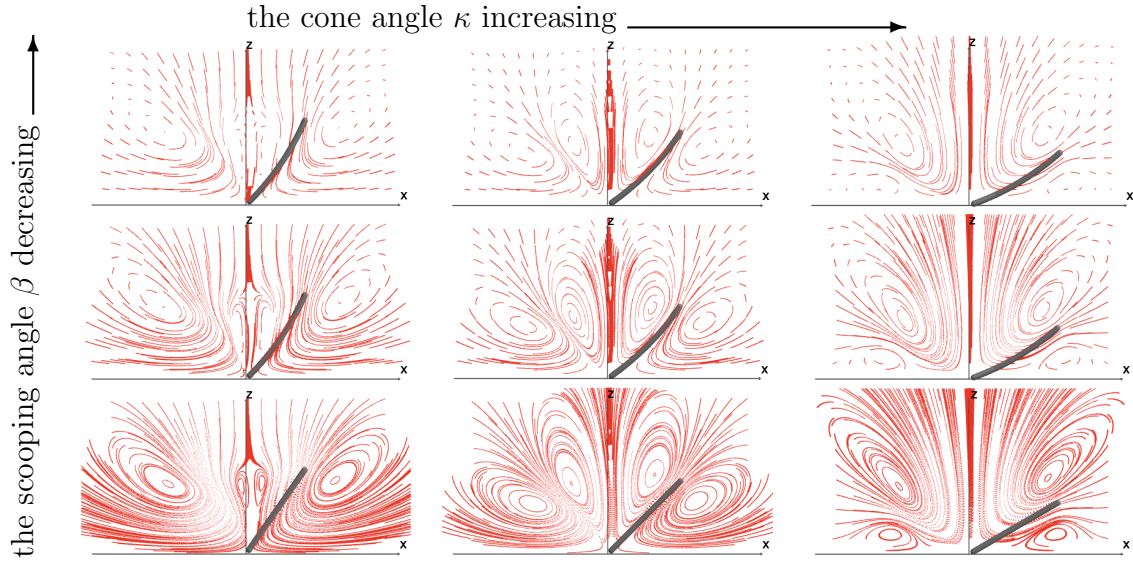
Table 7.1: Poincaré maps in the body frame as varying the scooping angle β and the cone angle κ.

angle and the direction of the rod's angular velocity. If a rod is scooping and rotating counter-clockwise from the top view in the lab frame, the tori on the Poincaré map in the body frame are counter-clockwise in the right half space. With the symmetry properties, they are clockwise in the left half space. On the other hand, if the rod is anti-scooping and rotating counter-clockwise, the sequence of points on tori on the Poincaré map will be reversed. With the reversibility of the flow, the direction of tori with a clockwise rotating rod can be attained.

7.3   Time reversibility

The flow is in the Stokes regime and has no time dependence other than through time-dependent boundary conditions. The time-reversibility is conserved. If the particle is neutrally buoyant, keeping the scooping angle fixed and reversing the direction of the rotation is equivalent to reversing time on the trajectory. The particle will move backward along the time-forward path.
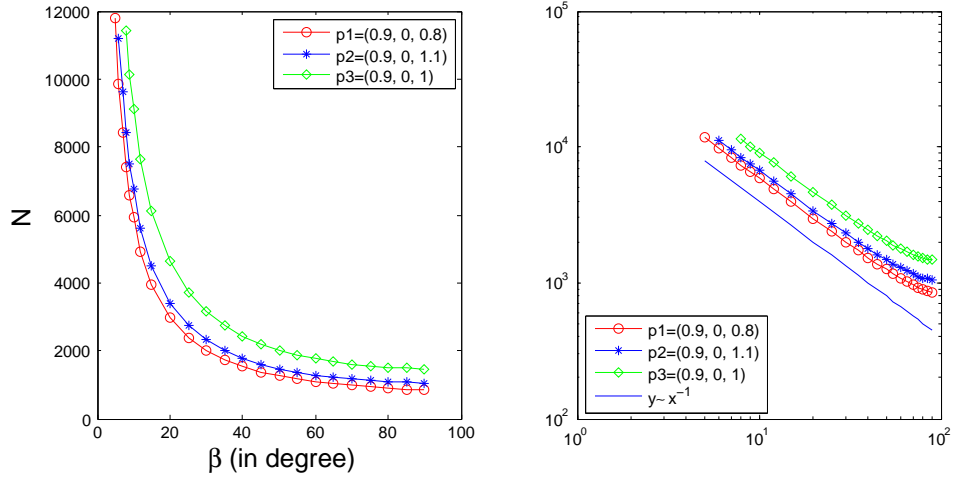
Figure 7.9: Time (in the number of rod's revolutions N) to complete a torus for a fluid particle at three different positions pi $(i = 1, 2, 3)$ with different scooping angle β. The right plot is the loglog plot to show the decay rate.

Since the induced flow is nonlinear, the torus exists even if the particle is buoyant. The reversibility, however, is no longer conserved for buoyant particles. If the buoyant force raises the particle, the center of the torus will shift downward. Otherwise the center moves upward, compared to the center of the torus of a neutrally buoyant particle. With neutrally buoyant particles, Poincaré maps with different scooping angles are similar in the sense that the difference is in small scale as shown in each column of Table 7.1. When the time reversibility is broken by the buoyancy effect, buoyancy introduces a new phenomenon to the Poincaré maps when changing the scooping angle. If adding a The non-negligible, constant buoyant velocity into the system, Poincaré maps are noticeably changed with different scooping angles.

Such conclusions can be drawn from the velocity field for buoyant particles. The governing equation for the Stokes flow is a linear differential equation. When a particle is not neutrally buoyant, the velocity for this tracking particle can be written as $\mathbf{u}' = \mathbf{u} + Q\mathbf{e}_z$, where Q is the velocity due to the buoyant force in the vertical direction $\mathbf{e}_z$. When $\min(w) < Q < \max(w)$, the z component of the location of the zero vertical

velocity in the spatial locations is modified by Q. Then, the height of the torus' center in the flow is changed. Therefore, the center of the torus is shifted. For example, when the rod rotates counter-clockwise and $Q > 0$, the buoyant force raises the particle. The original equilibrium position (x_0, y_0, z_0) is shifted to where the velocity is $w(x_1, y_1, z_1) = -Q$, which is above the original center of the torus from the monotonic properties of the velocity component $w(x, y, z)$. Notice that if the velocity in the vertical direction $w + Q$ does not change sign, then z on the buoyant particle trajectory either increases or decrease over time. In such cases, the buoyant force is so strong that the particle will either rise and escape or descend to the no-slip bottom. These buoyant particles are not able to create any full tori regardless their initial positions in the flow.

Figure 7.10 shows Poincaré maps of the buoyant particles with different Q and two different scooping angles. In each column, the buoyant force gets stronger from the top to the bottom but with the same cone angle and scooping angle. The stronger the buoyant force is, the more to the torus is changed. For a neutrally buoyant particle, the torus will always be closed even though the time to complete the torus grows. For a buoyant particle, the buoyant velocity can be dominant part of the total velocity comparing to the velocity induced by the rod. In such situations, the particle will rise and escape on an open trajectory if it is already far from the cone. In each row, the two Poincaré maps show the difference from complete scooping (on the left) to complete anti-scooping (on the right) with the same buoyant force, which raises the particles. Especially, as we have plotted here, the rod is spinning counter-clockwise and anti-scooping, the tori on the Poincaré maps will break earlier than those with the bent rod scooping based on the orientation of the tori.
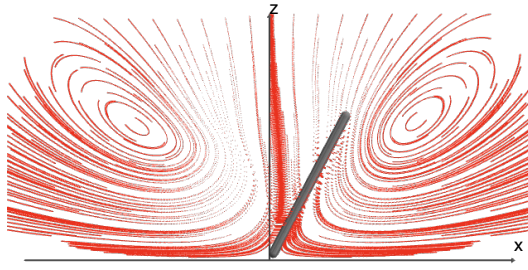
(a) $Q = 0.00001$, $\kappa \approx 27^o$ and $\beta = 90^o$
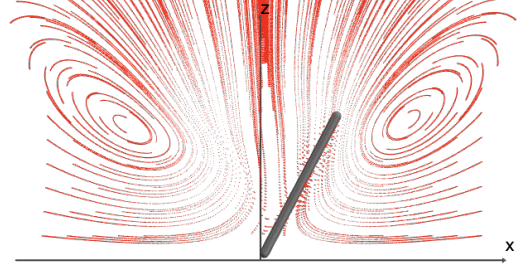
(b) $Q = 0.00001$, $\kappa \approx 27^o$ and $\beta = -90^o$

(c) $Q = 0.001$, $\kappa \approx 27^o$ and $\beta = 90^o$

(d) $Q = 0.001$, $\kappa \approx 27^o$ and $\beta = -90^o$

(e) $Q = 0.01$, $\kappa \approx 27^o$ and $\beta = 90^o$

(f) $Q = 0.01$, $\kappa \approx 27^o$ and $\beta = -90^o$
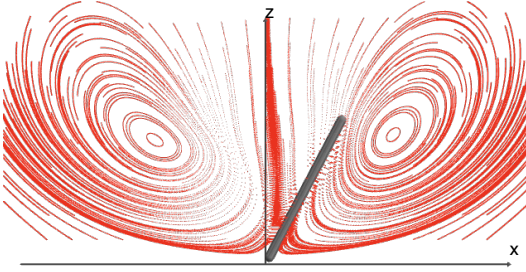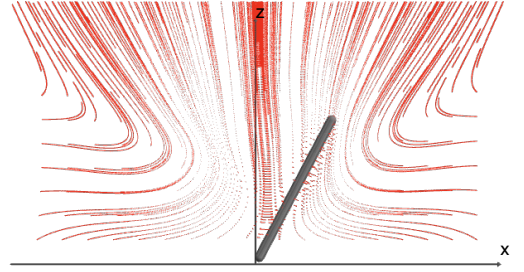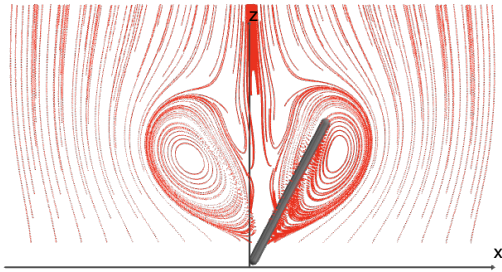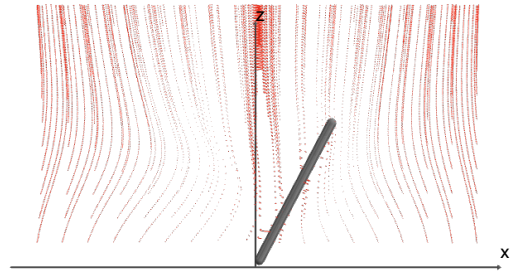
Figure 7.10: Poincaré maps for buoyant particles. Q is the constant vertical velocity due to buoyancy.

7.4 Drag and torque on the bent rod

With the singularities distributed along the centerline of the slender rod, we have obtained the velocity field of the flow generated by the rod. With these information, we further compute the force and torque exerted on the bent slender rod in the body frame, where the bent rod is tilted in the x-z plane with a cone angle κ. The hydrodynamic force applied to the body is important to understand the stability of the motion, and such information can help to design the experimental instruments.

The hydrodynamic force exerted on the slender body from the fluid is given by

$$\mathbf{f}(\mathbf{x}) = -\boldsymbol{\sigma} \cdot \hat{\mathbf{n}} = -\left(\sigma_{1k}\hat{n}_k, \sigma_{2k}\hat{n}_k, \sigma_{3k}\hat{n}_k\right), \qquad (7.7)$$

where $\mathbf{x}$ is any point on the surface of the body, $\hat{\mathbf{n}}$ is the outward normal at $\mathbf{x}$, and

$$\sigma_{\mathrm{ik}} = -p\delta_{\mathrm{ik}} + \mu\left(\frac{\partial u_i}{\partial x_k} + \frac{\partial u_k}{\partial x_i}\right)$$

is the stress tensor associated with a fluid motion with the velocity $\mathbf{u}$. p denotes the pressure field, and δ_{ik} is the Kronecker delta function. With the properties of the delta function, the total hydrodynamic force exerted on the rod is

$$\begin{aligned}
\mathbf{F} &= \int_{S_c} (-\boldsymbol{\sigma} \cdot \hat{\mathbf{n}})\, dS = \int_{\mathrm{v}} \left(\nabla p_{\mathrm{S}} - \mu\nabla^2 \mathbf{u}_{\mathrm{S}}\right) d\mathrm{v} = \int_{\mathrm{v}} \mathbf{f}_{\mathrm{S}} d\mathrm{v} \\
&= 8\pi\mu \int_{\mathrm{v}} \boldsymbol{\alpha}(s)\delta(\mathbf{x} - \mathbf{x}_s) d\mathrm{v} = 8\pi\mu \int_0^\ell \boldsymbol{\alpha}(s) ds.
\end{aligned}$$

Since the strength of the singularity is known, each component of the drag on the body

is

$$F_1 = 8\pi\mu \int_0^\ell \alpha_1 \, ds$$

$$= -\frac{\pi\mu a\epsilon\omega}{4}\left\{-2\ell\cos(\frac{\ell}{2a})(7+\cos(2\kappa))\sin(\beta)+2a\sin(\frac{3\ell}{2a})\sin(\beta)\sin^2(\kappa)+\right.$$

$$\left.\sin(\frac{\ell}{2a})\left[a(25+7\cos(2\kappa))\sin(\beta)+\left(-\ell+a\sin(\frac{\ell}{a})\right)\sin(2\beta)\sin(2\kappa)\right]\right\},$$

$$F_2 = 8\pi\mu \int_0^\ell \alpha_2 \, ds$$

$$= -\frac{\pi\mu}{2}a\epsilon\omega\left\{8\ell\cos^2(\beta)\sin(\frac{\ell}{2a})\sin(\kappa)-16a\cos(\beta)\cos(\kappa)\sin(\frac{\ell}{2a})\right.$$

$$+\left(6\ell\sin(\frac{\ell}{2a})-a\cos(\frac{3\ell}{2a})\right)\sin^2(\beta)\sin(\kappa)$$

$$\left.+\cos(\frac{\ell}{2a})\left(8\ell\cos(\beta)\cos(\kappa)+a\sin^2(\beta)\sin(\kappa)\right)\right\},$$

$$F_3 = 8\pi\mu \int_0^\ell \alpha_3 \, ds$$

$$= \frac{\pi\mu}{2}a\epsilon\omega\sin(\beta)\sin(\kappa)\left\{-\cos(\kappa)\left[2\ell\cos(\frac{\ell}{2a})+a\left(\sin(\frac{3\ell}{2a})-7\sin(\frac{\ell}{2a})\right)\right]-\right.$$

$$\left.2\cos(\beta)\sin(\frac{\ell}{2a})\left(\ell-a\sin(\frac{\ell}{a})\right)\sin(\kappa)\right\}.$$

The torque on the sender body at the origin equals $\int_S \mathbf{x}\times\mathbf{f}\,ds$, where $\mathbf{x}$ is any point on the body and $\mathbf{f}$ is the hydrodynamic force exerted on the slender bent rod. Given the flow field, the hydrodynamic force is $\mathbf{f} = -\boldsymbol{\sigma}\cdot\hat{\mathbf{n}}$ in (7.7). The pressure field and the velocity field for a Stokeslet at $\mathbf{y}$ with the strength $\boldsymbol{\alpha}$ is

$$p_S(\mathbf{x},\mathbf{y};\boldsymbol{\alpha}) = 2\mu\frac{\boldsymbol{\alpha}\cdot(\mathbf{x}-\mathbf{y})}{|\mathbf{x}-\mathbf{y})|^3},$$

$$\mathbf{u}_S(\mathbf{x},\mathbf{y};\boldsymbol{\alpha}) = \frac{\boldsymbol{\alpha}}{|\mathbf{x}-\mathbf{y})|}+\frac{(\boldsymbol{\alpha}\cdot(\mathbf{x}-\mathbf{y})))(\mathbf{x}-\mathbf{y}))}{|\mathbf{x}-\mathbf{y})|^3}.$$

With the divergence theorem, it is found that

$$T(0)_i \;=\; -\int_\nu \epsilon^{\text{ijk}} x_j \frac{\partial \sigma_{\text{km}}}{\partial x_m}\, dv.$$

So,

$$T(0)_1 \;=\; -\int_\nu \left(\epsilon^{12k} x_2 \frac{\partial \sigma_{\text{km}}}{\partial x_m} + \epsilon^{13k} x_3 \frac{\partial \sigma_{\text{km}}}{\partial x_m} \right) dv = -\int_\nu \left(x_2 (\text{Div}(\sigma))_3 - x_3 (\text{Div}(\sigma))_2 \right) dv,$$

$$T(0)_2 \;=\; -\int_\nu \left(x_3 (\text{Div}(\sigma))_1 - x_1 (\text{Div}(\sigma))_3 \right) dv,$$

$$T(0)_3 \;=\; -\int_\nu \left(x_1 (\text{Div}(\sigma))_2 - x_2 (\text{Div}(\sigma))_1 \right) dv.$$

Utilizing the divergence of the stress tensor to determine the total force on a slender bent rod, we find that $\text{Div}(\boldsymbol{\sigma}) = -8\pi\mu\boldsymbol{\alpha}\delta(\mathbf{x} - \mathbf{y})$. Then, the torque on the rod is

$$T(0)_1 = \int_\nu \left(x_2 8\pi\mu\alpha_3\delta(x - y) - x_3 8\pi\mu\alpha_2\delta(x - y) \right) dv$$

$$= 8\pi\mu \int_0^\ell \left(x_2(s)\alpha_3(s) - x_3(s)\alpha_2(s) \right)\, ds,$$

$$T(0)_2 = \int_\nu \left(x_3 8\pi\mu\alpha_1\delta(x - y) - x_1 8\pi\mu\alpha_3\delta(x - y) \right) dv$$

$$= 8\pi\mu \int_0^\ell \left(x_3(s)\alpha_1(s) - x_1(s)\alpha_3(s) \right)\, ds,$$

$$T(0)_3 = \int_\nu \left(x_1 8\pi\mu\alpha_2\delta(x - y) - x_2 8\pi\mu\alpha_1\delta(x - y) \right) dv$$

$$= 8\pi\mu \int_0^\ell \left(x_1(s)\alpha_2(s) - x_2(s)\alpha_1(s) \right)\, ds.$$

Consequently,

$$
\begin{aligned}
T(0)_1 &= 8\pi\mu \int_0^\ell \left\{ \left[-2a\sin(\frac{\ell-s}{2a})\sin(\frac{s}{2a})\sin(\beta) \right] \left[\frac{1}{2}a\epsilon\omega\sin^2(\frac{s}{2a})\sin(\beta) \right.\right. \\
&\qquad \left. \sin(\kappa)\left(\cos(\frac{\ell-2s}{2a})\cos(\kappa) + \cos(\beta)\sin(\frac{\ell-2s}{2a})\sin(\kappa) \right) \right] - \\
&\qquad \left[2a\cos(\frac{\ell-s}{2a})\cos(\kappa)\sin(\frac{s}{2a}) + 2a\cos(\beta)\sin(\frac{\ell-s}{2a})\sin(\frac{s}{2a})\sin(\kappa) \right] \\
&\qquad \left[-\frac{a\epsilon\omega}{4}\sin(\frac{s}{2a})\left(4\cos(\frac{\ell-s}{2a})\cos^2(\beta)\sin(\kappa) - 4\sin(\frac{\ell-s}{2a})\cos(\beta)\cos(\kappa) \right.\right. \\
&\qquad \left.\left.\left. + \left(\cos(\frac{\ell-3s}{2a}) + 3\cos(\frac{\ell-s}{2a}) \right)\sin^2(\beta)\sin(\kappa) \right) \right] \right\} ds \\
&= \frac{a^2\pi\epsilon\mu\,\omega}{4}\left[-16a\cos(\beta)\cos(2\kappa) + 8\ell\cos(\beta)\cos(2\kappa)\sin(\frac{\ell}{a}) + \right. \\
&\qquad \left(2a(3+\cos(2\beta))\sin(\frac{\ell}{a}) + (2\ell - a\sin(\frac{2\ell}{a}))\sin^2(\beta) \right)\sin(2\kappa) + \\
&\qquad \left. 2\cos(\frac{\ell}{a})\left(8a\cos(\beta)\cos(2\kappa) - \ell(3+\cos(2\beta))\sin(2\kappa) \right) \right],
\end{aligned}
$$

$$
\begin{aligned}
T(0)_2 &= 8\pi\mu \int_0^\ell \left\{ \left[2a\cos(\frac{\ell-s}{2a})\cos(\kappa)\sin(\frac{s}{2a}) + 2a\cos(\beta)\sin(\frac{\ell-s}{2a})\sin(\frac{s}{2a})\sin(\kappa) \right] \right. \\
&\qquad \left[-\frac{1}{4}a\epsilon\omega\sin(\frac{s}{2a})\sin(\beta)\left(4\cos^2(\kappa)\sin(\frac{\ell-s}{2a}) + 2\cos(\beta)\cos(\kappa) \right.\right. \\
&\qquad \left.\left. \sin(\frac{\ell-2s}{2a})\sin(\frac{s}{2a})\sin(\kappa) + \left(\sin(\frac{\ell-3s}{2a}) + 3\sin(\frac{\ell-s}{2a}) \right)\sin^2(\kappa) \right) \right] - \\
&\qquad \left[2a\cos(\frac{\ell-s}{2a})\sin(\frac{s}{2a})\sin(\kappa) - 2a\cos(\beta)\cos(\kappa)\sin(\frac{\ell-s}{2a})\sin(\frac{s}{2a}) \right] \\
&\qquad \frac{a\epsilon\omega}{2}\sin^2(\frac{s}{2a})\sin(\beta)\sin(\kappa) \\
&\qquad \left.\left(\cos(\frac{\ell-2s}{2a})\cos(\kappa) + \sin(\frac{\ell-2s}{2a})\cos(\beta)\sin(\kappa) \right) \right\} ds \\
&= \frac{1}{2}a^2\pi\epsilon\mu\omega\sin(\beta)\left[4\cos(\kappa)\left(-2a + 2a\cos(\frac{\ell}{a}) + \ell\sin(\frac{\ell}{a}) \right) + \right. \\
&\qquad \left. \cos(\beta)\left(-2\ell - 4\ell\cos(\frac{\ell}{a}) + 4a\sin(\frac{\ell}{a}) + a\sin(\frac{2\ell}{a}) \right)\sin(\kappa) \right],
\end{aligned}
$$

and

$$
\begin{aligned}
T(0)_3 &= 8\pi\mu \int_0^\ell \left\{ \sin(\frac{s}{2a}) \left[-2a\cos(\beta)\cos(\kappa)\sin(\frac{\ell-s}{2a}) + 2a\cos(\frac{\ell-s}{2a})\sin(\kappa) \right] \right. \\
&\quad \left[-\frac{1}{4}a\epsilon\omega\sin(\frac{s}{2a}) \left(-4\cos(\beta)\cos(\kappa)\sin(\frac{\ell-s}{2a}) + 4\cos(\frac{\ell-s}{2a})\cos^2(\beta) \right. \right. \\
&\quad \left. \left. \sin(\kappa) + \left(\cos(\frac{\ell-3s}{2a}) + 3\cos(\frac{\ell-s}{2a}) \right) \sin^2(\beta)\sin(\kappa) \right) \right] - \\
&\quad 2a\sin(\frac{\ell-s}{2a})\sin(\frac{s}{2a})\sin(\beta)\frac{a\epsilon\omega}{4}\sin(\frac{s}{2a})\sin(\beta) \left[4\cos^2(\kappa)\sin(\frac{\ell-s}{2a}) + \right. \\
&\quad \cos(\beta)\sin(\frac{\ell-2s}{2a})\sin(\frac{s}{2a})\sin(2\kappa) \\
&\quad \left. \left. + \left(\sin(\frac{\ell-3s}{2a}) + 3\sin(\frac{\ell-s}{2a}) \right) \sin^2(\kappa) \right] \right\} ds \\
&= \frac{1}{16}a^2\pi\epsilon\mu\omega \left\{ -68\ell - 8\ell\cos(\frac{\ell}{a}) + 8\ell\cos(\frac{\ell}{a})\cos(2\beta) + 4\ell\cos(2\beta) + \right. \\
&\quad 72a\sin(\frac{\ell}{a}) + 2a\sin(\frac{2\ell}{a}) - 4a\sin(\frac{\ell}{a} - 2\beta) - a\sin(\frac{2\ell}{a} - 2\beta) + 2\cos(2\kappa) \\
&\quad \left[-4(3 + \cos(2\beta)) \left(\ell\cos(\frac{\ell}{a}) - a\sin(\frac{\ell}{a}) \right) + 2 \left(2\ell - a\sin(\frac{2\ell}{a}) \right) \sin^2(\beta) \right] - \\
&\quad a\sin(\frac{2\ell}{a} + 2\beta) - 4a\sin(\frac{\ell}{a} + 2\beta) + \\
&\quad \left. 64\cos(\beta)\sin(\frac{\ell}{2a}) \left(-\ell\cos(\frac{\ell}{2a}) + 2a\sin(\frac{\ell}{2a}) \right) \sin(2\kappa) \right\}.
\end{aligned}
$$

Figure 7.11 is a group of plots about the torque at the base of the bent rod (the apex of the cone) with different scooping angle β and cone angle κ. The curvature of the bent rod is 0.4cm^{-1}, the rod's body length is $\ell = 1$, $\omega = \frac{2\pi}{5}$ radian/second, the radius of the cross-section of the bent rod is $r = 0.0375$cm. So, the slenderness $\epsilon = \frac{1}{\log(1/0.03750)} \sim 0.30$. The dynamic viscosity of the fluid is $\mu = 3200cP$. The torque is in the dimensions of force times distance, using the unit dyne centimeter (g· cm$^2/s^2$) in the cgs unit system.

Figure 7.11a shows the three components of the torque at the base of the rod in the body frame as functions of the scooping angle β for the cone angle $\kappa = \frac{\pi}{6}$. Similarly,

152

(a) $\kappa = \frac{\pi}{6}$

(b) $\kappa = \frac{\pi}{4}$

(c) Belly out $\beta = 0$

(d) Scoop $\beta = \frac{\pi}{2}$
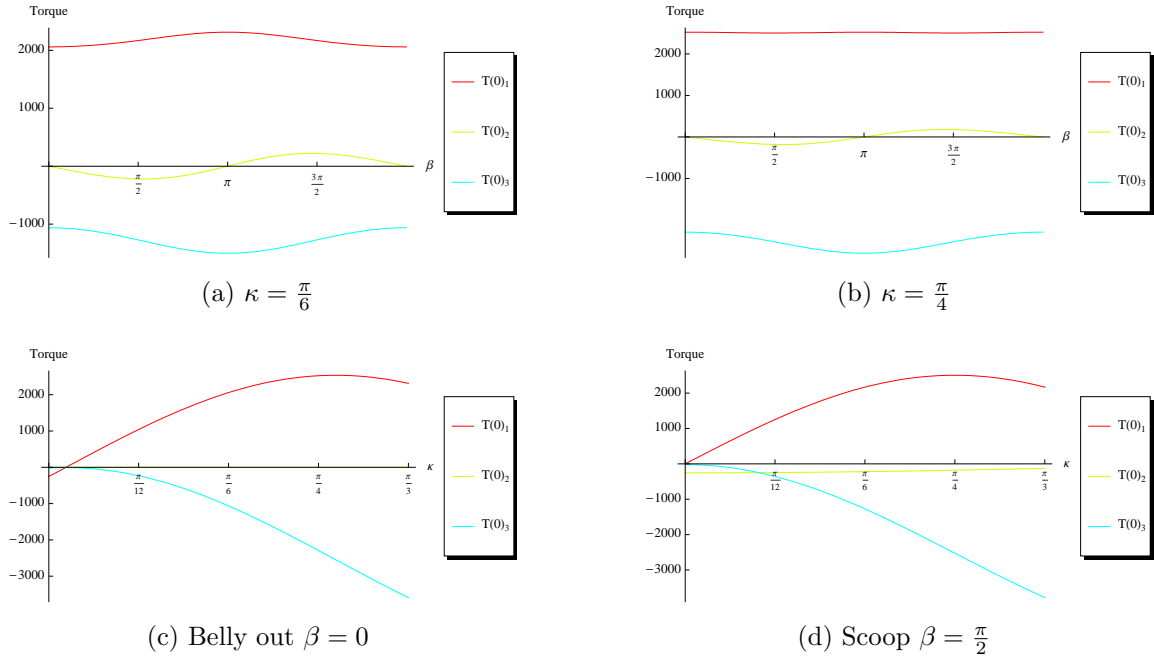
Figure 7.11: The torque at the origin as functions of the scooping angle β or the cone angle κ.

(a) $T(0)_1$

(b) $T(0)_2$

(c) $T(0)_3$
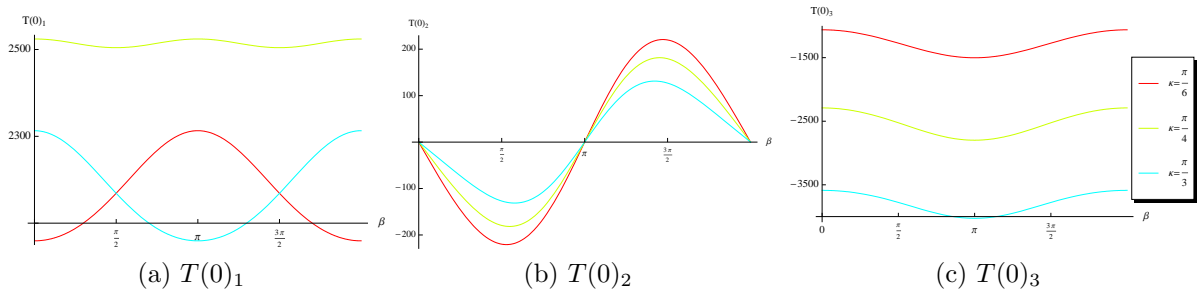
Figure 7.12: Comparisons of each component of the torque with different values of the cone angle κ.

153

Figure 7.11b shows the components with $\kappa = \frac{\pi}{4}$. When the rod is belly in or belly out, these figures show the second component (in the y-direction) vanishes. Figure 7.11c and 7.11d show the three components of the torque at the base of the rod as functions of the cone angle κ for two different scooping angle $\beta = 0$ and $\beta = \frac{\pi}{2}$, respectively. These two figures show the variation of torque with respect to the cone angle κ. Figure 7.12 shows the comparisons of individual components of the torque at the base of the rod as functions of the scooping angle κ for three different values of the cone angle $\kappa = \frac{\pi}{6}$, $\frac{\pi}{4}$ and $\frac{\pi}{3}$.

7.5 Experimental study

To study the flow, we build a mathematical model with the slender body theory and provide theoretical predictions. Besides numerical simulation, we have conducted experimental studies for both the straight rod and the bent rod cases to examine the flows. In this section, we provide the experimental data for the bent rod sweeping out a cone above a no-slip plane, and compare them with our model's predictions. The experimental verification has two purposes: first, the experimental data help to verify our model and demonstrate the order of our asymptotic results; second, based on our theoretical model we explore the flow experimentally.

7.5.1 Toroidal structure

When a fluid particle moves in the flow generated by a bent rod sweeping out a cone, but not belly in or belly out, a toroidal structure appears in the particle trajectories. Figure 7.13 shows the toroidal structure captured in Karo corn syrup with injected red food dye. The torus on the lower left corner is a fluid particle trajectory from the model. Both the experiment and the model capture the closed torus near the bent rod.
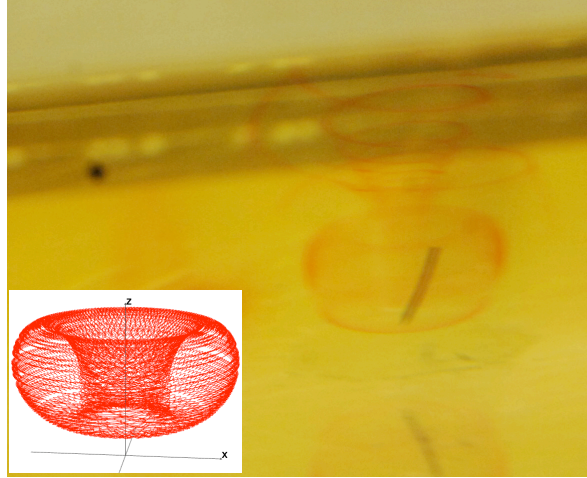
Figure 7.13: A torus captured with red dye and a torus created with the model in the lab frame.

Besides this qualitative comparison, we pursue a quantitative comparison between the model and the experimental data.

The flow not only has a rich parameter space but also shows complicated spatial structure. Therefore, the trajectory is very sensitive to the location of the fluid particle. The initial 2D experiments we carried out are helpful to capture the properties of the fluid. However, it is very difficult to obtain a fair comparison based on approximated initial positions. With fully 3D experimental capability, we explore the complex flow structure and quantitatively compare the experimental data with theoretical predictions.

We take videos from two cameras, one of which is in front of the tank (front view) and the other is on the left side of the tank (side view), then track the particle trajectory from these videos. Figure 7.14 shows 2D tracking trajectories in pixel coordinates from both cameras, when the rod is rotating counter-clockwise and scooping. The purpose of the color on the trajectory is to show the overlap structure in 2D. The particle goes downward in the center and come up in the outer layer. Figure 7.15 is 2D tracking trajectory for the same particle and the same setup of the rod, but the rod is rotating clockwise. To the flow, it is equivalent to the rod counter-clockwise rotating and anti-
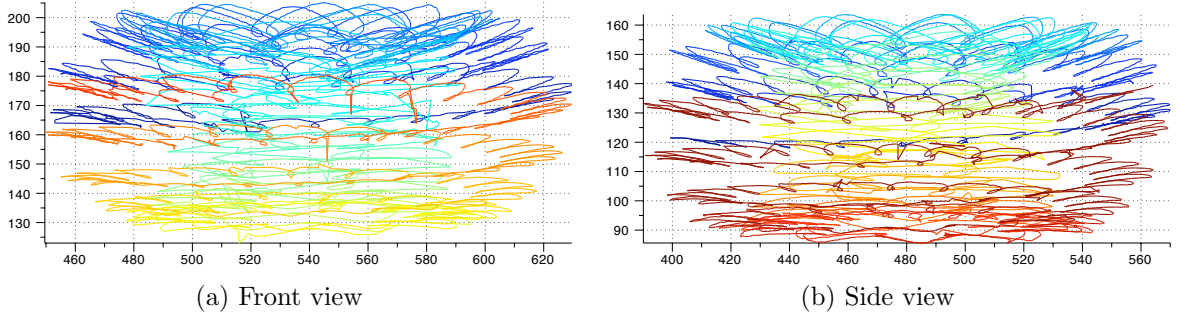
Figure 7.14: An experimental trajectory tracked from two camera-views in pixel coordinates. The rod is scooping and rotating counter-clockwise from the top view.
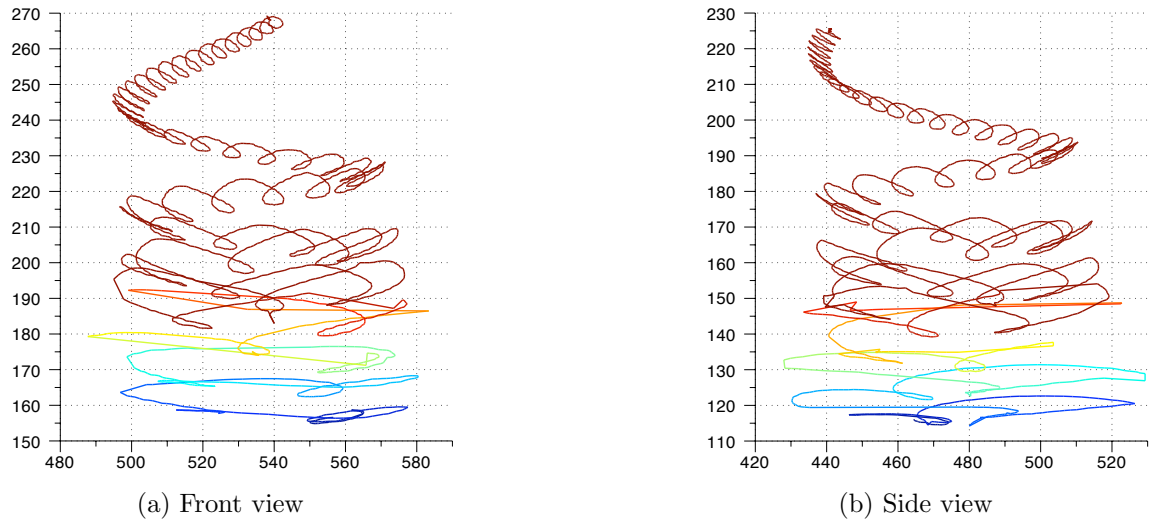
Figure 7.15: Tracked trajectories when the rod is scooping and rotating clockwise from top view (opposite to the motion for Figure 7.14).

scooping. The experimental trajectories verify the prediction of the direction of the torus, even though based on results for a buoyant particle. Here, the particle trajectory starts with blue and progresses to dark red.

7.5.2 Quantitative comparison

Figure 7.16 shows short-time comparison of the particle trajectories with experimental data in red and the theoretical prediction in blue. One position of the rod is plotted to demonstrate the scale. From this plot, the model and experiment have good

(a) Top view   (b) Side view
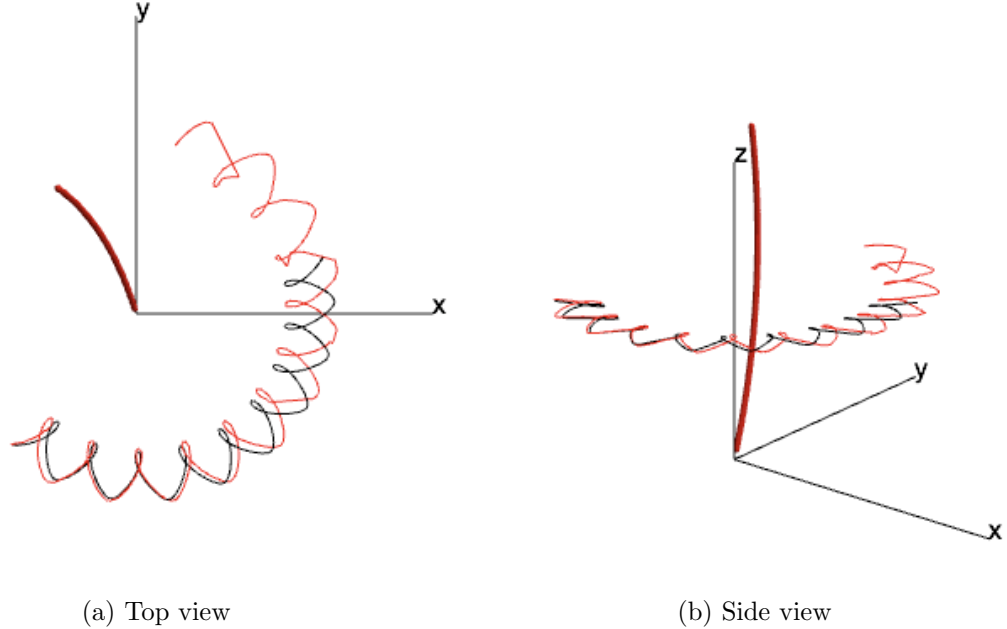
Figure 7.16: Comparison of the experimental trajectory in Karo corn syrup to a numerical one with static parameters in the model. The buoyancy constant $Q = 0.0093$, the scooping angle $\beta = 60^o$ and the cone angle $\kappa = 22^o$. In the model, the length of the rod is 1, the radius of the rod is 0.0367961, and the curvature of the rod is $k = 0.395604$. The time is rescaled with one revolution of the rod.

agreement for short and intermediate time periods. Figure 7.17 shows 2D projections of both the numerical and the experimental trajectories over very long time periods.

To better illustrate the trajectories, we implement Poincaré maps of the trajectories. From the Poincaré map Figure 7.18, we see that there are medium scale fluctuations along the torus in the experimental data (red). With static scooping angle and cone angle, the theoretical prediction is a smooth torus (blue). With dynamic cone angle and static scooping angle 60° , which is the angle used for a static numerical trajectory and close to the average of the scooping angle in the experimental data, the Poincaré map is the fluctuating black trajectory in Figure 7.18.

(a) Top view   (b) 3D view
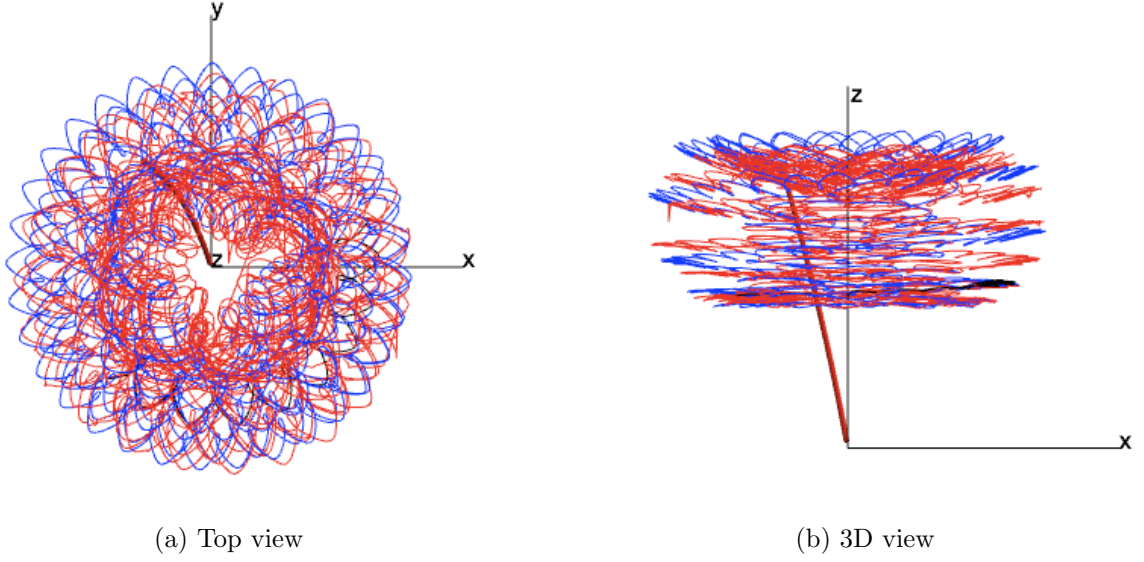
Figure 7.17: Long-time comparison of the experimental trajectory (red) with the numerical trajectory (blue) in Figure 7.16.
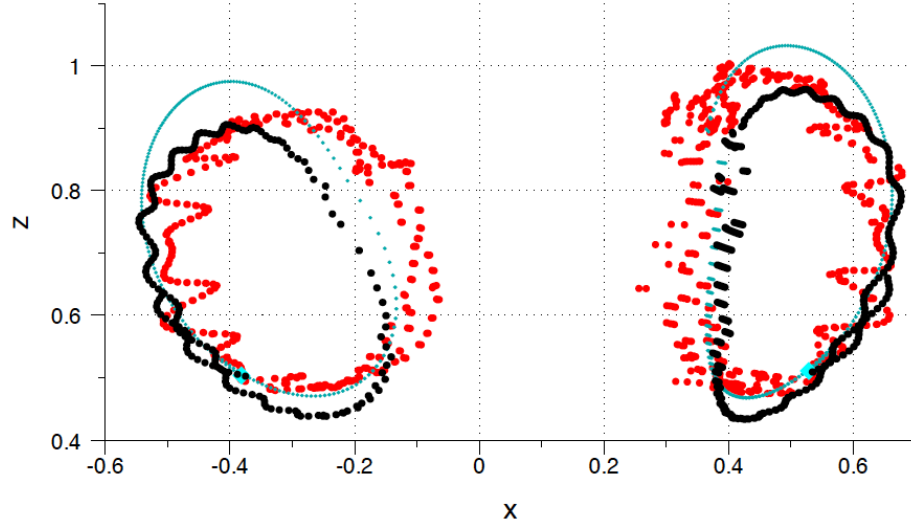
Figure 7.18: Comparison of the Poincaré map of experimental and numerical trajectories. The red dots are generated by the experimental trajectory. For the blue trajectory, the cone angle $\kappa = 23^o$ is static. For the black numerical trajectory, the cone angle $\kappa = 25^o - 2^o \sin(\frac{2\pi t}{75}) + \sin(4\pi t)$ is dynamic. For both numerical trajectories, the buoyant velocity constant $Q = 0.0093$, the scooping angle $\beta = 60^o$, and the number of revolution is $N = 200$. The blue dot indicates the initial position for these trajectories.

(a) Front view   (b) Side view
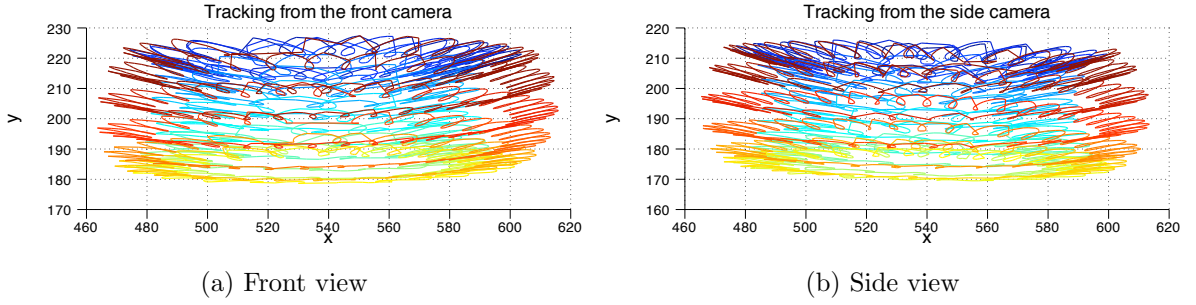
Figure 7.19: Tracked trajectories in the silicone oil when the rod is scooping and rotating clockwise from the top view.
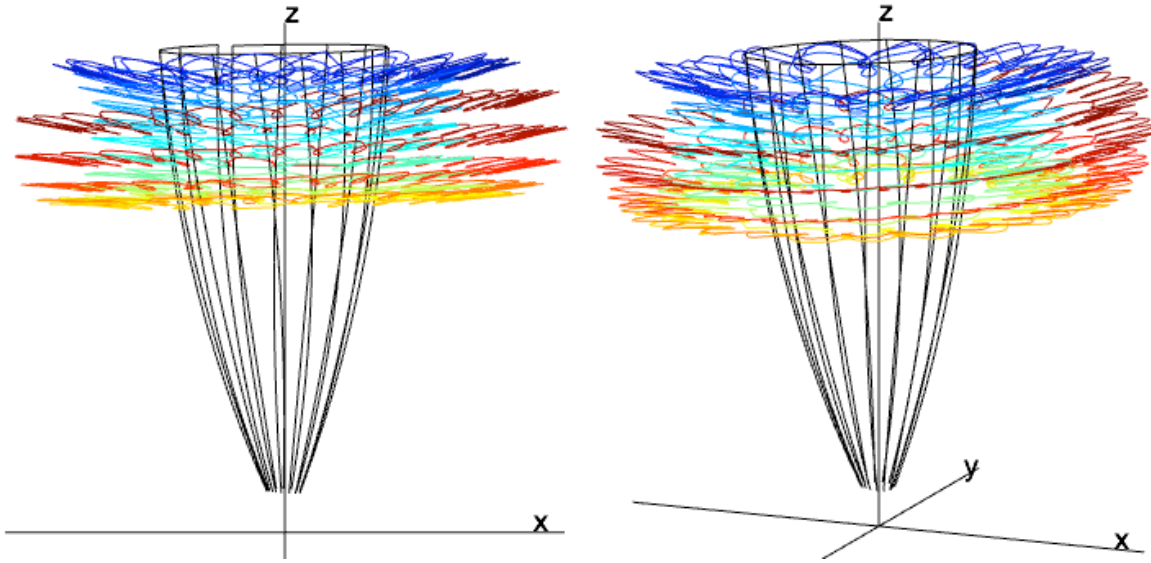
Figure 7.20: 3D tracked trajectory and a few positions of the rod

Inhomogeneity is observed in Karo corn syrup, and it is reduced in silicone oil. Even though there are other effects in silicone oil, we provide experimental data from silicone oil as well. For these experiments in silicone oil, we apply the improved silhouette techniques, extract the dynamic angles, and use them in the model. Figure 7.19 and 7.20 show the tracked 2D trajectory of an air bubble in silicone oil [73] and the reconstructed 3D trajectory. The rod is rotating counter-clockwise and scooping from the top view.

Figure 7.21 shows the angles associated with this experiment [35]. Each dot on the plots presents information from one frame of the video. The magnification window

159
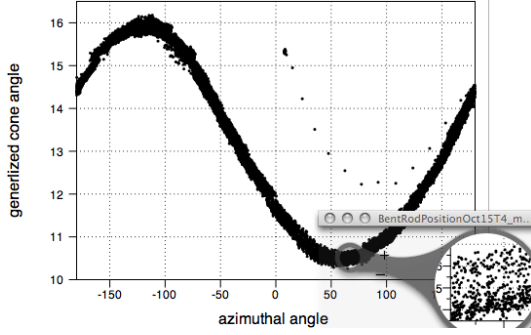
(a) Cone angle VS azimuthal angle
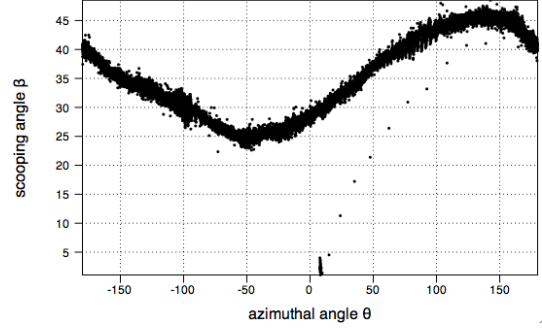
(b) Scooping angle VS azimuthal angle

Figure 7.21: Tracked trajectories in silicone oil when the rod is scooping and rotating clockwise from top view.

shows a small portion of the clouds of dots. There are a few dots scattered above the clouds when the azimuthal angle θ is between 0° and 180°. This is due to the transient when we start the motor. Figure 7.21a shows the generalized cone angle ϕ over time as a function of the corresponding azimuthal angle. Figure 7.21b shows the dynamic scooping angles versus the azimuthal angles. The azimuthal angles and the cone angles specify the rod's positions on the cone, and the scooping angles determine the orientation of the rod at each position. From these two plots, the rod sweeps out a dynamic tilted cone. We use these angles in the model to run the simulation.

For the simulation, we not only consider the tracked dynamic angles in the model but also the buoyancy effect of the air bubble. Figure 7.22 shows two views of the experimental trajectory (red) and the numerical trajectories (gray). One rod position is plotted to show the relative scale. The initial position of the trajectories is $(0.0652893, -0.378317, 0.659856)$. The length of the rod is 1, the cross-sectional radius is $r = 0.3750$, and the curvature is $K = 1/2.419$. So, the slenderness parameter $\epsilon = \frac{1}{log(\ell/r)} \sim 0.30$. Epicycles on the numerical trajectory appear smaller than the experimental epicycles.

160

(a) 3D view   (b) Top view
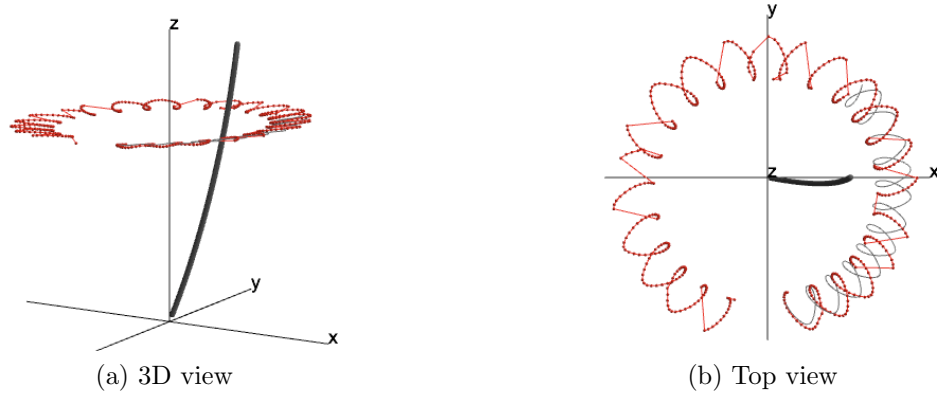
Figure 7.22: Comparison of numerical trajectory (grey) with experimental trajectory (red), which is in the silicone oil when the rod is scooping and rotating clockwise from the top view.

7.5.3 List of issues

From the comparisons between the experimental data and the theoretical prediction, we see that there are agreements between the model and the experiment, but also discrepancies. Qualitatively, the epicycles, the large orbits and the toroidal structure in the experimental trajectories are in agreement with the theoretical prediction. However, there are quantitative discrepancies between the experimental Lagrangian trajectory and the theoretical trajectory, especially over long time scale. We list and discuss the possible issues with the model and the experimental data.

For the model,

1. The velocity field obtained using the slender body is a leading order approximation. We provide the error analysis of the slender body theory for a straight rod sweeping out a double in free space in Appendix B. From those analysis, the discrepancies in the fluid particle trajectory would be expected with the slenderness for our experiments. Also, the slender body theory is invalid within a radius distance from the tips of the slender body. Such close encounter has happened both in the experiment and the model.

161

2. Besides the systematic error due to the leading order approximation of the velocity field, the numerical error for the model is accumulated from the ODE solver. However, this numerical error can be reduced by choosing small time steps. In our numerical trajectories such effects are negligible.

3. The higher order asymptotics are not necessary, if there is no chaos in the fluctuating system. Then the slender body orbit is accurate far from the boundaries. If there is chaos, then both the experiment and the model will observe wildly different phenomena. Estimation for the differences of the orbit in terms of the slenderness ϵ is helpful to understand the discrepancy.

For experiments,

1. From Poincaré maps of the experimental trajectories and videos, we learn that rotation rate of the rod is not constant. The fluctuation in the rotation rate is not a problem because the Reynolds number is still small enough to keep the flow in the Stokes' regime. However, this will effect the azimuthal angles in the model, especially when we feed the tracking data into the model.

2. From the experiment data shown in Figure 7.14-7.18, the base of the rod slides within a small circle of an approximate radius $0.15mm$. Such motion will contribute to an inaccuracy of the cone angle, for which it could be reasonable to add or subtract one degree to the cone angle. Now we take the center of this small circle as the center of the cone. The sliding needs to be considered in the model, which will be including in the future work.

3. Without thermal control of the experiment, the slow convection detected in the tank. Such background flow will influence the particle trajectory, more apparently on the long-time trajectory.

4. Dynamic scooping angle and cone angle are measured in the experiments, which generate zigzagging trajectories.

5. For the experiments, inhomogeneity in fluid, density stratification, oil laying above Karo corn syrup to prevent evaporation complicate the fluid.

6. The solubility rate of air bubbles in silicone oil varies over time. The Faxen correction is very small based on the small radius of the bubbles and the velocity field. However, the buoyant force is also changed. The nonlinearity of the system makes the influence hard to predict over long time scale.

7. Based on the 3D calibration, the error due to the alignment of cameras is minimized, if the vertical of the cameral view is parallel to gravity and perpendicular to the no-slip flat bottom of the tank.

7.5.4   Effect of thermal convection

The discrepancies between the experimental trajectory and the numerical prediction may be explained by taking account of the approximation of the slender body theory, the dynamics of the experiments, the buoyancy effect, and thermal effects in highly viscous fluids. However, the thermal effect is not controlled in our experiment. In this section, we briefly study the thermal effects with a simplified situation.

When the Rayleigh number exceeds some critical value, the background flow is no longer stationary. The convection is a very slow motion. For the experiments, thermal effect convection was indeed detected in our highly viscous fluids. Unfortunately, it is hard to measure globally. Fortunately, our model has the ability to handle any given background flow, even if time dependent. To better understand the thermal effect, we check the flow with a straight rod sweeping out a double cone with a uniform background flow in free space.
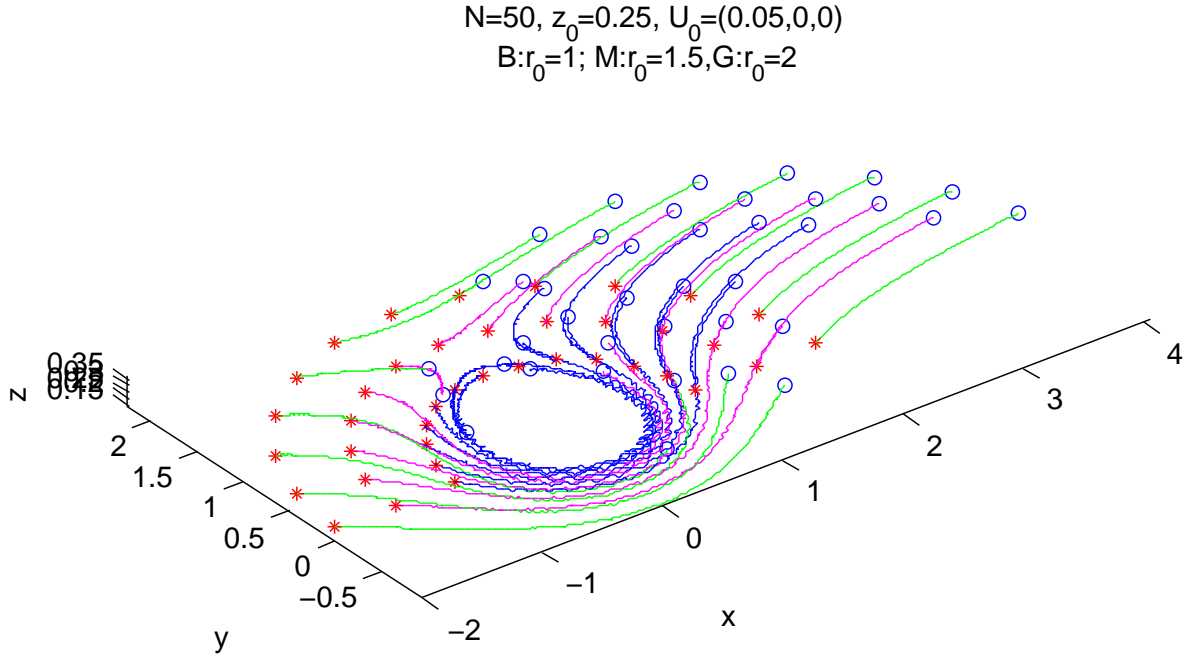
Figure 7.23: Fluid particle trajectories with a straight rod sweeping out a double cone in free space. The number of revolution of the rod is $N = 40$, and the uniform background flow is $(0.05, 0, 0)$. The particles are initialized at red stars with the initial the initial height $z_0 = 0.25$. For blue trajectories, $r_0 = 1$ in the cylindrical coordinates for the initial positions, and $r_0 = 1.5$, $r_0 = 2$ for the magenta and green, respectively.

Figure 7.23 show the fluid particle trajectories when a straight rod sweeps out a double cone in free space. This verifies that if the flow induced by the rod is dominant then there are closed orbits near the cone. While the particle moves away from the rod, the background flow is comparable to the flow induced by the rod, then the particles move along open trajectories. Figure 7.24 shows the effect of the magnitude of the uniform background flow to the fluid particle trajectories.

Go back to Chapter 6, where we compare the experimental trajectory with the model for the straight case. The trajectories in Figure 6.8 are effected by the convection based on the asymmetry of the trajectory in intermediate time.
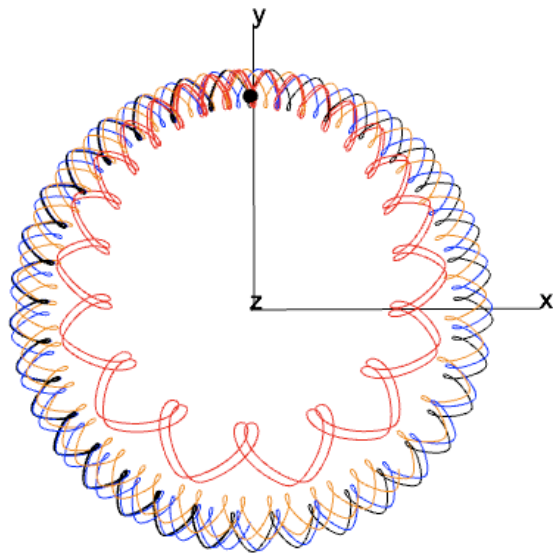
Figure 7.24: Fluid particle trajectories with a straight rod sweeping out a double cone in free space. The fluid is at rest for the black trajectories. The uniform background flow is $(0.0005, 0, 0)$, $(0.005, 0, 0)$, and $(0.05, 0, 0)$ for the blue, yellow, and red trajectory, respectively.

Chapter 8

A swimming related application of the slender body theory in Stokes flows

The slender body theory has been developed for a long time [75, 21, 74, 3, 39]. It provides a good asymptotic solution for flows generated by a slender body, if ignoring the end effect. The end effects can be attained with higher order singularities [38]. In this chapter, we report a swimming-related application of the slender body theory. We study the velocity field, the fluid particle trajectory and the flux introduced by the periodic motion of a slender body. This study may shade light on the efficiency of swimming or propelling in the low-Reynolds-number regime.

8.1 The problem

The cylindrical slender body (red) is attached to a fuselage (gray) by a fine wire and moves along the track (green) on the fuselage as shown in Figure 8.1. In the fuselage's body frame, the cylindrical slender body moves periodically in a plane. Assume in the fuselage's body frame the surrounding fluid is stationary, the configuration of the
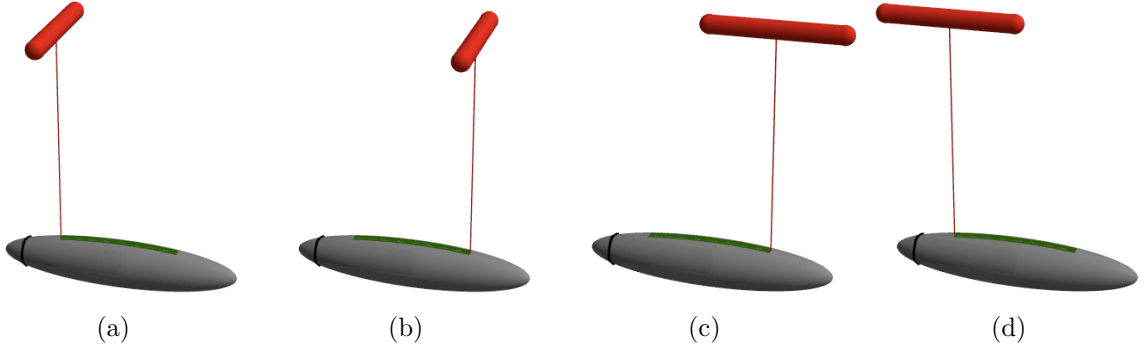
Figure 8.1: Swimmer.

periodic motion of the rigid slender body is show in Figure 8.2. We examine on the flow induced by the slender body in this chapter. Study of the effect of the fuselage and the whole system will be pursued in the future work.

The body moves periodically from step (a) to step (e), divided into 4 phases considering its motion and direction. After one revolution, the body returns to its original position in the fuselage frame. If the fuselage is fixed and the surrounding fluid is at rest, the background flow in the fuselage frame is stationary. If the fuselage is free in a stationary fluid, the background flow in the fuselage frame depends on the motion of the system. We focus on the case when the background flow in the fuselage frame is at rest, and refer the fuselage frame as the lab frame in the rest of this chapter. Since the flow is in the Stokes regime, inertia effect is negligible and transient is neglect. We focus on the steady Stokes flow for each phase. Generally, two types of motion are considered, uniform translation and pure rotation.

The half length of the cylindrical slender body ℓ is much large compared with its cross-sectional radius r ($r \ll \ell$). We study the flow induced by the slender body when it moves periodically in the laboratory frame, which is selected that the slender body is always in the x-y plane. Beside the laboratory frame (the fuselage frame), another important reference frame used here is the body frame, which is a moving frame. The
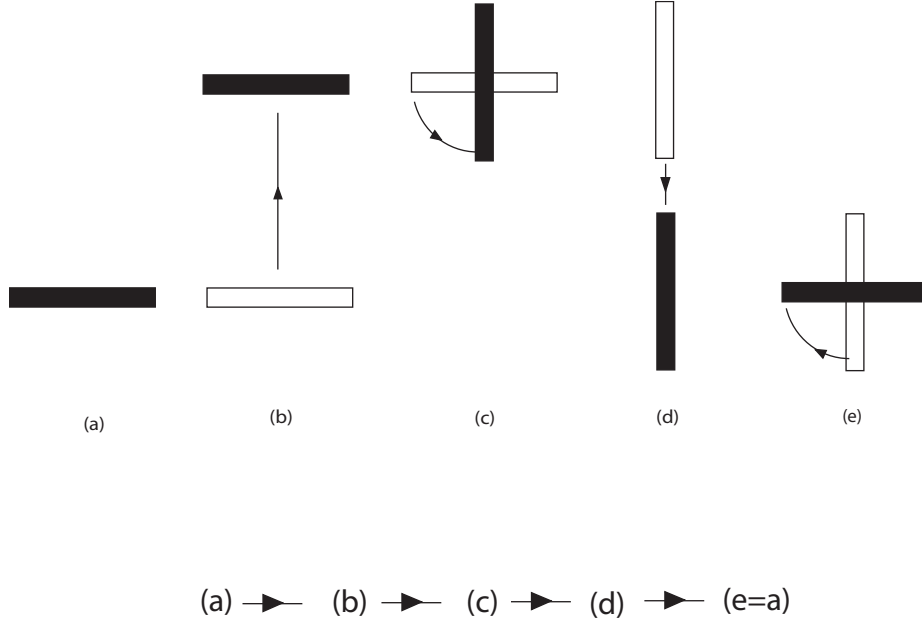
Figure 8.2: Configuration of the periodic motion of the slender body in the x-y plane.

velocity field is presented with explicit formulae using the slender body theory.

8.2   The velocity field for each step

In this section, we provide the velocity field of the flow induced by the cylindrical slender body in each step of the periodic motion. Phase 1 is the first step from (a) to (b) in Figure 8.2, Phase 2 is from (b) to (c), etc. During phase 1 and phase 3, the slender body moves uniformly. During phase 2 and phase 4, the body purely rotates either clockwise or counter-clockwise in the fluid. We first consider the flow induced by the cylindrical slender body when it moves with uniform velocity in phase 1 and phase 3, then switch to the rotating flow in phase 2 and phase 4.

8.2.1 Phase 1: from step (a) to step (b)

In phase 1, the slender body moves perpendicular to its axis in the x-y plane. The midpoint is shifted from $(0,0,0)$ to $(0, U\,T_1, 0)$, where T_1 is the time period, and U the uniform velocity in the y-direction. In the body frame, the background flow is a uniform flow $\mathbf{U} = (U_1, U_2, U_3) = (0, -U, 0)$. By distributing Stokeslet along the center-line of the body, the velocity of the flow is constructed with the slender body theory [3]. Based on the ratio of the velocity to the strength, the strength of Stokeslet is

$$
\begin{cases}
\alpha_1 = \frac{\varepsilon U_1}{4} = 0; \\[2mm]
\alpha_2 = \frac{\varepsilon U_2}{2} = \frac{\varepsilon U}{2}; \\[2mm]
\alpha_3 = \frac{\varepsilon U_3}{2} = 0.
\end{cases}
$$

So, the velocity field in the body frame is

$$
\mathbf{u}(\mathbf{x}) \;=\; \mathbf{U} + \int_{-\ell}^{\ell} \mathbf{u}_{\mathrm{S}}(\mathbf{x} - \mathbf{x}_s; \boldsymbol{\alpha})ds, \tag{8.1}
$$

where $\mathbf{u}_{\mathrm{S}}$ is the Stokeslet (see appendix A), $\mathbf{x}_s = (x_s, y_s, z_s) = (s, 0, 0)$ is the center-line of the slender body, $\mathbf{x} = (x, y, z)$, and $\boldsymbol{\alpha} = (\alpha_1, \alpha_2, \alpha_3)$.

After substituting the strength of the Stokeslet into (8.1) and computing the integrals explicitly, the velocity field in the body frame is

$$
\begin{aligned}
u_1(\mathbf{x}) \;&=\; \int_{-\ell}^{\ell} \left\{ \frac{\alpha_1}{\left[(x-s)^2 + r^2\right]^{1/2}} + \frac{(x-s)\left[(x-s)\,\alpha_1 + y\alpha_2 + z\alpha_3\right]}{\left[(x-s)^2 + r^2\right]^{\frac{3}{2}}} \right\} ds \\[2mm]
&=\; \int_{-\ell}^{\ell} \frac{(x-s)\,y\alpha_2}{\left[(x-s)^2 + r^2\right]^{\frac{3}{2}}} ds = \frac{\varepsilon U}{2} y \left(\frac{1}{\sqrt{r^2 + (\ell - x)^2}} - \frac{1}{\sqrt{r^2 + (x+\ell)^2}} \right),
\end{aligned} \tag{8.2}
$$

$$u_2(\mathbf{x}) = -U + \int_{-\ell}^{\ell} \left\{ \frac{\alpha_2}{\left[(x-s)^2 + r^2\right]^{1/2}} + \frac{y\left[(x-s)\alpha_1 + y\alpha_2 + z\alpha_3\right]}{\left[(x-s)^2 + r^2\right]^{\frac{3}{2}}} \right\} ds$$

$$= -U + \int_{-\ell}^{\ell} \left\{ \frac{\alpha_2}{\left[(x-s)^2 + r^2\right]^{1/2}} + \frac{y^2\alpha_2}{\left[(x-s)^2 + r^2\right]^{\frac{3}{2}}} \right\} ds$$

$$= -U + \frac{\varepsilon U}{2} \log\left(\frac{\ell + \sqrt{r^2 + (\ell - x)^2} - x}{-\ell + \sqrt{r^2 + (\ell + x)^2} - x} \right) \tag{8.3}$$

$$+ \frac{\varepsilon U}{2} \frac{y^2}{r^2} \left(\frac{\ell - x}{\sqrt{r^2 + (\ell - x)^2}} - \frac{-\ell - x}{\sqrt{r^2 + (\ell + x)^2}} \right),$$

$$u_3(\mathbf{x}) = \int_{-\ell}^{\ell} \left\{ \frac{\alpha_3}{\left[(x-s)^2 + r^2\right]^{1/2}} + \frac{z\left[(x-s)\alpha_1 + y\alpha_2 + z\alpha_3\right]}{\left[(x-s)^2 + r^2\right]^{\frac{3}{2}}} \right\} ds \tag{8.4}$$

$$= \int_{-\ell}^{\ell} \frac{yz\alpha_2}{\left[(x-s)^2 + r^2\right]^{\frac{3}{2}}} ds = \frac{\varepsilon U}{2} \frac{yz}{r^2} \left(\frac{\ell - x}{\sqrt{r^2 + (x-\ell)^2}} - \frac{-\ell - x}{\sqrt{r^2 + (x+\ell)^2}} \right),$$

where $r^2 = y^2 + z^2$, since

$$\int \frac{1}{\left[(x-s)^2 + r^2\right]^{1/2}} ds = \log\left(s + \sqrt{r^2 + (s-x)^2} - x \right),$$

$$\int \frac{1}{\left\{ (x-s)^2 + r^2 \right\}^{\frac{3}{2}}} ds = \frac{s - x}{r^2 \sqrt{r^2 + (s-x)^2}},$$

$$\int \frac{(x-s)}{\left[(x-s)^2 + r^2\right]^{\frac{3}{2}}} ds = \frac{1}{\sqrt{r^2 + (s-x)^2}}.$$

If $y^2 + z^2 \le r^2$ and $-\ell \le x \le \ell$, then the fluid particle is on or inside the slender body, which is outside the fluid. If $y^2 + z^2 \le r^2$ and $|x| > \ell$, then the fluid particle is along the slender body. Especially, if $y^2 + z^2 = 0$ ($y = z = 0$) and $|x| \ge \ell$, then the

fluid particle is along the longitudinal of the slender body,

$$
\begin{aligned}
u_1(\mathbf{x}) &= y\alpha_2 \int_{-\ell}^{\ell} \frac{(x-s)}{[(x-s)^2+r^2]^{\frac{3}{2}}} ds = 0, \\
u_3(\mathbf{x}) &= yz\alpha_2 \int_{-\ell}^{\ell} \frac{1}{[(x-s)^2+r^2]^{\frac{3}{2}}} ds = 0, \\
u_2(\mathbf{x}) &= -U + \alpha_2 \int_{-\ell}^{\ell} \frac{1}{\left[(x-s)^2+r^2\right]^{1/2}} ds + y^2\alpha_2 \int_{-\ell}^{\ell} \frac{1}{\left[(x-s)^2+r^2\right]^{\frac{3}{2}}} ds \\
&= -U + \alpha_2 \int_{-\ell}^{\ell} \frac{1}{|x-s|} ds + y^2\alpha_2 \int_{-\ell}^{\ell} \frac{1}{|x-s|^3} ds \\
&= -U - \mathrm{sgn}(x)\alpha_2 \log\left(\frac{\ell-x}{\ell+x}\right).
\end{aligned}
$$

The above velocity field is in the moving body frame. To obtain the velocity field in the lab frame, we apply the transformation between these two frames.

From the lab frame (x_L, y_L, z_L) to the moving body frame (x, y, z):

$$
\begin{cases}
x &= x_L, \\
y &= y_L - Ut, \\
z &= z_L.
\end{cases}
$$

So, the velocity field in the lab frame

$$
\mathbf{u}_L(\mathbf{x}_L) = \frac{d\mathbf{x}_L}{dt} = \frac{d\mathbf{x}}{dt} + U\mathbf{e}_y = U\mathbf{e}_y + \mathbf{u}(\mathbf{x} - Ut\mathbf{e}_y). \tag{8.5}
$$

Figure 8.3 shows two groups of fluid particle trajectories in the x-y plane in the laboratory frame. The initial positions of the fluid particle are either at $y = -0.1$ or $y = 0.6$. While the cylindrical slender body moves from $y = 0$ to $y = 1$ with uniform velocity $(0, 1, 0)$, the fluid particles moves with the same direction. When the slender body passes some fluid particles (green) initially in front of the slender body, these particles have been pushed aside. The blue thick horizontal lines indicate the initial and end

171
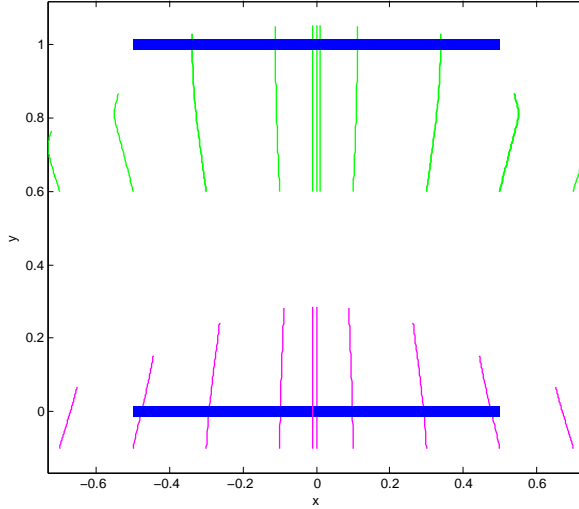
Figure 8.3: Two groups of fluid particle trajectories in the flow introduced by a translation of the cylindrical slender body perpendicular to its axis. The length of the slender body is 1, i.e., $\ell = 0.5$ in the model, $U = 1$, and $T_1 = 1$. The blue thick lines indicates the initial and the end positions of the body. The particles are in the x-y plane and will not leave the plane due to the symmetry of the flow. The green trajectories are for particles initially in front of the body. The magenta particles are following the body.

positions of the slender body.

8.2.2 Phase 3: from step (c) to step (d)

In phase 3, the flow is induced by the longitudinal translation of the slender body. The midpoint of the slender body moves from $(0, U\,T_1, 0)$ to $(0,0,0)$ with uniform velocity $(0, -U, 0)$ in the laboratory frame. To be consistent with the frame transformation in phase 1, we choose the body frame where the slender body is along the y-axis. The Stokeslets are distributed over the portion $-\ell \leq y \leq \ell$. Similarly as in phase 1, the strength of the Stokeslet is a uniform vector.

Applying the ratio of the velocity to the strength of the singularity, we find the strength of the Stokeslet is

$$
\begin{cases}
\alpha_1 = \frac{\varepsilon U_1}{2} = 0, \\[2mm]
\alpha_2 = \frac{\varepsilon U_2}{4} = \frac{\varepsilon U}{4}, \\[2mm]
\alpha_3 = \frac{\varepsilon U_3}{3} = 0.
\end{cases}
$$

172

The velocity field in the body frame is

$$\mathbf{u}(\mathbf{x}) = \mathbf{U} + \int_{-\ell}^{\ell} \mathbf{u}_S(\mathbf{x} - \mathbf{x}_s; \boldsymbol{\alpha}) ds.$$

After evaluating the integrals, the velocity is

$$u_1(\mathbf{x}) = \frac{\varepsilon U}{4} \left(\frac{x}{\sqrt{r^2 + (\ell - y)^2}} - \frac{x}{\sqrt{r^2 + (\ell + y)^2}} \right), \tag{8.6}$$

$$u_2(\mathbf{x}) = U + \frac{\varepsilon U}{4} \left[2\log \left(\frac{\ell + \sqrt{r^2 + (\ell - y)^2} - y}{-\ell + \sqrt{r^2 + (\ell + y)^2} - y} \right) \right.$$

$$\left. - \frac{\ell - y}{\sqrt{r^2 + (\ell - y)^2}} - \frac{\ell + y}{\sqrt{r^2 + (\ell + y)^2}} \right], \tag{8.7}$$

$$u_3(\mathbf{x}) = \frac{\varepsilon U}{4} \left(\frac{z}{\sqrt{r^2 + (\ell - y)^2}} - \frac{z}{\sqrt{r^2 + (\ell + y)^2}} \right), \tag{8.8}$$

where $r^2 = x^2 + z^2$.

Since the body moves along the positive y-axis with constant velocity U, the transformation between the fixed lab frame (x_L, y_L, z_L) and the moving body frame (x, y, z) is

$$x = x_L, \quad y = y_L - Ut, \quad z = z_L.$$

The velocity field in the lab frame is derived from the velocity field (8.6)-(8.8) in the body frame with (8.5).

Figure 8.4 shows three groups of fluid particle trajectories when the body longitudinal translates with its center from $(0, 0, 0)$ to $(0, 2, 0)$. The uniform velocity in the lab frame is $(0, 1, 0)$. Here the body moves along an opposite direction compared to the periodic motion sketched in Figure 8.2. The purpose is to show the fluid flow in
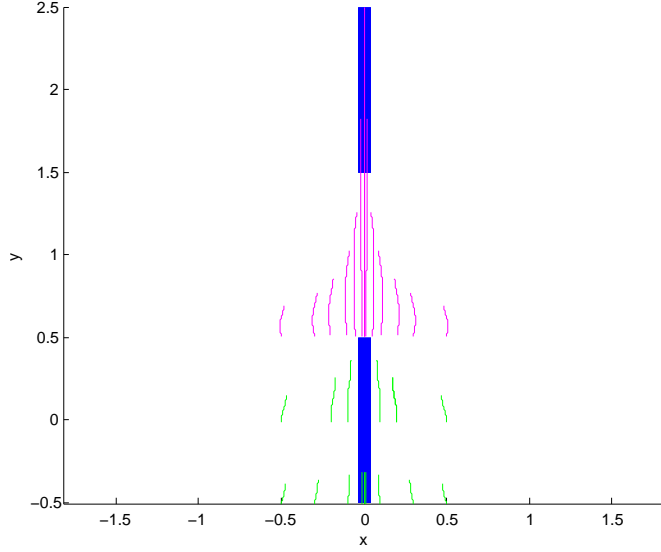
Figure 8.4: Three groups of fluid particle trajectories when the cylindrical body longitudinal translates from the bottom to the top positions indicating by the thick blue lines. The geometry of the body is kept the same as in Figure 8.3, $U = 1$ and $T_1 = 2$. The initial positions of these three groups of the fluid particles are distributed on three horizontal lines.

each phase first. When we combine the motions together, the proper direction will be set. From these trajectories, we see particles move along the direction of the body's motion. From the magenta trajectories, the fluid particles are pushed aside when the body passes the particles and move toward the center after the body passes them. Also, the particles initially close to the tip $(0, 0.5, 0)$ go inside the body, which is due to neglecting of the end effect and the first approximation of the slender body solution. The no-slip boundary condition is approximated.

8.2.3 Phase 2: from step (b) to step (c)

In phase 2 and phase 4, the cylindrical slender body rotates counter-clockwise or clockwise. When the slender body rotates counter-clockwise in the laboratory frame from step (b) to step (c) in Figure 8.2, the rod is fixed along the x-axis and the background flow is the clockwise rotating flow in the body frame. The body rotates about its midpoint with constant angular velocity ω in the x-y plane.

- One end of the slender body moves from $(\ell, UT_1, 0)$ to $(0, UT_1 + \ell, 0)$.

- The other end of the slender body moves from $(-\ell, UT_1, 0)$ to $(0, UT_1 - \ell, 0)$.

- If the rotation time period is T_2, the angular velocity is $\omega = \frac{\pi}{2T_2}$.

In the body frame, with linear distribution of Stokeslet along the center-line, the velocity field is

$$
\mathbf{u}(\mathbf{x}) = \mathbf{U} + \int_{-\ell}^{\ell} \mathbf{u}_S(\mathbf{x} - \mathbf{x}_s; \boldsymbol{\alpha}(s)) ds,
$$

where $\mathbf{x}_s = (x_s, y_s, z_s) = (s, 0, 0)$ is the center-line of the slender body, $\mathbf{x} = (x, y, z)$, and $\boldsymbol{\alpha} = (\alpha_1, \alpha_2, \alpha_3) = \frac{\omega\varepsilon}{2}(0, s, 0)$. The velocity field is

$$
\begin{aligned}
u_1(\mathbf{x}) &= \omega y + \frac{\omega\varepsilon}{2} \int_{-\ell}^{\ell} \frac{(x-s)ys}{[(x-s)^2 + y^2 + z^2]^{3/2}} ds \\
&= \omega y + \frac{\omega\varepsilon y}{2} \int_{-\ell}^{\ell} \frac{(x-s)s}{[(x-s)^2 + y^2 + z^2]^{3/2}} ds, \\
u_2(\mathbf{x}) &= -\omega x + \frac{\omega\varepsilon}{2} \int_{-\ell}^{\ell} \left\{ \frac{s}{[(x-s)^2 + y^2 + z^2]^{1/2}} + \frac{y^2 s}{[(x-s)^2 + y^2 + z^2]^{\frac{3}{2}}} \right\} ds \\
&= -\omega x + \frac{\omega\varepsilon}{2} \int_{-\ell}^{\ell} \frac{s}{[(x-s)^2 + y^2 + z^2]^{1/2}} ds + \frac{\omega\varepsilon y^2}{2} \int_{-\ell}^{\ell} \frac{s}{\{(x-s)^2 + y^2 + z^2\}^{\frac{3}{2}}} ds, \\
u_3(\mathbf{x}) &= \frac{\omega\varepsilon}{2} \int_{-\ell}^{\ell} \frac{yzs}{[(x-s)^2 + y^2 + z^2]^{\frac{3}{2}}} ds = \frac{\omega\varepsilon yz}{2} \int_{-\ell}^{\ell} \frac{s}{[(x-s)^2 + y^2 + z^2]^{\frac{3}{2}}} ds.
\end{aligned}
$$

Since

$$
\begin{aligned}
\int \frac{s}{[(x-s)^2 + r^2]^{1/2}} ds &= \sqrt{(x-s)^2 + r^2} + x \log\left(s - x + \sqrt{(x-s)^2 + r^2}\right), \\
\int \frac{s}{[(x-s)^2 + r^2]^{\frac{3}{2}}} ds &= \frac{(s-x)x - r^2}{r^2\sqrt{(x-s)^2 + r^2}}, \\
\int \frac{(x-s)s}{[(x-s)^2 + r^2]^{3/2}} ds &= \frac{s}{\sqrt{(x-s)^2 + r^2}} - \log\left(s - x + \sqrt{(x-s)^2 + r^2}\right),
\end{aligned}
$$

175

the velocity field in the body frame is

$$
\begin{aligned}
u_1(\mathbf{x}) &= \omega y + \frac{\omega \varepsilon y}{2} \left[\frac{\ell}{\sqrt{(x-\ell)^2 + r^2}} + \frac{\ell}{\sqrt{(x+\ell)^2 + r^2}} \right. \\
&\quad \left. - \log \left(\frac{\ell - x + \sqrt{(x-\ell)^2 + r^2}}{-\ell - x + \sqrt{(x+\ell)^2 + r^2}} \right) \right], \tag{8.9} \\
u_2(\mathbf{x}) &= -\omega x + \frac{\omega \varepsilon}{2} \left[\sqrt{(x-\ell)^2 + r^2} - \sqrt{(x+\ell)^2 + r^2} \right. \\
&\quad \left. + x \log \left(\frac{\ell - x + \sqrt{(x-\ell)^2 + r^2}}{-\ell - x + \sqrt{(x+\ell)^2 + r^2}} \right) \right] \tag{8.10} \\
&\quad + \frac{\omega \varepsilon y^2}{2} \left[\frac{(\ell - x)x - r^2}{r^2 \sqrt{(x-\ell)^2 + r^2}} + \frac{(\ell + x)x + r^2}{r^2 \sqrt{(x+\ell)^2 + r^2}} \right], \\
u_3(\mathbf{x}) &= \frac{\omega \varepsilon y z}{2} \left[\frac{(\ell - x)x - r^2}{r^2 \sqrt{(x-\ell)^2 + r^2}} + \frac{(\ell + x)x + r^2}{r^2 \sqrt{(x+\ell)^2 + r^2}} \right], \tag{8.11}
\end{aligned}
$$

where $r^2 = y^2 + z^2$.

With the velocity field (8.9)-(8.11) in the body frame, the velocity field in the lab frame is determined by applying the transformation matrix between these two frames. Note the transformation matrix between the body frame $\mathbf{x}_b$ and the lab frame $\mathbf{x}_L$ as $R_\omega(t)$. Then

$$
\mathbf{x}_L = R_\omega(t) \mathbf{x}_b.
$$

For the constant angular velocity $\omega(t) = \omega t$, the background flow in the body frame is $\mathbf{U}(\mathbf{x}) = \omega(y, -x, 0)$ and the transformation matrix is

$$
R_\omega(t) = \begin{pmatrix} \cos(\omega t) & -\sin(\omega t) & 0 \\ \sin(\omega t) & \cos(\omega t) & 0 \\ 0 & 0 & 1 \end{pmatrix}.
$$
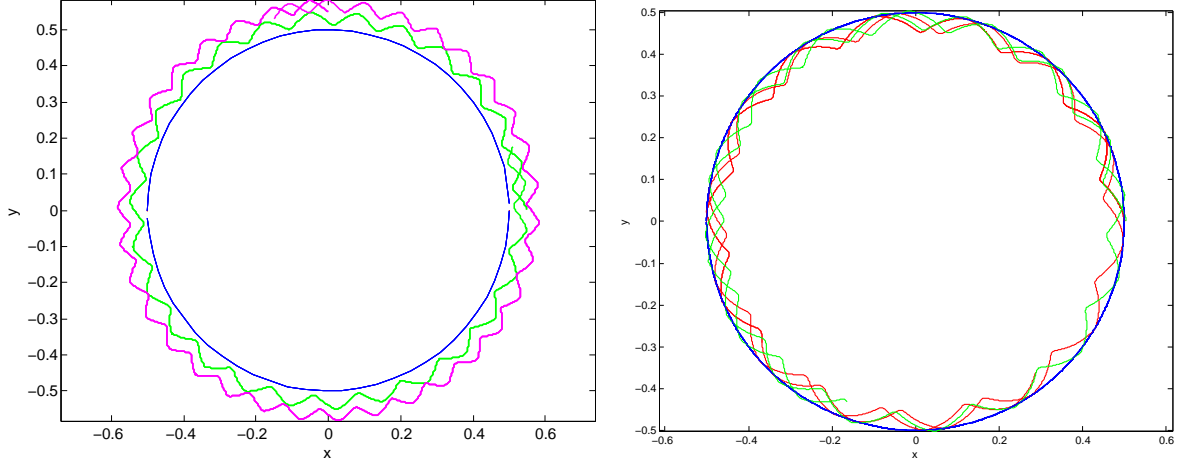
(a) Two fluid particle trajectories (green and magenta) initially outside the blue circle.

(b) Two fluid particle trajectories (green and red) initially inside the blue circle.

Figure 8.5: Fluid particle trajectories in the flow introduced by the counter-clockwise rotation of the slender body in the x-y plane. Here, $\ell = 0.5$. The blue circle is the imprint of the slender body's tips.

The velocity field in the lab frame is

$$
\begin{aligned}
\mathbf{u}_L(\mathbf{x}_L) &= \frac{d\mathbf{x}_L}{dt} = \frac{d(R_\omega \mathbf{x}_b)}{dt} = \dot{R}_\omega R_\omega^T \mathbf{x}_L + R_\omega \mathbf{u}\left(R_\omega^T \mathbf{x}_L\right) \\
&= \omega \begin{pmatrix} 0 & -1 & 0 \\ 1 & 0 & 0 \\ 0 & 0 & 0 \end{pmatrix} \begin{pmatrix} x_L \\ y_L \\ z_L \end{pmatrix} + \begin{pmatrix} \cos(\omega t) & -\sin(\omega t) & 0 \\ \sin(\omega t) & \cos(\omega t) & 0 \\ 0 & 0 & 1 \end{pmatrix} \mathbf{u}\left(R_\omega^T \mathbf{x}_L\right).
\end{aligned}
$$

Figure 8.5a shows two fluid particle trajectories when the slender body rotates counterclockwise at the center of the lab frame within 15 revolutions of the slender body. Figure 8.5b shows two fluid particle trajectories in the x-y plane when their initial positions are close to the tip of the slender body. These two fluid particles are inside the blue orbit of the slender body tips.
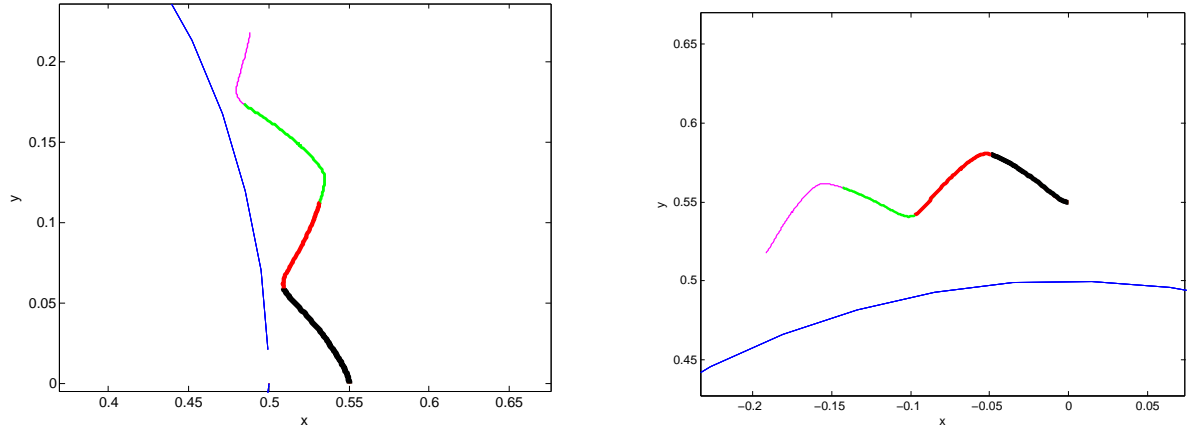
Figure 8.6: Two fluid particle trajectories within one revolution of the counter-clockwise rotation of the slender body ($\ell = 0.5$). The fluid particle trajectories are indicated by different colors for each quarter of the rotation. The blue trajectory is the imprint of the tips of the slender body.
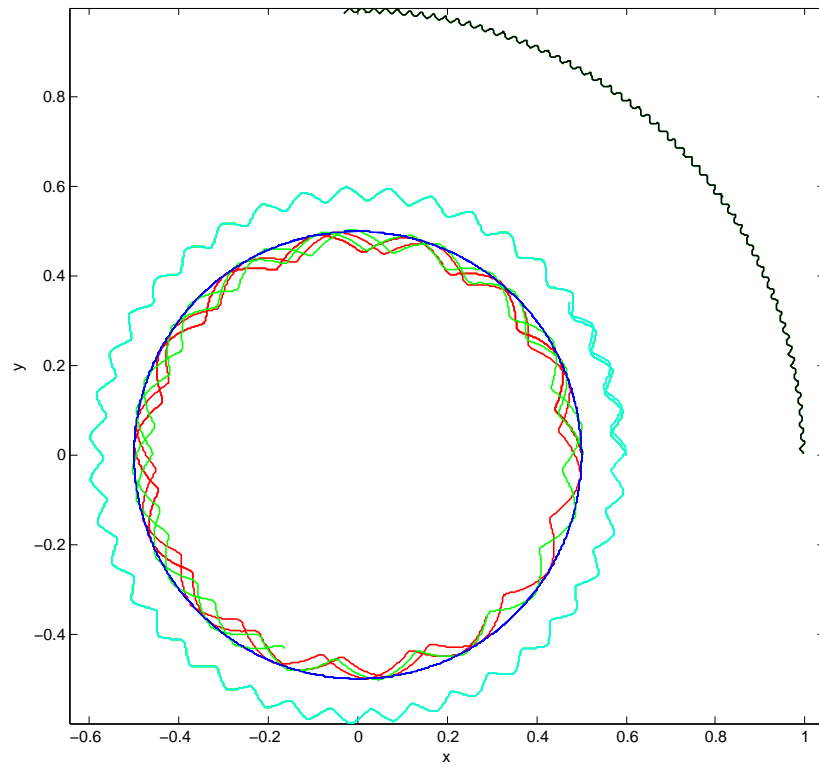
Figure 8.7: Numerical trajectories in the velocity field introduced by the anti-clockwise rotation of the slender body with $\ell = 0.5$, $U = 1$ and $T_1 = 2$.

Since the slender body has been shifted horizontally in phase 1 before its rotation, the following transformation is applied the coordinates

$$x' = x, \quad y' = y - U\,T_1, \quad z' = z.$$

We ignore the above translation for the study of this phase itself. Such translation will be considered when we examine the whole period of the slender body motion.

8.2.4 Phase 4: from step (d) to step (e)

In phase 4, the slender body clockwise rotates about its midpoint $(0,0,0)$ with constant angular velocity ω in the x-y plane in the lab frame.

- One end of the slender body moves from $(0, \ell, 0)$ to $(\ell, 0, 0)$;

- The other end of the slender body moves from $(0, -\ell, 0)$ to $(-\ell, 0, 0)$;

- The rotating time period is T_2, so the frequency is $\omega = \frac{\pi}{2T_2}$.

Similar to the velocity (8.9)-(8.11) constructed in phase 2, we linearly distribute Stokeslets along the center-line of the slender body, which is along the y-axis ($-\ell \leq y \leq \ell$) in the body frame. Since the slender body rotates clockwise in the lab frame, the background flow in the body frame is counter-clockwise rotation flow. The velocity

179

field in the body frame is

$$
\begin{aligned}
u_1(\mathbf{x}) &= -\omega y + \frac{\omega\varepsilon}{2}\int_{-\ell}^{\ell}\frac{s}{[(y-s)^2+r^2]^{1/2}}ds + \frac{\omega\varepsilon x^2}{2}\int_{-\ell}^{\ell}\frac{s}{[(y-s)^2+r^2]^{\frac{3}{2}}}ds \\
&= -\omega y + \frac{\omega\varepsilon}{2}\left\{\sqrt{(y-\ell)^2+r^2}-\sqrt{(y+\ell)^2+r^2}\right. \\
&\quad\left. +y\log\left(\frac{\ell-y+\sqrt{(y-\ell)^2+r^2}}{-\ell-y+\sqrt{(y+\ell)^2+r^2}}\right)\right\} \\
&\quad +\frac{\omega\varepsilon x^2}{2}\left[\frac{(\ell-y)y-r^2}{r^2\sqrt{(y-\ell)^2+r^2}}-\frac{(-\ell-y)y-r^2}{r^2\sqrt{(y+\ell)^2+r^2}}\right], \\
u_2(\mathbf{x}) &= \omega x + \frac{\omega\varepsilon x}{2}\int_{-\ell}^{\ell}\frac{(y-s)s}{[(y-s)^2+r^2]^{3/2}}ds \\
&= \omega x + \frac{\omega\varepsilon x}{2}\left\{\frac{\ell}{\sqrt{(y-\ell)^2+r^2}}-\frac{-\ell}{\sqrt{(x+\ell)^2+r^2}}\right. \\
&\quad\left. -\log\left(\frac{\ell-y+\sqrt{(y-\ell)^2+r^2}}{-\ell-x+\sqrt{(y+\ell)^2+r^2}}\right)\right\}, \\
u_3(\mathbf{x}) &= \frac{\omega\varepsilon x z}{2}\int_{-\ell}^{\ell}\frac{s}{[(y-s)^2+r^2]^{\frac{3}{2}}}ds \\
&= \frac{\omega\varepsilon x z}{2}\left[\frac{(\ell-y)y-r^2}{r^2\sqrt{(y-\ell)^2+r^2}}-\frac{(-\ell-y)y-r^2}{r^2\sqrt{(y+\ell)^2+r^2}}\right],
\end{aligned}
$$

where $r^2 = x^2 + z^2$.

If $x^2 + z^2 = 0$ and $|y| > \ell$, then the fluid particle is along the axis of the slender body. The velocity field is

$$
\begin{aligned}
u_1(\mathbf{x}) &= -\omega y + \frac{\omega\varepsilon}{2}\int_{-\ell}^{\ell}\frac{s}{|y-s|}ds + \frac{\omega\varepsilon x^2}{2}\int_{-\ell}^{\ell}\frac{s}{|y-s|^3}ds \\
&= -\omega y - \frac{\omega\varepsilon}{2}\text{sign}(y)\left(2\ell + y\log\left|\frac{\ell-y}{\ell+y}\right|\right), \\
u_2(\mathbf{x}) &= u_3(\mathbf{x}) = 0.
\end{aligned}
$$

In phase 2, the body is along the x-axis in the body frame. However, the body is along y-axis in the body frame for phase 4. Before applying the transformation matrix

180

in phase 2, we need change the coordinates

$$\mathbf{x}_L = \begin{pmatrix} 1 & 0 & 0 \\ 0 & -1 & 0 \\ 0 & 0 & 1 \end{pmatrix} \mathbf{x}'_L,$$

where $\mathbf{x}_L$ is in the laboratory frame and $\mathbf{x}'_L$ is the coordinates in the laboratory frame in phase 2, then rotate the slender body in the x-y plane. For constant angular velocity $\omega(t) = \omega t$, the background flow is $\mathbf{u}(\mathbf{x}) = \omega(y, -x, 0)$.

Due to the time reversibility of the Stokes flow, the fluid particle trajectories in this phase is easily to understand with the fluid particle trajectories in phase 2. We skip fluid particle trajectory in this phase and illustrate the flow with the whole periodic motion of the slender body.

8.3 Fluid particle trajectories

With the velocity field for the fluid motion during each step, we examine the fluid particle trajectories when the slender body moves periodically as shown in Figure 8.2. During each period, the proper transformation matrix is applied from the body frame to the lab frame. A relation for the uniform translation velocity and the rotation rate is selected to make the linear velocity of the tips equal between two phases.

In Figure 8.8, the magenta curves are fluid particle trajectories during one period at different locations. The blue curves and red lines are part of the imprint of the slender body's tips. The half length of the slender body is $\ell = 0.5$, and $U = 1$. The uniform translation is in the y-direction. The slender body rotates clockwise at the origin, and rotates counter-clockwise at $(0, 2, 0)$. From these trajectories, the motion generated by the rotation of the slender body contribute less than the uniform translation.
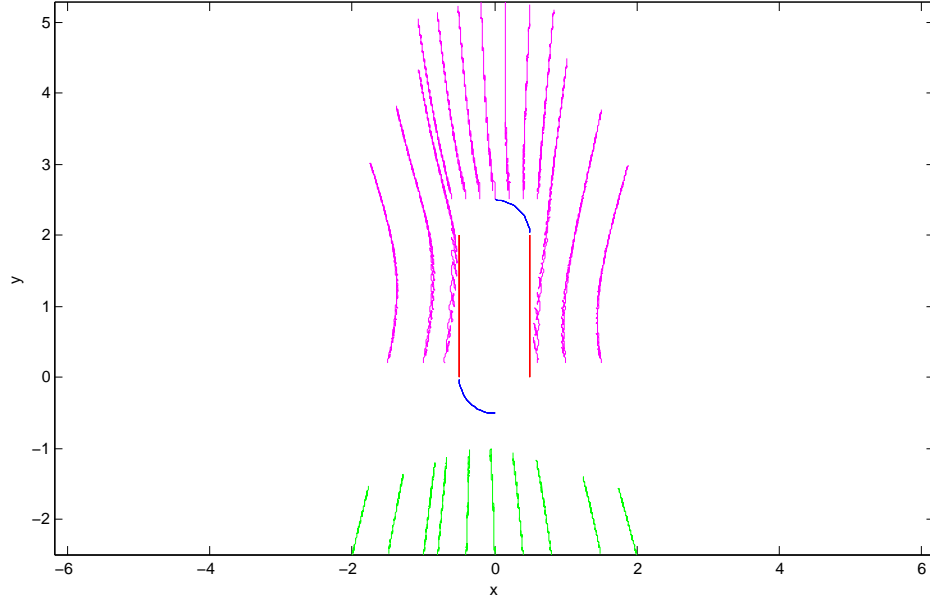
Figure 8.9: Two groups of fluid particle trajectories and part of imprints of the periodic motion of the slender body. All the particles move upward over time. Here the half body length is $\ell = 0.5$, $U = 1$, and $T_1 = 2$.

Figure 8.9 and 8.10 shows the fluid particle trajectories when the slender body moves periodically as shown in Figure 8.2. All the trajectories are in the x-y plane. From these trajectories, there are directional fluid transport due to the periodic motion of the slender body. The transport is along the transversal translation direction (opposite to the longitudinal translation) of the slender body. The comparison between Figure 8.10a and 8.10b shows the transport is stronger if the uniform motion last longer when the uniform velocity is fixed.
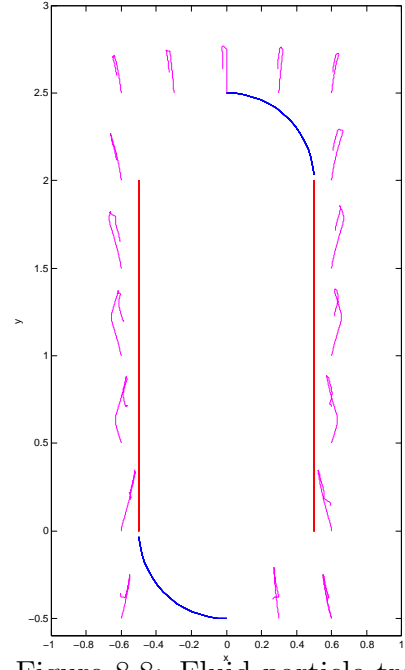
Figure 8.8: Fluid particle trajectories within one period.

(a) $T_1 = 1$.   (b) $T_1 = 2$.
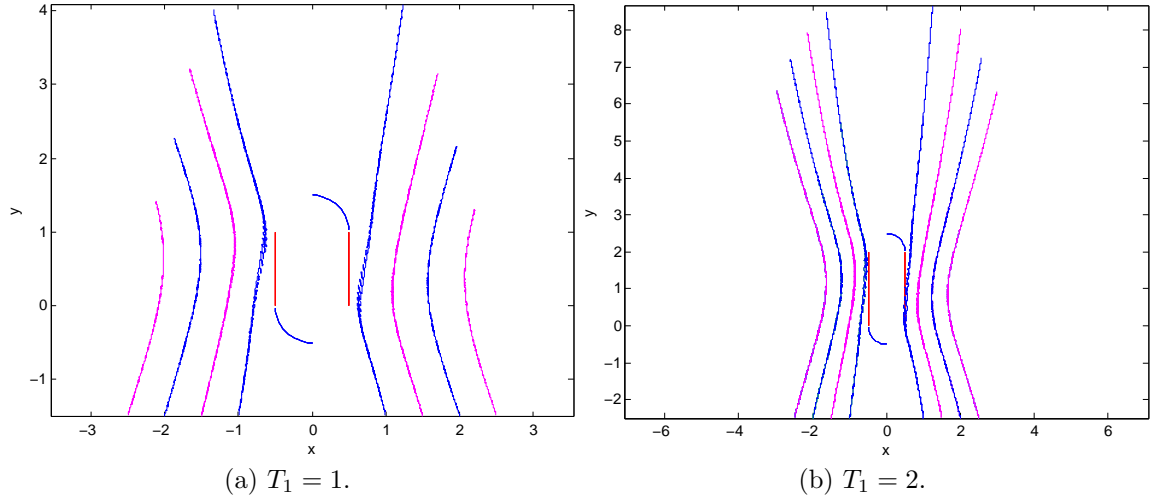
Figure 8.10: Two groups of fluid particle trajectories in the x-y plane. Their initial positions are at $y = -1.5$ or -2.5. Here, $\ell = 0.5$, $U = 1$ and different values of T_1. Part of the imprint of the tips are plotted at the center of these plots.

8.4 The far field

To examine the flow transport, it is worth checking the flow in the far field. In this section, we study the asymptotic solution of the far-field velocity field for the flow induced by the slender body in each step. For convenience, parentheses are drops for trigonometry functions.

8.4.1 Uniform transition

Consider a distribution of Stokeslets over the portion $-\ell < s < \ell$ of the x-axis with strength $\boldsymbol{\alpha}(s) = (\alpha_1(s), \alpha_2(s), \alpha_3(s))$, the velocity field $\mathbf{u} = (u_1, u_2, u_3)$ at $\mathbf{x}$ due to this

force distribution is

$$
u_1(\mathbf{x}; \boldsymbol{\alpha}) = \int_{-\ell}^{\ell} \left\{ \frac{\alpha_1(s)}{\left[(x-s)^2 + r^2\right]^{1/2}} + \frac{(x-s)\left[(x-s)\,\alpha_1(s) + y\alpha_2(s) + z\alpha_3(s)\right]}{\left[(x-s)^2 + r^2\right]^{\frac{3}{2}}} \right\} ds,
$$

$$
u_2(\mathbf{x}; \boldsymbol{\alpha}) = \int_{-\ell}^{\ell} \left\{ \frac{\alpha_2(s)}{\left[(x-s)^2 + r^2\right]^{1/2}} + \frac{y\left[(x-s)\,\alpha_1(s) + y\alpha_2(s) + z\alpha_3(s)\right]}{\left[(x-s)^2 + r^2\right]^{\frac{3}{2}}} \right\} ds,
$$

$$
u_3(\mathbf{x}; \boldsymbol{\alpha}) = \int_{-\ell}^{\ell} \left\{ \frac{\alpha_3(s)}{\left[(x-s)^2 + r^2\right]^{1/2}} + \frac{z\left[(x-s)\,\alpha_1(s) + y\alpha_2(s) + z\alpha_3(s)\right]}{\left[(x-s)^2 + r^2\right]^{\frac{3}{2}}} \right\} ds,
$$

where $r^2 = y^2 + z^2$.

As the observation point $\mathbf{x}$ is far from the body, we examine the far-field velocity. Hence, a non-dimensional formulation is introduced. Let

$$
\mathbf{x}' = \frac{\mathbf{x}}{R}, \qquad s' = \frac{s}{\ell}, \qquad \boldsymbol{\alpha}' = \frac{\boldsymbol{\alpha}}{U} \tag{8.12}
$$

in which R is a characteristic length assumed to be large and U is a characteristic velocity. Note r as the non-dimensional radius, $r^2 = (y')^2 + (z')^2$, and

$$
\epsilon_0 = \frac{\ell}{R_0} \tag{8.13}
$$

as the small parameter for the far-field velocity. The details for the far-field velocity are provided in Appendix E. Since the far-field limit of the velocity field is of interest, we examine $\epsilon_0 \to 0$ in the limit of $R_0 \to 0$.

Consider the velocity field due to a line distribution of uniform Stokeslets with

184

strength

$$
\begin{cases}
\alpha_1(s) &= \frac{\varepsilon U_1}{4}; \\[2mm]
\alpha_3(s) &= \frac{\varepsilon U_2}{2}; \\[2mm]
\alpha_2(s) &= \frac{\varepsilon U_3}{2}.
\end{cases}
$$

From the leading order of the far-field velocity

$$
u_1(\mathbf{x}; \boldsymbol{\alpha}) = \epsilon_0 \left[\frac{2}{|\mathbf{x}|} \alpha_1 + \frac{2x^2}{|\mathbf{x}|^3} \alpha_1 + \frac{2xy}{|\mathbf{x}|^3} \alpha_2 + \frac{2xz}{|\mathbf{x}|^3} \alpha_3 \right] + O(\epsilon_0^3) \tag{8.14}
$$

$$
u_2(\mathbf{x}; \boldsymbol{\alpha}) = \epsilon_0 \left[\frac{2}{|\mathbf{x}|} \alpha_2 + \frac{2xy}{|\mathbf{x}|^3} \alpha_1 + \frac{2y^2}{|\mathbf{x}|^3} \alpha_2 + \frac{2yz}{|\mathbf{x}|^3} \alpha_3 \right] + O(\epsilon_0^3) \tag{8.15}
$$

$$
u_3(\mathbf{x}; \boldsymbol{\alpha}) = \epsilon_0 \left[\frac{2}{|\mathbf{x}|} \alpha_3 + \frac{2xz}{|\mathbf{x}|^3} \alpha_1 + \frac{2yz}{|\mathbf{x}|^3} \alpha_2 + \frac{2x_3^2}{|\mathbf{x}|^3} \alpha_3 \right] + O(\epsilon_0^3) \tag{8.16}
$$

The far-field velocity of the induced velocity in Phase 1   Since the slender body moves in the x-y plane and for phase 1

$$
\alpha_1 = \alpha_3 = 0, \ \text{ and } \ \alpha_2 = \frac{\varepsilon U}{2},
$$

the leading order of the far-field velocity field for the induced flow is

$$
\begin{aligned}
\frac{dx}{dt} &= \epsilon_0 \frac{2xy}{|\mathbf{x}|^3} \alpha_2 + O(\epsilon_0^3), \\[2mm]
\frac{dy}{dt} &= \epsilon_0 \left[\frac{2}{|\mathbf{x}|} \alpha_2 + \frac{2y^2}{|\mathbf{x}|^3} \alpha_2 \right] + O(\epsilon_0^3), \\[2mm]
\frac{dz}{dt} &= \epsilon_0 \left[\frac{2yz}{|\mathbf{x}|^3} \alpha_2 \right] + O(\epsilon_0^3).
\end{aligned}
$$

If the particle's initial position is in the x-y plane, then $z = 0$ is always true on the

185
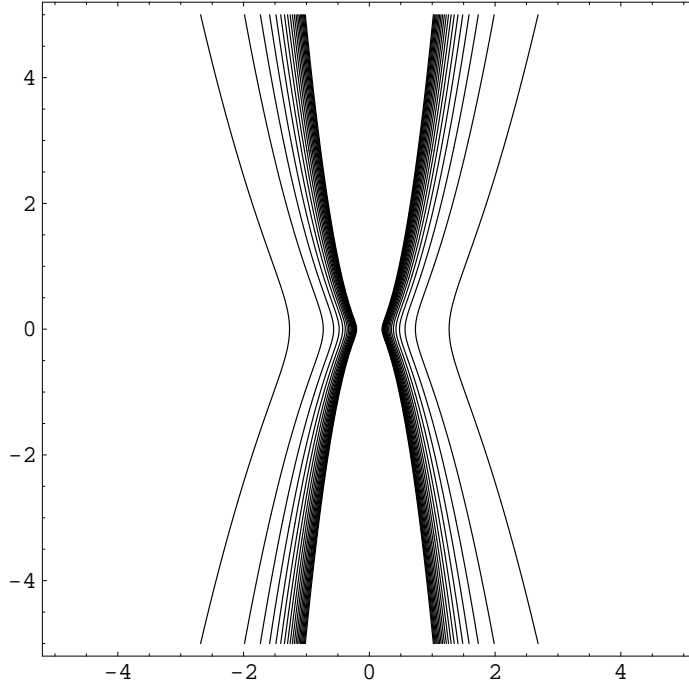
Figure 8.11: Contour plot for exact solution (8.17) of the far-field trajectory.

fluid particle trajectory

$$
\begin{aligned}
\frac{dx}{dt} &= 2\epsilon_0\alpha_2 \frac{xy}{(x^2+y^2)^{\frac{3}{2}}} + O(\epsilon_0^3), \\
\frac{dy}{dt} &= 2\epsilon_0\alpha_2 \left[\frac{1}{\sqrt{x^2+y^2}} + \frac{y^2}{(x^2+y^2)^{\frac{3}{2}}} \right] + O(\epsilon_0^3), \\
\frac{dz}{dt} &= O(\epsilon_0^3).
\end{aligned}
$$

From the velocity field, we find the fluid particle trajectory equation in the x-y plane,

$$
\frac{dy}{dx} = \frac{x^2+2y^2}{xy}, \Longrightarrow \frac{1}{x^2} + \frac{y^2}{x^4} = \text{constant}. \tag{8.17}
$$

Since the slender body moving in the x-y plane and for phase 1 with background

186

flow $(0, -U, 0)$ and

$$\alpha_1 = \alpha_3 = 0, \text{ and } \alpha_2 = -\frac{\varepsilon U}{2},$$

the far-field velocity field in the body frame is

$$\frac{dx}{dt} = \epsilon_0 \frac{2xy}{|\mathbf{x}|^3} \alpha_2 + O(\epsilon_0^3),$$

$$\frac{dy}{dt} = -U + \epsilon_0 \left[\frac{2}{|\mathbf{x}|} \alpha_2 + \frac{2y^2}{|\mathbf{x}|^3} \alpha_2 \right] + O(\epsilon_0^3),$$

$$\frac{dz}{dt} = \epsilon_0 \left[\frac{2yz}{|\mathbf{x}|^3} \alpha_2 \right] + O(\epsilon_0^3).$$

If the particle's initial position is in the x-y plane, then

$$\frac{dx}{dt} = 2\epsilon_0 \alpha_2 \frac{xy}{(x^2 + y^2)^{\frac{3}{2}}} + O(\epsilon_0^3),$$

$$\frac{dy}{dt} = -U + 2\epsilon_0 \alpha_2 \left[\frac{1}{\sqrt{x^2 + y^2}} + \frac{y^2}{(x^2 + y^2)^{\frac{3}{2}}} \right] + O(\epsilon_0^3),$$

$$\frac{dz}{dt} = O(\epsilon_0^3).$$

From the above velocity field,

$$\frac{dx}{dy} = \frac{\frac{xy}{(x^2+y^2)^{\frac{3}{2}}}}{-\frac{U}{2\epsilon_0\alpha_2} + \left[\frac{1}{\sqrt{x^2+y^2}} + \frac{y^2}{(x^2+y^2)^{\frac{3}{2}}} \right]},$$

$$\implies \left\{ -\frac{U}{2\epsilon_0\alpha_2} + \left[\frac{1}{\sqrt{x^2 + y^2}} + \frac{y^2}{(x^2 + y^2)^{\frac{3}{2}}} \right] \right\} dx - \frac{xy}{(x^2 + y^2)^{\frac{3}{2}}} dy = 0.$$

Applying the integral factor $\mu(x, y) = x$,

$$\left\{ -\frac{Ux}{2\epsilon_0\alpha_2} + \left[\frac{x}{\sqrt{x^2+y^2}} + \frac{xy^2}{(x^2+y^2)^{\frac{3}{2}}} \right] \right\} dx - \frac{x^2 y}{(x^2+y^2)^{\frac{3}{2}}} dy = 0$$

$$d\left[-\frac{Ux^2}{4\epsilon_0\alpha_2} + \sqrt{x^2+y^2} - \frac{y^2}{\sqrt{x^2+y^2}} \right] = 0$$

$$d\left[-\frac{Ux^2}{4\epsilon_0\alpha_2} + \frac{x^2}{\sqrt{x^2+y^2}} \right] = 0$$

$$-Ux^2 + 4\epsilon_0\alpha_2 \frac{x^2}{\sqrt{x^2+y^2}} = \text{constant.} \qquad (8.18)$$

Equation (8.18) is the fluid particle trajectory equation in the body frame. As the velocity component in the z-direction vanishes for any fluid particle initially in the x-y plane, we only need check the fluid particle trajectory in the x-y plane in the lab frame. In the laboratory frame (x', y'),

$$\begin{cases} x' &= x \\ y' &= y + Ut \end{cases} \quad \text{and} \quad \begin{cases} x &= x' \\ y &= y' - Ut \end{cases}.$$

So, the particle trajectory equation is

$$-Ux^2 + 4\epsilon_0\alpha_2 \frac{x^2}{\sqrt{x^2+(y-Ut)^2}} = \text{constant.} \qquad (8.19)$$

The far-field velocity in phase 3 can be obtained similarly from (8.14)-(8.16) with corresponding background flow.
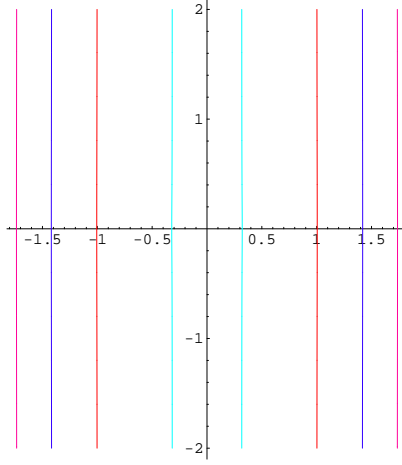
Figure 8.12: Contour plot for the exact solution (8.18) of the far-field trajectory.

8.4.2 Rotation

During phase 2 and phase 4, the body rotates about its midpoint with constant angular velocity ω in the (x, y) plane. In the body frame, the velocity field is

$$u_1(\mathbf{x}) = \omega y + \frac{\omega\varepsilon}{2}\int_{-\ell}^{\ell}\frac{(x-s)ys}{[(x-s)^2 + y^2 + z^2]^{3/2}}ds,$$

$$u_2(\mathbf{x}) = -\omega x + \frac{\omega\varepsilon}{2}\int_{-\ell}^{\ell}\left\{\frac{s}{[(x-s)^2 + y^2 + z^2]^{1/2}} + \frac{y^2 s}{[(x-s)^2 + y^2 + z^2]^{\frac{3}{2}}}\right\}ds,$$

$$u_3(\mathbf{x}) = \frac{\omega\varepsilon}{2}\int_{-\ell}^{\ell}\left\{\frac{yzs}{[(x-s)^2 + y^2 + z^2]^{\frac{3}{2}}}\right\}ds.$$

Non-dimensionalize the velocity as for the uniform translation in the previous subsection, the far-field velocity field is

$$u_1(\mathbf{x}) = \omega R y + \frac{\omega\varepsilon\ell y}{2}\left[\left(\frac{3x^2}{|\mathbf{x}|^5} - \frac{1}{|\mathbf{x}|^3}\right)\frac{2}{3}\epsilon_0^2 + O(\epsilon_0^4)\right],$$

$$u_2(\mathbf{x}) = -\omega R x + \frac{\omega\varepsilon\ell}{2}\left[\frac{x}{|\mathbf{x}|^3}\frac{2\epsilon_0^2}{3} + O(\epsilon_0^4)\right] + \frac{\omega\varepsilon\ell y^2}{2}\left[\frac{3x}{|\mathbf{x}|^5}\frac{2}{3}\epsilon_0^2 + O(\epsilon_0^4)\right],$$

$$u_3(\mathbf{x}) = \frac{\omega\varepsilon\ell yz}{2}\left[\frac{3x}{|\mathbf{x}|^5}\frac{2}{3}\epsilon_0^2 + O(\epsilon_0^4)\right].$$

189

More details about the non-dimensionalization are provided in Appendix E. If the high order terms are negligible, the fluid particle trajectory is governed by

$$\frac{dx}{dt} = \omega R y + \frac{\omega \varepsilon \ell y}{3}\left(\frac{3x^2}{|\mathbf{x}|^5} - \frac{1}{|\mathbf{x}|^3}\right)\epsilon_0^2 + O(\epsilon_0^4),$$

$$\frac{dy}{dt} = -\omega R x + \frac{\omega \varepsilon \ell x}{3|\mathbf{x}|^3}\epsilon_0^2 + \frac{\omega \varepsilon \ell x y^2}{|\mathbf{x}|^5}\epsilon_0^2 + O(\epsilon_0^4),$$

$$\frac{dz}{dt} = \omega \varepsilon \ell y z \frac{x}{|\mathbf{x}|^5}\epsilon_0^2 + O(\epsilon_0^3).$$

If the fluid particle is in the x-y plane initially, i.e., $z = 0$ and $|\mathbf{x}| = \sqrt{x^2 + y^2}$, keep the leading order of the far field velocity

$$\frac{dx}{dt} = \omega R y + \frac{\omega \varepsilon \ell y}{3}\frac{2x^2 - y^2}{(x^2 + y^2)^{5/2}}\epsilon_0^2 + O(\epsilon_0^4),$$

$$\frac{dy}{dt} = -\omega R x + \frac{\omega \varepsilon \ell x (x^2 + 4y^2)}{3(x^2 + y^2)^{5/2}}\epsilon_0^2 + O(\epsilon_0^4),$$

$$\frac{dz}{dt} = 0.$$

If the fluid particles is in the x-y plane, they will be restricted in that plane. For the ODE system in the x-y plane in the body frame

$$\frac{dx}{dt} = \omega R y + \frac{\omega \varepsilon \ell y (2x^2 - y^2)}{3(x^2 + y^2)^{5/2}}\epsilon_0^2,$$

$$\frac{dy}{dt} = -\omega R x + \frac{\omega \varepsilon \ell x (x^2 + 4y^2)}{3(x^2 + y^2)^{5/2}}\epsilon_0^2.$$

Rewrite the equations and apply the integrating factor $\mu(x, y) = 3\sqrt{x^2 + y^2}$,

$$\left[3\omega R y \sqrt{x^2 + y^2} + \frac{\omega \varepsilon \ell \epsilon_0^2 y (2x^2 - y^2)}{(x^2 + y^2)^2}\right] dy$$

$$+ \left[3\omega R x \sqrt{x^2 + y^2} - \frac{\omega \varepsilon \ell \epsilon_0^2 x (x^2 + 4y^2)}{(x^2 + y^2)^2}\right] dx = 0$$

$$\implies d\left(\omega R (x^2 + y^2)^{\frac{3}{2}} - \frac{\omega \varepsilon \ell \epsilon_0^2}{2}\left(\log(x^2 + y^2) + \frac{3x^2}{x^2 + y^2}\right)\right) = 0.$$

190
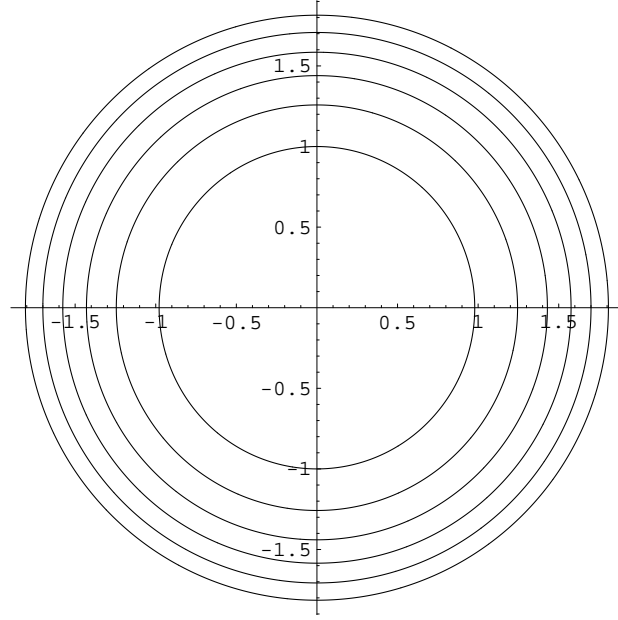
Figure 8.13: Contour plot for (8.20).

So, the far-field fluid particle trajectory equation in the x-y plane is

$$\omega R(x^2 + y^2)^{\frac{3}{2}} - \frac{\omega \varepsilon \ell \epsilon_0^2}{2} \left(\log(x^2 + y^2) + \frac{3x^2}{x^2 + y^2} \right) = \text{constant}. \qquad (8.20)$$

Figure 8.13 shows the contour plots of fluid particle trajectories (8.20), where the dominant flow is the rotating background flow.

In polar coordinates,

$$
\begin{aligned}
\frac{dx}{dt} &= \omega R r \sin \theta + \frac{\omega \varepsilon \ell \sin \theta (3 \cos^2 \theta - 1)}{3r^2} \epsilon_0^2, \\
\frac{dy}{dt} &= -\omega R r \cos \theta + \frac{\omega \varepsilon \ell \cos \theta (1 + 3 \sin^2 \theta)}{3r^3} \epsilon_0^2,
\end{aligned}
$$

191

and

$$\frac{d\theta}{dt} = \frac{\partial\theta}{\partial x}\frac{dx}{dt} + \frac{\partial\theta}{\partial y}\frac{dy}{dt} = -\frac{\sin\theta}{r}\frac{dx}{dt} + \frac{\cos\theta}{r}\frac{dy}{dt} = -\omega R + \frac{\omega\varepsilon\ell}{3r^3}\epsilon_0^2,$$

$$\frac{dr}{dt} = \frac{\partial r}{\partial x}\frac{dx}{dt} + \frac{\partial r}{\partial y}\frac{dy}{dt} = \cos\theta\frac{dx}{dt} + \sin\theta\frac{dy}{dt} = \frac{\omega\varepsilon\ell\epsilon_0^2\sin\theta\cos\theta}{r^2}.$$

Thus

$$\frac{d\theta}{dt} = -\omega R + \frac{\omega\varepsilon\ell}{3r^3}\epsilon_0^2,$$

$$\frac{dr}{dt} = \frac{\omega\varepsilon\ell\epsilon_0^2\sin\theta\cos\theta}{r^2}.$$

The far-field fluid particle trajectory in the polar coordinates in the body frame is

$$\omega Rr^3 - \omega\varepsilon\ell\epsilon_0^2\log(r) - \frac{3\omega\varepsilon\ell\epsilon_0^2}{2}\cos 2\theta = C = \text{constant.} \qquad (8.21)$$

Rewriting (8.21), we get

$$\cos 2\theta = 2\frac{\omega Rr^3 - \omega\varepsilon\ell\epsilon_0^2\log(r) - C}{3\omega\varepsilon\ell\epsilon_0^2}. \qquad (8.22)$$

Substitute the above equation into $\frac{dr}{dt}$,

$$\frac{dr}{dt} = \pm\epsilon_0^2\frac{\omega\varepsilon\ell\sqrt{1 - 4\left(\frac{\omega Rr^3 - \omega\varepsilon\ell\log(r) - C}{3\omega\varepsilon\ell\epsilon_0^2}\right)^2}}{2r^2}.$$

The equation shows the change in the radial direction can be captured only with higher order solutions, which verifies the results demonstrated with the contour plots.

In the laboratory frame   Change variables, the velocity field in the laboratory frame is

$$\mathbf{u}_L = -\mathbf{U}(\mathbf{x}^*) + R_\omega \mathbf{u}_b(R_\omega^T \mathbf{x}^*)$$

where $R_\omega = \begin{pmatrix} \cos(\omega t) & -\sin(\omega t) & 0 \\ \sin(\omega t) & \cos(\omega t) & 0 \\ 0 & 0 & 1 \end{pmatrix}$.

Thus,

$$\frac{dx_m}{dt} = \frac{\omega \varepsilon \ell \, (y\cos(\omega t) - x\sin(\omega t)) \, \left(3\,(x\cos(\omega t) + y\sin(\omega t))^2 - x^2 - y^2 \right)}{3(x^2 + y^2)^{5/2}} \epsilon_0^2,$$

$$\frac{dy_m}{dt} = \frac{\omega \varepsilon \ell \, (x\cos(\omega t) + y\sin(\omega t)) \, \left(x^2 + y^2 + 3\,(y\cos(\omega t) - x\sin(\omega t))^2 \right)}{3(x^2 + y^2)^{5/2}} \epsilon_0^2,$$

and

$$\frac{dx_L}{dt} = \cos(\omega t)\frac{dx_m}{dt} - \sin(\omega t)\frac{dy_m}{dt}$$

$$= \frac{\omega \varepsilon \ell \epsilon_0^2}{3(x^2 + y^2)^{5/2}} \left[-y(x^2 + y^2) + 3x^2 y \cos(2\omega t) - \frac{3}{2}x(x^2 - y^2)\sin(2\omega t) \right],$$

$$\frac{dy_L}{dt} = \sin(\omega t)\frac{dx_m}{dt} + \cos(\omega t)\frac{dy_m}{dt}$$

$$= \frac{\omega \varepsilon \ell \epsilon_0^2}{3(x^2 + y^2)^{5/2}} \left[x(x^2 + y^2) + 3xy^2 \cos(2\omega t) + \frac{3}{2}y(x^2 - y^2)\sin(2\omega t) \right].$$

In summary, the velocity in the x-y plane in the lab frame is

$$\frac{dx}{dt} = \frac{\omega \varepsilon \ell \epsilon_0^2}{3(x^2 + y^2)^{5/2}} \left[-y(x^2 + y^2) + 3x^2 y \cos(2\omega t) - \frac{3}{2}x(x^2 - y^2)\sin(2\omega t) \right],$$

$$\frac{dy}{dt} = \frac{\omega \varepsilon \ell \epsilon_0^2}{3(x^2 + y^2)^{5/2}} \left[x(x^2 + y^2) + 3xy^2 \cos(2\omega t) + \frac{3}{2}y(x^2 - y^2)\sin(2\omega t) \right].$$

Applying the transformation from the rectangular coordinates to the polar coordi-

nates

$$\begin{cases} x & = & r\cos\theta \\ y & = & r\sin\theta \end{cases} \quad \begin{cases} \frac{\partial r}{\partial x} & = & \cos\theta \\ \frac{\partial r}{\partial y} & = & \sin\theta \end{cases} \quad \begin{cases} \frac{\partial\theta}{\partial x} & = & -\frac{\sin\theta}{r} \\ \frac{\partial\theta}{\partial y} & = & \frac{\cos\theta}{r} \end{cases} \quad,$$

we have

$$\frac{dx}{dt} = \frac{\omega\varepsilon\ell\epsilon_0^2}{3r^2}\left[-\sin\theta + 3\cos^2\theta\sin\theta\cos(2\omega t) - \frac{3}{2}\cos\theta(\cos^2\theta - \sin^2\theta)\sin(2\omega t)\right],$$

$$\frac{dy}{dt} = \frac{\omega\varepsilon\ell\epsilon_0^2}{3r^2}\left[\cos\theta + 3\cos\theta\sin^2\theta\cos(2\omega t) + \frac{3}{2}\sin\theta(\cos^2\theta - \sin^2\theta)\sin(2\omega t)\right].$$

For the polar coordinates,

$$\frac{d\theta}{dt} = \frac{\partial\theta}{\partial x}\frac{dx}{dt} + \frac{\partial\theta}{\partial y}\frac{dy}{dt} = -\frac{\sin\theta}{r}\frac{dx}{dt} + \frac{\cos\theta}{r}\frac{dy}{dt}$$

$$= \frac{\omega\varepsilon\ell\epsilon_0^2}{r^3}\left[\frac{1}{3} + \frac{1}{4}\sin 4\theta\sin(2\omega t)\right],$$

$$\frac{dr}{dt} = \frac{\partial r}{\partial x}\frac{dx}{dt} + \frac{\partial r}{\partial y}\frac{dy}{dt} = \cos\theta\frac{dx}{dt} + \sin\theta\frac{dy}{dt}$$

$$= \frac{\omega\varepsilon\ell\epsilon_0^2}{3r^2}\left[\frac{3}{2}\sin 2\theta\cos(2\omega t) - \frac{3}{2}\cos^2 2\theta\sin(2\omega t)\right].$$

Define the average as $\bar{f}(\cdot) = \frac{1}{T}\int_0^T f(\cdot, t)dt$, then the average equations for the fluid motion are

$$\begin{cases} \frac{d\bar{\theta}}{dt} & = & \frac{\omega\varepsilon\ell\epsilon_0^2}{3r^3} \\ \frac{d\bar{r}}{dt} & = & 0 \end{cases} \Longrightarrow \begin{cases} \bar{\theta} & = & \frac{\omega\varepsilon\ell\epsilon_0^2}{3r(0)^3}t \\ \bar{r} & = & r(0) \end{cases}. \tag{8.23}$$

From the averaged equation, the radial component of the fluid particle trajectory is a constant. The azimuthal angle is a monotonic function of time t.

From the equation of fluid particle trajectory in the body frame (8.20)

$$\omega R(x^2 + y^2)^{\frac{3}{2}} - \frac{\omega \varepsilon \ell \epsilon_0^2}{2}\left(\log(x^2 + y^2) + \frac{3x^2}{x^2 + y^2}\right) = \text{constant},$$

and the relations:

From body frame to lab frame,

$$\begin{pmatrix} x_L \\ y_L \\ z_L \end{pmatrix} = \begin{pmatrix} \cos(\omega t) & -\sin(\omega t) & 0 \\ \sin(\omega t) & \cos(\omega t) & 0 \\ 0 & 0 & 1 \end{pmatrix} \begin{pmatrix} x_b \\ y_b \\ z_b \end{pmatrix} = \begin{pmatrix} x_b \cos(\omega t) - y_b \sin(\omega t) \\ y_b \cos(\omega t) + x_b \sin(\omega t) \\ z_b \end{pmatrix}$$

From the lab frame to the body frame,

$$\begin{pmatrix} x_b \\ y_b \\ z_b \end{pmatrix} = \begin{pmatrix} \cos(\omega t) & \sin(\omega t) & 0 \\ -\sin(\omega t) & \cos(\omega t) & 0 \\ 0 & 0 & 1 \end{pmatrix} \begin{pmatrix} x_L \\ y_L \\ z_L \end{pmatrix} = \begin{pmatrix} x_L \cos(\omega t) + y_L \sin(\omega t) \\ y_L \cos(\omega t) - x_L \sin(\omega t) \\ z_L \end{pmatrix},$$

the equation of trajectory in the laboratory frame is

$$\omega R(x^2 + y^2)^{\frac{3}{2}} - \frac{\omega \varepsilon \ell \epsilon_0^2}{2}\left(\log(x^2 + y^2) + \frac{3(x \cos(\omega t) + y \sin(\omega t))^2}{x^2 + y^2}\right) = \text{constant}.$$

Sometime (x, y, z) are used in both the body frame and the lab frame without subscription, if we specify the frame. In polar coordinates, it is

$$\omega R r^3 - \frac{\omega \varepsilon \ell \epsilon_0^2}{2}\left(\log(r^2) + 3(\cos\theta\cos(\omega t) + \sin\theta\sin(\omega t))^2\right) = \text{constant},$$

$$\omega R r^3 - \omega \varepsilon \ell \epsilon_0^2 \log(r) - \frac{3\omega \varepsilon \ell \epsilon_0^2}{2}\cos^2(\theta - \omega t) = \text{constant}.$$

Figure 8.14 and 8.15 show the comparison of the far-field fluid particle trajectories with the averaged trajectory.
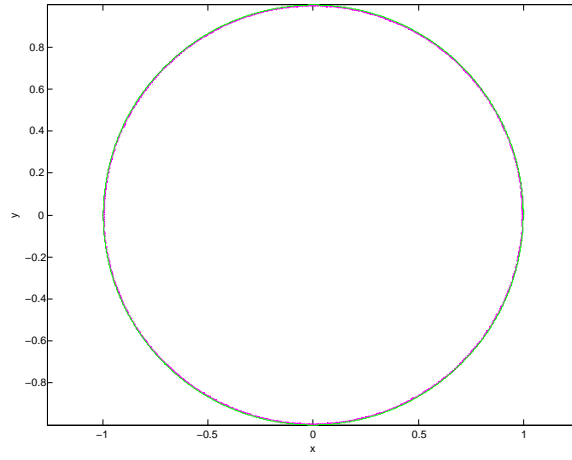
Figure 8.14: Contour plot for exact solution (8.20) (purple) of the far-field trajectory and the averaged trajectory from (8.23) (green).
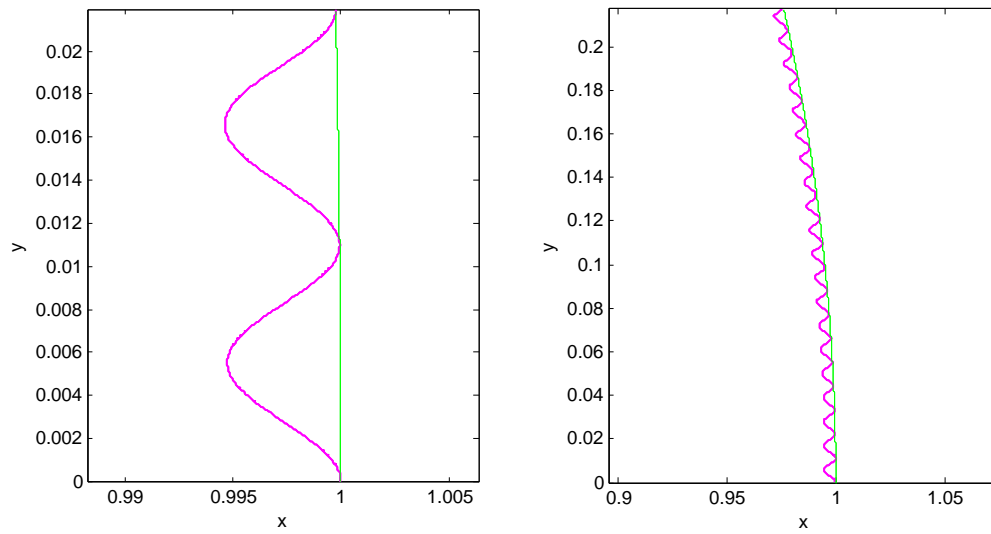
Figure 8.15: Zoom in on Figure 8.14.

8.5 Flux through a vertical plane at $y = y_0$

To better under the flow induced by the slender rod, we study the flux through a vertical plane at $y = y_0$ far from the body. During one period of the slender body motion, the rotation of the slender body in phase 2 can be viewed as the reverse of rotation in phase 4. Due to reversibility of the Stokes flow, the total flux introduced by these two phases equals to each other by neglecting the different of the distance. Thus, we only compute the flux during the uniform translations, which is the dominant part of the total flux.

The equation of flux F at an instantaneous time t through the vertical plane $(x, z) \in (-L, L) \times (-H, H)$ at $y = y_0$ is

$$F = \int_{-H}^{H} dz \int_{-L}^{L} dx \left. \frac{dy}{dt} \right|_{y=y_0}.$$

8.5.1 Flux during the horizontal shift

In phase 1, the slender body shift perpendicular to its axis. During this horizontal shift, the velocity component $\frac{dy}{dt}$ in the body frame at $y = y_0$ is

$$
\begin{aligned}
\left. \frac{dy}{dt} \right|_{y=y_0} = \ & -U + \alpha_2 \log \left(\frac{\ell - x + \sqrt{r^2 + (\ell - x)^2}}{-\ell - x + \sqrt{r^2 + (\ell + x)^2}} \right) \\
& + \frac{y^2 \alpha_2}{r^2} \left[\frac{\ell - x}{\sqrt{r^2 + (\ell - x)^2}} - \frac{-\ell - x}{\sqrt{r^2 + (\ell + x)^2}} \right],
\end{aligned}
$$

where $r^2 = y_0^2 + z^2$. In the laboratory frame, it is

$$\frac{dy}{dt}\Big|_{y=y_0} = \alpha_2 \left[\log \left(\frac{\ell + \sqrt{(y_0 - Ut)^2 + z^2 + (\ell - x)^2} - x}{-\ell + \sqrt{(y_0 - Ut)^2 + z^2 + (\ell + x)^2} - x} \right) \right.$$
$$\left. + \frac{(y_0 - Ut)^2}{r^2} \left(\frac{\ell - x}{\sqrt{(y_0 - Ut)^2 + z^2 + (\ell - x)^2}} + \frac{\ell + x}{\sqrt{(y_0 - Ut)^2 + z^2 + (\ell + x)^2}} \right) \right].$$

Flux during phase 1 through the plane at $y = y_0$ is

$$\text{Flux}_1(\alpha_2, L, y, H, U, \ell, t) = \int_{-H}^{H} dz \int_{-L}^{L} dx \frac{dy}{dt}\Big|_{y=y_0}$$
$$= \alpha_2 \int_{-H}^{H} dz \int_{-L}^{L} dx \log \left(\frac{\ell + \sqrt{(y_0 - Ut)^2 + z^2 + (\ell - x)^2} - x}{-\ell + \sqrt{(y_0 - Ut)^2 + z^2 + (\ell + x)^2} - x} \right)$$
$$+ \alpha_2 \int_{-H}^{H} dz \int_{-L}^{L} dx \frac{(y_0 - Ut)^2}{r^2} \left(\frac{\ell - x}{\sqrt{(y_0 - Ut)^2 + z^2 + (\ell - x)^2}} + \frac{\ell + x}{\sqrt{(y_0 - Ut)^2 + z^2 + (\ell + x)^2}} \right)$$
$$= \alpha_2 \left\{ 2H \left(\sqrt{H^2 + (\ell - L)^2 + (y - Ut)^2} - \sqrt{H^2 + (\ell + L)^2 + (y - Ut)^2} \right) \right.$$
$$+ ((\ell - L)^2 + (y - Ut)^2) \log \left(\frac{-H + \sqrt{H^2 + (\ell - L)^2 + (y - Ut)^2}}{H + \sqrt{H^2 + (\ell - L)^2 + (y - Ut)^2}} \right)$$
$$- ((\ell + L)^2 + (y - Ut)^2) \log \left(\frac{-H + \sqrt{H^2 + (\ell + L)^2 + (y - Ut)^2}}{H + \sqrt{H^2 + (\ell + L)^2 + (y - Ut)^2}} \right)$$
$$- 2H(\ell - L) \log \left(\frac{\ell - L + \sqrt{H^2 + (\ell - L)^2 + (y - Ut)^2}}{-\ell + L + \sqrt{H^2 + (\ell - L)^2 + (y - Ut)^2}} \right)$$
$$\left. + 2H(\ell + L) \log \left(\frac{\ell + L + \sqrt{H^2 + (\ell + L)^2 + (y - Ut)^2}}{-\ell - L + \sqrt{H^2 + (\ell + L)^2 + (y - Ut)^2}} \right) \right\}.$$

As $y \to \infty$,

$$\text{Flux}_1(\alpha_2, L, y, H, U, \ell, t) \sim \frac{16\alpha_2 H\ell L}{y}.$$

When $x \to \infty$,

$$\text{Flux}_1(\alpha_2, L, y, H, U, \ell, t) \sim 8\alpha_2 H\ell \left(\log(L) + 1 \right) + 4\alpha_2 H\ell \log \left(\frac{4}{H^2 + (y - Ut)^2} \right).$$

When $z \to \infty$,

$$\text{Flux}_1(\alpha_2, L, y, H, U, \ell, t) \sim 8\alpha_2 \ell L \log(H) + 4\alpha_2 \ell L(3 + \log(4))$$
$$+\alpha_2 \left\{ \left[(\ell - L)^2 + (y - Ut)^2 \right] \log \left[(\ell - L)^2 + (y - Ut)^2 \right] - \right.$$
$$\left. \left[(\ell + L)^2 + (y - Ut)^2 \right] \log \left[(\ell + L)^2 + (y - Ut)^2 \right] \right\}.$$

8.5.2 Flux during the longitudinal translation

In phase 3, the slender body translates longitudinally along its axis. The velocity component u_2 in the body frame is

$$\frac{dy}{dt} = U + \alpha_2 \left[2 \log \left(\frac{\ell + \sqrt{r^2 + (\ell - y)^2} - y}{-\ell + \sqrt{r^2 + (\ell + y)^2} - y} \right) - \frac{\ell - y}{\sqrt{r^2 + (\ell - y)^2}} - \frac{\ell + y}{\sqrt{r^2 + (\ell + y)^2}} \right],$$

where $r^2 = x^2 + z^2$. In the laboratory frame, it is

$$\frac{dy}{dt} = 2\alpha_2 \log \left(\frac{\ell + \sqrt{r^2 + (\ell - y - UT_1 - Ut)^2} - (y - UT_1 + Ut)}{-\ell + \sqrt{r^2 + (\ell + y - UT_1 + Ut)^2} - (y - UT_1 + Ut)} \right)$$
$$+ \alpha_2 \left(-\frac{\ell - y + UT_1 - Ut}{\sqrt{r^2 + (\ell - y + UT_1 - Ut)^2}} - \frac{\ell + y - UT_1 + Ut}{\sqrt{r^2 + (\ell + y - UT_1 + Ut)^2}} \right).$$

At $y = y_0$,

$$\frac{dy}{dt} \bigg|_{y=y_0} = 2\alpha_2 \log \left(\frac{\ell + \sqrt{r^2 + (\ell - y_0 - UT_1 - Ut)^2} - (y_0 - UT_1 + Ut)}{-\ell + \sqrt{r^2 + (\ell + y_0 - UT_1 + Ut)^2} - (y_0 - UT_1 + Ut)} \right)$$
$$+ \alpha_2 \left(-\frac{\ell - y_0 + UT_1 - Ut}{\sqrt{r^2 + (\ell - y_0 + UT_1 - Ut)^2}} - \frac{\ell + y_0 - UT_1 + Ut}{\sqrt{r^2 + (\ell + y_0 - UT_1 + Ut)^2}} \right)$$

Flux during phase 3 at the vertical plane $y = y_0$ is

$$\text{Flux}_3(\alpha_2, L, y, H, U, \ell, t) = \int_{-H}^{H} dz \int_{-L}^{L} dx \left. \frac{dy}{dt} \right|_{y=y_0}$$
$$= \alpha_2 \int_{-H}^{H} dz \int_{-L}^{L} dx \int_{-\ell}^{\ell} \left\{ \frac{1}{\left[(y-s)^2 + r^2 \right]^{1/2}} + \frac{(y-s)^2}{\left[(y-s)^2 + r^2 \right]^{\frac{3}{2}}} \right\} ds$$

Explicitly,

$$\text{Flux}_3(\alpha_2, L, y, H, U, \ell, t)$$

$$= -2\alpha_2 \left\{ 2L^2 \left[\arctan\left(\frac{H(\ell-y)}{L\sqrt{H^2+L^2+(y-\ell)^2}} \right) + \arctan\left(\frac{H(\ell+y)}{L\sqrt{H^2+L^2+(\ell+y)^2}} \right) \right] \right.$$

$$+2H^2 \left[\arctan\left(\frac{L(\ell-y)}{H\sqrt{H^2+L^2+(y-\ell)^2}} \right) + \arctan\left(\frac{L(\ell+y)}{H\sqrt{H^2+L^2+(\ell+y)^2}} \right) \right]$$

$$+L(\ell-y)\log\left(\frac{-H+\sqrt{H^2+L^2+(y-\ell)^2}}{H+\sqrt{H^2+L^2+(y-\ell)^2}} \right) + H(\ell-y)\log\left(\frac{-L+\sqrt{H^2+L^2+(y-\ell)^2}}{L+\sqrt{H^2+L^2+(y-\ell)^2}} \right)$$

$$-L(\ell+y)\log\left(\frac{H+\sqrt{H^2+L^2+(\ell+y)^2}}{-H+\sqrt{H^2+L^2+(\ell+y)^2}} \right) - H(\ell+y)\log\left(\frac{L+\sqrt{H^2+L^2+(\ell+y)^2}}{-L+\sqrt{H^2+L^2+(\ell+y)^2}} \right)$$

$$\left. +4HL\log\left(\frac{-\ell-y+\sqrt{H^2+L^2+(\ell+y)^2}}{\ell-y+\sqrt{H^2+L^2+(y-\ell)^2}} \right) \right\}.$$

As $y \to \infty$,

$$\text{Flux}_3(\alpha_2, L, y, H, U, \ell, t) \sim \frac{16\alpha_2 H\ell L}{y}.$$

When $x \to \infty$,

$$\text{Flux}_3(\alpha_2, L, y, H, U, \ell, t)$$

$$\sim \quad 8\alpha_2 H\ell \log(L) - 2H\alpha_2 \left\{ -8\ell + 2H \left[\arctan\left(\frac{\ell-y}{H} \right) + \arctan\left(\frac{\ell+y}{H} \right) \right] \right.$$

$$\left. +(\ell-y)\log\left(\frac{H^2+(y-\ell)^2}{4} \right) - (\ell+y)\log\left(\frac{4}{H^2+(\ell+y)^2} \right) \right\}.$$

As $z \to \infty$,

$$\text{Flux}_3(\alpha_2, L, y, H, U, \ell, t)$$

$$\sim \quad 8\alpha_2 L\ell \log(H) - 2L\alpha_2 \left\{ -8\ell + 2L \left[\arctan\left(\frac{\ell-y}{L} \right) + \arctan\left(\frac{\ell+y}{L} \right) \right] \right.$$

$$\left. +(\ell-y)\log\left(\frac{L^2+(y-\ell)^2}{4} \right) - (\ell+y)\log\left(\frac{4}{L^2+(\ell+y)^2} \right) \right\}.$$

Chapter 9

Conclusions and future work

This thesis reports mainly as two parts about flow patterns and flow and rigid obstacles interactions in the Stokes regime. The first part focuses on the analytical and numerical study of Stokes linear shear or rotating flow past a sphere or spheroid. In the second part, the rigid bodies in the flow are irregular compared to spheres or spheroids. We experimentally and theoretically study the flow induced by a slender rod either straight or bent sweeping out a cone above a no-slip plane.

In the first part, based on the velocity field of a rigid sphere immersed in a linear shear flow, we have derived the fluid particle trajectory equations in closed quadrature when the sphere's center is in the zero-velocity of the background linear shear. Using the trajectory equations, we have obtained the explicit formula for the stagnation points on the sphere and explored the blocking phenomenon in the streamlines. The cross-sectional area of the blocked flow at infinity equals infinity, which is a physically unobserved property of the Stokes flow. With linearized velocity field near the surface of sphere, we have found the explicit formula for the imprint on the sphere, where the no-slip boundary is imposed.

If the sphere's center is out of the zero-velocity plane blocking phenomenon is captured numerically. Starting from the velocity field, we find the analytical results for the stagnation points and the critical points in the interior of the flow. Complicated

bifurcation structures are studied in terms of the dimensionless distance, U, from the center of the sphere to the zero-velocity plane of the background linear shear. A 3D eddy appears with special values of U. With linearized velocity near the surface of the sphere, the trajectory of the imprint is also achieved.

If the sphere is fixed in the linear shear flow, there is no closed streamline emerged in contrast to the well-known closed orbits for the linear shear past a freely rotating cylinder or sphere [23, 1, 42, 62, 53, 77, 54]. We have reviewed the linear shear past a freely rotating sphere and estimate the height of the closed streamline near the sphere, when the sphere's center is in the zero-velocity plane. When the sphere is embedded in purely rotating background flows, the explicit fluid particle trajectory equation and stagnation points in the flow are obtained.

When the embedded rigid body becomes a prolate spheroid, we study the case when the center of the spheroid is in the zero-velocity plane of the background shear. The orientational spheroid is either upright or tilted in the symmetry plane of the flow, along or against the background streamline. Even though the trajectory equation is not available explicitly, the blocking phenomenon has been illustrated numerically. We have found the critical points in the interior of the flow, and derived the formula of the stagnation points on the spheroid. We have also checked how stagnation points migrate as the eccentricity of the spheroid changes.

If the major axis of the spheroid is perpendicular to the background stream (upright), the flow structure is similar to the spherical case. When the spheroid is tilted, the broken symmetry offered by a tilted spheroid geometry induces new three-dimensional effects on streamline deflection. The deflection can be viewed as effective positive or negative suction in the horizontal direction orthogonal to the background flow depending on the tilt orientation.

While our findings have led to improved understanding about shear flows past an

obstacle, they have been limited to the Stokes flow regime. It will be useful to improve the physical description of the flow if we can include the Oseen correction into the governing equations, thus take into account the inertial effects of real fluids. This would lead to finding a correction for the blockage area we computed in the Stokes limit, possibly making it finite. We also want to design an experiment based on these theoretical studies. This will allow for the assessment of effects of boundary conditions at a finite range. Moreover, the investigation of general linear unsteady Stokes flows past rigid bodies will be interesting. Such problems have natural implications in the rheology of complex fluids and fluid-solid mixtures, applications to micro-fluidic mixing devices and their biological counterparts.

In the second part of this thesis, we have aimed to understand flows induced by a slender rod precessing in a cone that mimics the motion of primary nodal cilia. We have studied the flow with the 3D experiment, theoretical modeling and numerics. For the straight rod case, we study the flow generated by the straight rod sweeping out a tilted cone, which carries time information both in the laboratory frame and in the body frame. Near the cone, the fluid particle follows a small time scale epicycle corresponding to almost one revolution of the rod and a long time orbit surround the cone, which is similar to the trajectory with an upright cone. Due to the tilt, depending on the scale of the large orbit, the trajectory is deformed dramatically with respect to the no-slip plane. For the upright cone, except the fluctuation during each epicycle, the trajectory stays at the relatively fixed level. Both closed periodic trajectories and open trajectories are observed, which is a new phenomena introduced by the tilt. Flux through a vertical plane parallel to the cone axis is evaluated to show the fluid transport. Using the dynamic cone angle and approximate convection detected from the experiments, the experimental and theoretical data show excellent agreement.

For the bent rod sweeping a cone above the no-slip plane, a toroidal structure

203

has been captured. In a short or intermediate time, the fluid particle trajectories are similar to the straight rod case. Over very long time scale, the particle trajectory stay on the surface of a torus. Using the Poincaré map as an effective tool, we have examined the multiple parameters that have influences on the tori. Both our model and the experiment have verified this toroidal structure in the fluid particle trajectories. With fully 3D experimental ability, we quantitatively compare the model with the experiment. However, the discrepancies show up in a short time comparison of the trajectories. Possible issues have been discussed. We have reported the relative studies for simplified flows.

We have only studied the flow generated by rigid rods. However, our model is feasible to extend to flexible cilia with small curvatures. In the future, we want to study the flexible rod with small curvatures. It will be interesting to further model flows induced by multiple cilia, study hydrodynamic interactions between separated cilia, and assess wall effects in the flow in the future work. Increased fidelity of the models could be achieved by investigating non-Newtonian effects naturally existing in biological contexts.

Appendix A

Fundamental singularities and the slender body theory

The fundamental singularities used in this thesis are listed without the details about the derivation and their components. Details could be referred to Chwang & Wu [19] and Leiterman [48]. In addition, the slender body theory is briefly summarized with emphasis on the strength ratio with respect to the velocity field [3]. The purpose of the repetition is to make the thesis self-contained.

A.1 Singularities

For Stokes flows, fundamental singular solutions are available, which are useful for constructing solutions for more complicated boundary conditions. The Stokeslet $\mathbf{u}_{\mathrm{S}}$ is a fundamental solution of the Stokes equation for a single point force,

$$
\begin{aligned}
\mu \nabla^2 \mathbf{u} + \mathbf{f}_{\mathrm{S}} &= \nabla p, \\
\nabla \cdot \mathbf{u} &= 0,
\end{aligned}
\tag{A.1}
$$

where $\mathbf{f}_{\mathrm{S}} = 8\pi\mu\boldsymbol{\alpha}\delta(\mathbf{x})$, and

$$
\begin{aligned}
\mathbf{u}_{\mathrm{S}}(\mathbf{x}; \boldsymbol{\alpha}) &= \frac{\boldsymbol{\alpha}}{|\mathbf{x}|} + \frac{(\mathbf{x} \cdot \boldsymbol{\alpha})\mathbf{x}}{|\mathbf{x}|^3} \\
p_{\mathrm{S}}(\mathbf{x}; \boldsymbol{\alpha}) &= -2\mu \frac{\mathbf{x} \cdot \boldsymbol{\alpha}}{|\mathbf{x}|^3}.
\end{aligned}
$$

Here $\boldsymbol{\alpha}$ is the strength of the singularity located at the origin, $\mathbf{x} = (x, y, z)$ and $|\mathbf{x}| = \sqrt{x^2 + y^2 + z^2}$. Due to the linear property of the Stokes equations, a derivative of any order of $\mathbf{u}_S$ and $p_S(\mathbf{x}; \boldsymbol{\alpha})$ is also a solution of (A.1) with corresponding derivative of $\mathbf{f}_S$. The Stokes doublet is

$$\mathbf{u}_{SD}(\mathbf{x}; \boldsymbol{\alpha}, \boldsymbol{\beta}) = -(\boldsymbol{\beta} \cdot \nabla)\mathbf{u}_S(\mathbf{x}; \boldsymbol{\alpha}) = \frac{(\boldsymbol{\beta} \times \boldsymbol{\alpha}) \times \mathbf{x}}{|\mathbf{x}|^3} - \frac{(\boldsymbol{\alpha}.\boldsymbol{\beta})\mathbf{x}}{|\mathbf{x}|^3} + 3\frac{(\boldsymbol{\alpha} \cdot \mathbf{x})(\boldsymbol{\beta} \cdot \mathbf{x})\mathbf{x}}{|\mathbf{x}|^5}.$$

The symmetric component of a Stokes doublet is a stresslet

$$\mathbf{u}_{SS}(\mathbf{x}; \boldsymbol{\alpha}, \boldsymbol{\beta}) = \frac{1}{2}[\mathbf{u}_{SD}(\mathbf{x}; \boldsymbol{\beta}, \boldsymbol{\alpha}) + \mathbf{u}_{SD}(\mathbf{x}; \boldsymbol{\alpha}, \boldsymbol{\beta})] = -\frac{(\boldsymbol{\alpha} \cdot \boldsymbol{\beta})\mathbf{x}}{|\mathbf{x}|^3} + \frac{3(\boldsymbol{\alpha} \cdot \mathbf{x})(\boldsymbol{\beta} \cdot \mathbf{x})\mathbf{x}}{|\mathbf{x}|^5}.$$

The antisymmetric component of a Stokes doublet is Rotlet or couplet

$$\mathbf{u}_R(\mathbf{x}; \boldsymbol{\gamma}) = \frac{1}{2}[\mathbf{u}_{SD}(\mathbf{x}; \boldsymbol{\beta}, \boldsymbol{\alpha}) - \mathbf{u}_{SD}(\mathbf{x}; \boldsymbol{\alpha}, \boldsymbol{\beta})] = \frac{1}{2}\nabla \times \mathbf{u}_S(\mathbf{x}; \boldsymbol{\gamma}) = \frac{\boldsymbol{\gamma} \times \mathbf{x}}{|\mathbf{x}|^3},$$

where $\boldsymbol{\gamma} = \boldsymbol{\alpha} \times \boldsymbol{\beta}$.

A potential doublet is

$$\mathbf{u}_D(\mathbf{x}; \boldsymbol{\delta}) = \frac{1}{2}\nabla^2 \times \mathbf{u}_S(\mathbf{x}; \boldsymbol{\delta}) = -\frac{\boldsymbol{\delta}}{|\mathbf{x}|^3} + \frac{3(\boldsymbol{\delta} \cdot \mathbf{x})\mathbf{x}}{|\mathbf{x}|^5},$$

where $\boldsymbol{\delta}$ is the doublet strength.

A.2   Canonical results of the slender body theory

Many important applications of Stokes flow involves elongated particles, such as slender rods and glass and carbon fibres. However, analytical solutions exist for a limited range of particle shapes, for example, sphere and spheroid. Consider the body is slender, i.e., its length 2ℓ is much larger than its radius r_0, asymptotic solutions

to the equation of fluid flow can be constructed by slender-body theory, which is first developed by Burgers [13].

The velocity field due to the presence of the body is approximated by a distribution of Stokeslets along the center-line of the body,

$$\mathbf{u}(\mathbf{x}) = \int_{-\ell}^{\ell} \mathbf{u}_S(\mathbf{x} - \mathbf{x}_s; \boldsymbol{\alpha}) ds, \tag{A.2}$$

where $\mathbf{x}$ is the observation position and $\mathbf{x}_s$ is the location of the Stokeslet depending on s. If the body is along the x-axis and Stokeslets are distributed over the portion $-\ell \leq x \leq \ell$ of the x axis, the canonical results for uniform flow (U_1, U_2, U_3) past a rigid cylindrical body are restated here.

Assume the strength of the Stokeslet $\boldsymbol{\alpha}$ is uniform, a constant vector, then the total velocity field is

$$u_1(\mathbf{x}) = U_1 - \alpha_1 \int_{-\ell}^{\ell} \frac{1}{\sqrt{(x-s)^2 + y^2 + z^2}} ds - \alpha_1 \int_{-\ell}^{\ell} \frac{(x-s)^2}{((x-s)^2 + y^2 + z^2)^{\frac{3}{2}}} ds$$
$$- (\alpha_2 y + \alpha_3 z) \int_{-\ell}^{\ell} \frac{(x-s)}{((x-s)^2 + y^2 + z^2)^{\frac{3}{2}}} ds,$$

$$u_2(\mathbf{x}) = U_2 + \alpha_2 \int_{-\ell}^{\ell} \frac{1}{\sqrt{(x-s)^2 + y^2 + z^2}} ds - \alpha_1 y \int_{-\ell}^{\ell} \frac{(x-s)}{((x-s)^2 + y^2 + z^2)^{\frac{3}{2}}} ds$$
$$- (\alpha_2 y^2 + \alpha_3 y z) \int_{-\ell}^{\ell} \frac{1}{((x-s)^2 + y^2 + z^2)^{\frac{3}{2}}} ds,$$

$$u_3(\mathbf{x}) = U_3 - \alpha_3 \int_{-\ell}^{\ell} \frac{1}{\sqrt{(x-s)^2 + y^2 + z^2}} ds - \alpha_1 z \int_{-\ell}^{\ell} \frac{(x-s)}{((x-s)^2 + y^2 + z^2)^{\frac{3}{2}}} z ds$$
$$- (\alpha_2 y z + \alpha_3 z^2) \int_{-\ell}^{\ell} \frac{1}{((x-s)^2 + y^2 + z^2)^{\frac{3}{2}}} z ds,$$

To determine the strength $\boldsymbol{\alpha}$, we impose the no-slip boundary condition on the surface

of the slender body $y_0^2 + z_0^2 = r_0^2$ and $-\ell \le x_0 \le \ell$.

$$
\begin{aligned}
0 &= U_1 - \alpha_1 \int_{-\ell}^{\ell} \frac{1}{\sqrt{(x_0 - s)^2 + r_0^2}} ds - \alpha_1 \int_{-\ell}^{\ell} \frac{(x_0 - s)^2}{((x_0 - s)^2 + r_0^2)^{\frac{3}{2}}} ds \\
&\quad - (\alpha_2 y_0 + \alpha_3 z_0) \int_{-\ell}^{\ell} \frac{(x_0 - s)}{((x - s)^2 + r_0^2)^{\frac{3}{2}}} ds, \\
0 &= U_2 - \alpha_2 \int_{-\ell}^{\ell} \frac{1}{\sqrt{(x_0 - s)^2 + r_0^2}} ds - \alpha_1 y_0 \int_{-\ell}^{\ell} \frac{(x_0 - s)}{((x_0 - s)^2 + r_0^2)^{\frac{3}{2}}} ds \\
&\quad - (\alpha_2 y_0^2 + \alpha_3 y_0 z_0) \int_{-\ell}^{\ell} \frac{1}{((x - s)^2 + r_0^2)^{\frac{3}{2}}} ds, \\
0 &= U_3 - \alpha_3 \int_{-\ell}^{\ell} \frac{1}{\sqrt{(x_0 - s)^2 + r_0^2}} ds - \alpha_1 z_0 \int_{-\ell}^{\ell} \frac{(x_0 - s)}{((x_0 - s)^2 + r_0^2)^{\frac{3}{2}}} z_0 ds \\
&\quad - (\alpha_2 y_0 z_0 + \alpha_3 z_0^2) \int_{-\ell}^{\ell} \frac{1}{((x_0 - s)^2 + r_0^2)^{\frac{3}{2}}} z ds,
\end{aligned}
$$

Away from the ends of the slender body, as the radius of the body $r_0 \to 0$,

$$
\begin{aligned}
\int_{-\ell}^{\ell} \frac{1}{\sqrt{(x_0 - s)^2 + r_0^2}} ds &= \log\left(s + \sqrt{r_0^2 + (s - x_0)^2} - x_0 \right) \Big|_{s=-\ell}^{s=\ell} \\
&= \log\left(\frac{\sqrt{\left(\frac{r_0}{\ell}\right)^2 + \left(1 - \frac{x_0}{\ell}\right)^2} + \left(1 - \frac{x_0}{\ell}\right)}{\sqrt{\left(\frac{r_0}{\ell}\right)^2 + \left(1 + \frac{x_0}{\ell}\right)^2} - \left(1 + \frac{x_0}{\ell}\right)} \right) \sim \log\left(\frac{\left(1 - \frac{x_0}{\ell}\right) + \frac{\left(\frac{r_0}{\ell}\right)^2}{2\left(1-\frac{x_0}{\ell}\right)} + \left(1 - \frac{x_0}{\ell}\right)}{\left(1 + \frac{x_0}{\ell}\right) + \frac{\left(\frac{r_0}{\ell}\right)^2}{2\left(1+\frac{x_0}{\ell}\right)} - \left(1 + \frac{x_0}{\ell}\right)} \right) \\
&= \log\left(\frac{2\left(1 - \frac{x_0}{\ell}\right) 2\left(1 + \frac{x_0}{\ell}\right) + \frac{\left(\frac{r_0}{\ell}\right)^2}{\left(1-\frac{x_0}{\ell}\right)}\left(1 + \frac{x_0}{\ell}\right)}{\left(\frac{r_0}{\ell}\right)^2} \right) \\
&\sim \log\left(\frac{4\left(1 - \frac{x_0}{\ell}\right)\left(1 + \frac{x_0}{\ell}\right)}{\left(\frac{r_0}{\ell}\right)^2} \right) = 2\log\left(\frac{2\ell}{r_0}\right) + \log\left(1 - \left(\frac{x_0}{\ell}\right)^2\right)
\end{aligned}
$$

Note $\epsilon = \log\left(\frac{2\ell}{r_0}\right)^{-1}$ as the slenderness parameter, then

$$
\int_{-\ell}^{\ell} \frac{1}{\sqrt{(x_0 - s)^2 + r_0^2}} ds \sim \frac{2}{\epsilon}
$$

208

Also,

$$\int_{-\ell}^{\ell} \frac{1}{\left((x_0 - s)^2 + r_0^2\right)^{3/2}} ds = \left. \frac{s - x_0}{r_0^2 \sqrt{r_0^2 + (s - x_0)^2}} \right|_{s=-\ell}^{s=\ell}$$

$$= \frac{\ell - x_0}{r_0^2 \sqrt{r_0^2 + (\ell - x_0)^2}} + \frac{\ell + x_0}{r_0^2 \sqrt{r_0^2 + (\ell + x_0)^2}}$$

$$= \frac{1}{r_0^2} \left(\frac{1 - \frac{x_0}{\ell}}{\sqrt{\left(\frac{r_0}{\ell}\right)^2 + \left(1 - \frac{x_0}{\ell}\right)^2}} + \frac{1 + \frac{x_0}{\ell}}{\sqrt{\left(\frac{r_0}{\ell}\right)^2 + \left(1 + \frac{x_0}{\ell}\right)^2}} \right)$$

$$\sim \frac{1}{r_0^2} \left(2 - \frac{1}{2} \left(\frac{\ell^2}{(\ell - x_0)^2} + \frac{\ell^2}{(\ell + x_0)^2} \right) \left(\frac{r_0}{\ell}\right)^2 \right)$$

So, the leading order is

$$\int_{-\ell}^{\ell} \frac{1}{\left((x_0 - s)^2 + r_0^2\right)^{3/2}} ds \quad \sim \quad \frac{2}{r_0^2}, \text{ as } r_0 \to 0.$$

Since

$$\int_{-\ell}^{\ell} \frac{(x_0 - s)}{\left((x_0 - s)^2 + r_0^2\right)^{3/2}} ds = \left. \frac{1}{\sqrt{r_0^2 + (s - x_0)^2}} \right|_{s=-\ell}^{s=\ell}$$

$$= \frac{1}{\sqrt{r_0^2 + (\ell - x_0)^2}} - \frac{1}{\sqrt{r_0^2 + (\ell + x_0)^2}}$$

$$= \frac{1}{\ell} \left(\frac{1}{\sqrt{\left(\frac{r_0}{\ell}\right)^2 + \left(1 - \frac{x_0}{\ell}\right)^2}} - \frac{1}{\sqrt{\left(\frac{r_0}{\ell}\right)^2 + \left(1 + \frac{x_0}{\ell}\right)^2}} \right)$$

$$\sim \frac{1}{\ell} \left(\frac{1}{1 - \frac{x_0}{\ell}} - \frac{1}{1 + \frac{x_0}{\ell}} + \left(-\frac{1}{2(\ell - x_0)^3} + \frac{1}{2(\ell + x_0)^3} \right) \left(\frac{r_0}{\ell}\right)^2 \right),$$

the leading order of this integral is

$$\int_{-\ell}^{\ell} \frac{(x_0 - s)}{\left((x_0 - s)^2 + r_0^2\right)^{3/2}} ds \sim \frac{1}{\ell - x_0} - \frac{1}{\ell + x_0}.$$

From the above results,

$$\int_{-\ell}^{\ell} \frac{(x_0 - s)^2}{((x_0 - s)^2 + r_0^2)^{3/2}} ds = \int_{-\ell}^{\ell} \frac{1}{\sqrt{(x_0 - s)^2 + r_0^2}} ds - \int_{-\ell}^{\ell} \frac{r_0^2}{((x_0 - s)^2 + r_0^2)^{3/2}} ds$$

$$\sim \frac{2}{\epsilon}$$

In summary, the boundary conditions are

$$\begin{aligned}
0 &= U_1 - \alpha_1 \frac{2}{\epsilon} - \alpha_1 \frac{2}{\epsilon}, \\
0 &= U_2 - \alpha_2 \frac{2}{\epsilon}, \\
0 &= U_3 - \alpha_3 \frac{2}{\epsilon}.
\end{aligned}$$

So, the strength $\boldsymbol{\alpha}$ is determined as

$$\alpha_1 = \frac{U_1 \epsilon}{4} \quad \text{in the direction parallel to the body's axis,}$$

$$\alpha_2 = \frac{U_2 \epsilon}{2} \text{ and } \alpha_3 = \frac{U_3 \epsilon}{2} \text{ in the direction perpendicular to the body's axis.}$$

Notice the factor 2 of α_1 compared to α_2 and α_3.

Be ware that the slender-body asymptotic velocity is accurate for small slenderness $\epsilon = \log^{-1}\left(\frac{2\ell}{r_0}\right)$ away from the ends of the body.

For other flow past a slender body, an asymptotic solution can be found by applying the same mechanism.

Appendix B

Error analysis of the velocity field when approximating a prolate spheroid in the flow with a slender body

Slender body theory is a good approximate for the arbitrary cross section body immersed in stokes flow, if the body is slender. It gives a first order approximation and not accurate near the ends of the body. In this appendix, we provide the error analysis for approximating a prolate spheroid with a slender body. In both cases, we check the velocity fields and compute the error, since the velocity field is exact Stokes solution for a prolate spheroid case.

In the first section, we check the error when a uniform flow past a spheroid compare to the approximation of uniform flow past a slender body. In the second section, we check the error for slender body theory when the body sweeps out a double cone.

B.1 Uniform flow past a spheroid or slender body

B.1.1 Uniform flow past a spheroid

Based on the singularity method, by employing a line distribution of Stokeslets and potential doublets between the foci $x = -c$ and c, the exact velocity of uniform fluid flow $U_1 \mathbf{e}_x + U_2 \mathbf{e}_y$ past a prolate spheroid is given by [19]

$$
\begin{aligned}
\mathbf{u}(\mathbf{x}) &= U_1 \mathbf{e}_x + U_2 \mathbf{e}_y - \int_{-c}^{c} \left(\mathbf{u}_S \left(\mathbf{x} - \mathbf{s}; \alpha_1 \mathbf{e}_x \right) + \mathbf{u}_S \left(\mathbf{x} - \mathbf{s}; \alpha_2 \mathbf{e}_y \right) \right) ds \\
&\quad + \int_{-c}^{c} \left(c^2 - s^2 \right) \left(\mathbf{u}_D \left(\mathbf{x} - \mathbf{s}; \beta_1 \mathbf{e}_x \right) + \mathbf{u}_D \left(\mathbf{x} - \mathbf{s}; \beta_2 \mathbf{e}_y \right) \right) ds,
\end{aligned} \tag{B.1}
$$

in which

$$
\begin{aligned}
\alpha_1 &= \frac{2\beta_1 e^2}{1 - e^2} = \frac{U_1 e^2}{-2e + (1 + e^2) L_e}, \\
\alpha_2 &= \frac{2\beta_2 e^2}{1 - e^2} = \frac{2 U_2 e^2}{2e + (3e^2 - 1) L_e},
\end{aligned}
$$

are the strength of the singularities with $L_e = \log\left(\frac{1+e}{1-e}\right)$ (e is the eccentricity). In component format, the velocity field is

$$
\begin{aligned}
u_1(\mathbf{x}) &= U_1 - \int_{-c}^{c} \frac{\alpha_1}{\{(x-s)^2 + r^2\}^{1/2}} \, ds - \int_{-c}^{c} \frac{(x-s)^2 \alpha_1}{\{(x-s)^2 + r^2\}^{\frac{3}{2}}} \, ds \\
&\quad - \int_{-c}^{c} \frac{(x-s) y \alpha_2}{\{(x-s)^2 + r^2\}^{\frac{3}{2}}} \, ds - \int_{-c}^{c} \frac{\beta_1 \left(c^2 - s^2 \right)}{\{(x-s)^2 + r^2\}^{3/2}} \, ds \\
&\quad + \int_{-c}^{c} \left(c^2 - s^2 \right) \frac{3(x-s)^2 \beta_1}{\{(x-s)^2 + r^2\}^{\frac{5}{2}}} \, ds + \int_{-c}^{c} \left(c^2 - s^2 \right) \frac{3(x-s) y \beta_2}{\{(x-s)^2 + r^2\}^{\frac{5}{2}}} \, ds \\
&= U_1 - \alpha_1 I_1 - \alpha_1 I_2 - \alpha_2 y I_3 - \beta_1 I_5 + 3\alpha_2 y I_8 + 3\beta_1 I_9,
\end{aligned} \tag{B.2}
$$

$$u_2(\mathbf{x}) = U_2 - \int_{-c}^{c} \frac{\alpha_2}{\{(x-s)^2 + r^2\}^{1/2}}\, ds - \int_{-c}^{c} \frac{y(x-s)\alpha_1}{\{(x-s)^2 + r^2\}^{\frac{3}{2}}}\, ds$$
$$- \int_{-c}^{c} \frac{y^2 \alpha_2}{\{(x-s)^2 + r^2\}^{\frac{3}{2}}}\, ds - \int_{-c}^{c} \frac{\beta_2\,(c^2 - s^2)}{\{(x-s)^2 + r^2\}^{3/2}}\, ds \qquad \text{(B.3)}$$
$$+ \int_{-c}^{c} (c^2 - s^2)\, \frac{3y(x-s)\beta_1}{\{(x-s)^2 + r^2\}^{\frac{5}{2}}}\, ds + \int_{-c}^{c} (c^2 - s^2)\, \frac{3y^2 \beta_2}{\{(x-s)^2 + r^2\}^{\frac{5}{2}}}\, ds$$
$$= U_2 - \alpha_2 I_1 - \alpha_1 y I_3 - \alpha_2 y^2 I_4 - \alpha_2 I_5 + 3\alpha_2 y^2 I_6 + 3\beta_1 y I_8,$$

$$u_3(\mathbf{x}) = - \int_{-c}^{c} \frac{z(x-s)\alpha_1}{\{(x-s)^2 + r^2\}^{\frac{3}{2}}}\, ds - \int_{-c}^{c} \frac{yz\alpha_2}{\{(x-s)^2 + r^2\}^{\frac{3}{2}}}\, ds \qquad \text{(B.4)}$$
$$+ \int_{-c}^{c} (c^2 - s^2)\, \frac{3z(x-s)\beta_1}{\{(x-s)^2 + r^2\}^{\frac{5}{2}}}\, ds + \int_{-c}^{c} (c^2 - s^2)\, \frac{3yz\beta_2}{\{(x-s)^2 + r^2\}^{\frac{5}{2}}}\, ds$$
$$= -\alpha_1 z I_3 - \alpha_2 yz I_4 + 3\alpha_2 yz I_6 + 3\beta_1 z I_8.$$

Here, these definite integrals are defined as following and can be integrated explicitly,

$$I_1 = \int_{-c}^{c} \frac{1}{((x-s)^2 + r^2)^{1/2}}\, ds, \quad I_2 = \int_{-c}^{c} \frac{(x-s)^2}{((x-s)^2 + r^2)^{3/2}}\, ds, \quad I_3 = \int_{-c}^{c} \frac{(x-s)}{\{(x-s)^2 + r^2\}^{\frac{3}{2}}}\, ds,$$

$$I_4 = \int_{-c}^{c} \frac{1}{((x-s)^2 + r^2)^{3/2}}\, ds, \quad I_5 = \int_{-c}^{c} \frac{(c^2-s^2)}{((x-s)^2 + r^2)^{3/2}}\, ds, \quad I_6 = \int_{-c}^{c} \frac{(c^2 - s^2)}{((x-s)^2 + r^2)^{5/2}}\, ds,$$

$$I_7 = \int_{-c}^{c} \frac{(c^2 - s^2)(x-s)}{((x-s)^2 + r^2)^{3/2}}\, ds, \quad I_8 = \int_{-c}^{c} \frac{(c^2-s^2)(x-s)}{((x-s)^2 + r^2)^{5/2}}\, ds, \quad I_9 = \int_{-c}^{c} \frac{(c^2 - s^2)(x-s)^2}{((x-s)^2 + r^2)^{5/2}}\, ds.$$

After substituting these integral into the velocity field (B.2)-(B.4), the velocity field

in detail is

$$u_1(\mathbf{x}) = U_1 - \frac{2e^2 U_2 y}{2e + (3e^2 - 1)\, L_e} \left(\frac{1}{\sqrt{(x-c)^2 + r^2}} - \frac{1}{\sqrt{(x+c)^2 + r^2}} \right)$$

$$+ \frac{2\,(1 - e^2)\, U_2 y}{(2e + (3e^2 - 1)\, L_e)\, r^2} \left(\frac{x^2 + r^2 + cx}{\sqrt{(x+c)^2 + r^2}} - \frac{x^2 + r^2 - cx}{\sqrt{(x-c)^2 + r^2}} \right)$$

$$- \frac{(1 - e^2)\, U_1}{2\,(-2e + (1 + e^2)\, L_e)} \left[\frac{(x+c)\sqrt{(x-c)^2 + r^2} + (c-x)\sqrt{(x+c)^2 + r^2}}{r^2} \right.$$

$$\left. + 2 \log \left(\frac{x + c + \sqrt{(x+c)^2 + r^2}}{x - c + \sqrt{(x-c)^2 + r^2}} \right) \right]$$

$$+ \frac{(1 - e^2)\, U_1}{2\,(-2e + (1 + e^2)\, L_e)\, r^2} \left(\frac{-(x+c)^2 (x-c) + (3c - x)r^2}{\sqrt{(c+x)^2 + r^2}} \right.$$

$$\left. + \frac{(x-c)^2 (x+c) + (3c + x)r^2}{\sqrt{(c-x)^2 + r^2}} \right) - \frac{2 e^2 U_1}{(1 + e^2)\, L_e - 2e} \log \left(\frac{x + c + \sqrt{(x+c)^2 + r^2}}{x - c + \sqrt{(x-c)^2 + r^2}} \right)$$

$$- \frac{e^2 U_1}{-2e + (1 + e^2)\, L_e} \left(\frac{x - c}{\sqrt{(x-c)^2 + r^2}} - \frac{x + c}{\sqrt{(x+c)^2 + r^2}} \right),$$

214

$$u_2(\mathbf{x}) = U_2 - \frac{e^2 U_1 y}{-2e + (1+e^2)\, L_e} \left(\frac{1}{\sqrt{(x-c)^2 + r^2}} - \frac{1}{\sqrt{(x+c)^2 + r^2}} \right)$$

$$+ \frac{(1-e^2)\, U_1 y}{(-2e + (1+e^2)\, L_e)\, r^2} \left(\frac{x^2 + r^2 + cx}{\sqrt{(x+c)^2 + r^2}} - \frac{x^2 + r^2 - cx}{\sqrt{(x-c)^2 + r^2}} \right)$$

$$- \frac{2e^2 U_2 y^2}{(2e + (3e^2-1)\, L_e)\, r^2} \left(\frac{x+c}{\sqrt{(x+c)^2 + r^2}} - \frac{x-c}{\sqrt{(x-c)^2 + r^2}} \right)$$

$$+ \frac{2\,(1-e^2)\, U_2 y^2}{(2e + (3e^2-1)\, L_e) r^4} \left(\frac{-(x+c)^2(x-c) - xr^2}{\sqrt{(x+c)^2 + r^2}} + \frac{(x-c)^2(x+c) + xr^2}{\sqrt{(x-c)^2 + r^2}} \right)$$

$$- \frac{(1-e^2)\, U_2}{2e + (3e^2-1)\, L_e} \left(\frac{(x+c)\sqrt{(x-c)^2 + r^2} + (c-x)\sqrt{(x+c)^2 + r^2}}{r^2} \right)$$

$$+ \frac{(1-3e^2)\, U_2}{2e + (3e^2-1)\, L_e} \log\left(\frac{x + c + \sqrt{(x+c)^2 + r^2}}{x - c + \sqrt{(x-c)^2 + r^2}} \right),$$

$$u_3(\mathbf{x}) = - \frac{e^2 U_1 z}{-2e + (1+e^2)\, L_e} \left(\frac{1}{\sqrt{(x-c)^2 + r^2}} - \frac{1}{\sqrt{(x+c)^2 + r^2}} \right)$$

$$+ \frac{(1-e^2)\, U_1 z}{r^2 \,(-2e + (1+e^2)\, L_e)} \left(\frac{x^2 + r^2 + cx}{\sqrt{(x+c)^2 + r^2}} - \frac{x^2 + r^2 - cx}{\sqrt{(x-c)^2 + r^2}} \right)$$

$$- \frac{2e^2 U_2 yz}{(2e + (3e^2-1)\, L_e) r^2} \left(\frac{x+c}{\sqrt{(x+c)^2 + r^2}} - \frac{x-c}{\sqrt{(x-c)^2 + r^2}} \right)$$

$$+ \frac{2\,(1-e^2)\, U_2 yz}{(2e + (3e^2-1)\, L_e) r^4} \left(\frac{(x-c)^2(x+c) + xr^2}{\sqrt{(x-c)^2 + r^2}} - \frac{(x+c)^2(x-c) + xr^2}{\sqrt{(x+c)^2 + r^2}} \right),$$

in which $r^2 = y^2 + z^2$.

B.1.2 Uniform flow past a slender body

Based on the slender body theory, the velocity of uniform fluid flow $U_1 \mathbf{e}_x + U_2 \mathbf{e}_y$ past a slender body by employing a line distribution of Stokeslets between the centerline of the slender body $x = -\ell$ and ℓ given by (the length of the body is 2ℓ and the radius of the body is r_0)

$$\mathbf{v}(\mathbf{x}) = U_1 \mathbf{e}_x + U_2 \mathbf{e}_y - \int_{-\ell}^{\ell} \left(\mathbf{u}_S\left(\mathbf{x} - \mathbf{s}; \alpha_1 \mathbf{e}_x\right) + \mathbf{u}_S\left(\mathbf{x} - \mathbf{s}; \alpha_2 \mathbf{e}_y\right) \right) ds$$

where $\boldsymbol{\alpha} = (\alpha_1, \alpha_2, \alpha_3) = \epsilon(\frac{U_1}{4}, \frac{U_2}{2}, 0)$, and $\epsilon = \log\left(\frac{2\ell}{r_0}\right)^{-1}$. So,

$$v_1(\mathbf{x}) = U_1 - \int_{-\ell}^{\ell} \left[\frac{\alpha_1}{\{(x-s)^2 + r^2\}^{1/2}} + \frac{(x-s)\left((x-s)\alpha_1 + y\alpha_2\right)}{\{(x-s)^2 + r^2\}^{\frac{3}{2}}} \right] ds, \quad (\text{B.5})$$

$$v_2(\mathbf{x}) = U_2 - \int_{-\ell}^{\ell} \left[\frac{\alpha_2}{\{(x-s)^2 + r^2\}^{1/2}} + \frac{y\left((x-s)\alpha_1 + y\alpha_2\right)}{\{(x-s)^2 + r^2\}^{\frac{3}{2}}} \right] ds, \quad (\text{B.6})$$

$$v_3(\mathbf{x}) = - \int_{-\ell}^{\ell} \frac{z\left((x-s)\alpha_1 + y\alpha_2\right)}{\{(x-s)^2 + r^2\}^{\frac{3}{2}}} ds, \quad (\text{B.7})$$

where $r^2 = y^2 + z^2$. After substituting the strength $\boldsymbol{\alpha}$ into the velocity field and computing the integrals, the velocity field is

$$v_1(\mathbf{x}) = U_1 - \frac{U_1\epsilon}{4}\log\left(\frac{x + \ell + \sqrt{(x+\ell)^2 + y^2 + z^2}}{x - \ell + \sqrt{(x-\ell)^2 + y^2 + z^2}} \right)$$

$$- \frac{U_2\epsilon}{2}y\left(\frac{1}{\sqrt{(x-\ell)^2 + y^2 + z^2}} - \frac{1}{\sqrt{(x+\ell)^2 + y^2 + z^2}} \right)$$

$$- \frac{U_1\epsilon}{4}\left[\frac{x-\ell}{\sqrt{(x-\ell)^2 + y^2 + z^2}} - \frac{x+\ell}{\sqrt{(x+\ell)^2 + y^2 + z^2}} \right.$$

$$\left. + \log\left(\frac{x + \ell + \sqrt{(x+\ell)^2 + y^2 + z^2}}{x - \ell + \sqrt{(x-\ell)^2 + y^2 + z^2}} \right) \right],$$

$$v_2(\mathbf{x}) = U_2 - \frac{U_1\epsilon}{4}y\left(\frac{1}{\sqrt{(x-\ell)^2 + y^2 + z^2}} - \frac{1}{\sqrt{(x+\ell)^2 + y^2 + z^2}} \right)$$

$$+ \frac{U_2\epsilon}{2}\frac{y^2}{(y^2 + z^2)}\left(\frac{x-\ell}{\sqrt{(x-\ell)^2 + y^2 + z^2}} - \frac{x+\ell}{\sqrt{(x+\ell)^2 + y^2 + z^2}} \right)$$

$$- \frac{U_2\epsilon}{2}\log\left(\frac{x + \ell + \sqrt{(x+\ell)^2 + y^2 + z^2}}{x - \ell + \sqrt{(x-\ell)^2 + y^2 + z^2}} \right),$$

$$v_3(\mathbf{x}) = - \frac{U_1\epsilon}{4}z\left(\frac{1}{\sqrt{(x-\ell)^2 + y^2 + z^2}} - \frac{1}{\sqrt{(x+\ell)^2 + y^2 + z^2}} \right)$$

$$- \frac{U_2\epsilon}{2}\frac{yz}{(y^2 + z^2)}\left(\frac{x+\ell}{\sqrt{(x+\ell)^2 + y^2 + z^2}} - \frac{x-\ell}{\sqrt{(x-\ell)^2 + y^2 + z^2}} \right).$$

B.1.3   Error analysis with uniform background flow

To compare the velocity fairly, we set the semimajor axis of the spheroid and the half body length of the slender body ℓ be the unit, and the semiminor axis of the spheroid and the radius of the slender body be r_0. Then, from the slender body theory $\epsilon = \log\left(\frac{2}{r_0}\right)^{-1}$. Since we are especially interested in the uniform flow perpendicular to the centerline of the body, the uniform flow is $U_2 \mathbf{e}_y$. The error of the velocity with background flow in the other direction can be obtained similarly. The absolute error is computed by subtracting the exact velocity (B.2)-(B.4) by the slender body approximation (B.5)- (B.7). The leading order of the absolute error due to approximating the spheroid with a slender body is

$$
\frac{U_2 \epsilon^2}{4}
\begin{pmatrix}
\frac{y}{2}\left(\frac{1}{\sqrt{(x+1)^2+y^2+z^2}} - \frac{1}{\sqrt{(x-1)^2+y^2+z^2}} \right) \\
\frac{y^2}{y^2+z^2}\left(\frac{1-x}{\sqrt{(x-1)^2+y^2+z^2}} + \frac{1+x}{\sqrt{(x+1)^2+y^2+z^2}} \right) + \log\left(\frac{x+1+\sqrt{(x+1)^2+y^2+z^2}}{x-1+\sqrt{(x-1)^2+y^2+z^2}} \right) \\
\frac{yz}{(y^2+z^2)}\left(\frac{x-1}{\sqrt{(x-1)^2+y^2+z^2}} - \frac{x+1}{\sqrt{(x+1)^2+y^2+z^2}} \right)
\end{pmatrix}
$$

In summary, when a uniform flow $U_2 \mathbf{e}_y$ past a spheroid $\frac{x^2}{\ell^2} + \frac{y^2+z^2}{r_0^2} = 1$ compare the flow past a slender body along the x-axis with $\ell = 1$ and radius r_0, the leading order of the absolute error is ϵ^2 for all the components. The relative error of the velocity is trivial because of the background flow. It is the same order as the absolute error. The relative error of the induced velocity is in the order of ϵ, which verifies that the velocity field of the slender body theory is asymptotic to the exact velocity field as $\epsilon \to 0$.

To approximate the spheroid with a slender body, the slender body result can be improved if the slenderness $\epsilon = \frac{1}{\log(\frac{2\ell}{r}) - \frac{1}{2}}$, which is the limit observed from the strength

of the Stokeslet for the spheroid. Then, the error is in higher order

$$
\begin{aligned}
\text{err1} \quad = \quad & \frac{U_2 y r^2}{1 + 2\log\left(\frac{2}{r}\right)} \left\{ \frac{x}{(y^2 + z^2)} \left[\frac{1 + x}{\sqrt{(x+1)^2 + y^2 + z^2}} + \frac{1 - x}{\sqrt{(x-1)^2 + y^2 + z^2}} \right] \right. \\
& - \frac{1 + 3\log\left(\frac{2}{r}\right)}{1 + 2\log\left(\frac{2}{r}\right)} \left[\frac{1}{\sqrt{(x-1)^2 + y^2 + z^2}} - \frac{1}{\sqrt{(x+1)^2 + y^2 + z^2}} \right] \\
& + \left. \frac{1}{2} \left[\frac{1 + x}{\left((x+1)^2 + y^2 + z^2\right)^{\frac{3}{2}}} - \frac{1 - x}{\left((x-1)^2 + y^2 + z^2\right)^{\frac{3}{2}}} \right] \right\},
\end{aligned}
$$

$$
\begin{aligned}
\text{err2} \quad = \quad & \frac{U_2 r^2}{\left(1 + 2\log\left(\frac{2}{r}\right)\right)} \left\{ -\frac{y^2}{2\left(y^2 + z^2\right)} \left[\frac{(-1 + x)^2}{\left((x-1)^2 + y^2 + z^2\right)^{\frac{3}{2}}} + \frac{(1 + x)^2}{\left((x+1)^2 + y^2 + z^2\right)^{\frac{3}{2}}} \right. \right. \\
& - \frac{x}{\sqrt{(x-1)^2 + y^2 + z^2}} + \frac{x}{\sqrt{(x+1)^2 + y^2 + z^2}} \\
& \left. - \frac{1}{1 + 2\log\left(\frac{2}{r}\right)} \left(\frac{1 - x}{\sqrt{(x-1)^2 + y^2 + z^2}} + \frac{1 + x}{\sqrt{(x+1)^2 + y^2 + z^2}} \right) \right] \\
& + \frac{y^2}{\left(y^2 + z^2\right)^2} \left[\frac{1 - x^2 + x^3 + x\left(-1 + y^2 + z^2\right)}{\sqrt{(x-1)^2 + y^2 + z^2}} \right. \\
& \left. - \frac{-1 + x^2 + x^3 + x\left(-1 + y^2 + z^2\right)}{\sqrt{(x+1)^2 + y^2 + z^2}} \right] - \\
& \frac{1}{2} \left(\frac{(1 + x)\sqrt{(x-1)^2 + y^2 + z^2}}{y^2 + z^2} - \frac{(-1 + x)\sqrt{(x+1)^2 + y^2 + z^2}}{y^2 + z^2} \right. \\
& \left. - \log\left[\frac{1 + x + \sqrt{(x+1)^2 + y^2 + z^2}}{-1 + x + \sqrt{(x-1)^2 + y^2 + z^2}} \right] \right) + \\
& \frac{1}{2\left(1 + 2\log\left(\frac{2}{r}\right)\right)} \left[\left(\frac{1}{\sqrt{(x+1)^2 + y^2 + z^2}} + \frac{1}{\sqrt{(x-1)^2 + y^2 + z^2}} \right) \right. \\
& \left. \left. \left(1 + 2\log\left(\frac{2}{r}\right)\right) - 2\log\left(\frac{2}{r}\right)\log\left[\frac{1 + x + \sqrt{(x+1)^2 + y^2 + z^2}}{-1 + x + \sqrt{(x-1)^2 + y^2 + z^2}} \right] \right] \right\},
\end{aligned}
$$

$$
\begin{aligned}
\text{err3} \quad = \quad & \frac{U_2 yz}{2\left(y^2+z^2\right)^2}\frac{r^2}{\left(1+2\log\left(\frac{2}{r}\right)\right)}\left\{\left(y^2+z^2\right)\right. \\
& \left[x\left(\frac{1}{\sqrt{1-2x+x^2+y^2+z^2}}-\frac{1}{\sqrt{1+2x+x^2+y^2+z^2}}\right)\right. \\
& -\frac{(x+1)^2}{\left((x+1)^2+y^2+z^2\right)^{\frac{3}{2}}}-\frac{(x-1)^2}{\left((x-1)^2+y^2+z^2\right)^{\frac{3}{2}}} \\
& \left.+\frac{1}{\left(1+2\log\left(\frac{2}{r}\right)\right)}\left(\frac{1-x}{\sqrt{(x-1)^2+y^2+z^2}}+\frac{1+x}{\sqrt{(x+1)^2+y^2+z^2}}\right)\right] \\
& +2\left[\frac{(x-1)^2}{\sqrt{(x-1)^2+y^2+z^2}}+\frac{(x+1)^2}{\sqrt{(x+1)^2+y^2+z^2}}\right] \\
& \left.+2x\left[\sqrt{(x-1)^2+y^2+z^2}-\sqrt{(x+1)^2+y^2+z^2}\right]\right\}.
\end{aligned}
$$

In these equations, we set $\ell = 1$.

B.2 A spheroid or slender body sweeping out a double cone

In this section, we document the velocity field of a prolate spheroid sweeping out a double cone in free space and the flow induced by the cylindrical slender body. We compare the velocity field of these two cases by taking the same length and radius of the bodies as the previous section. In both cases, the flow is time independent in the body frame, where the body is stationary and the background can be decomposed as several simple linear shear. For linear shear flows past a prolate spheroid, the exact solution has been obtained based on the exact solution [19]. Applying their results, we provide the velocity field consistent with the notation in [48].

In the lab frame, the prolate spheroid or the slender body sweeps a cone with angular velocity $(0,0,\omega)$ and the background flow is at rest. The cone angle κ is defined from

the axis of the cone to the centerline of the body. In the body frame, we assume the spheroid and the cylindrical slender body is along the x-axis. For the spheroid,

$$\frac{x^2}{\ell^2} + \frac{y^2 + z^2}{r_0^2} = 1.$$

So, the half foci length $c = \sqrt{\ell^2 - r_0^2} = e\ell$. For the slender body, $y^2 + z^2 = r_0^2$ when $-\ell \leq x \leq \ell$.

In this body frame, we distribute the singularity along the x-axis. For the spheroid, the singularities are distributed between two foci. For the slender body, Stokeslets are linearly distributed between two ends $x = -\ell$ and ℓ. From the lab frame $\mathbf{x}_L$ to the body frame $\mathbf{x}$,

$$\mathbf{x} = R_\kappa^T R_\omega^T \mathbf{x}_L,$$

where

$$R_\omega = \begin{pmatrix} \cos(\omega t) & -\sin(\omega t) & 0 \\ \sin(\omega t) & \cos(\omega t) & 0 \\ 0 & 0 & 1 \end{pmatrix} \text{ and } R_\kappa = \begin{pmatrix} \sin(\kappa) & 0 & -\cos(\kappa) \\ 0 & 1 & 0 \\ \cos(\kappa) & 0 & \sin(\kappa) \end{pmatrix}.$$

The relation of the velocity between the lab frame $\mathbf{u}_L(\mathbf{x}_L)$ and the velocity in the body frame $\mathbf{u}(\mathbf{x})$ can be derived from the transformation of the frames. The velocity field in the lab frame is

$$\begin{aligned} \mathbf{u}_L(\mathbf{x}_L) &= \frac{d\mathbf{x}_L}{dt} = \frac{d(R_\omega R_\kappa \mathbf{x})}{dt} = \dot{R}_\omega R_\kappa \mathbf{x} + R_\omega R_\kappa \frac{d\mathbf{x}}{dt} \\ &= \dot{R}_\omega R_\kappa \mathbf{x} + R_\omega R_\kappa \mathbf{u}(\mathbf{x}) = \dot{R}_\omega R_\kappa^T \mathbf{x}_L + R_\omega R_\kappa \mathbf{u}(R_\kappa^T R_\omega^T \mathbf{x}_L). \end{aligned}$$

Similarly,

$$\mathbf{u}(\mathbf{x}) = \frac{d\mathbf{x}}{dt} = R_\kappa^T \dot{R}_\omega^T \mathbf{x}_L + R_\kappa^T R_\omega^T \mathbf{u}_L(\mathbf{x}_L) = R_\kappa^T \dot{R}_\omega^T R_\omega R_\kappa \mathbf{x} + R_\kappa^T R_\omega^T \mathbf{u}_L(R_\omega R_\kappa \mathbf{x}).$$

If the background flow is at rest in the lab frame,

$$\mathbf{U}_0(\mathbf{x}) = R_\kappa^T \dot{R}_\omega^T R_\omega R_\kappa \mathbf{x} = \omega \begin{pmatrix} y\sin(\kappa) \\ z\cos(\kappa) - x\sin(\kappa) \\ -y\cos(\kappa) \end{pmatrix} \tag{B.8}$$

is the background flow in the body frame.

After obtaining the velocity in the body frame, we compare the velocity field in the body frame directly. The error in the lab frame will be the same order by changing frames.

B.2.1   A spheroid sweeps out a double cone

When a spheroid sweeping out a double cone in free space, from the exact solution for shear flow past a prolate spheroid in [19], the exact solution [48] the solution of potential flow past a prolate spheroid based on the singularity method, is constructed by employing a line distribution of stresslet, rotlet, and potential doublets between the foci $-c$ and c given by

$$\begin{aligned} \mathbf{u}(\mathbf{x}) \ &= \ \mathbf{U}_0(\mathbf{x}) + \omega\sin(\kappa)\left(\int_{-c}^{c} \left(c^2 - \xi^2\right)\left(\alpha\mathbf{u}_{\mathrm{SS}}\left(\mathbf{x} - \boldsymbol{\xi}; \mathbf{e}_x, \mathbf{e}_y\right) + \gamma_1\mathbf{u}_{\mathrm{R}}\left(\mathbf{x} - \boldsymbol{\xi}, \mathbf{e}_z\right)\right)d\xi \right. \\ &\qquad \left. +\beta\int_{-c}^{c} \left(c^2 - \xi^2\right)^2 \partial_y \mathbf{u}_{\mathrm{D}}\left(\mathbf{x} - \boldsymbol{\xi}; \mathbf{e}_x\right)d\xi\right) + \\ &\qquad \omega\gamma_2\cos(\kappa)\int_{-c}^{c} \left(c^2 - \xi^2\right)\mathbf{u}_{\mathrm{R}}\left(\mathbf{x} - \boldsymbol{\xi}; \mathbf{e}_x\right)d\xi, \end{aligned}$$

where

$$\alpha = \frac{e^2}{-2e + (1 + e^2)\, L_e}, \qquad \beta = \frac{1 - e^2}{4\left(-2e + (1 + e^2)\, L_e\right)},$$

$$\gamma_1 = \frac{2 - e^2}{-2e + (1 + e^2)\, L_e}, \qquad \gamma_2 = \frac{1 - e^2}{2e - (1 - e^2)\, L_e}.$$

In detail, the velocity field is

$$
\begin{aligned}
u_1(\mathbf{x}) &= \omega y \sin(\kappa) + \omega \sin(\kappa) \left[\int_{-c}^{c} (c^2 - \xi^2) \left(\frac{3\alpha y (x - \xi)^2}{R^5} - \frac{\gamma_1 y}{R^3} \right) d\xi \right. \\
&\quad \left. + \beta \int_{-c}^{c} (c^2 - \xi^2)^2 \left(-\frac{3y}{R^5} - \frac{15 y (x - \xi)^2}{R^7} \right) d\xi \right] \\
&= \omega y \sin(\kappa) + \omega \sin(\kappa) y (3\alpha\, I_1 - \gamma_1\, I_2 - 3\beta\, I_3 - 15\beta\, I_4),
\end{aligned}
\tag{B.9}
$$

$$
\begin{aligned}
u_2(\mathbf{x}) &= -\omega x \sin(\kappa) + \omega z \cos(\kappa) + \\
&\quad \omega \sin(\kappa) \left(\int_{-c}^{c} (c^2 - \xi^2) \left(\frac{3\alpha (x - \xi) y^2}{R^5} + \frac{\gamma_1 (x - \xi)}{R^3} \right) d\xi \right. \\
&\quad \left. + \beta \int_{-c}^{c} (c^2 - \xi^2)^2 \left(-\frac{15 y^2 (x - \xi)}{R^7} + \frac{3 (x - \xi)}{R^5} \right) d\xi \right) \\
&\quad + \omega \gamma_2 \cos(\kappa) \int_{-c}^{c} \frac{(c^2 - \xi^2)\, z}{R^3} d\xi \\
&= -\omega x \sin(\kappa) + \omega z \cos(\kappa) + \\
&\quad \omega \sin(\kappa)(3\alpha y^2\, I_5 + \gamma_1\, I_7 - 15 y^2 \beta\, I_6 + 3\beta\, I_8) + \omega \gamma_2 \cos(\kappa) z\, I_2,
\end{aligned}
\tag{B.10}
$$

$$
\begin{aligned}
u_3(\mathbf{x}) &= -\omega y \cos(\kappa) + \omega \gamma_2 \cos(\kappa) \int_{-c}^{c} \frac{(c^2 - \xi^2)\, y}{R^3} d\xi \\
&\quad + \omega \sin(\kappa) \left(\int_{-c}^{c} (c^2 - \xi^2) \frac{3\alpha (x - \xi) yz}{R^5} d\xi - \beta \int_{-c}^{c} (c^2 - \xi^2)^2 \frac{15 yz (x - \xi)}{R^7} d\xi \right) \\
&= -\omega y \cos(\kappa) + \omega \sin(\kappa)(3\alpha yz\, I_5 - 15\beta yz\, I_6) + \omega \cos(\kappa) \gamma_2 y\, I_2,
\end{aligned}
\tag{B.11}
$$

222

where

$$I_1 = \int_{-c}^{c} \frac{(c^2 - \xi^2)(x - \xi)^2}{R^5} d\xi, \quad I_2 = \int_{-c}^{c} \frac{(c^2 - \xi^2)}{R^3} d\xi,$$

$$I_3 = \int_{-c}^{c} \frac{(c^2 - \xi^2)^2}{R^5} d\xi, \quad\quad I_4 = \int_{-c}^{c} \frac{(c^2 - \xi^2)^2 (x - \xi)^2}{R^7} d\xi,$$

$$I_5 = \int_{-c}^{c} (c^2 - \xi^2) \frac{(x - \xi)}{R^5} d\xi, \quad I_6 = \int_{-c}^{c} (c^2 - \xi^2)^2 \frac{(x - \xi)}{R^7} d\xi,$$

$$I_7 = \int_{-c}^{c} \frac{(c^2 - \xi^2)(x - \xi)}{R^3} d\xi, \quad I_8 = \int_{-c}^{c} (c^2 - \xi^2)^2 \frac{(x - \xi)}{R^5} d\xi,$$

and $R^2 = (x - \xi)^2 + y^2 + z^2$.

For each of these integrals, we integrate explicitly as the following equations.

$$
\begin{aligned}
I_1 \;=\; & -\frac{x + c}{3\left((x - c)^2 + y^2 + z^2\right)^{1/2}} - \frac{(x + c)(x - c)^2 - 2(2c + x)(y^2 + z^2)}{3(y^2 + z^2)\sqrt{(x - c)^2 + y^2 + z^2}} \\
& + \frac{x - c}{3\left((x + c)^2 + y^2 + z^2\right)^{\frac{1}{2}}} - \frac{(x - c)(x + c)^2 + 2(2c - x)(y^2 + z^2)}{3(y^2 + z^2)\sqrt{(x + c)^2 + y^2 + z^2}} \\
& - \log\left(\frac{c + x + \sqrt{(x + c)^2 + y^2 + z^2}}{-c + x + \sqrt{(x - c)^2 + y^2 + z^2}}\right).
\end{aligned}
$$

$$
\begin{aligned}
I_2 \;=\; & \frac{(x + c)\sqrt{(x - c)^2 + y^2 + z^2}}{(y^2 + z^2)} - \frac{(x - c)\sqrt{(x + c)^2 + y^2 + z^2}}{(y^2 + z^2)} \\
& - \log\left(\frac{c + x + \sqrt{(x + c)^2 + y^2 + z^2}}{-c + x + \sqrt{(x - c)^2 + y^2 + z^2}}\right).
\end{aligned}
$$

$$I_3 = -\frac{1}{3\left(y^2+z^2\right)^2}\left\{\sqrt{(c-x)^2+y^2+z^2}\left[2(x+c)^2(x-c)+(5x+3c)\left(y^2+z^2\right)\right]\right.$$
$$\left.+\sqrt{(x+c)^2+y^2+z^2}\left[-2(x-c)^2(x+c)-(5x-3c)\left(y^2+z^2\right)\right]\right\}$$
$$+\log\left(\frac{c+x+\sqrt{(x+c)^2+y^2+z^2}}{-c+x+\sqrt{(x-c)^2+y^2+z^2}}\right).$$

$$I_4 = \frac{1}{15}\left(\frac{2(c-x)^3(x+c)^2}{\left(y^2+z^2\right)^2\sqrt{(c-x)^2+y^2+z^2}}+\frac{2(c-x)^2(c+x)^3}{\left(y^2+z^2\right)^2\sqrt{(x+c)^2+y^2+z^2}}\right.$$
$$-\frac{5c^3-7c^2x+c\left(-17x^2+15\left(y^2+z^2\right)\right)+x\left(19x^2+17\left(y^2+z^2\right)\right)}{\left(y^2+z^2\right)\sqrt{(c-x)^2+y^2+z^2}}$$
$$\left.-\frac{5c^3+7c^2x+c\left(-17x^2+15\left(y^2+z^2\right)\right)-x\left(19x^2+17\left(y^2+z^2\right)\right)}{\left(y^2+z^2\right)\sqrt{(x+c)^2+y^2+z^2}}\right)$$
$$+\log\left(\frac{c+x+\sqrt{(x+c)^2+y^2+z^2}}{-c+x+\sqrt{(x-c)^2+y^2+z^2}}\right).$$

$$I_5 = -\frac{2\left(-cx+x^2+y^2+z^2\right)}{3\left(y^2+z^2\right)\sqrt{(x-c)^2+y^2+z^2}}+\frac{2\left(cx+x^2+y^2+z^2\right)}{3\left(y^2+z^2\right)\sqrt{(x+c)^2+y^2+z^2}}.$$

$$I_6 = \frac{8}{\left(15\left(y^2+z^2\right)^2\left((c-x)^2+y^2+z^2\right)\left((x+c)^2+y^2+z^2\right)\right)}$$
$$\left\{\left(\sqrt{(c-x)^2+y^2+z^2}-\sqrt{(x+c)^2+y^2+z^2}\right)\right.$$
$$\left(c^4x^2+\left(x^2+y^2+z^2\right)^3+c^2\left(-2x^4-x^2\left(y^2+z^2\right)+\left(y^2+z^2\right)^2\right)\right)$$
$$+cx\left(c^4-2c^2x^2+\left(x^2+y^2+z^2\right)^2\right)$$
$$\left.\left(\sqrt{(c-x)^2+y^2+z^2}+\sqrt{(x+c)^2+y^2+z^2}\right)\right\}.$$

$$I_7 = 2\sqrt{(x-c)^2+y^2+z^2}-2\sqrt{(x+c)^2+y^2+z^2}$$
$$+2x\log\left(\frac{c+x+\sqrt{(x+c)^2+y^2+z^2}}{-c+x+\sqrt{(x-c)^2+y^2+z^2}}\right).$$

$$I_8 = \frac{4\sqrt{(x+c)^2 + y^2 + z^2}\,(cx - x^2 + 2\,(y^2 + z^2))}{3\,(y^2 + z^2)} +$$

$$\frac{4\sqrt{(c-x)^2 + y^2 + z^2}\,(cx + x^2 - 2\,(y^2 + z^2))}{3\,(y^2 + z^2)}$$

$$-4\log\left(\frac{c + x + \sqrt{(x+c)^2 + y^2 + z^2}}{-c + x + \sqrt{(x-c)^2 + y^2 + z^2}}\right).$$

When $r^2 = y^2 + z^2 = 0$, the above formulae are not valid. However, these integrals reduce to even simpler cases, which can be integrated easily.

B.2.2   A slender body sweeps out a double cone

When the body is tilted in the x-z plane and sweeps a double cone with the cone angle κ, the velocity in the body frame is constructed by distribution of Stokeslet along the centerline of the body. In the body frame, the body is along the x-axis $(-\ell \leq x \leq \ell)$. The strength of the Stokeslet is a linear function of the arc-length $\boldsymbol{\alpha} = \frac{\epsilon\omega\sin(\kappa)}{2}(0, s, 0)$.

The velocity field in detail is

$$v_1(\mathbf{x}) = \omega y \sin(\kappa) + \int_{-\ell}^{\ell} \frac{(x - \xi)\, y \alpha_2 \xi}{\left\{(x - \xi)^2 + r^2\right\}^{\frac{3}{2}}}\, d\xi$$

$$= \omega y \sin(\kappa) + \frac{\epsilon\, \omega \sin(\kappa) y}{2} \left[\frac{\ell}{\sqrt{(x + \ell)^2 + r^2}} + \frac{\ell}{\sqrt{(x - \ell)^2 + r^2}} \right. \qquad (\text{B.12})$$

$$\left. - \log\left(\frac{x + \ell + \sqrt{(x + \ell)^2 + r^2}}{x - \ell + \sqrt{(x - \ell)^2 + r^2}} \right) \right],$$

$$v_2(\mathbf{x}) = \omega z \cos(\kappa) - \omega x \sin(\kappa) + \int_{-\ell}^{\ell} \frac{\alpha_2 \xi}{\sqrt{(x - \xi)^2 + r^2}}\, d\xi + \int_{-\ell}^{\ell} \frac{x_2^2 \alpha_2 \xi}{\left\{(x - \xi)^2 + r^2\right\}^{\frac{3}{2}}}\, d\xi$$

$$= \omega z \cos(\kappa) - \omega x \sin(\kappa) + \frac{\epsilon \omega \sin(\kappa) y^2}{2r^2} \left(\frac{(x + \ell)x + r^2}{\sqrt{(x + \ell)^2 + r^2}} - \frac{(x - \ell)x + r^2}{\sqrt{(x - \ell)^2 + r^2}} \right)$$

$$+ \frac{\epsilon \omega \sin(\kappa)}{2} \left[-\sqrt{(x + \ell)^2 + r^2} + \sqrt{(x - \ell)^2 + r^2} \right. \qquad (\text{B.13})$$

$$\left. + x \log\left(\frac{x + \ell + \sqrt{(x + \ell)^2 + r^2}}{x - \ell + \sqrt{(x - \ell)^2 + r^2}} \right) \right],$$

$$v_3(\mathbf{x}) = -\omega y \cos(\kappa) + \int_{-\ell}^{\ell} \frac{z y \alpha_2 \xi}{\left\{(x - \xi)^2 + r^2\right\}^{\frac{3}{2}}}\, d\xi \qquad (\text{B.14})$$

$$= -\omega y \cos(\kappa) + \frac{\epsilon \omega \sin(\kappa) yz}{2r^2} \left(\frac{(x + \ell)x + r^2}{\sqrt{(x + \ell)^2 + r^2}} - \frac{(x - \ell)x + r^2}{\sqrt{(x - \ell)^2 + r^2}} \right),$$

where $r^2 = y^2 + z^2$.

B.2.3   Error in the velocity field of the slender body theory

Since the relation from the body frame to the lab frame holds for both the spheroid and the slender body, to analysis the error by approximating the spheroid with the slender body, we compare the velocity field in the body frame. Similar to the velocity field, the error in the lab frame can be obtained by the transformation of the error in the body frame. In the body frame, the velocity field for the background flow (B.8)

226

past a prolate spheroid

$$\frac{x^2}{\ell^2} + \frac{y^2 + z^2}{r_0^2} = 1$$

is $\mathbf{u}(\mathbf{x})$ in (B.9)-(B.11). The velocity field for the flow past a cylindrical slender body

$$\frac{y^2 + z^2}{r_0^2} = 1 \ (-\ell \le x \le \ell)$$

is $\mathbf{v}(\mathbf{x})$ in (B.12)-(B.14). (From the above equations of bodies, the major axis of spheroid or the axis of the slender body is along the x-axis in the body frame.) Since the velocity field $\mathbf{u}(\mathbf{x})$ for the spheroid is exact Stokes solution. If we approximate the body with a slender body, the error due to the slender body is the velocity difference $\mathbf{u}(\mathbf{x}) - \mathbf{v}(\mathbf{x})$, which can be computed explicitly from (B.9)-(B.11) and (B.12)-(B.14). The leading order of the difference, the error from the slender body theory, is

$$\text{erru1} = -\frac{y\epsilon^2\omega\sin(\kappa)}{4} \left\{ -\frac{1}{\sqrt{(x-1)^2 + y^2 + z^2}} - \frac{1}{\sqrt{(x+1)^2 + y^2 + z^2}} \right.$$
$$\left. + \log\left(\frac{1 + x + \sqrt{(x+1)^2 + y^2 + z^2}}{-1 + x + \sqrt{(x-1)^2 + y^2 + z^2}} \right) \right\},$$

$$\text{erru2} = \frac{\epsilon^2\omega\sin(\kappa)}{-4\left(y^2 + z^2\right)} \left(x(y^2 + 2z^2) \left(\frac{1}{\sqrt{(x-1)^2 + y^2 + z^2}} + \frac{1}{\sqrt{(x+1)^2 + y^2 + z^2}} \right) \right.$$
$$+ (y^2 + z^2 + \left(x^2 + y^2 + z^2\right)z^2) \left(\frac{1}{\sqrt{(x+1)^2 + y^2 + z^2}} - \frac{1}{\sqrt{(x-1)^2 + y^2 + z^2}} \right)$$
$$\left. - x\left(y^2 + z^2\right) \log\left(\frac{1 + x + \sqrt{(x+1)^2 + y^2 + z^2}}{-1 + x + \sqrt{(x-1)^2 + y^2 + z^2}} \right) \right),$$

$$\text{erru3} = \frac{\epsilon^2\omega\sin(\kappa)yz}{4(y^2 + z^2)\sqrt{(x-1)^2 + y^2 + z^2}\sqrt{(x+1)^2 + y^2 + z^2}}$$
$$((x^2 + y^2 + z^2 + x)\sqrt{(x-1)^2 + y^2 + z^2} - (x^2 + y^2 + z^2 - x)\sqrt{(x+1)^2 + y^2 + z^2}).$$

From the above error analysis, the error of the slender body theory is in the order of $O(\epsilon^2)$. In the body frame, the background flow is not zero, which makes the asymptotics always hold. To the verify the velocity induced by the slender body is asymptotic to the exact solution, we check the induced velocity of the body by subtracting the background flow in the velocity formulae. When the background flow is subtracted, the induced velocities for both case decay zero as $\epsilon \to 0$. And the leading order of the relative error of the induced velocity is in the order of $O(\epsilon)$, which confirms that the slender body theory result is a valid asymptotic solution.

Similar to the uniform flow, we observe that with the slenderness $\epsilon = \frac{1}{\log(\frac{2\ell}{r}) - \frac{1}{2}}$ the asymptotic solution is improved. With $\epsilon = \frac{1}{\log(\frac{2\ell}{r}) - \frac{1}{2}}$ in the slender body result and

$\ell = 1$, the error in the velocity field is

$$\text{err1} = \frac{y\omega \sin(\kappa)r^2}{8} \left\{ \frac{-4}{(y^2 + z^2)\left(1 - 2\log\left(\frac{2}{r}\right)\right)} \right.$$

$$\left(\frac{1 - x}{\sqrt{(x-1)^2 + y^2 + z^2}} + \frac{1 + x}{\sqrt{(x+1)^2 + y^2 + z^2}} \right)$$

$$+ \frac{4\left(1 - 3\log\left(\frac{2}{r}\right)\right)}{\left(1 - 2\log\left(\frac{2}{r}\right)\right)^2} \left[\frac{(1+x)\sqrt{(x-1)^2 + y^2 + z^2}}{y^2 + z^2} + \frac{(1-x)\sqrt{(x+1)^2 + y^2 + z^2}}{y^2 + z^2} \right.$$

$$\left. - \log\left(\frac{1 + x + \sqrt{(x+1)^2 + y^2 + z^2}}{-1 + x + \sqrt{(x-1)^2 + y^2 + z^2}} \right) \right]$$

$$+ \frac{1}{\left(1 - 2\log\left(\frac{2}{r}\right)\right)(y^2 + z^2)^2}$$

$$\left[\left(\sqrt{(x+1)^2 + y^2 + z^2} + \sqrt{(x-1)^2 + y^2 + z^2} \right)\left(2 - 2x^2 - 3y^2 - 3z^2\right) \right.$$

$$\left. + \left(\sqrt{(x+1)^2 + y^2 + z^2} - \sqrt{(x-1)^2 + y^2 + z^2} \right) x \left(2x^2 + 5y^2 + 5z^2 - 2\right) \right]$$

$$+ \frac{3}{1 - 2\log\left(\frac{2}{r}\right)} \log\left(\frac{1 + x + \sqrt{(x+1)^2 + y^2 + z^2}}{-1 + x + \sqrt{(x-1)^2 + y^2 + z^2}} \right)$$

$$- \frac{1}{(y^2 + z^2)^2 \left(1 - 2\log\left(\frac{2}{r}\right)\right)}$$

$$\left[\left(\frac{1}{\sqrt{(x+1)^2 + y^2 + z^2}} - \frac{1}{\sqrt{(x-1)^2 + y^2 + z^2}} \right) \right.$$

$$\left(-2x^5 + x^3\left(4 - 19y^2 - 19z^2\right) - x\left(2 + 17y^4 - 7z^2 + 17z^4 + y^2\left(-7 + 34z^2\right)\right)\right)$$

$$+ \left(\frac{1}{\sqrt{(x+1)^2 + y^2 + z^2}} + \frac{1}{\sqrt{(x-1)^2 + y^2 + z^2}} \right)$$

$$\left(-2 - 2x^4 + 15y^4 + 5z^2 + 15z^4 + x^2\left(4 - 17y^2 - 17z^2\right) + 5y^2\left(1 + 6z^2\right)\right)$$

$$\left. -15\left(y^2 + z^2\right)^2 \log\left(\frac{1 + x + \sqrt{(x+1)^2 + y^2 + z^2}}{-1 + x + \sqrt{(x-1)^2 + y^2 + z^2}} \right) \right]$$

$$+ \frac{2}{(y^2 + z^2)\left((x-1)^2 + y^2 + z^2\right)^{3/2}\left((x+1)^2 + y^2 + z^2\right)^{3/2}\left(1 - 2\log\left(\frac{2}{r}\right)\right)^2}$$

$$\left[2\left(1 - 2\log\left(\frac{2}{r}\right)\right)\left((1+x)^3\left((x-1)^2 + y^2 + z^2\right)^{\frac{3}{2}} + (1-x)^3\left((x+1)^2 + y^2 + z^2\right)^{\frac{3}{2}}\right) \right.$$

$$+ \left((x-1)^2 + y^2 + z^2\right)\left((x+1)^2 + y^2 + z^2\right)\left(-2 + 2\log\left(\frac{2}{r}\right)\right)$$

$$\left(x\left(-1 + x^2 + y^2 + z^2\right)\left(\sqrt{(x-1)^2 + y^2 + z^2} - \sqrt{(x+1)^2 + y^2 + z^2}\right)\right)$$

$$+ \left(-1 + x^2 - 3y^2 - 3z^2\right)\left(\sqrt{(x-1)^2 + y^2 + z^2} + \sqrt{(x+1)^2 + y^2 + z^2}\right)$$

$$+3\left(y^2+z^2\right)\sqrt{(x-1)^2+y^2+z^2}\sqrt{(x+1)^2+y^2+z^2}$$
$$\log\left(\frac{1+x+\sqrt{(x+1)^2+y^2+z^2}}{-1+x+\sqrt{(x-1)^2+y^2+z^2}}\right)\Big)\Big]\Big\},$$

$$\text{err2} = \frac{r^2}{2}\omega \left\{ \cos(\kappa) \left[\frac{(1+x)\sqrt{(x-1)^2+y^2+z^2}}{y^2+z^2} + \frac{(1-x)\sqrt{(x+1)^2+y^2+z^2}}{y^2+z^2} \right. \right.$$

$$\left. - \log\left(\frac{x+1+\sqrt{(x+1)^2+y^2+z^2}}{x-1+\sqrt{(x-1)^2+y^2+z^2}} \right) \right]$$

$$+ \left[\frac{y^2}{y^2+z^2} \left(\frac{-1}{1-2\log\left(\frac{2}{r}\right)} \left(\frac{3(-1+x)\left(-x+x^2+y^2+z^2\right)}{\left((x-1)^2+y^2+z^2\right)^{3/2}} \right. \right. \right.$$

$$+ \frac{2\left(-x+x^2+y^2+z^2\right)}{\sqrt{(x-1)^2+y^2+z^2}} + \frac{3(1+x)\left(x+x^2+y^2+z^2\right)}{\left((x+1)^2+y^2+z^2\right)^{3/2}} - \frac{2\left(x+x^2+y^2+z^2\right)}{\sqrt{(x+1)^2+y^2+z^2}}$$

$$+ \frac{-6x^2-3x^3-2\left(y^2+z^2\right)-3x\left(1+y^2+z^2\right)}{\left((x+1)^2+y^2+z^2\right)^{3/2}}$$

$$\left. + \frac{6x^2-3x^3+2\left(y^2+z^2\right)-3x\left(1+y^2+z^2\right)}{\left((x-1)^2+y^2+z^2\right)^{3/2}} \right)$$

$$\left. + \frac{2\log\left(\frac{2}{r}\right)}{\left(1-2\log\left(\frac{2}{r}\right)\right)^2} \left(\frac{\left(x^2+y^2+z^2+x\right)}{\sqrt{(x+1)^2+y^2+z^2}} - \frac{\left(x^2+y^2+z^2-x\right)}{\sqrt{(x-1)^2+y^2+z^2}} \right) \right)$$

$$+ \frac{2y^2}{\left(y^2+z^2\right)^2 \left(-1+2\log\left(\frac{2}{r}\right)\right)}$$

$$\left(\frac{\left(x^3+x^4+x\left(-1+y^2+z^2\right)+\left(y^2+z^2\right)^2+x^2\left(-1+2y^2+2z^2\right)\right)}{\sqrt{(x+1)^2+y^2+z^2}} \right.$$

$$\left. - \frac{\left(-x^3+x^4-x\left(-1+y^2+z^2\right)+\left(y^2+z^2\right)^2+x^2\left(-1+2y^2+2z^2\right)\right)}{\sqrt{(x-1)^2+y^2+z^2}} \right)$$

$$+ \frac{1}{1-2\log\left(\frac{2}{r}\right)} \left(\frac{1}{\sqrt{(x-1)^2+y^2+z^2}} - \frac{1}{\sqrt{(x+1)^2+y^2+z^2}} \right)$$

$$+ \frac{-2+6\log\left(\frac{2}{r}\right)}{\left(1-2\log\left(\frac{2}{r}\right)\right)^2} \left(\sqrt{(x-1)^2+y^2+z^2} - \sqrt{(x+1)^2+y^2+z^2} \right.$$

$$\left. + x\log\left(\frac{x+1+\sqrt{(x+1)^2+y^2+z^2}}{x-1+\sqrt{(x-1)^2+y^2+z^2}} \right) \right)$$

$$- \frac{1}{\left(y^2+z^2\right)\left(1-2\log\left(\frac{2}{r}\right)\right)} \left(\left(x^2-2\left(y^2+z^2\right)+x\right)\sqrt{(x-1)^2+y^2+z^2} \right.$$

$$- \left(x^2-2\left(y^2+z^2\right)-x\right)\sqrt{(x+1)^2+y^2+z^2}$$

$$\left. \left. \left. - 3x\left(y^2+z^2\right)\log\left(\frac{x+1+\sqrt{(x+1)^2+y^2+z^2}}{x-1+\sqrt{(x-1)^2+y^2+z^2}} \right) \right) \right] \sin(\kappa) \right\},$$

$$\text{err3} = \frac{yz\omega r^2}{2} \left\{ \cos(\kappa) \left[\frac{(1+x)\sqrt{(x-1)^2 + y^2 + z^2}}{y^2 + z^2} - \frac{(-1+x)\sqrt{(x+1)^2 + y^2 + z^2}}{y^2 + z^2} \right. \right.$$

$$\left. - \log\left(\frac{x+1+\sqrt{(x+1)^2 + y^2 + z^2}}{x-1+\sqrt{(x-1)^2 + y^2 + z^2}} \right) \right]$$

$$+ \left[\left((y^2 + z^2) \left(\left((y^2 + z^2 + 2(x^4 + (y^2 + z^2)^2 + x^2(3 + 2y^2 + 2z^2))) \right. \right. \right. \right.$$

$$\left(((x+1)^2 + y^2 + z^2)^{\frac{3}{2}} - ((x-1)^2 + y^2 + z^2)^{\frac{3}{2}} \right)$$

$$-2\left(3x^3 + x(1 + 3y^2 + 3z^2)\right) \left(((x+1)^2 + y^2 + z^2)^{\frac{3}{2}} + ((x-1)^2 + y^2 + z^2)^{\frac{3}{2}} \right) \right)$$

$$\left(-1 + 2\log\left(\frac{2}{r}\right) \right) / \left(((x-1)^2 + y^2 + z^2)^{3/2} \left((x+1)^2 + y^2 + z^2\right)^{3/2} \right)$$

$$+ \left(-\frac{-x + x^2 + y^2 + z^2}{\sqrt{(x-1)^2 + y^2 + z^2}} + \frac{x + x^2 + y^2 + z^2}{\sqrt{(x+1)^2 + y^2 + z^2}} \right) 2\log\left(\frac{2}{r}\right) \right)$$

$$-2\left(\left(x^6 + (y^2 + z^2)^2 \left(1 + y^2 + z^2\right) + x^4 \left(-2 + 3y^2 + 3z^2\right) \right. \right.$$

$$\left. + x^2 \left(-1 - 3y^4 + z^2 - 3z^4 + y^2 \left(1 - 6z^2\right)\right) \right)$$

$$\left(\sqrt{(x-1)^2 + y^2 + z^2} - \sqrt{(x+1)^2 + y^2 + z^2} \right)$$

$$+ \left(x \left(1 + x^4 + 2x^2\left(-1 + y^2 + z^2\right) + \left(y^2 + z^2\right)^2\right) \right)$$

$$\left(\sqrt{(x-1)^2 + y^2 + z^2} + \sqrt{(x+1)^2 + y^2 + z^2} \right) \right) \left(-1 + 2\log\left(\frac{2}{r}\right) \right) \Big/$$

$$\left. \left. \left(((x-1)^2 + y^2 + z^2) \left((x+1)^2 + y^2 + z^2\right) \right) \right) \right] \frac{\sin(\kappa)}{\left((y^2 + z^2)^2 \left(1 - 2\log\left(\frac{2}{r}\right)\right)^2 \right)} \right\}.$$

Figure B.1-B.4 are comparisons of the fluid particle trajectories from flows induced by a spheroid with a slender body in the laboratory frame. In these figures, the black trajectories are from the exact Stokes solution in the flow generated by a spheroid; the red trajectories are from the asymptotic solution by approximating the spheroid with a cylindrical slender body with the slenderness $\epsilon = \frac{1}{\log(\frac{2\ell}{r}) - \frac{1}{2}}$; the purple trajectories are from the asymptotic solution with $\epsilon = \frac{1}{\log(\frac{2\ell}{r})}$. The half length of the slender body ℓ equals to the semimajor axis of the spheroid $a = 1$ and the radius of the slender body r equals to the semiminor axis of the spheroid b, i.e., the spheroid inscribes in the slender

body. The comparison is made for different radius of the slender body by varying the eccentricity $e = \sqrt{1 - b^2/a^2}$.

Figure B.1 shows trajectories with an initial location $(-0.46, 0, 0.4)$ with eccentricity $e = 0.995$, 0.9995 and 0.99995. Only side view of Figure C.1b is provided here, since the top view is the better view of the comparison. From this group of plots, we find trajectories with the slenderness $\epsilon = \frac{1}{\log(\frac{2\ell}{r}) - \frac{1}{2}}$ in the asymptotic solution converges well to the exact solution. Figure B.2 shows the comparison of the exact solution to the asymptotic solution with $\epsilon = \frac{1}{\log(\frac{2\ell}{r}) - \frac{1}{2}}$ with $e = 0.9995$.

Figure B.3 shows trajectories starting from a different initial location $(-0.7, 0, 0.4)$ with eccentricity $e = 0.995$, 0.9995 and 0.99995. Only top view of these trajectories are plotted here. Similarly to the previous plots, the black trajectories are from the exact spheroid solution and the red trajectories are from the asymptotic solution with $\epsilon = \frac{1}{\log(\frac{2\ell}{r}) - \frac{1}{2}}$. These trajectories are consistent with the conclusion that the velocity with the slender body theory for a slender body is asymptotic to the exact solution of a spheroid when the slenderness $\epsilon \to 0$.

Finally, Figure B.4 shows the comparison of fluid particle trajectories in the free space with initial position selected in the straight rod above a no-slip plane experiment shown in Figure 6.8.

When $a = 1$, for these eccentricities $e = 0.995$, 0.9995, 0.99995, the semiminor axis b is 0.1, 0.032, and 0.01, respectively. The corresponding slenderness $\epsilon = \log^{-1}(\frac{2\ell}{r})$ is 0.33, 0.24, 0.19. The slenderness $\epsilon = \frac{1}{\log(\frac{\ell}{r}) - \frac{1}{2}}$ is 0.40, 0.27, 0.21.
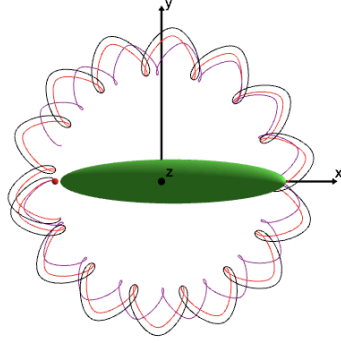
(a) Top view ($e = 0.995$)
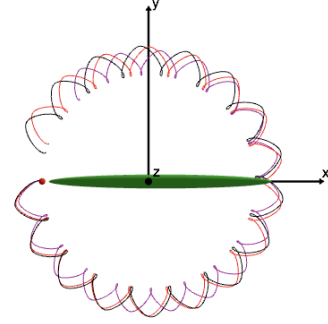
(b) Top view ($e = 0.9995$)
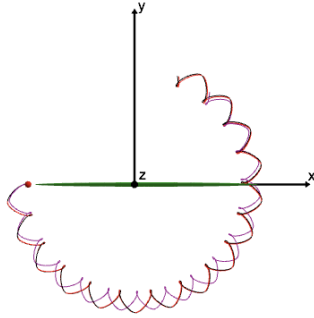
(c) Top view ($e = 0.99995$)
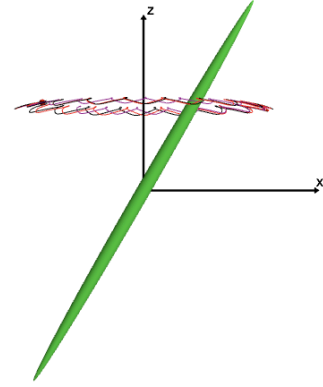
(d) Side view of (b) ($e = 0.9995$)

Figure B.1: Fluid particle trajectories from initial position $x = -0.46$, $y = 0$, and $z = 0.4$. The black trajectories are the exact solution for the spheroid case, the purple trajectories are the slender body result with the slenderness $\epsilon = \frac{1}{\log(\frac{2\ell}{r})}$, and the red trajectories are with $\epsilon = \frac{1}{\log(\frac{2\ell}{r}) - \frac{1}{2}}$. The spheroid is inscribed in the cylindrical slender body. e is the eccentricity of the prolate spheroid.
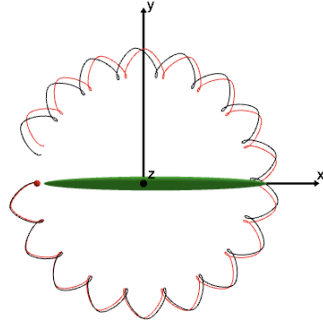
(a) Top view ($e = 0.9995$)
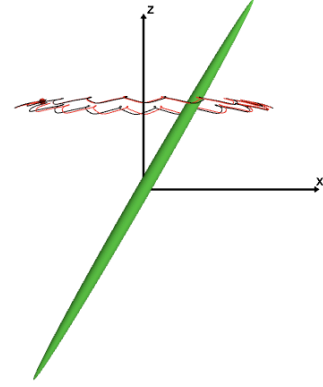
(b) Side view ($e = 0.9995$)

Figure B.2: Compare the exact fluid particle trajectories (black) with the slender body approximation (red) with $\epsilon = \frac{1}{\log(\frac{2\ell}{r})}$. The initial position of trajectories is $x = -0.46$, $y = 0$, and $z = 0.4$.
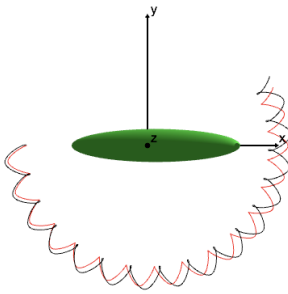
(a) Top view ($e = 0.995$)
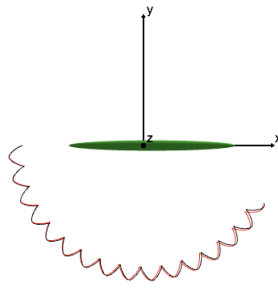
(b) Top view ($e = 0.9995$)
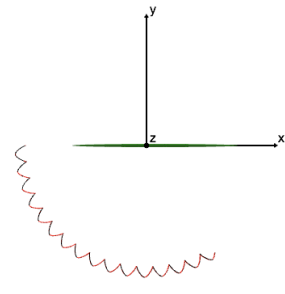
(c) Top view ($e = 0.99995$)

Figure B.3: Similar to Figure B.2, but with the initial position $x = -0.7$, $y = 0$, and $z = 0.4$.

(a) Top view   (b) Side view
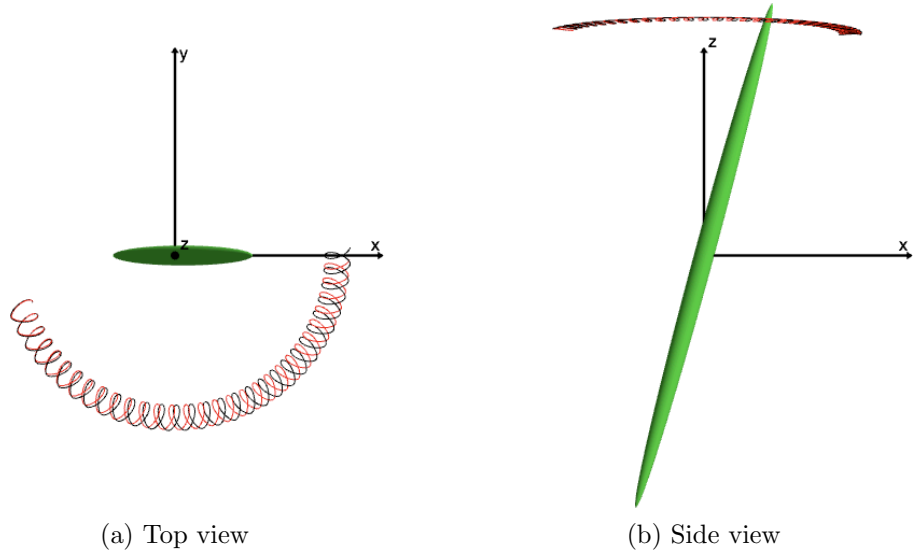
Figure B.4: Trajectories in flows generated by a spheroid (black) and a slender body (red) sweeping out a double cone in free space. The initial position is the same as in Figure 6.8. For the red slender body theory trajectory, the slenderness $\epsilon = \frac{1}{\log(\frac{\ell}{r})-\frac{1}{2}}$.
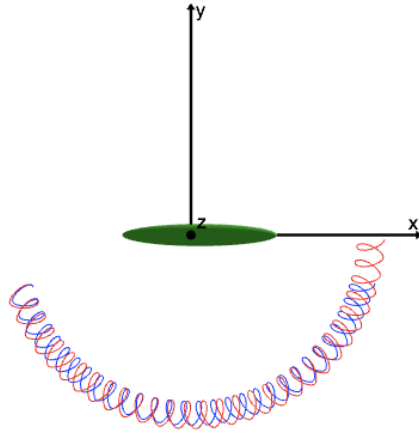
Figure B.5: Trajectories with different definitions of ϵ in the slender body theory. The red trajectory is the same as in Figure B.4 with $\epsilon = \frac{1}{\log(\frac{\ell}{r})-\frac{1}{2}}$. The blue trajectory is with $\epsilon = \log^{-1}(\frac{2\ell}{r})$.

Appendix C

Higher order asymptotic solutions for flows past a spheroid

For linear flow past a spheroid in free space, there are exact solutions available [36, 19, 41]. With the slender body theory, asymptotic solutions can be found when using a cylindrical slender body to approximate the spheroid. The leading order asymptotic solutions have been studied well with analytical error in $O(\epsilon^2)$ [21, 3, 48] , where ϵ is the slenderness parameter. The error analysis are documented in Appendix B for uniform flow past a spheroid and improved slender body results for a slender rod sweeping out a double cone in free space. For a slender body approximating the spheroid, we provide the leading order slender body results and the higher order results for several basic flows in this appendix. The spheroid is inscribed to the cylindrical slender body. The major axis of the spheroid $2a$ equals the length of the slender body 2ℓ, and the semi-minor axis of the spheroid b equals to the cross-sectional radius of the slender body r.

If the exact solution has been reported in this thesis before, we concisely document the slender body results for both leading order approximation or higher order results. Beside the asymptotic solutions, we derive the exact solution for the spheroid for the spheroid sweeping a single cone.

C.1   Uniform background flow

When a uniform flow $U_1 \mathbf{e}_x + U_2 \mathbf{e}_y$ past a prolate spheroid, the flow is approximated with the uniform flow past a cylindrical slender body. Assuming the slender body along the x- axis from $x = -\ell$ to $x = \ell$, the asymptotic velocity field is

$$\mathbf{u}(\mathbf{x}) = U_1 \mathbf{e}_x + U_2 \mathbf{e}_y - \int_{-\ell}^{\ell} \left(\mathbf{U}_S \left(\mathbf{x} - \boldsymbol{\xi}; \alpha_1 \mathbf{e}_x \right) + \mathbf{U}_S \left(\mathbf{x} - \boldsymbol{\xi}; \alpha_2 \mathbf{e}_y \right) \right) d\xi, \tag{C.1}$$

where $\mathbf{x} - \boldsymbol{\xi} = (x - \xi, y, z)$.

From the canonical slender body theory, the constants in the strength of the Stokeslet are

$$\alpha_1 = \frac{U_1}{4} \frac{1}{\log\left(\frac{2\ell}{r}\right)}$$

$$\text{and} \quad \alpha_2 = \frac{U_2}{2} \frac{1}{\log\left(\frac{2\ell}{r}\right)}$$

for the leading order asymptotic solution. The error for the velocity is $O(\epsilon^2)$, where $\epsilon = \frac{1}{\log\left(\frac{2\ell}{r}\right)}$ is the slenderness parameter.

Comparing with the exact solution for the uniform flow past a spheroid (B.1), we find that the asymptotic velocity is accurate to $O\left(\left(\frac{r}{\ell} \right)^2 \right)$ with the following modified constants

$$\begin{aligned} \alpha_1 &= \frac{U_1}{4} \frac{1}{\log\left(\frac{2\ell}{r}\right) - \frac{1}{2}}, \\ \alpha_2 &= \frac{U_2}{2} \frac{1}{\log\left(\frac{2\ell}{r}\right) + \frac{1}{2}}. \end{aligned}$$

Notice the difference between the tangential direction and the normal direction.

C.2 Linear shear flow past a slender body

Similar to the uniform flow, when shear flow $\Omega x \mathbf{e}_y$ past a spheroid along the x-axis $(-\ell \leq x \leq \ell)$, the asymptotic velocity field is

$$\mathbf{u}(\mathbf{x}) = \Omega x \mathbf{e}_y - \int_{-\ell}^{\ell} \mathbf{U}_S(\mathbf{x} - \boldsymbol{\xi}; \alpha_2 \xi \mathbf{e}_y) d\xi, \tag{C.2}$$

where $\mathbf{x} - \boldsymbol{\xi} = (x - \xi, y, z)$. We use a cylindrical slender body to approximate the spheroid. The velocity is obtained with linear distributed Stokeslet along the center-line.

From the slender body theory, the leading order asymptotic solution with

$$\alpha_2 = \frac{\Omega \epsilon}{2} = \frac{\Omega}{2} \frac{1}{\log\left(\frac{2\ell}{r}\right)}.$$

With

$$\alpha_2 = \frac{\Omega}{4} \frac{1}{\log\left(\frac{2\ell}{r}\right) - \frac{1}{2}},$$

the asymptotic velocity is accurate to $O\left(\left(\frac{r}{\ell}\right)^2\right)$.

C.3 Shear flow $\Omega z \mathbf{e}_x$ past an upright spheroid above the x-y plane

For shear flow $\Omega z \mathbf{e}_x$ past an upright spheroid above the x-y plane, we approximate the flow with the shear flow past a slender body. Then, the slender body is to approximate the spheroid $\frac{x^2+y^2}{b^2} + \frac{(z-a)^2}{a^2} = 1$ or $\frac{x^2+y^2}{r^2} + \frac{(z-\ell)^2}{\ell^2} = 1$. The exact solution for the spheroid can be attained from (B.1) and (3.1) by moving the origin to the center of the spheroid.

Based on the slender body theory, the velocity of shear flow $\Omega z \mathbf{e}_x$ past a slender

body by employing a linear distribution of Stokeslets between the centerline of the slender body $z = 0$ and 2ℓ is given by (the length of the body is 2ℓ)

$$\mathbf{u}(\mathbf{x}) = \Omega z \mathbf{e}_x - \int_0^{2\ell} \mathbf{U}_{\mathrm{S}}(\mathbf{x} - \boldsymbol{\xi}; \alpha_1 \xi \mathbf{e}_x) d\xi, \tag{C.3}$$

where $\mathbf{x} - \boldsymbol{\xi} = (x, y, z - \xi)$ and $\alpha_1 = \frac{\Omega \epsilon}{2} = \frac{\Omega}{2\log\left(\frac{2\ell}{r}\right)}$ for the leading order solution.

Since the background flow is not symmetric with respect to the center of the spheroid, we decompose the background flow into a shear flow plus a uniform flow to achieve the higher order asymptotic solution. Then, both flows are symmetric with respect to the center of the body.

The higher order velocity field is

$$\mathbf{u}(\mathbf{x}) = \Omega z \mathbf{e}_x + \int_0^{2\ell} \mathbf{U}_{\mathrm{S}}(\mathbf{x} - \boldsymbol{\xi}; (\beta_1 - \alpha_1)\,\mathbf{e}_x) d\xi - \int_0^{2\ell} \mathbf{U}_{\mathrm{S}}(\mathbf{x} - \boldsymbol{\xi}; \beta_1 \xi \mathbf{e}_x) d\xi, \tag{C.4}$$

where $\mathbf{x} - \boldsymbol{\xi} = (x, y, z - \xi)$, $\alpha_1 = \frac{\Omega \ell}{2\left(\log\left(\frac{2\ell}{d}\right) + \frac{1}{2}\right)}$ and $\beta_1 = \frac{\Omega}{2\left(\log\left(\frac{2\ell}{d}\right) - \frac{1}{2}\right)}$.

C.4   A prolate spheroid sweeping a single cone in free space

When a spheroid or a slender body sweeps out a single cone above the x-y plane in free space, we derive the exact solution for the spheroid and asymptotic solutions for the slender body in the body frame. There are two body frames. In one body frame $\mathbf{x}_b = (x_b, y_b, z_b)$, the body is titled in the x-z plane and the cone is above the x-y plane. Such a body frame is convenient when we add the no-slip boundary on the x-y plane. In this frame, the slender body is an approximation of the titled spheroid above the

x-y plane

$$\frac{(x_b \sin(\kappa) + z_b \cos(\kappa) - a)^2}{a^2} + \frac{(-x_b \cos(\kappa) + z_b \sin(\kappa))^2}{b^2} = 1 \qquad \text{(C.5)}$$

or $\frac{(x_b \sin(\kappa) + z_b \cos(\kappa) - L)^2}{\ell^2} + \frac{(-x_b \cos(\kappa) + z_b \sin(\kappa))^2}{r^2} = 1$, where κ is the cone angle. The back-

ground in this titled spheroid body frame is $(\omega y_b, -\omega x_b, 0)$, in which ω is the angular

velocity of the spheroid. The transformation between the body frame $\mathbf{x}_b$ to the lab

frame $\mathbf{x}_L$ is

$$\mathbf{x}_L = R_\omega \mathbf{x}_b, \qquad \text{(C.6)}$$

where $R_\omega = \begin{pmatrix} \cos(\omega t) & -\sin(\omega t) & 0 \\ \sin(\omega t) & \cos(\omega t) & 0 \\ 0 & 0 & 1 \end{pmatrix}$. The leading order asymptotic solution is

given directly in this tilted spheroid body frame.

The other body frame is the general body frame where the spheroid and the slender

body are along the x-axis. The origin is the center of the rigid body. The transformation

between the tilted spheroid body $\mathbf{x}_b$ and the general body frame $\mathbf{x}$ is

$$\begin{pmatrix} x_b \\ y_b \\ z_b \end{pmatrix} = \begin{pmatrix} \sin(\kappa) & 0 & -\cos(\kappa) \\ 0 & 1 & 0 \\ \cos(\kappa) & 0 & \sin(\kappa) \end{pmatrix} \begin{pmatrix} x + \ell \\ y \\ z \end{pmatrix}.$$

From the background flow in the tilted spheroid body frame $(\omega y_b, -\omega x_b, 0)$, the back-

ground flow in the general body frame is

$$\mathbf{U} = \begin{pmatrix} y\omega \sin(\kappa) \\ -\omega(-z \cos(\kappa) + (\ell + x) \sin(\kappa)) \\ -y\omega \cos(\kappa) \end{pmatrix}. \qquad \text{(C.7)}$$

The higher order asymptotic solution is derived in the general body frame and trans-
formed into the tilted spheroid body frame. The exact solution for a spheroid is derived
in this general frame in the next section.

Employing a linear distribution of Stokeslets between the centerline of the slender
body (the length of the body is 2ℓ), the leading order asymptotic solution is

$$\mathbf{u}(\mathbf{x}) = y_b \omega \mathbf{e}_x - \omega x_b \mathbf{e}_y + \int_0^{2\ell} \mathbf{U}_S(\mathbf{x}_b - \boldsymbol{\xi}; \alpha_2 \xi \mathbf{e}_y) d\xi, \tag{C.8}$$

where $\mathbf{x}_b - \boldsymbol{\xi} = (x_b - \xi \sin(\kappa), y_b, z_b - \xi \cos(\kappa))$ and $\alpha_2 = \frac{\omega \sin(\kappa)}{2 \log\left(\frac{2\ell}{r}\right)}$.

To get the higher order approximation, we first consider the flow in the general
body frame, where the background flow is $\begin{pmatrix} y\omega \sin(\kappa) \\ -\omega(-z\cos(\kappa) + (\ell + x)\sin(\kappa)) \\ -y\omega \cos(\kappa) \end{pmatrix}$. The
velocity field is

$$
\begin{aligned}
\mathbf{u}(\mathbf{x}) &= \omega y \sin(\kappa)\mathbf{e}_x + \omega z \cos(\kappa)\mathbf{e}_y - \omega y \cos(\kappa)\mathbf{e}_z - \omega\ell \sin(\kappa)\mathbf{e}_y - \omega x \sin(\kappa)\mathbf{e}_y \\
&\quad + \int_{-\ell}^{\ell} \mathbf{U}_S\left(\mathbf{x} - \boldsymbol{\xi}; \alpha_1 \mathbf{e}_y\right) d\xi + \int_{-\ell}^{\ell} \mathbf{U}_S\left(\mathbf{x} - \boldsymbol{\xi}; \beta_1 \xi \mathbf{e}_y\right) d\xi
\end{aligned} \tag{C.9}
$$

where $\mathbf{x} - \boldsymbol{\xi} = (x - \xi, y, z)$ and

$$\alpha_1 = \frac{\omega\ell \sin(\kappa)}{2\left(\log\left(\frac{2\ell}{r}\right) + \frac{1}{2}\right)},$$

and

$$\beta_1 = \frac{\omega \sin(\kappa)}{2\left(\log\left(\frac{2\ell}{r}\right) - \frac{1}{2}\right)}.$$

Rewriting the higher order velocity field (C.9) in the tilted spheroid body frame,

we get

$$\mathbf{u}_b\left(\mathbf{x}_b\right) = y_b\omega\mathbf{e}_x - \omega x_b\mathbf{e}_y + \int_0^{2\ell} \mathbf{U}_{\mathrm{S}}(\mathbf{x}_b - \boldsymbol{s}; (\alpha_1 - \beta_1\ell)\,\mathbf{e}_y)ds + \int_0^{2\ell} \mathbf{U}_{\mathrm{S}}(\mathbf{x}_b - \boldsymbol{s}; \beta_1\xi\mathbf{e}_y)ds,$$

$$(\mathrm{C}.10)$$

where $\mathbf{x}_b - \boldsymbol{s} = (x_b - s\sin(\kappa), y_b, z_b - s\cos(\kappa))$.

In detail,

$$
\begin{aligned}
u_{\mathrm{b}1}\left(x_b\right) &= y_b\omega + \int_0^{2\ell} \frac{(\alpha_1 - \beta_1\ell)\,y_b(x_b - s\sin(\kappa))}{\{(x_b - s\sin(\kappa))^2 + y_b^2 + (z_b - s\cos(\kappa))^2\}^{\frac{3}{2}}}\,ds \\
&\quad + \int_0^{2\ell} \frac{\beta_1 y_b s(x_b - s\sin(\kappa))}{\{(x_b - s\sin(\kappa))^2 + y_b^2 + (z_b - s\cos(\kappa))^2\}^{\frac{3}{2}}}\,ds, \\[6pt]
u_{\mathrm{b}2}\left(x_b\right) &= -x_b\omega + \int_0^{2\ell} \left(\frac{\alpha_1 - \beta_1\ell}{\{(x_b - s\sin(\kappa))^2 + y_b^2 + (z_b - s\cos(\kappa))^2\}^{\frac{1}{2}}} + \right. \\
&\quad \left. \frac{(\alpha_1 - \beta_1\ell)\,y_b^2}{\{(x_b - s\sin(\kappa))^2 + y_b^2 + (z_b - s\cos(\kappa))^2\}^{\frac{3}{2}}} \right) ds \\
&\quad + \int_0^{2\ell} \left(\frac{\beta_1 s}{\{(x_b - s\sin(\kappa))^2 + y_b^2 + (z_b - s\cos(\kappa))^2\}^{\frac{1}{2}}} \right. \\
&\quad \left. + \frac{\beta_1 y_b^2 s}{\{(x_b - s\sin(\kappa))^2 + y_b^2 + (z_b - s\cos(\kappa))^2\}^{\frac{3}{2}}} \right) ds, \\[6pt]
u_{\mathrm{b}3}\left(x_b\right) &= \int_0^{2\ell} \frac{(\alpha_1 - \beta_1\ell)\,y_b(z_b - s\cos(\kappa))}{\{(x_b - s\sin(\kappa))^2 + y_b^2 + (z_b - s\cos(\kappa))^2\}^{\frac{3}{2}}}\,ds \\
&\quad + \int_0^{2\ell} \frac{\beta_1 y_b s(z_b - s\cos(\kappa))}{\{(x_b - s\sin(\kappa))^2 + y_b^2 + (z_b - s\cos(\kappa))^2\}^{\frac{3}{2}}}\,ds.
\end{aligned}
$$

For the higher order asymptotic solution, the induced velocity is due to uniformly distributed Stokeslet on the center-line with strength $(0, (\alpha_1 - \beta_1\ell), 0)$ and linear distributed Stokeslet with strength $(0, \beta_1, 0)$.

C.5 Exact solution for the spheroid sweeping a single cone

When a spheroid sweeps out a single upright cone above the x-y plane, the background flow in the tilted spheroid body frame is $(\omega y_b, -\omega x_b, 0)$ and the background flow in the general body frame is $\omega y \sin(\kappa)\mathbf{e}_x + \omega z \cos(\kappa)\mathbf{e}_y - \omega y \cos(\kappa)\mathbf{e}_z - \omega a \sin(\kappa)\mathbf{e}_y - \omega x \sin(\kappa)\mathbf{e}_y$. Since the spheroid is along the x-axis, $\mathbf{x} - \boldsymbol{\xi} = (x - \xi, y, z)$ in the following formulae.

For uniform flow $-\omega a \sin(\kappa)\mathbf{e}_x$ past a spheroid, the exact velocity field is [19]

$$\mathbf{u}(\mathbf{x}) = U_2 \mathbf{e}_y - \int_{-c}^{c} \alpha_2 \mathbf{U}_S \left(\mathbf{x} - \boldsymbol{\xi}, \mathbf{e}_y \right) d\xi + \int_{-c}^{c} \left(c^2 - \xi^2 \right) \beta_2 \mathbf{U}_D \left(\mathbf{x} - \boldsymbol{\xi}, \mathbf{e}_y \right) d\xi, \quad \text{(C.11)}$$

where

$$U_2 = -\omega a \sin(\kappa), \quad \alpha_2 = \frac{2\beta_2 e^2}{1-e^2} = \frac{2U_2 e^2}{2e + (3e^2 - 1)L_e}, \quad \beta_2 = \frac{U_2 \left(1 - e^2 \right)}{2e + (3e^2 - 1) L_e},$$

and $L_e = \log \left(\frac{1+e}{1-e} \right)$.

For shear flow $y\omega \sin(\kappa)\mathbf{e}_y$ past a spheroid, the exact velocity field is [19]

$$\begin{aligned}
\mathbf{u}(\mathbf{x}) &= \Omega_3 y \mathbf{e}_x + \int_{-c}^{c} \left(c^2 - \xi^2 \right) \left(\alpha_3 \mathbf{U}_{SS}(\mathbf{x} - \boldsymbol{\xi}; \mathbf{e}_x, \mathbf{e}_y) + \gamma_3 \mathbf{U}_R \left(\mathbf{x} - \boldsymbol{\xi}; \mathbf{e}_z \right) \right) d\xi \\
&+ \beta_3 \int_{-c}^{c} \left(c^2 - \xi^2 \right)^2 \frac{\partial}{\partial y} \mathbf{U}_D \left(\mathbf{x} - \boldsymbol{\xi}; \mathbf{e}_x \right) d\xi, \quad \text{(C.12)}
\end{aligned}$$

where $\Omega_3 = \omega \sin(\kappa)$ and

$$
\begin{aligned}
\gamma_3 &= \Omega_3 \frac{1 - e^2}{-2e + (1 + e^2)\, L_e}, \\[2mm]
\alpha_3 &= \frac{4e^2}{1 - e^2}\beta_3 = 2e^2\gamma_3 \frac{-2e + L_e}{2e\,(2e^2 - 3) + 3\,(1 - e^2)\, L_e} \\[2mm]
&= 2\Omega_3 e^2 \frac{1 - e^2}{-2e + (1 + e^2)\, L_e} \frac{-2e + L_e}{2e\,(2e^2 - 3) + 3\,(1 - e^2)\, L_e}, \\[4mm]
\beta_3 &= \frac{\Omega_3}{2} \frac{(1 - e^2)^2}{-2e + (1 + e^2)\, L_e} \frac{-2e + L_e}{2e\,(2e^2 - 3) + 3\,(1 - e^2)\, L_e}.
\end{aligned}
$$

For shear flow $\omega z \cos(\kappa)\mathbf{e}_y$ past a spheroid, the exact velocity field is [19]

$$
\begin{aligned}
\mathbf{u}(\mathbf{x}) &= \Omega_1 z \mathbf{e}_y + \int_{-c}^{c} \left(c^2 - \xi^2\right) \left(\alpha_4 \mathbf{U}_{\mathrm{SS}}(\mathbf{x} - \boldsymbol{\xi}; \mathbf{e}_y, \mathbf{e}_z) + \gamma_4 \mathbf{U}_{\mathrm{R}}\left(\mathbf{x} - \boldsymbol{\xi}; \mathbf{e}_x\right)\right) d\xi \\
&\quad + \beta_4 \int_{-c}^{c} \left(c^2 - \xi^2\right)^2 \frac{\partial}{\partial z} \mathbf{U}_{\mathrm{D}}\left(\mathbf{x} - \boldsymbol{\xi}; \mathbf{e}_y\right) d\xi,
\end{aligned}
\tag{C.13}
$$

where

$$
\begin{aligned}
\Omega_1 &= \omega \cos(\kappa), \qquad \gamma_4 = \frac{\Omega_1}{2} \frac{1 - e^2}{2e - (1 - e^2)\, L_e}, \\[2mm]
\alpha_4 &= \frac{4e^2}{1 - e^2}\beta_4 = \frac{2\Omega_1 e^2 \,(1 - e^2)}{2e\,(3 - 5e^2) - 3\,(1 - e^2)^2\, L_e}, \\[2mm]
\beta_4 &= \frac{\Omega_1}{2} \frac{(1 - e^2)^2}{2e\,(3 - 5e^2) - 3\,(1 - e^2)^2\, L_e}.
\end{aligned}
$$

For shear flow $-\omega x \sin(\kappa)\mathbf{e}_y$ past a spheroid, the velocity field is [19]

$$
\begin{aligned}
\mathbf{u}(\mathbf{x}) &= \Omega_3' x \mathbf{e}_y - \int_{-c}^{c} \left(c^2 - \xi^2\right) \left(\alpha_3' \mathbf{U}_{\mathrm{SS}}(\mathbf{x} - \boldsymbol{\xi}; \mathbf{e}_x, \mathbf{e}_y) + \gamma_3' \mathbf{U}_{\mathrm{R}}\left(\mathbf{x} - \boldsymbol{\xi}; \mathbf{e}_z\right)\right) d\xi \\
&\quad - \beta_3' \int_{-c}^{c} \left(c^2 - \xi^2\right)^2 \frac{\partial}{\partial x} \mathbf{U}_{\mathrm{D}}\left(\mathbf{x} - \boldsymbol{\xi}; \mathbf{e}_y\right) d\xi,
\end{aligned}
\tag{C.14}
$$

where

$$\Omega_3' = -\omega\sin(\kappa), \qquad \gamma_3' = \Omega_3'\frac{1}{-2e+(1+e^2)\,L_e},$$

$$\alpha_3' = \frac{4e^2}{1-e^2}\beta_3' = e^2\gamma_3'\frac{-2e+(1-e^2)\,L_e}{2e\,(2e^2-3)+3\,(1-e^2)\,L_e}$$

$$= \Omega_3'e^2\frac{1}{-2e+(1+e^2)\,L_e}\frac{-2e+(1-e^2)\,L_e}{2e\,(2e^2-3)+3\,(1-e^2)\,L_e},$$

$$\beta_3' = \frac{\Omega_3'}{4}\frac{1-e^2}{-2e+(1+e^2)\,L_e}\frac{-2e+(1-e^2)\,L_e}{2e\,(2e^2-3)+3\,(1-e^2)\,L_e}.$$

For shear flow $-y\omega\cos(\kappa)\mathbf{e}_z$ past a spheroid, the velocity field is [19]

$$\mathbf{u}(\mathbf{x}) = \Omega_5 y\mathbf{e}_z + \int_{-c}^{c}\left(c^2-\xi^2\right)(\alpha_5\mathbf{U}_{\mathrm{SS}}(\mathbf{x}-\boldsymbol{\xi};\mathbf{e}_z,\mathbf{e}_y)+\gamma_5\mathbf{U}_{\mathrm{R}}\left(\mathbf{x}-\boldsymbol{\xi};\mathbf{e}_x\right))d\xi$$

$$+\beta_5\int_{-c}^{c}\left(c^2-\xi^2\right)^2\frac{\partial}{\partial y}\mathbf{U}_{\mathrm{D}}\left(\mathbf{x}-\boldsymbol{\xi};\mathbf{e}_z\right)d\xi, \quad \text{(C.15)}$$

where

$$\Omega_5 = -\omega\cos(\kappa), \qquad \gamma_5 = \frac{\Omega_5}{2}\frac{1-e^2}{2e-(1-e^2)\,L_e},$$

$$\alpha_5 = \frac{4e^2}{1-e^2}\beta_5 = \frac{2\Omega_5 e^2\,(1-e^2)}{2e\,(3-5e^2)-3\,(1-e^2)^2\,L_e},$$

$$\beta_5 = \frac{\Omega_5}{2}\frac{(1-e^2)^2}{2e\,(3-5e^2)-3\,(1-e^2)^2\,L_e}.$$

For shear flow $-y_b\omega\cos(\kappa)\mathbf{e}_z$ past a spheroid, we adopt the velocity from (C.13) for shear flow $\Omega_1 z\mathbf{e}_y$ past a spheroid. The exact velocity field is

$$\mathbf{u}(\mathbf{x}) = \Omega_5 y\mathbf{e}_z + \int_{-c}^{c}\left(c^2-\xi^2\right)(\alpha_5\mathbf{U}_{\mathrm{SS}}\left(\mathbf{x}-\boldsymbol{\xi};\mathbf{e}_z,\mathbf{e}_y\right)-\gamma_5\mathbf{U}_{\mathrm{R}}(\mathbf{x}-\boldsymbol{\xi};\mathbf{e}_x))d\xi$$

$$+\beta_5\int_{-c}^{c}\left(c^2-\xi^2\right)^2\partial_y\mathbf{U}_{\mathrm{D}}(\mathbf{x}-\boldsymbol{\xi};\mathbf{e}_z)d\xi, \qquad \text{(C.16)}$$

where

$$\Omega_5 = -\omega\cos(\kappa), \qquad \gamma_5 = \frac{\Omega_5}{2}\frac{1-e^2}{2e-(1-e^2)\,L_e},$$

$$\alpha_5 = \frac{4e^2}{1-e^2}\beta_5 = \frac{2\Omega_5 e^2\,(1-e^2)}{2e\,(3-5e^2)-3\,(1-e^2)^2\,L_e},$$

$$\beta_5 = \frac{\Omega_5}{2}\frac{(1-e^2)^2}{2e\,(3-5e^2)-3\,(1-e^2)^2\,L_e}.$$

In summary, the velocity field is

$$
\begin{aligned}
\mathbf{u}(\mathbf{x}) =\ & -\omega a\sin(\kappa)\mathbf{e}_y + \omega\sin(\kappa)y\mathbf{e}_x + \omega\cos(\kappa)z\mathbf{e}_y - \omega\sin(\kappa)x\mathbf{e}_y - \omega\cos(\kappa)y\mathbf{e}_z \\
& - \int_{-c}^{c} \alpha_2 \mathbf{U}_S\,(\mathbf{x}-\boldsymbol{\xi},\mathbf{e}_y)\,d\xi + \int_{-c}^{c} \left(c^2-\xi^2\right)\beta_2\mathbf{U}_D\,(\mathbf{x}-\boldsymbol{\xi},\mathbf{e}_y)\,d\xi \\
& + \int_{-c}^{c} \left(c^2-\xi^2\right)(\alpha_1\mathbf{U}_{SS}(\mathbf{x}-\boldsymbol{\xi};\mathbf{e}_x,\mathbf{e}_y) + \gamma_1\mathbf{U}_R\,(\mathbf{x}-\boldsymbol{\xi};\mathbf{e}_z) + \gamma_2\mathbf{U}_R(\mathbf{x}-\boldsymbol{\xi};\mathbf{e}_x))d\xi \\
& + \beta_1 \int_{-c}^{c} \left(c^2-\xi^2\right)^2 \frac{\partial}{\partial y}\mathbf{U}_D\,(\mathbf{x}-\boldsymbol{\xi};\mathbf{e}_x)\,d\xi,
\end{aligned}
\tag{C.17}
$$

where

$$\alpha_1 = \frac{e^2\omega\sin(\kappa)}{-2e+(1+e^2)\,L_e},$$

$$\alpha_2 = \frac{-2\omega a\sin(\kappa)e^2}{2e+(3e^2-1)\,L_e},$$

$$\beta_1 = \frac{(1-e^2)\,\omega\sin(\kappa)}{4\,(-2e+(1+e^2)\,L_e)},$$

$$\beta_2 = \frac{-\omega a\sin(\kappa)\,(1-e^2)}{2e+(3e^2-1)\,L_e},$$

$$\gamma_1 = \frac{(2-e^2)\,\omega\sin(\kappa)}{-2e+(1+e^2)\,L_e},$$

$$\gamma_2 = \frac{(1-e^2)\,\omega\cos(\kappa)}{2e+(-1+e^2)\,L_e}.$$

To get the exact solution (C.17), we have applied the following identities to the velocity

field,

$$\mathbf{U}_{\mathrm{SS}}\left(\mathbf{x}-\boldsymbol{\xi};\mathbf{e}_y,\mathbf{e}_z\right) = \mathbf{U}_{\mathrm{SS}}\left(\mathbf{x}-\boldsymbol{\xi};\mathbf{e}_z,\mathbf{e}_y\right),$$

$$\frac{\partial}{\partial x}\mathbf{U}_{\mathrm{D}}\left(\mathbf{x}-\boldsymbol{\xi};\mathbf{e}_y\right) = \frac{\partial}{\partial y}\mathbf{U}_{\mathrm{D}}\left(\mathbf{x}-\boldsymbol{\xi};\mathbf{e}_z\right),$$

$$\frac{\partial}{\partial y}\mathbf{U}_{\mathrm{D}}\left(\mathbf{x}-\boldsymbol{\xi};\mathbf{e}_x\right) = \frac{\partial}{\partial x}\mathbf{U}_{\mathrm{D}}\left(\mathbf{x}-\boldsymbol{\xi};\mathbf{e}_y\right).$$

Figure C.1 shows fluid particle trajectories from two initial positions. For each position, there are three trajectories based on different velocity field. The black trajectory is from the exact solution when a spheroid sweeps out a single cone in free space. The red trajectory is the higher order slender body result and the blue trajectory is the leading order slender body result. These trajectories verify the improvement of the higher order asymptotic solutions. The dashed circle in the top view indicates the top of the cone.
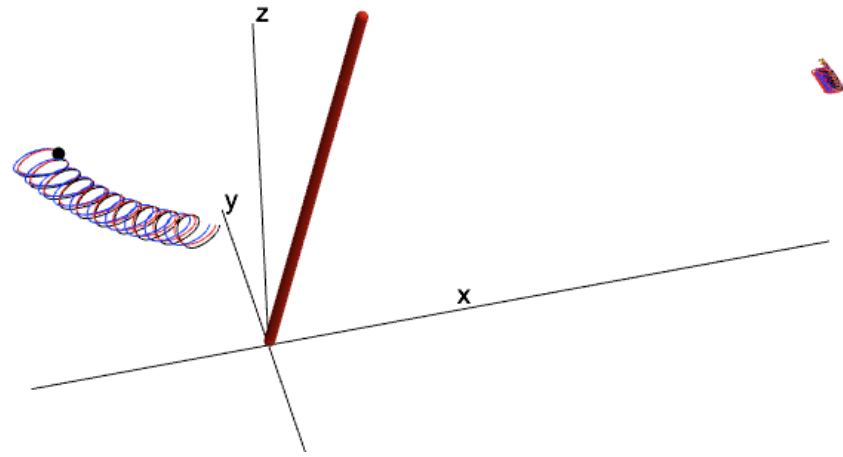
(a) 3D view
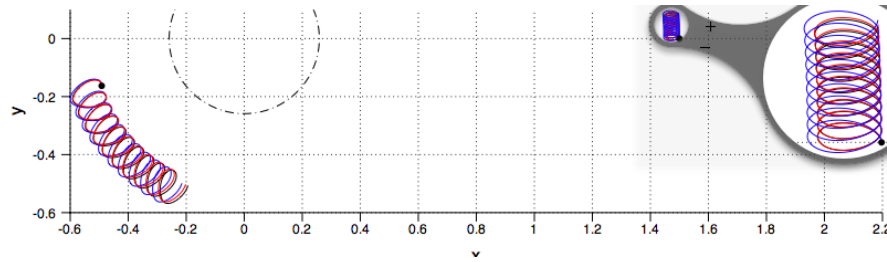
(b) Top view

Figure C.1: Fluid particle trajectories from the two initial positions with the exact solution for a spheroid sweeping a single cone, the leading order slender body approximation, and the higher order slender body approximation.

Appendix D

Slender body theory for a partial torus

We provide the leading order slender body results for uniform flow past a partial torus.

Consider a particle torus in the x-y plane, with body length 2ℓ. The radius of the torus is a, and the cross sectional radius is b. On the surface of the torus, $\left(a - \sqrt{x^2 + y^2}\right)^2 + z^2 = b^2$. In the curvilinear orthogonal coordinate system (r_1, θ, ψ),

$$x = (a + r_1 \cos(\psi)) \cos(\theta),$$

$$y = (a + r_1 \cos(\psi)) \sin(\theta),$$

$$z = r_1 \sin(\psi).$$

Along the center-line of the torus, $\sqrt{x^2 + y^2} = a$. In terms of the arc-length $-\ell \leq s \leq \ell$, the center-line is

$$x_{\mathrm{S}} = a \cos(\frac{s}{a}), \tag{D.1}$$

$$y_{\mathrm{S}} = a \sin(\frac{s}{a}), \tag{D.2}$$

$$z_{\mathrm{S}} = 0. \tag{D.3}$$

The square of the distance from any point in the flow field to a point on the center-line

is

$$(x - x_\mathrm{S})^2 + (y - y_\mathrm{S})^2 + (z - z_\mathrm{S})^2 = \left(2a^2 \left(1 + \frac{r_1}{a} \cos(\psi) \right) \left(1 - \cos \left(\theta - \frac{s}{a} \right) \right) + r_1^2 \right). \quad \text{(D.4)}$$

The onsatz is the flow induced by the partial torus can be constructed with Stokeslet uniformly distributed along the center-line and the strength of the singularity is proportional to the local velocity at the center line. In the rectangular coordinates, the strength of the Stokeslet is noted as $(\alpha_1, \alpha_2, \alpha_3)^T$, the strength of the Stokeslet in the local coordinate is $(\alpha_\tau, \alpha_n, \alpha_b)^T$. α_τ, α_n, α_b are for tangential, normal and binormal, respectively. The basis of the local coordinates are the tangential direction $e_\tau = \left(\frac{\partial x_\mathrm{S}}{\partial s}, \frac{\partial y_\mathrm{S}}{\partial s}, \frac{\partial z_\mathrm{S}}{\partial s} \right)^T$, the normal direction $e_n = a \left(\frac{\partial^2 x_\mathrm{S}}{\partial s^2}, \frac{\partial^2 y_\mathrm{S}}{\partial s^2}, \frac{\partial^2 z_\mathrm{S}}{\partial s^2} \right)^T$, and the binormal direction $e_b = e_\tau \times e_n = (0, 0, 1)^T$. So,

$$\begin{pmatrix} \alpha_1 \\ \alpha_2 \\ \alpha_3 \end{pmatrix} = \begin{pmatrix} e_\tau & e_n & e_b \end{pmatrix} \begin{pmatrix} \alpha_\tau \\ \alpha_n \\ \alpha_b \end{pmatrix} = \begin{pmatrix} \frac{\partial x_\mathrm{S}}{\partial s} & a\frac{\partial^2 x_\mathrm{S}}{\partial s^2} & 0 \\ \frac{\partial y_\mathrm{S}}{\partial s} & a\frac{\partial^2 y_\mathrm{S}}{\partial s^2} & 0 \\ \frac{\partial z_\mathrm{S}}{\partial s} & a\frac{\partial^2 z_\mathrm{S}}{\partial s^2} & 1 \end{pmatrix} \begin{pmatrix} \alpha_\tau \\ \alpha_n \\ \alpha_b \end{pmatrix}$$

$$= \begin{pmatrix} -\sin\left(\frac{s}{a}\right) & -\cos\left(\frac{s}{a}\right) & 0 \\ \cos\left(\frac{s}{a}\right) & -\sin\left(\frac{s}{a}\right) & 0 \\ 0 & 0 & 1 \end{pmatrix} \begin{pmatrix} \alpha_\tau \\ \alpha_n \\ \alpha_b \end{pmatrix} \equiv R \begin{pmatrix} \alpha_\tau \\ \alpha_n \\ \alpha_b \end{pmatrix}.$$

From the onsatz,

$$\begin{pmatrix} \alpha_\tau \\ \alpha_n \\ \alpha_b \end{pmatrix} = \begin{pmatrix} c_1 & 0 & 0 \\ 0 & c_2 & 0 \\ 0 & 0 & c_3 \end{pmatrix} \begin{pmatrix} U_\tau \\ U_n \\ U_b \end{pmatrix}.$$

For the uniform flow past the partial torus $(U_1, U_2, U_3)^T$, the local velocity is $(U_\tau, U_n, U_b)^T = R^T (U_1, U_2, U_3)^T$.

In summary, the strength of the Stokeslet is

$$
\begin{pmatrix} \alpha_1 \\ \alpha_2 \\ \alpha_3 \end{pmatrix} = R \begin{pmatrix} \alpha_\tau \\ \alpha_n \\ \alpha_b \end{pmatrix} = R \begin{pmatrix} c_1 & 0 & 0 \\ 0 & c_2 & 0 \\ 0 & 0 & c_3 \end{pmatrix} \begin{pmatrix} U_\tau \\ U_n \\ U_b \end{pmatrix}
$$

$$
= \begin{pmatrix} \frac{1}{2}\left((c_1+c_2)U_1 - (c_1-c_2)\left(U_1\cos(\frac{2s}{a}) + U_2\sin\left(\frac{2s}{a}\right)\right)\right) \\ \frac{1}{2}\left((c_1+c_2)U_2 + (c_1-c_2)\left(U_2\cos(\frac{2s}{a}) - U_1\sin\left(\frac{2s}{a}\right)\right)\right) \\ c_3 U_3 \end{pmatrix}. \tag{D.5}
$$

D.1   Uniform flow $(0,0,U_3)$ past the partial torus

When the uniform background flow is $(0,0,U_3)$ in the direction perpendicular to the plane where the partial torus is, the velocity field of the flow is

$$
\begin{aligned}
u_1 &= -\int_{-\ell}^{\ell} \frac{\alpha_3(z-z_{\mathrm{S}})}{((x-x_{\mathrm{S}})^2 + (y-y_{\mathrm{S}})^2 + (z-z_{\mathrm{S}})^2)^{3/2}} (x-x_{\mathrm{S}})\, ds \\
&= -\int_{-\ell}^{\ell} \frac{\alpha_3 r_1 \sin(\psi)\left((a+r_1\cos(\psi))\cos(\frac{s_0}{a}) - a\cos(\frac{s}{a})\right)}{\left(2a^2\left(1+\frac{r_1}{a}\cos(\psi)\right)\left(1-\cos(\frac{s_0-s}{a})\right) + r_1^2\right)^{3/2}}\, ds, \\
u_2 &= -\int_{-\ell}^{\ell} \frac{\alpha_3(z-z_{\mathrm{S}})}{((x-x_{\mathrm{S}})^2 + (y-y_{\mathrm{S}})^2 + (z-z_{\mathrm{S}})^2)^{3/2}} (y-y_{\mathrm{S}})\, ds \\
&= -\int_{-\ell}^{\ell} \frac{\alpha_3 r_1 \sin(\psi)\left((a+r_1\cos(\psi))\sin(\frac{s_0}{a}) - a\sin(\frac{s}{a})\right)}{\left(2a^2\left(1+\frac{r_1}{a}\cos(\psi)\right)\left(1-\cos(\frac{s_0-s}{a})\right) + r_1^2\right)^{3/2}}\, ds, \\
u_3 &= U_3 - \int_{-\ell}^{\ell}\left(\frac{\alpha_3}{\sqrt{(x-x_{\mathrm{S}})^2 + (y-y_{\mathrm{S}})^2 + (z-z_{\mathrm{S}})^2}}\right. \\
&\qquad\left. + \frac{\alpha_3(z-z_{\mathrm{S}})^2}{((x-x_{\mathrm{S}})^2 + (y-y_{\mathrm{S}})^2 + (z-z_{\mathrm{S}})^2)^{3/2}}\right) ds \\
&= U_3 - \int_{-\ell}^{\ell}\left(\frac{\alpha_3}{\sqrt{2a^2\left(1+\frac{r_1}{a}\cos(\psi)\right)\left(1-\cos(\frac{s_0-s}{a})\right) + r_1^2}}\right. \\
&\qquad\left. + \frac{\alpha_3 r_1^2 \sin^2(\psi)}{\left(2a^2\left(1+\frac{r_1}{a}\cos(\psi)\right)\left(1-\cos(\frac{s_0-s}{a})\right) + r_1^2\right)^{3/2}}\right) ds.
\end{aligned}
$$

On the surface of the torus $r_1 = b$, the no-slip boundary condition leads

$$u_1 = -\int_{-\ell}^{\ell} \frac{\alpha_3 b \sin(\psi) \left((a + b\cos(\psi)) \cos\left(\frac{s_0}{a}\right) - a\cos\left(\frac{s}{a}\right) \right)}{\left(2a^2 \left(1 + \frac{b}{a}\cos(\psi)\right) \left(1 - \cos\left(\frac{s_0}{a} - \frac{s}{a}\right)\right) + b^2 \right)^{3/2}} \, ds = 0,$$

$$u_2 = -\int_{-\ell}^{\ell} \frac{\alpha_3 b \sin(\psi) \left((a + b\cos(\psi)) \sin\left(\frac{s_0}{a}\right) - a\sin\left(\frac{s}{a}\right) \right)}{\left(2a^2 \left(1 + \frac{b}{a}\cos(\psi)\right) \left(1 - \cos\left(\frac{s_0}{a} - \frac{s}{a}\right)\right) + b^2 \right)^{3/2}} \, ds = 0,$$

$$u_3 = U_3 - \int_{-\ell}^{\ell} \left(\frac{\alpha_3}{\sqrt{2a^2 \left(1 + \frac{b}{a}\cos(\psi)\right) \left(1 - \cos\left(\frac{s_0}{a} - \frac{s}{a}\right)\right) + b^2}} \right.$$

$$\left. + \frac{\alpha_3 b^2 \sin^2(\psi)}{\left(2a^2 \left(1 + \frac{b}{a}\cos(\psi)\right) \left(1 - \cos\left(\frac{s_0}{a} - \frac{s}{a}\right)\right) + b^2 \right)^{3/2}} \right) \, ds = 0.$$

Change of variable in the integral to make use of the stretched variable

$$\frac{s - s_0}{a} = \frac{b}{a} t, \quad ds = b \, dt.$$

Then,

$$\int_{-\ell}^{\ell} \frac{\alpha_3}{\sqrt{2a^2\left(1 + \frac{b}{a}\cos(\psi)\right)\left(1 - \cos\left(\frac{s_0}{a} - \frac{s}{a}\right)\right) + b^2}}\, ds$$

$$= \int_{\frac{-\ell-s_0}{b}}^{\frac{\ell-s_0}{b}} \frac{\alpha_3 b}{\sqrt{2a^2\left(1 + \frac{b}{a}\cos(\psi)\right)\left(1 - \cos\left(\frac{b}{a}t\right)\right) + b^2}}\, dt$$

$$\sim \int_{\frac{-\ell-s_0}{b}}^{\frac{\ell-s_0}{b}} \frac{\alpha_3 b}{\sqrt{a^2\left(1 + \frac{b}{a}\cos(\psi)\right)\left(\frac{b}{a}t\right)^2 + b^2}}\, dt$$

$$= \int_{\frac{-\ell-s_0}{b}}^{\frac{\ell-s_0}{b}} \frac{\alpha_3}{\sqrt{\left(1 + \frac{b}{a}\cos(\psi)\right)t^2 + 1}}\, dt$$

$$= \frac{\alpha_3}{\sqrt{\left(1 + \frac{b}{a}\cos(\psi)\right)}} \int_{\frac{-\ell-s_0}{b}}^{\frac{\ell-s_0}{b}} \frac{1}{\sqrt{t^2 + \frac{1}{\left(1 + \frac{b}{a}\cos(\psi)\right)}}}\, dt$$

$$= \frac{\alpha_3}{\sqrt{\left(1 + \frac{b}{a}\cos(\psi)\right)}} \log\left(\frac{\frac{\ell-s_0}{b} + \sqrt{\frac{1}{\left(1 + \frac{b}{a}\cos(\psi)\right)} + \left(\frac{\ell-s_0}{b}\right)^2}}{\frac{-\ell-s_0}{b} + \sqrt{\frac{1}{\left(1 + \frac{b}{a}\cos(\psi)\right)} + \left(\frac{-\ell-s_0}{b}\right)^2}}\right)$$

$$\sim \frac{\alpha_3}{\sqrt{\left(1 + \frac{b}{a}\cos(\psi)\right)}} \log\left(\frac{\frac{\ell-s_0}{b} + \sqrt{\frac{1}{\left(1 + \frac{b}{a}\cos(\psi)\right)} + \left(\frac{\ell-s_0}{b}\right)^2}}{\frac{-\ell-s_0}{b} + \sqrt{\frac{1}{\left(1 + \frac{b}{a}\cos(\psi)\right)} + \left(\frac{-\ell-s_0}{b}\right)^2}}\right)$$

$$\sim \alpha_3 \log\left(\frac{2\frac{\ell-s_0}{b}}{\frac{\frac{1}{\left(1 + \frac{b}{a}\cos(\psi)\right)}}{2\frac{\ell+s_0}{b}}}\right) \sim \alpha_3 \log\left(4\frac{\ell^2 - s_0^2}{b^2}\left(1 + \frac{b}{a}\cos(\psi)\right)\right)$$

$$\sim 2\alpha_3 \log\left(\frac{2\ell}{b}\right).$$

Away from the tips of the partial torus, the above asymptotic results is held.

Here, as $\frac{b}{a} \to 0$,

$$\frac{\ell - s_0}{b} + \sqrt{\frac{1}{\left(1 + \frac{b}{a}\cos(\psi)\right)} + \left(\frac{\ell - s_0}{b}\right)^2} \sim 2\frac{\ell - s_0}{b},$$

$$\frac{-\ell - s_0}{b} + \sqrt{\frac{1}{\left(1 + \frac{b}{a}\cos(\psi)\right)} + \left(\frac{-\ell - s_0}{b}\right)^2} \sim \frac{\frac{1}{\left(1 + \frac{b}{a}\cos(\psi)\right)}}{2\frac{\ell + s_0}{b}}.$$

The other integral involved in the velocity field are higher order. The leading order asymptotic solution has a strength $\boldsymbol{\alpha} = (0, 0, \frac{U_3}{2\log(\frac{2\ell}{b})})$.

D.2 Uniform flow $(U_1, 0, 0)$ past the partial torus

When the uniform background flow is $(U_1, 0, 0)$, the background flow is in both the tangential and the normal direction in the local coordinates. From equation (D.5), the strength in the rectangular coordinates is

$$\alpha = \begin{pmatrix} \frac{U_1}{2}\left((c_1 + c_2) - (c_1 - c_2)\cos(\frac{2s}{a})\right) \\ \frac{U_1}{2}(c_1 - c_2)\left(-\sin(\frac{2s}{a})\right) \\ 0 \end{pmatrix}.$$

The resulted velocity field is

$$
u_1 = U_1 - \int_{-\ell}^{\ell} \left(\frac{\alpha_1}{\sqrt{(x - x_S)^2 + (y - y_S)^2 + (z - z_S)^2}} \right.
$$

$$
\left. + \frac{\alpha_1(x - x_S) + \alpha_2(y - y_S) + \alpha_3(z - z_S)}{((x - x_S)^2 + (y - y_S)^2 + (z - z_S)^2)^{3/2}} (x - x_S) \right) \, ds
$$

$$
= U_1 - \int_{-\ell}^{\ell} \left(\frac{\frac{U_1}{2} \left((c_1 + c_2) - (c_1 - c_2) \cos\left(\frac{2s}{a}\right) \right)}{\sqrt{2a^2 \left(1 + \frac{r_1}{a} \cos(\psi) \right) \left(1 - \cos\left(\theta - \frac{s}{a}\right) \right) + r_1^2}} + \right.
$$

$$
\left(\frac{U_1}{2} \left((c_1 + c_2) - (c_1 - c_2) \cos\left(\frac{2s}{a}\right) \right) \right) \left((a + r_1 \cos(\psi)) \cos(\theta) - a \cos\left(\frac{s}{a}\right) \right) +
$$

$$
\frac{U_1}{2} (c_1 - c_2) \left(-\sin\left(\frac{2s}{a}\right) \right) \left((a + r_1 \cos(\psi)) \sin(\theta) - a \sin\left(\frac{s}{a}\right) \right) \bigg/
$$

$$
\left(2a^2 \left(1 + \frac{r_1}{a} \cos(\psi) \right) \left(1 - \cos\left(\theta - \frac{s}{a}\right) \right) + r_1^2 \right)^{3/2}
$$

$$
\left. \left((a + r_1 \cos(\psi)) \cos(\theta) - a \cos\left(\frac{s}{a}\right) \right) \right) \, ds,
$$

$$
u_2 = - \int_{-\ell}^{\ell} \left(\frac{\frac{U_1}{2}(c_1 - c_2)\left(-\sin\left(\frac{2s}{a}\right) \right)}{\sqrt{(x - x_S)^2 + (y - y_S)^2 + (z - z_S)^2}} \right.
$$

$$
\left. + \frac{\alpha_1(x - x_S) + \alpha_2(y - y_S) + \alpha_3(z - z_S)}{((x - x_S)^2 + (y - y_S)^2 + (z - z_S)^2)^{3/2}} (y - y_S) \right) \, ds
$$

$$
= - \int_{-\ell}^{\ell} \left(\frac{\frac{U_1}{2}(c_1 - c_2)\left(-\sin\left(\frac{2s}{a}\right) \right)}{\sqrt{2a^2 \left(1 + \frac{r_1}{a} \cos(\psi) \right) \left(1 - \cos\left(\theta - \frac{s}{a}\right) \right) + r_1^2}} \right.
$$

$$
+ \left(\frac{U_1}{2} \left((c_1 + c_2) - (c_1 - c_2) \cos\left(\frac{2s}{a}\right) \right) \right) \left((a + r_1 \cos(\psi)) \cos(\theta) - a \cos\left(\frac{s}{a}\right) \right)
$$

$$
+ \frac{U_1}{2} (c_1 - c_2) \left(-\sin\left(\frac{2s}{a}\right) \right) \left((a + r_1 \cos(\psi)) \sin(\theta) - a \sin\left(\frac{s}{a}\right) \right) \bigg/
$$

$$
\left(2a^2 \left(1 + \frac{r_1}{a} \cos(\psi) \right) \left(1 - \cos\left(\theta - \frac{s}{a}\right) \right) + r_1^2 \right)^{3/2}
$$

$$
\left. \left((a + r_1 \cos(\psi)) \sin(\theta) - a \sin\left(\frac{s}{a}\right) \right) \right) \, d\theta_s,
$$

$$u_3 = -\int_{-\ell}^{\ell} \left(\frac{\alpha_1(x-x_\mathrm{S}) + \alpha_2(y-y_\mathrm{S}) + \alpha_3(z-z_\mathrm{S})}{((x-x_\mathrm{S})^2 + (y-y_\mathrm{S})^2 + (z-z_\mathrm{S})^2)^{3/2}}(z-z_\mathrm{S}) \right) ds$$

$$= -\int_{-\ell}^{\ell} \left\{ \left[\frac{U_1}{2}\left((c_1+c_2) - (c_1-c_2)\cos(\frac{2s}{a}) \right) \left((a+r_1\cos(\psi))\cos(\theta) - a\cos\left(\frac{s}{a}\right) \right) \right. \right.$$

$$\left. + \frac{U_1}{2}(c_1-c_2)\left(-\sin(\frac{2s}{a})\right)\left((a+r_1\cos(\psi))\sin(\theta) - a\sin\left(\frac{s}{a}\right) \right) \right] \Big/$$

$$\left(2a^2\left(1+\frac{r_1}{a}\cos(\psi)\right)\left(1-\cos\left(\theta-\frac{s}{a}\right)\right) + r_1^2 \right)^{3/2} r_1\sin(\psi) \right\} d\theta_s.$$

On the surface of the partial torus $r_1 = b$, the no-slip boundary condition is imposed. Thus,

$$0 = U_1 - \int_{-\ell}^{\ell} \left\{ \frac{\frac{U_1}{2}\left((c_1+c_2) - (c_1-c_2)\cos(\frac{2s}{a}) \right)}{\sqrt{2a^2\left(1+\frac{b}{a}\cos(\psi)\right)\left(1-\cos\left(\theta-\frac{s}{a}\right)\right) + b^2}} + \right.$$

$$\left[\frac{U_1}{2}\left((c_1+c_2) - (c_1-c_2)\cos(\frac{2s}{a}) \right)\left((a+b\cos(\psi))\cos(\theta) - a\cos\left(\frac{s}{a}\right) \right) + \right.$$

$$\left. \frac{U_1}{2}(c_1-c_2)\left(-\sin(\frac{2s}{a})\right)\left((a+b\cos(\psi))\sin(\theta) - a\sin\left(\frac{s}{a}\right) \right) \right] \Big/$$

$$\left(2a^2\left(1+\frac{b}{a}\cos(\psi)\right)\left(1-\cos\left(\theta-\frac{s}{a}\right)\right) + b^2 \right)^{3/2}$$

$$\left. \left((a+b\cos(\psi))\cos(\theta) - a\cos\left(\frac{s}{a}\right) \right) \right\} ds,$$

$$0 = -\int_{-\ell}^{\ell} \left\{ \frac{\frac{U_1}{2}(c_1-c_2)\left(-\sin(\frac{2s}{a})\right)}{\sqrt{2a^2\left(1+\frac{b}{a}\cos(\psi)\right)\left(1-\cos\left(\theta-\frac{s}{a}\right)\right) + b^2}} + \right.$$

$$\left[\frac{U_1}{2}\left((c_1+c_2) - (c_1-c_2)\cos(\frac{2s}{a}) \right)\left((a+b\cos(\psi))\cos(\theta) - a\cos\left(\frac{s}{a}\right) \right) + \right.$$

$$\left. \frac{U_1}{2}(c_1-c_2)\left(-\sin(\frac{2s}{a})\right)\left((a+b\cos(\psi))\sin(\theta) - a\sin\left(\frac{s}{a}\right) \right) \right] \Big/$$

$$\left(2a^2\left(1+\frac{b}{a}\cos(\psi)\right)\left(1-\cos\left(\theta-\frac{s}{a}\right)\right) + b^2 \right)^{3/2}$$

$$\left. \left((a+b\cos(\psi))\sin(\theta) - a\sin\left(\frac{s}{a}\right) \right) \right\} ds,$$

$$0 = \int_{-\ell}^{\ell} \left\{ \left[\frac{U_1}{2} \left((c_1 + c_2) - (c_1 - c_2) \cos\left(\frac{2s}{a}\right) \right) \left((a + b\cos(\psi)) \cos(\theta) - a\cos\left(\frac{s}{a}\right) \right) \right. \right.$$

$$\left. + \frac{U_1}{2}(c_1 - c_2) \left(-\sin\left(\frac{2s}{a}\right) \right) \left((a + b\cos(\psi)) \sin[\theta] - a\sin\left(\frac{s}{a}\right) \right) \right] \Bigg/$$

$$\left(2a^2 \left(1 + \frac{b}{a}\cos(\psi) \right) \left(1 - \cos\left(\theta - \frac{s}{a}\right) \right) + b^2 \right)^{3/2} b\sin(\psi) \right\} ds.$$

In the following analysis, the observation position on the surface of the partial torus is $(r_1, \theta, \psi) = (b, \frac{s_0}{a}, \psi)$, where s_0 is the arc-length and the no-slip boundary condition is imposed. For the inner expansion, the integrals are determined by local contributions when s is close to s_0. Following Taylor expansions

$$b^2 + 2a^2 \left(1 - \cos\left(\frac{s}{a} - \frac{s_0}{a}\right) \right) \left(1 + \frac{b}{a}\cos(\psi) \right) \sim b^2 + (s - s_0)^2 \left(1 + \frac{b}{a}\cos(\psi) \right), \quad \text{(D.6)}$$

$$a\cos\left(\frac{s_0}{a}\right) - a\cos\left(\frac{s}{a}\right) \sim \sin\left(\frac{s_0}{a}\right)(s - s_0), \quad \text{(D.7)}$$

$$a\sin\left(\frac{s_0}{a}\right) - a\sin\left(\frac{s}{a}\right) \sim -\cos\left(\frac{s_0}{a}\right)(s - s_0) \quad \text{(D.8)}$$

will be applied to the analysis.

For u_1

For the velocity in the x direction, the boundary condition implies

$$0 = U_1 - \int_{-\ell}^{\ell} \left\{ \frac{\frac{U_1}{2}\left((c_1 + c_2) - (c_1 - c_2)\cos\left(\frac{2s}{a}\right) \right)}{\sqrt{2a^2 \left(1 + \frac{b}{a}\cos(\psi) \right) \left(1 - \cos\left(\frac{s_0}{a} - \frac{s}{a}\right) \right) + b^2}} + \right.$$

$$\left[\frac{U_1}{2} \left((c_1 + c_2) - (c_1 - c_2)\cos\left(\frac{2s}{a}\right) \right) \left((a + b\cos(\psi))\cos\left(\frac{s_0}{a}\right) - a\cos\left(\frac{s}{a}\right) \right) + \right.$$

$$\left. \frac{U_1}{2}(c_1 - c_2)\left(-\sin\left(\frac{2s}{a}\right) \right) \left((a + b\cos(\psi))\sin\left(\frac{s_0}{a}\right) - a\sin\left(\frac{s}{a}\right) \right) \right]$$

$$\left. \frac{\left((a + b\cos(\psi))\cos\left(\frac{s_0}{a}\right) - a\cos\left(\frac{s}{a}\right) \right)}{\left(2a^2 \left(1 + \frac{b}{a}\cos(\psi) \right) \left(1 - \cos\left(\frac{s_0}{a} - \frac{s}{a}\right) \right) + b^2 \right)^{3/2}} \right\} ds.$$

Substitute (D.6) into denominators of the above equation,

$$
0 = U_1 - \int_{-\ell}^{\ell} \left\{ \frac{\frac{U_1}{2}\left((c_1 + c_2) - (c_1 - c_2)\cos\left(\frac{2s}{a}\right)\right)}{\sqrt{b^2 + (s - s_0)^2 \left(1 + \frac{b\cos(\psi)}{a}\right)}} \right.
$$

$$
+ \frac{\left(-a\cos\left(\frac{s}{a}\right) + \cos\left(\frac{s_0}{a}\right)(a + b\cos(\psi))\right)}{\left(b^2 + \left(1 + \frac{b\cos(\psi)}{a}\right)(s - s_0)^2\right)^{3/2}}
$$

$$
\left[-\frac{1}{2}(c_1 - c_2)U_1 \sin\left(\frac{2s}{a}\right)\left(b\cos(\psi)\sin\left(\frac{s_0}{a}\right) - \cos\left(\frac{s_0}{a}\right)(s - s_0)\right)\right.
$$

$$
\left.\left. + \frac{1}{2}U_1\left(c_1 + c_2 - (c_1 - c_2)\cos\left(\frac{2s}{a}\right)\right)\left(b\cos\left(\frac{s_0}{a}\right)\cos(\psi) + \sin\left(\frac{s_0}{a}\right)(s - s_0)\right)\right]\right\} ds.
$$

Approximate s with s_0 and substitute (D.7) and (D.8) into the equation,

$$
0 = U_1 - \int_{-\ell}^{\ell} \left\{ \frac{\frac{U_1}{2}\left((c_1 + c_2) - (c_1 - c_2)\cos\left(\frac{2s_0}{a}\right)\right)}{\sqrt{b^2 + (s - s_0)^2 \left(1 + \frac{b\cos(\psi)}{a}\right)}} \right.
$$

$$
+ \frac{\left(\sin\left(\frac{s_0}{a}\right)(s - s_0) + b\cos\left(\frac{s_0}{a}\right)\cos(\psi)\right)}{\left(b^2 + \left(1 + \frac{b\cos(\psi)}{a}\right)(s - s_0)^2\right)^{3/2}}
$$

$$
\left[-\frac{U_1}{2}(c_1 - c_2)\sin\left(\frac{2s_0}{a}\right)\left(b\cos(\psi)\sin\left(\frac{s_0}{a}\right) - \cos\left(\frac{s_0}{a}\right)(s - s_0)\right)\right.
$$

$$
\left.\left. + \frac{U_1}{2}\left(c_1 + c_2 - (c_1 - c_2)\cos\left(\frac{2s_0}{a}\right)\right)\left(b\cos\left(\frac{s_0}{a}\right)\cos(\psi) + \sin\left(\frac{s_0}{a}\right)(s - s_0)\right)\right]\right\} ds.
$$

Expand the equation and reorganize the terms,

$$0 = U_1 - \frac{U_1}{2}\left((c_1 + c_2) - (c_1 - c_2)\cos\left(\frac{2s_0}{a}\right)\right)\int_{-\ell}^{\ell}\frac{1}{\sqrt{b^2 + (s-s_0)^2\left(1 + \frac{b\cos(\psi)}{a}\right)}}\,ds$$

$$-\frac{U_1(c_1 - c_2)}{4}\frac{\sin^2\left(\frac{2s_0}{a}\right)}{\left(1 + \frac{b\cos(\psi)}{a}\right)^{3/2}}\int_{-\ell}^{\ell}\frac{1}{\left(\frac{b^2}{\left(1 + \frac{b\cos(\psi)}{a}\right)} + (s-s_0)^2\right)^{1/2}}\,ds$$

$$+\frac{U_1(c_1 - c_2)}{4}\frac{\left(\sin\left(\frac{2s_0}{a}\right)\right)^2}{\left(1 + \frac{b\cos(\psi)}{a}\right)^{3/2}}\int_{-\ell}^{\ell}\frac{\frac{b^2}{\left(1 + \frac{b\cos(\psi)}{a}\right)}}{\left(\frac{b^2}{\left(1 + \frac{b\cos(\psi)}{a}\right)} + (s-s_0)^2\right)^{3/2}}\,ds$$

$$+\frac{U_1(c_1 - c_2)}{2}\sin\left(\frac{2s_0}{a}\right)\int_{-\ell}^{\ell}\frac{\left(b\left(\sin^2\left(\frac{s_0}{a}\right) - \cos^2\left(\frac{s_0}{a}\right)\right)(s-s_0)\cos(\psi) + b^2\cos\left(\frac{s_0}{a}\right)\cos^2(\psi)\sin\left(\frac{s_0}{a}\right)\right)}{\left(b^2 + \left(1 + \frac{b\cos(\psi)}{a}\right)(s-s_0)^2\right)^{3/2}}\,ds$$

$$-\frac{\sin^2\left(\frac{s_0}{a}\right)}{\left(1 + \frac{b\cos(\psi)}{a}\right)^{3/2}}\frac{U_1}{2}\left(c_1 + c_2 - (c_1 - c_2)\cos\left(\frac{2s_0}{a}\right)\right)\int_{-\ell}^{\ell}\frac{1}{\left(\frac{b^2}{\left(1 + \frac{b\cos(\psi)}{a}\right)} + (s-s_0)^2\right)^{1/2}}\,ds$$

$$+\frac{\sin^2\left(\frac{s_0}{a}\right)}{\left(1 + \frac{b\cos(\psi)}{a}\right)^{3/2}}\frac{U_1}{2}\left(c_1 + c_2 - (c_1 - c_2)\cos\left(\frac{2s_0}{a}\right)\right)\int_{-\ell}^{\ell}\frac{\frac{b^2}{\left(1 + \frac{b\cos(\psi)}{a}\right)}}{\left(\frac{b^2}{\left(1 + \frac{b\cos(\psi)}{a}\right)} + (s-s_0)^2\right)^{3/2}}\,ds$$

$$-\frac{U_1}{2}\left(c_1 + c_2 - (c_1 - c_2)\cos\left(\frac{2s_0}{a}\right)\right)\left(b\cos\left(\frac{s_0}{a}\right)\cos(\psi)\right)^2\int_{-\ell}^{\ell}\frac{1}{\left(b^2 + \left(1 + \frac{b\cos(\psi)}{a}\right)(s-s_0)^2\right)^{3/2}}\,ds$$

$$-\frac{U_1}{2}\left(c_1 + c_2 - (c_1 - c_2)\cos\left(\frac{2s_0}{a}\right)\right)b\sin\left(2\frac{s_0}{a}\right)\cos(\psi)\int_{-\ell}^{\ell}\frac{(s-s_0)}{\left(b^2 + \left(1 + \frac{b\cos(\psi)}{a}\right)(s-s_0)^2\right)^{3/2}}\,ds.$$

Drop the higher order terms,

$$
0 \sim U_1 - \frac{U_1}{2}(c_1 + c_2) \int_{-\ell}^{\ell} \frac{1}{\sqrt{b^2 + (s - s_0)^2 \left(1 + \frac{b\cos(\psi)}{a}\right)}} \, ds
$$

$$
+ \frac{U_1}{2}(c_1 - c_2) \cos(\frac{2s_0}{a}) \int_{-\ell}^{\ell} \frac{1}{\sqrt{b^2 + (s - s_0)^2 \left(1 + \frac{b\cos(\psi)}{a}\right)}} \, ds
$$

$$
- \frac{U_1}{4}(c_1 - c_2) \frac{\sin^2(\frac{2s_0}{a})}{\left(1 + \frac{b\cos(\psi)}{a}\right)^{3/2}} \int_{-\ell}^{\ell} \frac{1}{\sqrt{b^2 + (s - s_0)^2 \left(1 + \frac{b\cos(\psi)}{a}\right)}} \, ds
$$

$$
- \frac{\sin^2(\frac{s_0}{a}) U_1 \left(c_1 + c_2 - (c_1 - c_2) \cos(\frac{2s_0}{a})\right)}{2 \left(1 + \frac{b\cos(\psi)}{a}\right)^{3/2}} \int_{-\ell}^{\ell} \frac{1}{\sqrt{b^2 + (s - s_0)^2 \left(1 + \frac{b\cos(\psi)}{a}\right)}} \, ds
$$

$$
= U_1 + \left(-\frac{U_1}{2}(c_1 + c_2) + \frac{U_1}{2}(c_1 - c_2) \cos(\frac{2s_0}{a}) - \frac{1}{4}(c_1 - c_2) \frac{U_1 \sin^2(\frac{2s_0}{a})}{\left(1 + \frac{b\cos(\psi)}{a}\right)^{3/2}} \right.
$$

$$
\left. - \frac{\sin^2(\frac{s_0}{a})}{\left(1 + \frac{b\cos(\psi)}{a}\right)^{3/2}} \frac{U_1}{2} \left(c_1 + c_2 - (c_1 - c_2) \cos(\frac{2s_0}{a}) \right) \right)
$$

$$
\int_{-\ell}^{\ell} \frac{1}{\sqrt{b^2 + (s - s_0)^2 \left(1 + \frac{b\cos(\psi)}{a}\right)}} \, ds
$$

Thus, for the leading order,

$$
1 + \left(-\frac{1}{2}(c_1 + c_2) + \frac{1}{2}(c_1 - c_2) \cos(\frac{2s_0}{a}) - \frac{(c_1 - c_2)}{4} \frac{\sin^2(\frac{2s_0}{a})}{\left(1 + \frac{b\cos(\psi)}{a}\right)^{3/2}} - \right.
$$

$$
\left. \frac{\left(c_1 + c_2 - (c_1 - c_2) \cos(\frac{2s_0}{a})\right) \sin^2(\frac{s_0}{a})}{2 \left(1 + \frac{b\cos(\psi)}{a}\right)^{3/2}} \right) \int_{-\ell}^{\ell} \frac{1}{\sqrt{b^2 + (s - s_0)^2 \left(1 + \frac{b\cos(\psi)}{a}\right)}} \, ds = 0
$$

261

$$1 + \left(-\frac{1}{2}(c_1 + c_2) + \frac{1}{2}(c_1 - c_2)\cos(\frac{2s_0}{a}) - \frac{(c_1 - c_2)}{4}\sin^2(\frac{2s_0}{a}) - \right.$$

$$\left. \frac{1}{2}(c_1 + c_2)\sin^2(\frac{s_0}{a}) + \frac{1}{2}(c_1 - c_2)\cos(\frac{2s_0}{a})\sin^2(\frac{s_0}{a}) \right) 2\log\left(\frac{2\ell}{b}\right) = 0$$

$$1 + \frac{1}{2}\left(-2(2c_1 + c_2) + 4(c_1 - \frac{c_2}{2})\cos(\frac{2s0}{a}) \right)\log\left(\frac{2\ell}{b}\right) = 0$$

For u_2

The no-slip boundary condition for the y-direction velocity,

$$u_2 = -\int_{-\ell}^{\ell} \left\{ \frac{\frac{U_1}{2}(c_1 - c_2)\left(-\sin(\frac{2s}{a})\right)}{\sqrt{2a^2\left(1 + \frac{b}{a}\cos(\psi)\right)\left(1 - \cos\left(\frac{s_0}{a} - \frac{s}{a}\right)\right) + b^2}} + \right.$$

$$\left[\frac{U_1}{2}\left((c_1 + c_2) - (c_1 - c_2)\cos(\frac{2s}{a})\right)\left((a + b\cos(\psi))\cos(\frac{s_0}{a}) - a\cos\left(\frac{s}{a}\right)\right) + \right.$$

$$\left. \frac{U_1}{2}(c_1 - c_2)\left(-\sin(\frac{2s}{a})\right)\left((a + b\cos(\psi))\sin(\frac{s_0}{a}) - a\sin\left(\frac{s}{a}\right)\right) \right]$$

$$\left. \frac{\left((a + b\cos(\psi))\sin(\frac{s_0}{a}) - a\sin\left(\frac{s}{a}\right)\right)}{\left(2a^2\left(1 + \frac{b}{a}\cos(\psi)\right)\left(1 - \cos\left(\frac{s_0}{a} - \frac{s}{a}\right)\right) + b^2\right)^{3/2}} \right\} ds = 0.$$

Applying the Taylor expansions (D.6)-(D.8) to the above condition,

$$
\begin{aligned}
0 = & -\int_{-\ell}^{\ell} \left\{ \frac{\frac{U_1}{2}(c_1 - c_2)\left(-\sin(\frac{2s_0}{a})\right)}{\sqrt{b^2 + (s - s_0)^2 \left(1 + \frac{b\cos(\psi)}{a}\right)}} \right. \\
& + \frac{U_1\left(b\cos(\psi)\sin(\frac{s_0}{a}) - \cos(\frac{s_0}{a})(s - s_0)\right)}{2\left(b^2 + \frac{(a+b\cos(\psi))(s-s_0)^2}{a}\right)^{3/2}} \\
& \left[\left(c_1 + c_2 - (c_1 - c_2)\cos(\frac{2s_0}{a})\right)\left(b\cos(\frac{s_0}{a})\cos(\psi) + \sin(\frac{s_0}{a})(s - s_0)\right)\right. \\
& \left. \left. -(c_1 - c_2)\sin(\frac{2s_0}{a})\left(b\cos(\psi)\sin(\frac{s_0}{a}) - \cos(\frac{s_0}{a})(s - s_0)\right)\right]\right\} ds \\
= & -\int_{-\ell}^{\ell} \frac{\frac{U_1}{2}(c_1 - c_2)\left(-\sin(\frac{2s_0}{a})\right)}{\sqrt{b^2 + (s - s_0)^2 \left(1 + \frac{b\cos(\psi)}{a}\right)}} ds \\
& + \frac{U_1}{4}\left(c_1 + c_2 - (c_1 - c_2)\cos(\frac{2s_0}{a})\right)\sin(2\frac{s_0}{a})\int_{-\ell}^{\ell} \frac{(s - s_0)^2}{\left(b^2 + \frac{(a+b\cos(\psi))(s-s_0)^2}{a}\right)^{3/2}} ds \\
& - U_1\left(c_1 + c_2 - (c_1 - c_2)\cos(\frac{2s_0}{a})\right) \\
& \int_{-\ell}^{\ell} \frac{\left(\frac{b^2}{2}\sin(2\frac{s_0}{a})\cos^2(\psi) + b\cos(\psi)\left(\sin^2(\frac{s_0}{a}) - \cos^2(\frac{s_0}{a})\right)(s - s_0)\right)}{2\left(b^2 + \frac{(a+b\cos(\psi))(s-s_0)^2}{a}\right)^{3/2}} ds \\
& + U_1(c_1 - c_2)\sin(\frac{2s_0}{a})\int_{-\ell}^{\ell} \frac{\left(\cos(\frac{s_0}{a})(s - s_0)\right)^2}{2\left(b^2 + \frac{(a+b\cos(\psi))(s-s_0)^2}{a}\right)^{3/2}} ds \\
& + \frac{U_1\left(c_1 - c_2\right)\sin(\frac{2s_0}{a})}{2}\int_{-\ell}^{\ell} \frac{\left(\left(b\cos(\psi)\sin(\frac{s_0}{a})\right)^2 - b\cos(\psi)\sin(2\frac{s_0}{a})(s - s_0)\right)}{\left(b^2 + \frac{(a+b\cos(\psi))(s-s_0)^2}{a}\right)^{3/2}} ds.
\end{aligned}
$$

Drop the higher order term,

$$0 \sim \frac{U_1}{2}(c_1 - c_2)\sin(\frac{2s_0}{a}) \int_{-\ell}^{\ell} \frac{1}{\sqrt{b^2 + (s-s_0)^2\left(1 + \frac{b\cos(\psi)}{a}\right)}}\, ds$$

$$+\frac{U_1}{4}\left(c_1 + c_2 - (c_1 - c_2)\cos(\frac{2s_0}{a})\right)\sin(2\frac{s_0}{a})\int_{-\ell}^{\ell} \frac{1}{\left(b^2 + \frac{(a+b\cos(\psi))(s-s_0)^2}{a}\right)^{1/2}}\, ds$$

$$+\frac{U_1}{2}\left(\cos(\frac{s_0}{a})\right)^2 (c_1 - c_2)\sin(\frac{2s_0}{a})\int_{-\ell}^{\ell} \frac{1}{\left(b^2 + \frac{(a+b\cos(\psi))(s-s_0)^2}{a}\right)^{1/2}}\, ds.$$

So,

$$\frac{1}{2}(c_1 - c_2) + \frac{1}{4}\left(c_1 + c_2 - (c_1 - c_2)\cos(\frac{2s_0}{a})\right) + \frac{1}{2}\cos^2(\frac{s_0}{a})(c_1 - c_2) = 0$$

$$\implies c_1 = \frac{c_2}{2}.$$

Solve the linear system for the constant c_1 and c_2,

$$c_1 = \frac{c_2}{2}$$

$$1 + \frac{1}{2}\left(-2(2c_1 + c_2) + 4(c_1 - \frac{c_2}{2})\cos(\frac{2s0}{a})\right)\log\left(\frac{2\ell}{b}\right) = 0$$

$$c_1 = \frac{1}{4\log\left(\frac{2\ell}{b}\right)}, \quad \text{and} \quad c_2 = \frac{1}{2\log\left(\frac{2\ell}{b}\right)}.$$

For u_3

$$0 = -b\sin(\psi)\int_{-\ell}^{\ell}\left(-\frac{U_1}{2}(c_1 - c_2)\sin(\frac{2s_0}{a})\left(b\cos(\psi)\sin(\frac{s_0}{a}) - \cos(\frac{s_0}{a})(s - s_0)\right)\right.$$

$$+\frac{U_1}{2}\left(c_1 + c_2 - (c_1 - c_2)\cos(\frac{2s_0}{a})\right)\left(b\cos(\psi)\cos(\frac{s_0}{a}) + \sin(\frac{s_0}{a})(s - s_0)\right)\Bigg)$$

$$\frac{1}{\left(b^2 + (1 + \frac{b}{a}\cos(\psi))(s - s_0)^2\right)^{3/2}}ds$$

The leading order for this condition is zero, which is automatically satisfied, i.e. not contribute to the determination of the strength.

In summary, the strength of the Stokeslet in the rectangular coordinates is

$$\boldsymbol{\alpha} = \frac{U_1}{8}\frac{1}{\log\left(\frac{2\ell}{b}\right)}\begin{pmatrix}3 + \cos(\frac{2s}{a})\\ \sin(\frac{2s}{a})\\ 0\end{pmatrix}.$$

Appendix E

The far-field velocity for the flow induced by a slender body's translation or rotation

The asymptotic solution of the far-field velocity field for the flow induced by the slender body in each step.

E.1   Uniform transition

Consider a distribution of Stokeslets over the portion $-\ell < s < \ell$ of the x-axis with strength $\boldsymbol{\alpha}(s) = (\alpha_1(s), \alpha_2(s), \alpha_3(s))$, the velocity field $\mathbf{u} = (u_1, u_2, u_3)$ due to this force distribution is [48]

$$u_1(\mathbf{x}; \boldsymbol{\alpha}) = \int_{-\ell}^{\ell} \left\{ \frac{\alpha_1(s)}{\left[(x-s)^2 + r^2\right]^{1/2}} + \frac{(x-s)\left[(x-s)\,\alpha_1(s) + y\alpha_2(s) + z\alpha_3(s)\right]}{\left[(x-s)^2 + r^2\right]^{\frac{3}{2}}} \right\} ds$$

$$u_2(\mathbf{x}; \boldsymbol{\alpha}) = \int_{-\ell}^{\ell} \left\{ \frac{\alpha_2(s)}{\left[(x-s)^2 + r^2\right]^{1/2}} + \frac{y\left[(x-s)\,\alpha_1(s) + y\alpha_2(s) + z\alpha_3(s)\right]}{\left[(x-s)^2 + r^2\right]^{\frac{3}{2}}} \right\} ds$$

$$u_3(\mathbf{x}; \boldsymbol{\alpha}) = \int_{-\ell}^{\ell} \left\{ \frac{\alpha_3(s)}{\left[(x-s)^2 + r^2\right]^{1/2}} + \frac{z\left[(x-s)\,\alpha_1(s) + y\alpha_2(s) + z\alpha_3(s)\right]}{\left[(x-s)^2 + r^2\right]^{\frac{3}{2}}} \right\} ds$$

where $r^2 = y^2 + z^2$.

As the observation point $\mathbf{x}$ is far from the body, we examine the far-field velocity. Hence, a non-dimensional formulation is introduced. Let

$$\mathbf{x}' = \frac{\mathbf{x}}{R}, \qquad s' = \frac{s}{\ell}, \qquad \boldsymbol{\alpha}' = \frac{\boldsymbol{\alpha}}{U} \tag{E.1}$$

in which R is a characteristic length assumed to be large and U is a characteristic velocity. Rewriting the velocity field as functions of the non-dimensional variables in (E.1), we get

$$
\begin{aligned}
u_1'(\mathbf{x}'; \boldsymbol{\alpha}') &= \int_{-1}^{1} \frac{\ell \alpha_1'(s')}{\left[(Rx' - \ell s')^2 + R^2 r^2\right]^{1/2}} ds' + \\
&\quad \int_{-1}^{1} \frac{\ell\,(Rx' - \ell s')\left[(Rx' - \ell s')\,\alpha_1'(s') + Ry'\alpha_2'(s') + Rz'\alpha_3'(s')\right]}{\left[(Rx' - \ell s')^2 + R^2 r^2\right]^{\frac{3}{2}}} ds' \\
&= \epsilon_0 \int_{-1}^{1} \frac{\alpha_1'(s')}{\left[(x' - \epsilon_0 s')^2 + r^2\right]^{1/2}} ds' + \\
&\quad \epsilon_0 \int_{-1}^{1} \frac{(x' - \epsilon_0 s')\left[(x' - \epsilon_0 s')\,\alpha_1'(s') + y'\alpha_2'(s') + z'\alpha_3'(s')\right]}{\left[(x' - \epsilon_0 s')^2 + r^2\right]^{\frac{3}{2}}} ds',
\end{aligned}
$$

$$
\begin{aligned}
u_2'(\mathbf{x}'; \boldsymbol{\alpha}') &= \int_{-1}^{1} \frac{\ell \alpha_2'(s')}{\left[(Rx' - \ell s')^2 + R^2 r^2\right]^{1/2}} ds' + \\
&\quad \int_{-1}^{1} \frac{\ell Ry'\left[(Rx' - \ell s')\,\alpha_1'(s') + Ry'\alpha_2'(s') + Rz'\alpha_3'(s')\right]}{\left[(Rx' - \ell s')^2 + R^2 r^2\right]^{\frac{3}{2}}} ds' \\
&= \epsilon_0 \int_{-1}^{1} \frac{\alpha_2'(s')}{\left[(x' - \epsilon_0 s')^2 + r^2\right]^{1/2}} ds' + \\
&\quad \epsilon_0 \int_{-1}^{1} \frac{y'\left[(x' - \epsilon_0 s')\,\alpha_1'(s') + y'\alpha_2'(s') + z'\alpha_3'(s')\right]}{\left[(x' - \epsilon_0 s')^2 + r^2\right]^{\frac{3}{2}}} ds',
\end{aligned}
$$

$$u_3'(\mathbf{x}';\boldsymbol{\alpha}') = \int_{-1}^{1} \frac{\ell\alpha_3'(s')}{\left[(Rx'-\ell s')^2 + R^2 r^2\right]^{1/2}} ds' +$$

$$\int_{-1}^{1} \frac{\ell R z' \left[(Rx'-\ell s')\,\alpha_1'(s') + Ry'\alpha_2'(s') + Rz'\alpha_3'(s')\right]}{\left[(Rx'-\ell s')^2 + R^2 r^2\right]^{\frac{3}{2}}} ds'$$

$$= \epsilon_0 \int_{-1}^{1} \frac{\alpha_3'(s')}{\left[(x'-\epsilon_0 s')^2 + r^2\right]^{1/2}} ds' +$$

$$\epsilon_0 \int_{-1}^{1} \frac{z' \left[(x'-\epsilon_0 s')\,\alpha_1'(s') + y'\alpha_2'(s') + z'\alpha_3'(s')\right]}{\left[(x'-\epsilon_0 s')^2 + r^2\right]^{\frac{3}{2}}} ds',$$

where r is the non-dimensional radius, $r^2 = (y')^2 + (z')^2$, and

$$\epsilon_0 = \frac{\ell}{R_0} \tag{E.2}$$

is the small parameter for the far field. Since the far-field limit of the velocity field is of interest, we examine $\epsilon_0 \to 0$ in the limit $R_0 \to 0$.

Drop all the primes,

$$u_1(\mathbf{x};\boldsymbol{\alpha}) = \epsilon_0 \int_{-1}^{1} \frac{\alpha_1(s)}{\left[(x-\epsilon_0 s)^2 + r^2\right]^{1/2}} ds +$$

$$\epsilon_0 \int_{-1}^{1} \frac{(x-\epsilon_0 s)\left[(x-\epsilon_0 s)\,\alpha_1(s) + y\alpha_2(s) + z\alpha_3(s)\right]}{\left[(x-\epsilon_0 s)^2 + r^2\right]^{\frac{3}{2}}} ds,$$

$$= \epsilon_0 \left[I(\alpha_1) + I_2(\alpha_1) + yI_1(\alpha_2) + zI_1(\alpha_3)\right]$$

$$u_2(\mathbf{x};\boldsymbol{\alpha}) = \epsilon_0 \int_{-1}^{1} \frac{\alpha_2(s)}{\left[(x-\epsilon_0 s)^2 + r^2\right]^{1/2}} ds +$$

$$\epsilon_0 \int_{-1}^{1} \frac{y\left[(x-\epsilon_0 s)\,\alpha_1(s) + y\alpha_2(s) + z\alpha_3(s)\right]}{\left[(x-\epsilon_0 s)^2 + r^2\right]^{\frac{3}{2}}} ds,$$

$$= \epsilon_0 \left[I(\alpha_2) + yI_1(\alpha_1) + y^2 I_0(\alpha_2) + yzI_0(\alpha_3)\right]$$

$$u_3(\mathbf{x};\boldsymbol{\alpha}) = \epsilon_0 \int_{-1}^{1} \frac{\alpha_3(s)}{\left[(x-\epsilon_0 s)^2 + r^2\right]^{1/2}} ds +$$

$$\epsilon_0 \int_{-1}^{1} \frac{z\left[(x-\epsilon_0 s)\,\alpha_1(s) + y\alpha_2(s) + z\alpha_3(s)\right]}{\left[(x-\epsilon_0 s)^2 + r^2\right]^{\frac{3}{2}}} ds.$$

$$= \epsilon_0 \left[I(\alpha_3) + zI_1(\alpha_1) + yzI_0(\alpha_2) + x_3^2 I_0(\alpha_3)\right],$$

in terms of these integrals

$$I(\alpha) = \int_{-1}^{1} \frac{\alpha(s)}{\left[(x - \epsilon_0 s)^2 + r^2\right]^{1/2}} ds \qquad (\text{E.3})$$

$$I_0(\alpha) = \int_{-1}^{1} \frac{\alpha(s)}{\left[(x - \epsilon_0 s)^2 + r^2\right]^{3/2}} ds$$

$$I_1(\alpha) = \int_{-1}^{1} \frac{(x - \epsilon_0 s)\,\alpha(s)}{\left[(x - \epsilon_0 s)^2 + r^2\right]^{3/2}} ds$$

$$I_2(\alpha) = \int_{-1}^{1} \frac{(x - \epsilon_0 s)^2\,\alpha(s)}{\left[(x - \epsilon_0 s)^2 + r^2\right]^{3/2}} ds.$$

Examine the integrand of I in (E.3). Taylor expansion about $\epsilon_0 = 0$ provides

$$\frac{1}{\left[(x - \epsilon_0 s)^2 + r^2\right]^{1/2}} = \frac{1}{|\mathbf{x}|} + \frac{x}{|\mathbf{x}|^3} s\epsilon_0 + \frac{3x^2 - |\mathbf{x}|^2}{2|\mathbf{x}|^5} s^2 \epsilon_0^2 + O(\epsilon_0^3).$$

Substituting this expansion into I gives that

$$I(\alpha) = \frac{1}{|\mathbf{x}|} \int_{-1}^{1} \alpha(s) ds + \frac{x}{|\mathbf{x}|^3} \epsilon_0 \int_{-1}^{1} s\alpha(s) ds + \frac{3x^2 - |\mathbf{x}|^2}{2|\mathbf{x}|^5} \epsilon_0^2 \int_{-1}^{1} s^2 \alpha(s) ds + O(\epsilon_0^3).$$

Now examine the integrand of I_0. Since

$$\frac{1}{\left[(x - \epsilon_0 s)^2 + r^2\right]^{3/2}} = \frac{1}{|\mathbf{x}|^3} + \frac{3x}{|\mathbf{x}|^5} s\epsilon_0 + \frac{15x^2 - 3|\mathbf{x}|^2}{2|\mathbf{x}|^7} s^2 \epsilon_0^2 + O(\epsilon_0^3)$$

upon Taylor expanding about $\epsilon_0 = 0$,

$$I_0(\alpha) = \frac{1}{|\mathbf{x}|^3} \int_{-1}^{1} \alpha(s) ds + \frac{3x\epsilon_0}{|\mathbf{x}|^5} \int_{-1}^{1} s\alpha(s) ds + \frac{15x^2 - 3|\mathbf{x}|^2}{2|\mathbf{x}|^7} \epsilon_0^2 \int_{-1}^{1} s^2 \alpha(s) ds + O(\epsilon_0^3).$$

By applying Taylor expansion of the integrand of I_1 for $\epsilon_0 \to 0$,

$$\frac{(x - \epsilon_0 s)}{\left[(x - \epsilon_0 s)^2 + r^2\right]^{3/2}} = \frac{x}{|\mathbf{x}|^3} + \frac{3x^2 - |\mathbf{x}|^2}{|\mathbf{x}|^5} s\epsilon_0 + \frac{15x^3 - 9x|\mathbf{x}|^2}{2|\mathbf{x}|^7} s^2 \epsilon_0^2 + O(\epsilon_0^3),$$

the integral becomes

$$
\begin{aligned}
I_1(\alpha) \;=\; & \frac{x}{|\mathbf{x}|^3} \int_{-1}^{1} \alpha(s)ds + \frac{3x^2 - |\mathbf{x}|^2}{|\mathbf{x}|^5}\epsilon_0 \int_{-1}^{1} s\alpha(s)ds \\
& + \frac{15x^3 - 9x|\mathbf{x}|^2}{2|\mathbf{x}|^7}\epsilon_0^2 \int_{-1}^{1} s^2\alpha(s)ds + O(\epsilon_0^3).
\end{aligned}
$$

Upon Taylor expanding the integrand of I_2 about $\epsilon_0 = 0$,

$$
\frac{(x - \epsilon_0 s)^2}{\left[(x - \epsilon_0 s)^2 + r^2\right]^{3/2}} \;=\; \frac{x^2}{|\mathbf{x}|^3} + \frac{3x^3 - 2x|\mathbf{x}|^2}{|\mathbf{x}|^5}s\epsilon_0 + \frac{15x^4 - 15x^2|\mathbf{x}|^2 + 2|\mathbf{x}|^4}{2|\mathbf{x}|^7}s^2\epsilon_0^2 + O(\epsilon_0^3).
$$

Thus

$$
\begin{aligned}
I_2(\alpha) \;=\; & \frac{x^2}{|\mathbf{x}|^3} \int_{-1}^{1} \alpha(s)ds + \frac{3x^3 - 2x|\mathbf{x}|^2}{|\mathbf{x}|^5}\epsilon_0 \int_{-1}^{1} s\alpha(s)ds \\
& + \frac{15x^4 - 15x^2|\mathbf{x}|^2 + 2|\mathbf{x}|^4}{2|\mathbf{x}|^7}\epsilon_0^2 \int_{-1}^{1} s^2\alpha(s)ds + O(\epsilon_0^3).
\end{aligned}
$$

Uniform Stokeslets

Consider the velocity field due to a line distribution of uniform Stokeslets with strength

$$
\begin{cases}
\alpha_1(s) \;=\; \frac{\varepsilon U_1}{4}; \\[4pt]
\alpha_3(s) \;=\; \frac{\varepsilon U_2}{2}; \\[4pt]
\alpha_2(s) \;=\; \frac{\varepsilon U_3}{2}.
\end{cases}
$$

Since

$$\int_{-1}^{1} \alpha(s)ds = 2\alpha,$$

$$\int_{-1}^{1} s\alpha(s)ds = 0,$$

$$\int_{-1}^{1} s^2\alpha(s)ds = \frac{2}{3}\alpha,$$

$$I(\alpha) = \frac{2}{|\mathbf{x}|}\alpha + \frac{3x^2 - |\mathbf{x}|^2}{3|\mathbf{x}|^5}\epsilon_0^2\alpha + O(\epsilon_0^3), \tag{E.4}$$

$$I_0(\alpha) = \frac{2}{|\mathbf{x}|^3}\alpha + \frac{5x^2 - |\mathbf{x}|^2}{|\mathbf{x}|^7}\epsilon_0^2\alpha + O(\epsilon_0^3), \tag{E.5}$$

$$I_1(\alpha) = \frac{2x}{|\mathbf{x}|^3}\alpha + \frac{5x^3 - 3x|\mathbf{x}|^2}{|\mathbf{x}|^7}\epsilon_0^2\alpha + O(\epsilon_0^3), \tag{E.6}$$

$$I_2(\alpha) = \frac{2x^2}{|\mathbf{x}|^3}\alpha + \frac{15x^4 - 15x^2|\mathbf{x}|^2 + 2|\mathbf{x}|^4}{3|\mathbf{x}|^7}\epsilon_0^2\alpha + O(\epsilon_0^3). \tag{E.7}$$

Substitute the above integrals into the dimensionless velocity field,

$$u_1(\mathbf{x}; \boldsymbol{\alpha}) = \epsilon_0 \left[I(\alpha_1) + I_2(\alpha_1) + yI_1(\alpha_2) + zI_1(\alpha_3) \right]$$
$$= \epsilon_0 \left[\frac{2}{|\mathbf{x}|}\alpha_1 + \frac{3x^2 - |\mathbf{x}|^2}{3|\mathbf{x}|^5}\epsilon_0^2\alpha_1 \right] + \epsilon_0 \left[\frac{2x^2}{|\mathbf{x}|^3}\alpha_1 + \frac{15x^4 - 15x^2|\mathbf{x}|^2 + 2|\mathbf{x}|^4}{3|\mathbf{x}|^7}\epsilon_0^2\alpha_1 \right]$$
$$+ \epsilon_0 y \left[\frac{2x}{|\mathbf{x}|^3}\alpha_2 + \frac{5x^3 - 3x|\mathbf{x}|^2}{|\mathbf{x}|^7}\epsilon_0^2\alpha_2 \right] + \epsilon_0 z \left[\frac{2x}{|\mathbf{x}|^3}\alpha_3 + \frac{5x^3 - 3x|\mathbf{x}|^2}{|\mathbf{x}|^7}\epsilon_0^2\alpha_3 \right] + O(\epsilon_0^4)$$

$$u_2(\mathbf{x}; \boldsymbol{\alpha}) = \epsilon_0 \left[I(\alpha_2) + yI_1(\alpha_1) + y^2 I_0(\alpha_2) + yzI_0(\alpha_3) \right]$$
$$= \epsilon_0 \left[\frac{2}{|\mathbf{x}|}\alpha_2 + \frac{3x^2 - |\mathbf{x}|^2}{3|\mathbf{x}|^5}\epsilon_0^2\alpha_2 \right] + \epsilon_0 y \left[\frac{2x}{|\mathbf{x}|^3}\alpha_1 + \frac{5x^3 - 3x|\mathbf{x}|^2}{|\mathbf{x}|^7}\epsilon_0^2\alpha_1 \right]$$
$$+ \epsilon_0 y^2 \left[\frac{2}{|\mathbf{x}|^3}\alpha_2 + \frac{15x^2 - 3|\mathbf{x}|^2}{3|\mathbf{x}|^7}\epsilon_0^2\alpha_2 \right] + \epsilon_0 yz \left[\frac{2}{|\mathbf{x}|^3}\alpha_3 + \frac{15x^2 - 3|\mathbf{x}|^2}{3|\mathbf{x}|^7}\epsilon_0^2\alpha_3 \right] + O(\epsilon_0^4)$$

$$u_3(\mathbf{x}; \boldsymbol{\alpha}) = \epsilon_0 \left[I(\alpha_3) + zI_1(\alpha_1) + yzI_0(\alpha_2) + x_3^2 I_0(\alpha_3) \right]$$
$$= \epsilon_0 \left[\frac{2}{|\mathbf{x}|}\alpha_3 + \frac{3x^2 - |\mathbf{x}|^2}{3|\mathbf{x}|^5}\epsilon_0^2\alpha_3 \right] + \epsilon_0 z \left[\frac{2x}{|\mathbf{x}|^3}\alpha_1 + \frac{5x^3 - 3x|\mathbf{x}|^2}{|\mathbf{x}|^7}\epsilon_0^2\alpha_1 \right]$$
$$+ \epsilon_0 yz \left[\frac{2}{|\mathbf{x}|^3}\alpha_2 + \frac{5x^2 - |\mathbf{x}|^2}{|\mathbf{x}|^7}\epsilon_0^2\alpha_2 \right] + \epsilon_0 x_3^2 \left[\frac{2}{|\mathbf{x}|^3}\alpha_3 + \frac{5x^2 - |\mathbf{x}|^2}{|\mathbf{x}|^7}\epsilon_0^2\alpha_3 \right] + O(\epsilon_0^4)$$

Rewrite it in the order of ϵ,

$$
\begin{aligned}
u_1(\mathbf{x};\boldsymbol{\alpha}) &= \epsilon_0 \left[\frac{2}{|\mathbf{x}|}\alpha_1 + \frac{2x^2}{|\mathbf{x}|^3}\alpha_1 + \frac{2xy}{|\mathbf{x}|^3}\alpha_2 + \frac{2xz}{|\mathbf{x}|^3}\alpha_3 \right] \\
&\quad + \epsilon_0^3 \left[\frac{3x^2 - |\mathbf{x}|^2}{3|\mathbf{x}|^5}\alpha_1 + \frac{15x^4 - 15x^2|\mathbf{x}|^2 + 2|\mathbf{x}|^4}{3|\mathbf{x}|^7}\alpha_1 \right. \\
&\quad \left. + \frac{5x^3 - 3x|\mathbf{x}|^2}{|\mathbf{x}|^7}(y\alpha_2 + z\alpha_3) \right] + O(\epsilon_0^4) \tag{E.8}
\end{aligned}
$$

$$
\begin{aligned}
u_2(\mathbf{x};\boldsymbol{\alpha}) &= \epsilon_0 \left[\frac{2}{|\mathbf{x}|}\alpha_2 + \frac{2xy}{|\mathbf{x}|^3}\alpha_1 + \frac{2y^2}{|\mathbf{x}|^3}\alpha_2 + \frac{2yz}{|\mathbf{x}|^3}\alpha_3 \right] \\
&\quad + \epsilon_0^3 \left[\frac{3x^2 - |\mathbf{x}|^2}{3|\mathbf{x}|^5}\alpha_2 + y\frac{5x^3 - 3x|\mathbf{x}|^2}{|\mathbf{x}|^7}\alpha_1 + \frac{5x^2 - |\mathbf{x}|^2}{|\mathbf{x}|^7}(y^2\alpha_2 + yz\alpha_3) \right] \\
&\quad + O(\epsilon_0^4) \tag{E.9}
\end{aligned}
$$

$$
\begin{aligned}
u_3(\mathbf{x};\boldsymbol{\alpha}) &= \epsilon_0 \left[\frac{2}{|\mathbf{x}|}\alpha_3 + \frac{2xz}{|\mathbf{x}|^3}\alpha_1 + \frac{2yz}{|\mathbf{x}|^3}\alpha_2 + \frac{2x_3^2}{|\mathbf{x}|^3}\alpha_3 \right] \\
&\quad + \epsilon_0^3 \left[\frac{3x^2 - |\mathbf{x}|^2}{3|\mathbf{x}|^5}\alpha_3 + z\frac{5x^3 - 3x|\mathbf{x}|^2}{|\mathbf{x}|^7}\alpha_1 + \frac{5x^2 - |\mathbf{x}|^2}{|\mathbf{x}|^7}(yz\alpha_2 + x_3^2\alpha_3) \right] \\
&\quad + O(\epsilon_0^4) \tag{E.10}
\end{aligned}
$$

From the leading order of the far-field velocity

$$
u_1(\mathbf{x};\boldsymbol{\alpha}) = \epsilon_0 \left[\frac{2}{|\mathbf{x}|}\alpha_1 + \frac{2x^2}{|\mathbf{x}|^3}\alpha_1 + \frac{2xy}{|\mathbf{x}|^3}\alpha_2 + \frac{2xz}{|\mathbf{x}|^3}\alpha_3 \right] + O(\epsilon_0^3) \tag{E.11}
$$

$$
u_2(\mathbf{x};\boldsymbol{\alpha}) = \epsilon_0 \left[\frac{2}{|\mathbf{x}|}\alpha_2 + \frac{2xy}{|\mathbf{x}|^3}\alpha_1 + \frac{2y^2}{|\mathbf{x}|^3}\alpha_2 + \frac{2yz}{|\mathbf{x}|^3}\alpha_3 \right] + O(\epsilon_0^3) \tag{E.12}
$$

$$
u_3(\mathbf{x};\boldsymbol{\alpha}) = \epsilon_0 \left[\frac{2}{|\mathbf{x}|}\alpha_3 + \frac{2xz}{|\mathbf{x}|^3}\alpha_1 + \frac{2yz}{|\mathbf{x}|^3}\alpha_2 + \frac{2x_3^2}{|\mathbf{x}|^3}\alpha_3 \right] + O(\epsilon_0^3) \tag{E.13}
$$

the fluid particle trajectory is

$$
\begin{aligned}
\frac{dx}{dt} &= \epsilon_0 \left[\frac{2}{|\mathbf{x}|}\alpha_1 + \frac{2x^2}{|\mathbf{x}|^3}\alpha_1 + \frac{2xy}{|\mathbf{x}|^3}\alpha_2 + \frac{2xz}{|\mathbf{x}|^3}\alpha_3 \right] + O(\epsilon_0^3), \\
\frac{dy}{dt} &= \epsilon_0 \left[\frac{2}{|\mathbf{x}|}\alpha_2 + \frac{2xy}{|\mathbf{x}|^3}\alpha_1 + \frac{2y^2}{|\mathbf{x}|^3}\alpha_2 + \frac{2yz}{|\mathbf{x}|^3}\alpha_3 \right] + O(\epsilon_0^3), \\
\frac{dz}{dt} &= \epsilon_0 \left[\frac{2}{|\mathbf{x}|}\alpha_3 + \frac{2xz}{|\mathbf{x}|^3}\alpha_1 + \frac{2yz}{|\mathbf{x}|^3}\alpha_2 + \frac{2x_3^2}{|\mathbf{x}|^3}\alpha_3 \right] + O(\epsilon_0^3).
\end{aligned}
$$

E.2 Rotation

In this section, we derive the far-field for the flow induced by the rotation of the body about its midpoint with constant angular velocity ω in the (x, y) plane. This is a degenerate case of the slender body sweeping out a double cone.

If the rod is sweeping out a double cone, the velocity field in the body frame where the rod is tilted is [48]

$$
u_1(\mathbf{x}) = \omega y + \frac{\omega \varepsilon \sin(\kappa)}{2} \int_{-\ell}^{\ell} \frac{(x - s \sin(\kappa)) y s}{[(x - s \sin(\kappa))^2 + y^2 + (z - s \cos(\kappa))^2]^{3/2}} ds
$$

$$
u_2(\mathbf{x}) = -\omega x + \frac{\omega \varepsilon \sin(\kappa)}{2} \int_{-\ell}^{\ell} \left\{ \frac{s}{[(x - s \sin(\kappa))^2 + y^2 + (z - s \cos(\kappa))^2]^{1/2}} \right.
$$

$$
\left. + \frac{y^2 s}{[(x - s \sin(\kappa))^2 + y^2 + (z - s \cos k)^2]^{\frac{3}{2}}} \right\} ds
$$

$$
u_3(\mathbf{x}) = \frac{\omega \varepsilon \sin(\kappa)}{2} \int_{-\ell}^{\ell} \left\{ \frac{y(z - s \cos(\kappa)) s}{\left[(x - s \sin(\kappa))^2 + y^2 + (z - s \cos(\kappa))^2\right]^{\frac{3}{2}}} \right\} ds
$$

where angle κ is the cone angle from the positive z-axis to the body.

Non-dimensionalization To examine the velocity field as the observation point $\mathbf{x}$ gets far from the force distribution, a non-dimensional formulation is introduced. Let

$$
\mathbf{x}' = \frac{\mathbf{x}}{R}, \qquad s' = \frac{s}{\ell}, \tag{E.14}
$$

where R is a scalar parameter with the dimensions of length assumed to be large. The velocity field written as function of the non-dimensional variables in (E.14) becomes

$$u'_1(\mathbf{x}') = \omega Ry' + \frac{\omega\varepsilon\sin(\kappa)}{2} \int_{-1}^{1} \frac{(Rx'-\ell s'\sin(\kappa))Ry'\ell s'}{[(Rx'-\ell s'\sin(\kappa))^2+(Ry')^2+(Rz'-\ell s'\cos(\kappa))^2]^{3/2}} d(\ell s')$$

$$u'_2(\mathbf{x}') = -\omega Rx' + \frac{\omega\varepsilon\sin(\kappa)}{2} \int_{-1}^{1} \left\{ \frac{\ell s'}{[(Rx'-\ell s'\sin(\kappa))^2+(Ry')^2+(Rz'-\ell s'\cos(\kappa))^2]^{1/2}} \right.$$

$$\left. + \frac{(Ry')^2\ell s'}{[(Rx'-\ell s'\sin(\kappa))^2+(Ry')^2+(Rz'-\ell s'\cos(\kappa))^2]^{\frac{3}{2}}} \right\} d(\ell s')$$

$$u'_3(\mathbf{x}') = \frac{\omega\varepsilon\sin(\kappa)}{2} \int_{-1}^{1} \left\{ \frac{Ry'(Rz'-\ell s'\cos(\kappa))\ell s'}{\left[(Rx'-\ell s'\sin(\kappa))^2+(Ry')^2+(Rz'-\ell s'\cos(\kappa))^2\right]^{\frac{3}{2}}} \right\} d(\ell s').$$

Simplify above equations,

$$u'_1(\mathbf{x}') = \omega Ry' + \frac{\omega\varepsilon\ell\sin(\kappa)}{2} \int_{-1}^{1} \frac{(x'-\epsilon_0 s'\sin(\kappa))y'\epsilon_0 s'}{[(x'-\epsilon_0 s'\sin(\kappa))^2+(y')^2+(z'-\epsilon_0 s'\cos(\kappa))^2]^{3/2}} ds',$$

$$u'_2(\mathbf{x}') = -\omega Rx' + \frac{\omega\varepsilon\ell\sin(\kappa)}{2} \int_{-1}^{1} \left\{ \frac{\epsilon_0 s'}{[(x'-\epsilon_0 s'\sin(\kappa))^2+(y')^2+(z'-\epsilon_0 s'\cos(\kappa))^2]^{1/2}} \right.$$

$$\left. + \frac{(y')^2\epsilon_0 s'}{[(x'-\epsilon_0 s'\sin(\kappa))^2+(y')^2+(z'-\epsilon_0 s'\cos(\kappa))^2]^{\frac{3}{2}}} \right\} ds',$$

$$u'_3(\mathbf{x}') = \frac{\omega\varepsilon\ell\sin(\kappa)}{2} \int_{-1}^{1} \frac{y'(z'-\epsilon_0 s'\cos(\kappa))\epsilon_0 s'}{\left[(x'-\epsilon_0 s'\sin(\kappa))^2+(y')^2+(z'-\epsilon_0 s'\cos(\kappa))^2\right]^{\frac{3}{2}}} ds',$$

where $\epsilon_0 = \frac{\ell}{R}$. Drop all the primes,

$$u_1(\mathbf{x}) = \omega Ry + \frac{\omega\varepsilon\ell\sin(\kappa)}{2} \int_{-1}^{1} \frac{(x-\epsilon_0 s\sin(\kappa))y\epsilon_0 s}{[(x-\epsilon_0 s\sin(\kappa))^2+y^2+(z-\epsilon_0 s\cos(\kappa))^2]^{3/2}} ds,$$

$$u_2(\mathbf{x}) = -\omega Rx + \frac{\omega\varepsilon\ell\sin(\kappa)}{2} \int_{-1}^{1} \left\{ \frac{\epsilon_0 s}{[(x-\epsilon_0 s\sin(\kappa))^2+y^2+(z-\epsilon_0 s\cos(\kappa))^2]^{1/2}} \right.$$

$$\left. + \frac{y^2\epsilon_0 s}{[(x-\epsilon_0 s\sin(\kappa))^2+y^2+(z-\epsilon_0 s\cos(\kappa))^2]^{\frac{3}{2}}} \right\} ds,$$

$$u_3(\mathbf{x}) = \frac{\omega\varepsilon\ell\sin(\kappa)}{2} \int_{-1}^{1} \frac{y(z-\epsilon_0 s\cos(\kappa))\epsilon_0 s}{\left[(x-\epsilon_0 s\sin(\kappa))^2+y^2+(z-\epsilon_0 s\cos(\kappa))^2\right]^{\frac{3}{2}}} ds.$$

To examine the flow induced by a slender body rotating in the x-y plane as Phase

2 and Phase 4 in Chapter 8, we set the tilt angle $\kappa = \frac{\pi}{2}$. Then,

$$u_1(\mathbf{x}) = \omega R y + \frac{\omega \varepsilon \ell y \epsilon_0}{2} \int_{-1}^{1} \frac{(x - \epsilon_0 s)s}{[(x - \epsilon_0 s)^2 + y^2 + z^2]^{3/2}} ds,$$

$$u_2(\mathbf{x}) = -\omega R x + \frac{\omega \varepsilon \ell \epsilon_0}{2} \int_{-1}^{1} \left[\frac{s}{[(x - \epsilon_0 s)^2 + y^2 + z^2]^{1/2}} + \frac{y^2 s}{[(x - \epsilon_0 s)^2 + y^2 + z^2]^{\frac{3}{2}}} \right] ds,$$

$$u_3(\mathbf{x}) = \frac{\omega \varepsilon \ell y z \epsilon_0}{2} \int_{-1}^{1} \frac{s}{\left[(x - \epsilon_0 s)^2 + y^2 + z^2\right]^{\frac{3}{2}}} ds.$$

Since The Taylor expanding about $\epsilon_0 = 0$ gives,

$$\frac{(x - \epsilon_0 s)s}{[(x - \epsilon_0 s)^2 + y^2 + z^2]^{3/2}} = \frac{sx}{|\mathbf{x}|^3} + \left(\frac{3x^2}{|\mathbf{x}|^5} - \frac{1}{|\mathbf{x}|^3} \right) s^2 \epsilon_0 + \left(\frac{15x^3}{2|\mathbf{x}|^7} - \frac{9x}{2|\mathbf{x}|^5} \right) s^3 \epsilon_0^2 +$$
$$\left(\frac{35x^4}{2|\mathbf{x}|^9} - \frac{15x^2}{|\mathbf{x}|^7} + \frac{3}{2|\mathbf{x}|^5} \right) s^4 \epsilon_0^3 + O(\epsilon_0)^4,$$

$$\frac{s}{[(x - \epsilon_0 s)^2 + y^2 + z^2]^{1/2}} = \frac{s}{|\mathbf{x}|} + \frac{x}{|\mathbf{x}|^3} s^2 \epsilon_0 + \left(\frac{3x^2}{2|\mathbf{x}|^5} - \frac{1}{2|\mathbf{x}|^3} \right) s^3 \epsilon_0^2 +$$
$$\left(\frac{5x^3}{2|\mathbf{x}|^7} - \frac{3x}{2|\mathbf{x}|^5} \right) s^4 \epsilon_0^3 + O(\epsilon_0)^4,$$

$$\frac{s}{[(x - \epsilon_0 s)^2 + y^2 + z^2]^{\frac{3}{2}}} = \frac{s}{|\mathbf{x}|^3} + \frac{3x}{|\mathbf{x}|^5} s^2 \epsilon_0 + \left(\frac{15x^2}{2|\mathbf{x}|^7} - \frac{3}{2|\mathbf{x}|^5} \right) s^3 \epsilon_0^2 +$$
$$\left(\frac{35x^3}{2|\mathbf{x}|^9} - \frac{15x}{2|\mathbf{x}|^7} \right) s^4 \epsilon_0^3 + O(\epsilon_0)^4.$$

Upon the above Taylor expanding, the integrals are

$$\int_{-1}^{1} \frac{(x - \epsilon_0 s)s}{[(x - \epsilon_0 s)^2 + y^2 + z^2]^{\frac{3}{2}}} ds$$
$$= \frac{x}{|\mathbf{x}|^3} \int_{-1}^{1} s\, ds + \left(\frac{3x^2}{|\mathbf{x}|^5} - \frac{1}{|\mathbf{x}|^3} \right) \epsilon_0 \int_{-1}^{1} s^2 ds + \left(\frac{15x^3}{2|\mathbf{x}|^7} - \frac{9x}{2|\mathbf{x}|^5} \right) \epsilon_0^2 \int_{-1}^{1} s^3 ds$$
$$+ \left(\frac{35x^4}{2|\mathbf{x}|^9} - \frac{15x^2}{|\mathbf{x}|^7} + \frac{3}{2|\mathbf{x}|^5} \right) \epsilon_0^3 \int_{-1}^{1} s^4 ds + O(\epsilon_0^4)$$
$$= \left(\frac{3x^2}{|\mathbf{x}|^5} - \frac{1}{|\mathbf{x}|^3} \right) \frac{2}{3} \epsilon_0 + \left(\frac{35x^4}{2|\mathbf{x}|^9} - \frac{15x^2}{|\mathbf{x}|^7} + \frac{3}{2|\mathbf{x}|^5} \right) \frac{2}{5} \epsilon_0^3 + O(\epsilon_0^4),$$

275

$$\int_{-1}^{1} \frac{s}{[(x - \epsilon_0 s)^2 + y^2 + z^2]^{1/2}} ds$$

$$= \frac{1}{|\mathbf{x}|} \int_{-1}^{1} s\, ds + \frac{x}{|\mathbf{x}|^3} \epsilon_0 \int_{-1}^{1} s^2 ds + \left(\frac{3x^2}{2 |\mathbf{x}|^5} - \frac{1}{2 |\mathbf{x}|^3} \right) \epsilon_0^2 \int_{-1}^{1} s^3 ds$$

$$+ \left(\frac{5x^3}{2 |\mathbf{x}|^7} - \frac{3x}{2 |\mathbf{x}|^5} \right) \epsilon_0^3 \int_{-1}^{1} s^4 ds + O(\epsilon_0^4)$$

$$= \frac{x}{|\mathbf{x}|^3} \frac{2\epsilon_0}{3} + \left(\frac{5x^3}{2 |\mathbf{x}|^7} - \frac{3x}{2 |\mathbf{x}|^5} \right) \frac{2}{5} \epsilon_0^3 + O(\epsilon_0^4),$$

$$\int_{-1}^{1} \frac{s}{[(x - \epsilon_0 s)^2 + y^2 + z^2]^{\frac{3}{2}}} ds$$

$$= \frac{1}{|\mathbf{x}|^3} \int_{-1}^{1} ds + \frac{3x}{|\mathbf{x}|^5} \epsilon_0 \int_{-1}^{1} s^2 ds + \left(\frac{15x^2}{2 |\mathbf{x}|^7} - \frac{3}{2 |\mathbf{x}|^5} \right) \epsilon_0^2 \int_{-1}^{1} s^3 ds$$

$$+ \left(\frac{35x^3}{2 |\mathbf{x}|^9} - \frac{15x}{2 |\mathbf{x}|^7} \right) \epsilon_0^3 \int_{-1}^{1} s^4 ds + O(\epsilon_0^4)$$

$$= \frac{3x}{|\mathbf{x}|^5} \frac{2}{3} \epsilon_0 + \left(\frac{35x^3}{2 |\mathbf{x}|^9} - \frac{15x}{2 |\mathbf{x}|^7} \right) \frac{2\epsilon_0^3}{5} + O(\epsilon_0^5).$$

In summary,

$$\int_{-1}^{1} \frac{(x - \epsilon_0 s)s}{[(x - \epsilon_0 s)^2 + y^2 + z^2]^{3/2}} ds = \left(\frac{3x^2}{|\mathbf{x}|^5} - \frac{1}{|\mathbf{x}|^3} \right) \frac{2}{3} \epsilon_0$$

$$+ \left(\frac{35x^4}{2 |\mathbf{x}|^9} - \frac{15x^2}{|\mathbf{x}|^7} + \frac{3}{2 |\mathbf{x}|^5} \right) \frac{2}{5} \epsilon_0^3 + O(\epsilon_0^4),$$

$$\int_{-1}^{1} \frac{s}{[(x - \epsilon_0 s)^2 + y^2 + z^2]^{1/2}} ds = \frac{x}{|\mathbf{x}|^3} \frac{2}{3} \epsilon_0 + \left(\frac{5x^3}{|\mathbf{x}|^7} - \frac{3x}{|\mathbf{x}|^5} \right) \frac{1}{5} \epsilon_0^3 + O(\epsilon_0^4),$$

$$\int_{-1}^{1} \frac{s}{[(x - \epsilon_0 s)^2 + y^2 + z^2]^{\frac{3}{2}}} ds = \frac{3x}{|\mathbf{x}|^5} \frac{2}{3} \epsilon_0 + \left(\frac{7x^3}{|\mathbf{x}|^9} - \frac{3x}{|\mathbf{x}|^7} \right) \epsilon_0^3 + O(\epsilon_0^4).$$

So, the velocity field is

$$
\begin{aligned}
u_1(\mathbf{x}) &= \omega R y + \frac{\omega\varepsilon\ell y\epsilon_0}{2}\int_{-1}^{1}\frac{(x-\epsilon_0 s)s}{[(x-\epsilon_0 s)^2+y^2+z^2]^{3/2}}ds\\
&= \omega R y + \frac{\omega\varepsilon\ell y\epsilon_0}{2}\left\{\left(\frac{3x^2}{|\mathbf{x}|^5}-\frac{1}{|\mathbf{x}|^3}\right)\frac{2\epsilon_0}{3}+\left(\frac{35x^4}{2|\mathbf{x}|^9}-\frac{15x^2}{|\mathbf{x}|^7}+\frac{3}{2|\mathbf{x}|^5}\right)\frac{2\epsilon_0^3}{5}+O(\epsilon_0^4)\right\},\\[4pt]
u_2(\mathbf{x}) &= -\omega R x + \frac{\omega\varepsilon\ell\epsilon_0}{2}\int_{-1}^{1}\left\{\frac{s}{[(x-\epsilon_0 s)^2+y^2+z^2]^{1/2}}+\frac{y^2 s}{[(x-\epsilon_0 s)^2+y^2+z^2]^{\frac{3}{2}}}\right\}ds\\
&= -\omega R x + \frac{\omega\varepsilon\ell\epsilon_0}{2}\left\{\frac{x}{|\mathbf{x}|^3}\frac{2\epsilon_0}{3}+\left(\frac{5x^3}{|\mathbf{x}|^7}-\frac{3x}{|\mathbf{x}|^5}\right)\frac{1}{5}\epsilon_0^3+O(\epsilon_0^4)\right\}\\
&\quad+\frac{\omega\varepsilon\ell\epsilon_0 y^2}{2}\left\{\frac{3x}{|\mathbf{x}|^5}\frac{2}{3}\epsilon_0+\left(\frac{7x^3}{|\mathbf{x}|^9}-\frac{3x}{|\mathbf{x}|^7}\right)\epsilon_0^3+O(\epsilon_0^4)\right\},\\[4pt]
u_3(\mathbf{x}) &= \frac{\omega\varepsilon\ell yz\epsilon_0}{2}\int_{-1}^{1}\frac{s}{\left[(x-\epsilon_0 s)^2+y^2+z^2\right]^{\frac{3}{2}}}ds\\
&= \frac{\omega\varepsilon\ell yz\epsilon_0}{2}\left\{\frac{3x}{|\mathbf{x}|^5}\frac{2}{3}\epsilon_0+\left(\frac{7x^3}{|\mathbf{x}|^9}-\frac{3x}{|\mathbf{x}|^7}\right)\epsilon_0^3+O(\epsilon_0^4)\right\},
\end{aligned}
$$

which is

$$
\begin{aligned}
u_1(\mathbf{x}) &= \omega R y + \frac{\omega\varepsilon\ell y\epsilon_0}{2}\left\{\left(\frac{3x^2}{|\mathbf{x}|^5}-\frac{1}{|\mathbf{x}|^3}\right)\frac{2}{3}\epsilon_0+\left(\frac{35x^4}{2|\mathbf{x}|^9}-\frac{15x^2}{|\mathbf{x}|^7}+\frac{3}{2|\mathbf{x}|^5}\right)\frac{2}{5}\epsilon_0^3+O(\epsilon_0^4)\right\},\\[4pt]
u_2(\mathbf{x}) &= -\omega R x + \frac{\omega\varepsilon\ell\epsilon_0}{2}\left\{\frac{x}{|\mathbf{x}|^3}\frac{2\epsilon_0}{3}+\left(\frac{5x^3}{|\mathbf{x}|^7}-\frac{3x}{|\mathbf{x}|^5}\right)\frac{1}{5}\epsilon_0^3+O(\epsilon_0^4)\right\}\\
&\quad+\frac{\omega\varepsilon\ell\epsilon_0 y^2}{2}\left\{\frac{3x}{|\mathbf{x}|^5}\frac{2}{3}\epsilon_0+\left(\frac{7x^3}{|\mathbf{x}|^9}-\frac{3x}{|\mathbf{x}|^7}\right)\epsilon_0^3+O(\epsilon_0^4)\right\},\\[4pt]
u_3(\mathbf{x}) &= \frac{\omega\varepsilon\ell yz\epsilon_0}{2}\left\{\frac{3x}{|\mathbf{x}|^5}\frac{2}{3}\epsilon_0+\left(\frac{7x^3}{|\mathbf{x}|^9}-\frac{3x}{|\mathbf{x}|^7}\right)\epsilon_0^3+O(\epsilon_0^4)\right\}.
\end{aligned}
$$

Appendix F

Matlab scripts

The matlab scripts for a straight rod sweeping out a tilted cone and a bent rod sweeping out an upright above a no-slip plane are included here. Various different versions have been written for static cones and dynamic cones. The following matlab scripts are for the basic static cone. The dynamics cone cases can be obtained by changing parameters accordingly.

F.1   Matlab script for the straight rod case

```
% ————————main.m————————————
% a straight rod sweeping out a tilted cone above a no-slip plane
% parameter() initializes the parameters
% the velocity field is constructed directly in the lab frame in fun_tilt()
% integrals involved in the velocity fields are computed in
% fun_int_stokes() and fun_int_image()
% fun_int_stokes(): for the stokeslet along the center-line
% fun_int_image(): for the image system
% Written by: Longhua Zhao

% initial environment
clear all; clc; %clf;% close all;
```

```
global ell eps omega kappa lambda

[T0,T1,x0]=parameter();

options = odeset('RelTol',1e-8,'AbsTol',1e-8);

tspan=[T0 T1];
[t1,x1]=ode45('fun_tilt',tspan,x0,options);

tT=t1;
xX=x1;
[m1,n1]=size(x1);

% the centerline of the body along the x-axis
cx=-0:0.2:ell;
mg=length(cx);
cy=zeros(1,mg);
cz=cy;

% body tilted by an angle kappa
cy0=cy;
for j=1:mg
    cx0(j)= cx(j)*sin(kappa)-cz(j)*cos(kappa);
    cz0(j)= cx(j)*cos(kappa)+cz(j)*sin(kappa);
end
```

```matlab
% body tilted sweeping a cone
tg=0:0.1:2*pi/omega;
czt=cz0;
for p=1:length(tg)
    for j=1:mg
        cxt(j,p)=cos(omega*tg(p))*cx0(j)-sin(omega*tg(p))*cy0(j);
        cyt(j,p)=sin(omega*tg(p))*cx0(j)+cos(omega*tg(p))*cy0(j);
    end
end


% save the data for trajectory
save('x.data','xX','-ASCII','-append')


% ―――――――――――――parameter function――――――――――――
function [t0,t1,x0]=parameter();
global ell eps omega kappa lambda


ell = 1.d0; % rod body length


%eps = 0.01d0;
delta = 0.01; %cross sectional radius
eps = 1.0/log(1.0/delta); %slenderness: e= 1/log(1/d)


omega = 2*pi; % angular velocity
kappa = pi/6; % cone angle
```

```matlab
lambda = 5*pi/20; % tilt angle


t0 = 0.d0; % starting time
t1 = 100.0; % end time: number of revolutions


x0=zeros(1,3);
x0=[-0.1 0 1]; % initial position


%————————— velocity function—————————————
function [dxdt]=fun_tilt(t,xlab)


global ell eps omega kappa lambda


dxdt=zeros(size(xlab));


x= xlab(1);
y= xlab(2);
z= xlab(3);


A = sin(kappa)*cos(lambda)*cos(omega*t)+cos(kappa)*sin(lambda);
B = sin(kappa)*sin(omega*t);
C = cos(kappa)*cos(lambda)-sin(kappa)*cos(omega*t)*sin(lambda);


[u21L,I1L,I2L,I3L]=fun_int_stokes(A,B,C,x,y,z,ell);
[u210,I10,I20,I30]=fun_int_stokes(A,B,C,x,y,z,0);
[u23L,I4L,I5L,I6L,I7L,I8L,I9L]=fun_int_image(A,B,C,x,y,z,ell);
```

[u230,I40,I50,I60,I70,I80,I90]=fun_int_image(A,B,C,x,y,z,0);

u21= u21L-u210;

u23= u23L-u230;

I1=I1L-I10;

I2=I2L-I20;

I3=I3L-I30;

I4=I4L-I40;

I5=I5L-I50;

I6=I6L-I60;

I7=I7L-I70;

I8=I8L-I80;

I9=I9L-I90;

u11= x*y*I1 - (B*x+A*y)*I2 + A*B*I3;

u12= x*y*I4 - (B*x+A*y)*I5 + A*B*I6;

u13= 6*A*B*C*z*I9 - 6*C*z*(B*x+A*y)*I8 + 6*C*x*y*z*I7;

u22= B*B*I3-2*B*y*I2 + y*y*I1;

u24= B*B*I6 - 2*B*y*I5 + y*y*I4;

u25= 2*C*z*I5;

u26= 6*B*B*C*z*I9 - 12*B*C*y*z*I8 + 6*C*y*y*z*I7;

u31= -B*C*I6 + (C*y-B*z)*I5 + y*z*I4;

u32= B*C*I3 -(C*y+B*z)*I2 +y*z*I1;

u33= -2*B*C*I6 + 2*C*y*I5;

u34= -6*B*C*C*z*I9 + 6*C*z*(C*y-B*z)*I8 + 6*C*y*z*z*I7;

Alpha1 = -cos(lambda)*sin(kappa)*sin(omega*t)*omega* eps /2;

Alpha2 = cos(omega*t)* sin(kappa)*omega* eps /2;

Alpha3 = sin(lambda)*sin(kappa)*sin(omega*t)*omega*eps/2;

%velocity field

u1a2 = Alpha2*(u11-u12+u13);

u2a2 = Alpha2*(u21+u22-u23-u24-u25+u26);

u3a2 = Alpha2*(-u31+u32+u33+u34);

u1a1= Alpha1*(u21 + A^2*I3 - 2*A*x*I2 + x^2*I1 - u23 - A^2*I6 ...

+ 2*(A*x-C*z)*I5 - x^2*I4 + 6*A^2*C*z*I9 - 12*A*C*x*z*I8 + 6*C*x^2*z*I7);

u2a1= Alpha1*(A*B*I3 - (B*x + A*y)*I2 + x*y*I1 - A*B*I6 + (B*x + A*y)*I5 ...

- x*y*I4 + 6*A*B*C*z*I9 - 6*C*z*(B*x + A*y)*I8 + 6*C*x*y*z*I7);

u3a1= Alpha1*(A*C*I3 - (C*x + A*z)*I2 + x*z*I1 - x*z*I4 + (C*x + A*z)*I5 ...

- A*C*I6 - 6*A*C^2*z*I9 + 6*C*z*(C*x - A*z)*I8 + 6*C*x*z^2*I7);

u1a3= Alpha3*(A*C*I3 - (C*x + A*z)*I2 + x*z*I1 - A*C*I6 + (C*x + A*z)*I5

...

- x*z*I4 + 6*A*C^2*z*I9 - 6*C*z*(C*x - A*z)*I8 - 6*C*x*z^2*I7);

```
u2a3= Alpha3*(B*C*I3 - (C*y + B*z)*I2 + y*z*I1 - B*C*I6 + (C*y + B*z)*I5 ...
   - y*z*I4 + 6*B*C^2*z*I9 - 6*C*z*(C*y - B*z)*I8 - 6*C*y*z^2*I7);
u3a3= Alpha3*(u21 + C^2*I3 - 2*C*z*I2 + z^2*I1 - u23 - C^2*I6 ...
   - z^2*I4 - 6*C^3*z*I9 - 12*C^2*z^2*I8 - 6*C*z^3*I7);


u1= u1a1 + u1a2 + u1a3;
u2= u2a1 + u2a2 + u2a3;
u3= u3a1 + u3a2 + u3a3;


dxdt(1)= u1;
dxdt(2)= u2;
dxdt(3)= u3;


%————————integral involved in the Stokeslet part of the velocity——


function [u21,I1,I2,I3]=fun_int_stokes(A,B,C,x,y,z,s)


x2= x*x; y2= y*y; z2= z*z;
A2= A*A; B2= B*B; C2= C*C;


r2= x2+y2+z2;
const= A2+B2+C2;


sqM = (x-A*s)*(x-A*s)+(y-B*s)*(y-B*s)+(z-C*s)*(z-C*s);
%sqP = (x-A*s)*(x-A*s)+(y-B*s)*(y-B*s)+(z+C*s)*(z+C*s);
```

```matlab
tmpP = A*x+B*y+C*z;

%tmpM = A*x+B*y-C*z;


tmp1 = A2*x2 -B2*y2 +C2*z2;


comsqS = (A*z-C*x)^2+(B*z-C*y)^2+(A*y-B*x)^2;
if s-tmpP+sqrt(sqM)==0
    warning('divide by zero')
end
logpart= log(2) + log( (const*s-tmpP)/sqrt(const) +sqrt(sqM));
%------------------
% integral u21
%------------------
u21= sqrt(sqM)/const+tmpP*logpart/sqrt(const^3);


%------------------
% integral I1
%------------------
num= -x*(x-A*s) - y*(y-B*s) - z*(z-C*s);
I1= num/sqrt(sqM)/comsqS;


%------------------
% integral I2
%------------------
num11= (A*x+B*y)^2- (A*x-C*z)^2 + (B*y+C*z)^2 - comsqS + tmp1;
```

den1= const*sqrt(sqM)*comsqS;

I2= (s*num11-tmpP*r2)/den1+logpart/sqrt(const^3);

p1num= (A*x+B*y)^2 - 2*comsqS + (A*x+C*z)^2 + (B*y+C*z)^2 - tmp1;

p2num= -5*comsqS +(A*x+C*z)^2 + (B*y+C*z)^2 + (A*x+B*y)^2 - tmp1;

den2= const*sqrt(sqM);
den1= const*den2*comsqS;

I3= -r2*p1num/den1 +s*tmpP*p2num/den1+s*s/den2+3*tmpP*logpart/sqrt(const^5);

%—————————integrals involved in the image system——————————

function [u23,I4,I5,I6,I7,I8,I9]=fun_int_image(A,B,C,x,y,z,s)

x2= x*x; y2= y*y; z2= z*z;
A2= A*A; B2= B*B; C2= C*C;

r2= x2+y2+z2;
const=A2+B2+C2;

```matlab
%sqM = (x-A*s)*(x-A*s)+(y-B*s)*(y-B*s)+(z-C*s)*(z-C*s);

sqP = (x-A*s)*(x-A*s)+(y-B*s)*(y-B*s)+(z+C*s)*(z+C*s);


%tmpP = A*x+B*y+C*z;

tmpM = A*x+B*y-C*z;


tmp2 = A2*x2 +B2*y2 +C2*z2;


comsq = (A*y-B*x)^2 +(A*z+C*x)^2 +(C*y+B*z)^2;


logpart= log(2) + log( (const*s-tmpM)/sqrt(const) +sqrt(sqP));
%---------------------
% integral u23
%---------------------
u23= sqrt(sqP)/const+tmpM*logpart/sqrt(const^3);


%---------------------
% integral I4
%---------------------
num= -x*(x-A*s) - y*(y-B*s) - z*(z+C*s);
I4= num/sqrt(sqP)/comsq;


%---------------------
% integral I5
%---------------------
num11= (A*x+B*y)^2 -(A*x+C*z)^2 +(B*y-C*z)^2 -comsq + A2*x2 -B2*y2 +C2*z2;
```

```matlab
den1= const*sqrt(sqP)*comsq;

I5= (s*num11-tmpM*r2)/den1+logpart/sqrt(const^3);


%————————-
% integral I6
%————————-
p1num= (A*x+B*y)^2 + (A*x-C*z)^2 + (B*y-C*z)^2 - 2*comsq - tmp2;


p2num= (A*x-C*z)^2 + (B*y-C*z)^2 + (A*x+B*y)^2 - 5*comsq - tmp2;


den2= const*sqrt(sqP);
den1= const*den2*comsq;


I6= -r2*p1num/den1 +s*tmpM*p2num/den1+s*s/den2
+3*tmpM*logpart/sqrt(const^5);


%————————-
% integral I7
%————————-
p1num= (A*x+B*y)^2 - 2*comsq + (A*x-C*z)^2 ...
+(B*y-C*z)^2 - tmp2;


p2num= -5*(A*z+C*x)^2 - 5*(B*z+C*y)^2 - 5*(A*y-B*x)^2 +(A*x-C*z)^2 ...
+ (B*y-C*z)^2 + (A*x+B*y)^2 - tmp2;
```

den= sqrt(sqP^3)*comsq^2;

part3= ((A*y+B*x)^2 +(A*z-C*x)^2 +(C*y-B*z)^2+2*tmp2) *(const*s-3*tmpM);

I7= (2*s*tmpM^2*r2 -2/3*tmpM*r2^2 +s*s/3*part3)/den;

% integral I8
%—————————-

I8= (s*tmpM -r2)/3/sqrt(sqP^3)/comsq^2* (2*r2^2-4*s*tmpM*r2+3*s*s*comsq ...
+2*s*s*((A*x-C*z)^2 + (B*y-C*z)^2 + (A*x+B*y)^2- tmp2)) ;

%—————————-
% integral I9
%—————————-

p0num= 5*comsq + 2*((A*x+B*y)^2 + (B*y-C*z)^2 + (A*x+C*z)^2) -2*tmp2;

p2num= 3*comsq + (A*x-C*z)^2 + (B*y-C*z)^2 + (A*x+B*y)^2 - tmp2;

p3num= 2*(-A*B*x*y-A*C*x*z+B*C*y*z)* ...
(A2*(x2-7*(y2+z2)) + B2*(y2-7*(x2+z2)) + C2*(z2-7*(x2+y2))) ...
+C2^2*(z2^2 - 2*(x2+y2)^2 + 3*(x2+y2)*z2) ...
+B2^2*(y2^2 - 2*(x2+z2)^2 + 3*(x2+z2)*y2) ...
+A2^2*(x2^2 - 2*(z2+y2)^2 + 3*(z2+y2)*x2) ...
+B2*C2*(3*(y2^2-6*y2*z2+z2^2)-(z2+y2)*x2 -4*x2^2) ...
+A2*B2*(3*(y2^2-6*y2*x2+x2^2)-(x2+y2)*z2 -4*z2^2) ...

289

+A2*C2*(3*(x2^2-6*x2*z2+z2^2)-(z2+x2)*y2 -4*y2^2) ...

+32*A*B*C*x*y*z*tmpM;

p1num= p3num+const^2*r2^2;

den= 3*const^2*sqrt(sqP^3)*comsq^2;

I9= (-tmpM*r2^2*p0num +3*s*r2*p1num -6*s^2*tmpM^3*p2num

+2*s^3*const*p3num)/den ...

+logpart/sqrt(const^5);

F.2 Matlab script for the bent rod case

This is the matlab script for a bent rod sweeping out an upright cone above a no-slip plane.

% —————————————main.m————————————————

% a bend rod sweeping out an upright cone above a no-slip plane

% multPparameter() initializes the parameters

% the velocity field is constructed directly in the lab frame in fun_tilt()

% integrals involved in the velocity fields are computed in

% fun_int_stokes() and fun_int_image()

% fun_int_stokes(): for the stokeslet along the center-line

% fun_int_image(): for the image system

% Written by: Longhua Zhao

% initial environment

```matlab
clear all; clc; clf; % close all;


global Ell Eps Omega Kappa lambda delta Beta K

[T0,T1]=multPparameter();

save('SimParameters.data',...

'Ell','delta','Kappa','Omega','K','Beta','T0','T1','-ASCII')


p0=[1 0 0.8];


Nx=1;

Nz=1;

gy=1;


for gz=1:Nz

    for gx=1:Nx

        clear xX tT


        % color of the plots

        R=0.2;%1-0.1*gz;

        G=0;

        B=0+0.1*gx;

        [T0,T1]=multPparameter();

        %x0=[gridx(gx) gridy(gy), gridz(gz)];

        x0=p0(gz,:);


        options = odeset('RelTol',1e-10,'AbsTol',1e-10);
```

```matlab
tspan=[T0 T1];
[tT,xX]=ode45('Fvelocity',tspan,x0,options);
[m1,n1]=size(xX);


% the centerline of the body along the x-axis
hs=0:0.2:Ell;
Lhs=length(hs); cy0=zeros(1,Lhs); cz0=cy0;


% the centre-line of bent rod tilted by an angel Kappa
cx0 = -2/K*cos(Beta)*cos(Kappa)*sin(0.5*(Ell-hs)*K).*sin(0.5*hs*K) ...
+2/K*cos(0.5*(Ell-hs)*K).*sin(0.5*hs*K)*sin(Kappa);
cy0 = -2/K*sin(0.5*(Ell-hs)*K).*sin(0.5*hs*K)*sin(Beta);
cz0 = 2/K*cos(0.5*(Ell-hs)*K).*cos(Kappa).*sin(0.5*hs*K) ...
+2/K*cos(Beta).*sin(0.5*(Ell-hs)*K).*sin(0.5*hs*K)*sin(Kappa);


% body tilted sweeping a cone
tend=min(2*pi/Omega,T1);
tg=0:0.125:tend;
czt=cz0;
for p=1:length(tg)
    for j=1:Lhs
        cxt(j,p)=cos(Omega*tg(p))*cx0(j)-sin(Omega*tg(p))*cy0(j);
        cyt(j,p)=sin(Omega*tg(p))*cx0(j)+cos(Omega*tg(p))*cy0(j);
    end
end
```

```matlab
        save(['SimP',num2str(Nx*(gz-1)+gx+1),'_x.data'],'xX','-ASCII')

        save(['SimP',num2str(Nx*(gz-1)+gx+1),'_t.data'],'tT','-ASCII')

        save(['SimP',num2str(Nx*(gz-1)+gx+1),'_x_Body.data'],'xbody','-ASCII')

    end

end


function [t0,t1]=parameter();

global Ell Eps Omega Kappa lambda delta K Beta

% Ell is the arclength of the body

% Eps is the small dimensionless parameter

% Omega is the angular velocity

% Kappa is the cone angle

% lambda is the tilted angle of the cone

% delta is the slenderness radius/Ell

% K is the constant curvature of the rod

% Beta is the scooping angle


Ell = 1.d0;

K = 0.395604;


%Eps = 0.01d0;

delta = 0.0367961*1; % straight rod radius


%Eps = 1.0/log(2.0/delta); %e= 1/log(2/d)

Eps = 1.0/log(1.0/delta); %e= 1/log(1/d)
```

Omega = 2*pi; % angular velocity

Kappa=23*pi/180;

Beta = pi-(60.0)*pi/180;

% Beta= 0 for belly in

% Beta= pi/2 for scooping

% Beta= -pi/2 for anti-scooping

% Beta= pi for belly out

lambda = 0.d0; % tilted angle

t0 = 0.71;

t1 = 20.d0;

%————————-velocity field————————————————

function [dxdt]=Fvelocity(t,xlab);

global Ell Omega x y z

dxdt=zeros(size(xlab));

% change the position from lab frame to body frame,

% then compute the velocity in body frame.

x= xlab(1)* cos(Omega*t) + xlab(2)* sin(Omega*t);

y= xlab(2)* cos(Omega*t) - xlab(1)* sin(Omega*t);

z= xlab(3);

% compute the integral numerically with function in body frame

```
%dxdt=quadv(@(s)Fintegrand(s,3),0,Ell);

dxdt=quadv(@(s)multPFintegrandSandIMG(s,3),0,Ell);

u=dxdt(1);

v=dxdt(2);

w=dxdt(3);


% the constant velocity in the z-axis direction

% due to the buoyancy of the particle

Q=0.0093;

%Q=0; % neutrally buoyant particles

% % change the velocity from body frame to lab frame.

dxdt(1)= cos(Omega*t)*u - sin(Omega*t)*v;

dxdt(2)= sin(Omega*t)*u + cos(Omega*t)*v;

dxdt(3)= w+Q;


%————————————————————————————

% This is the function or compute the velocity field at X0=[x,y,z]

% The arclength of the bent rod is L, the rod has constant curvature K, and

% the rod sweeping an upright cone counter-clockwise with constant angular velocity

Omega.

% The scooping angle of the bent rod is Beta.

% The scooping angle is defined as:

% For belly-in, Beta=0, For Belly-out, Beta=Pi. The angle is defined

% counter-clockwise.

% The cone angle is Kappa.

%————————————————————————————
```

```matlab
function vel = multPFintegrandSandIMG(s,n)
vel = zeros(3,1);

global Ell Eps Omega Kappa K x y z Beta
multPparameter();
L = Ell;

a=1/K; % K is the constant curvature of the bent rod

xb = - 2*a*cos(Beta)*cos(Kappa)*sin(0.5*(L-s)/a)*sin(0.5*s/a) ...
+ 2*a*cos(0.5*(L-s)/a)*sin(0.5*s/a)*sin(Kappa);
yb = - 2*a*sin(0.5*(L-s)/a)*sin(0.5*s/a)*sin(Beta);
zb = 2*a*cos(0.5*(L-s)/a)*cos(Kappa)*sin(0.5*s/a) ...
+ 2*a*cos(Beta)*sin(0.5*(L-s)/a)*sin(0.5*s/a)*sin(Kappa);

% strength in body frame
%R^T *Epsilong*R*V_b
Alpha1=-(1/4)*a *Eps* Omega* sin(s/(2*a))*sin(Beta)*( ...
4*cos(Kappa)^2*sin((L-s)/(2*a))...
+2*cos(Beta)*cos(Kappa)*sin((L-2*s)/(2*a))*sin(s/(2*a))*sin(Kappa)...
+( sin((L-3*s)/(2*a))+3*sin((L-s)/(2*a)) )*sin(Kappa)^2 ...
);
Alpha2=-(1/4)*a *Eps* Omega* sin(s/(2*a))*( ...
-4*cos(Beta)*cos(Kappa)*sin((L-s)/(2*a)) ...
+4*cos((L-s)/(2*a))*cos(Beta)^2*sin(Kappa) ...
+( cos((L-3*s)/(2*a))+3*cos((L-s)/(2*a)) )*sin(Beta)^2*sin(Kappa)...
```

```
);
Alpha3=1/2*a *Eps* Omega* sin(s/(2*a))^2*sin(Beta)*sin(Kappa)*(...
cos((L-2*s)/(2*a))*cos(Kappa)+cos(Beta)*sin((L-2*s)/(2*a))*sin(Kappa));
Alpha1=-Alpha1;
Alpha2=-Alpha2;
Alpha3=-Alpha3;


Rx = x-xb;
Ry = y-yb;
Rz = z-zb;


% module of the (x-xb)
RM = sqrt(Rx^2+Ry^2+Rz^2);
imgRM = sqrt(Rx^2+Ry^2+(z+zb)^2);


imgax=Alpha1*Rx+Alpha2 *Ry-Alpha3*(z+zb);


F1=(Alpha1*Rx+Alpha2 *Ry+Alpha3*Rz)*Rx;
F2=(Alpha1*Rx+Alpha2 *Ry+Alpha3*Rz)*Ry;
F3=(Alpha1*Rx+Alpha2 *Ry+Alpha3*Rz)*Rz;


stokesu=Alpha1/RM+F1/(RM^3);
stokesv=Alpha2/RM+F2/(RM^3);
stokesw=Alpha3/RM+F3/(RM^3);


imageu= -Alpha1/imgRM- Rx*(Alpha1*Rx+Alpha2 *Ry+Alpha3*(z+zb))/(imgRM^3)
```

+...

2*zb*(-z*Alpha1/imgRM^3 + Rx*Alpha3/imgRM^3+3*z*Rx*imgax/imgRM^5);

imagev= -Alpha2/imgRM- Ry*(Alpha1*Rx+Alpha2 *Ry+Alpha3*(z+zb))/(imgRM^3)

+...

2*zb*(-z*Alpha2/imgRM^3 + Ry*Alpha3/imgRM^3+3*z*Ry*imgax/imgRM^5);

imagew= -Alpha3/imgRM- (z+zb)*(Alpha1*Rx+Alpha2 *Ry

+Alpha3*(z+zb))/(imgRM^3)+ ...

2*zb*(z*Alpha3/imgRM^3 +(Ry*Alpha2+Rx*Alpha1)/imgRM^3

+3*z*(z+zb)*imgax/imgRM^5);

vel(1)=stokesu+imageu;

vel(2)=stokesv+imagev;

vel(3)=stokesw+imagew;

Appendix G

Terminal velocity of falling spheres, spheroids or slender bodies

In this appendix, we summarize the terminal velocity of one body falling in the Stokes flow and compare the terminal velocity for different bodies and the results about the terminal velocity of two spheres falling in a fluid in Stokes regime. The density of the body ρ_m, the fluid density ρ_{fluid}, and the fluid viscosity μ are always the same to simplify the comparison. The types of bodies consider here are sphere, prolate or oblate spheroid, and cylindrical slender body.

G.1   Terminal velocity of a sphere in Stokes flow

By Stokes law, the hydrodynamics force on a rigid sphere with radius R falling in a highly viscous fluid in free space is

$$F = 6\pi\mu R u_\infty,$$

where u_∞ is the terminal velocity of the sphere and μ is the dynamic viscosity of the fluid. By Newton's law, when the sphere reaches its terminal velocity u_∞, the forces acting on the sphere are balanced, i.e.

$$6\pi\mu R u_\infty = \frac{4}{3}\pi R^3 \rho_{\text{fluid}} g - \frac{4}{3}\pi R^3 \rho_s g.$$

where g is the acceleration due to gravity, ρ_s is the density of the sphere, and ρ_{fluid} is the density of the fluid. So,

$$u_\infty = \frac{4}{3} \frac{\pi R^3 \left(\rho_{\text{fluid}} - \rho_s\right) g}{6\pi R\mu} = \frac{2}{9} \frac{R^2 \left(\rho_{\text{fluid}} - \rho_s\right) g}{\mu}. \tag{G.1}$$

Consider the Faxen correction, the drag on a stationary rigid sphere in the Stokes flow is

$$F = 6\pi\mu R(u + \frac{1}{6}R^2\nabla^2 u),$$

where R is radius of the sphere and μ is the viscosity of the fluid. The second term comes from Faxen correction. If the sphere reaches its terminal velocity, $\nabla^2 u_\infty = 0$, in this case, the terminal velocity should be the same as (G.1).

G.2   Terminal velocity of a spheroid

To break the symmetry of the sphere, the simplest deformation is a spheroid. The equation of a spheroid is

$$\frac{x^2}{a^2} + \frac{y^2 + z^2}{b^2} = 1.$$

If $a > b$, it is a prolate spheroid with the eccentricity $e = \sqrt{1 - \frac{b^2}{a^2}}$. Otherwise, it is an oblate spheroid and its eccentricity is $e = \sqrt{1 - \frac{a^2}{b^2}}$

The terminal velocities of both a prolate spheroid and an oblate spheroid are considered. Some results summarized here available in [19], [31], and [67].

G.2.1   Terminal velocity of a prolate spheroid

The terminal velocity of a prolate spheroid is derived from Chwang and Wu' s paper [19], where they give the exact velocity field and the force acting on the spheroid in a

uniform flow or linear shear flow.

If the spheroid is embedded in a uniform flow $u = U_1\mathbf{e}_x + U_2\mathbf{e}_y$, the force experienced by the spheroid is

$$F = 6\pi\mu a \left(D_1\mathbf{e}_x + D_2\mathbf{e}_y \right),$$

where $D_1 = \frac{8}{3}U_1 e^3 \left[-2e + (e^2 + 1) \ln \left(\frac{1+e}{1-e} \right) \right]^{-1}$, $D_2 = \frac{16}{3}U_2 e^3 \left[2e + (3e^2 - 1) \ln \left(\frac{1+e}{1-e} \right) \right]^{-1}$. The major axis of the spheroid is along the base vector $\mathbf{e}_x$. Regardless the stability, the spheroid can falling along its major axis (falling vertically) or perpendicular to its major axis (falling horizontally).

- When the prolate spheroid is falling vertically in the fluid with a terminal velocity U_1, the hydrodynamic force on the spheroid is

$$F = 6\pi\mu a D_1 \mathbf{e}_x = \frac{16\pi\mu a e^3 U_1}{-2e + (e^2 + 1) \ln \left(\frac{1+e}{1-e} \right)}.$$

  This formula can also be derived from Happel and Brenner [31], in which the hydrodynamic force on the prolate spheroid is originally

$$F_{\text{spheroid}} = 8\pi\mu c \frac{U}{(\tau_0^2 + 1) \coth^{-1} (\tau_0) - \tau_0},$$

  where we have utilized the following relation in the book, $\coth^{-1}(i\tau) = -i \coth^{-1}(\tau)$ and $\coth^{-1}(\tau) = \frac{1}{2} \ln \left(\frac{\tau+1}{\tau-1} \right)$, and $c = \sqrt{a^2 - b^2}$ is the usual half focal length. Since $\tau_0 = \frac{a}{c} = \left(1 - \frac{b^2}{a^2} \right)^{-1/2} = \frac{1}{e}$, in terms of the eccentricity of the spheroid e, $\coth^{-1}(\tau_0) = \frac{1}{2} \ln \left(\frac{1+e}{1-e} \right)$, $\tau_0 = \frac{1}{e}$, and $F_{\text{spheroid}} = 8\pi\mu a e \frac{U}{\left(\frac{1}{e^2} + 1 \right) \frac{1}{2} \ln \left(\frac{1+e}{1-e} \right) - \frac{1}{e}}$.

- When the prolate spheroid is falling horizontally (perpendicular to its major axis) in the fluid with a terminal velocity U_2, the hydrodynamic force acting on the spheroid is

$$F = 6\pi\mu a D_2 \mathbf{e}_y = \frac{32\pi\mu a e^3 U_2}{2e + (3e^2 - 1) \ln \left(\frac{1+e}{1-e} \right)}.$$

With U is the terminal velocity,

$$F_{\text{spheroid}} = F_{buoyancy} - F_{\text{gravity}} \tag{G.2}$$

by Newton's law. Since the volume of the prolate spheroid is $\frac{4}{3}\pi ab^2$ and the gravity of the spheroid is

$$F = mg = \rho_m V g = \frac{4}{3}\pi ab^2 \rho_m g,$$

the buoyant force is $F = \rho_{\text{fluid}} V g = \frac{4}{3}\pi ab^2 \rho_{\text{fluid}} g$, where ρ_m is the density of the spheroid.

Substitute the hydrodynamics force into the equation (G.2),

$$\frac{32\pi\mu ae^3 U}{2e + (3e^2 - 1)\ln\left(\frac{1+e}{1-e}\right)} = \frac{4}{3}\pi ab^2 \rho_{\text{fluid}} g - \frac{4}{3}\pi ab^2 \rho_m g.$$

The terminal velocity of the prolate spheroid falling horizontally in the fluid is

$$U = \frac{1}{24}\frac{b^2\left(\rho_{\text{fluid}} - \rho_m\right)g}{\mu e^3}\left[2e + \left(3e^2 - 1\right)\ln\left(\frac{1+e}{1-e}\right)\right]. \tag{G.3}$$

When the spheroid falls along its major axis (falling vertically),

$$\frac{16\pi\mu aU_1 e^3}{-2e + (e^2 + 1)\ln\left(\frac{1+e}{1-e}\right)} = \frac{4}{3}\pi ab^2 \rho_{\text{fluid}} g - \frac{4}{3}\pi ab^2 \rho_m g,$$

the terminal velocity of the prolate spheroid is

$$U = \frac{1}{12}\frac{b^2\left(\rho_{\text{fluid}} - \rho_m\right)g}{\mu e^3}\left[-2e + \left(e^2 + 1\right)\ln\left(\frac{1+e}{1-e}\right)\right]. \tag{G.4}$$

G.2.2   Terminal velocity of an oblate spheroid

A horizontal oblate spheroid with equatorial radius a is defined as $\frac{x^2+y^2}{a^2} + \frac{z^2}{b^2} = \frac{x^2+y^2}{a^2} + \frac{z^2}{a^2(1-\epsilon)^2} = 1$, in which b is the polar radius and $\epsilon = 1 - \frac{b}{a}$. From [31], the

hydrodynamic force exerted by the fluid on an oblate spheroid falling along its minor axis (horizontal oblate spheroid) is

$$F_z = -\frac{6\pi\mu a U}{\frac{3}{4}\sqrt{\lambda^2 + 1}\left[\lambda - (\lambda^2 - 1)\cot^{-1}(\lambda)\right]} = -6\pi\mu a U K,$$

where

$$K = \frac{1}{\frac{3}{4}\sqrt{\lambda^2 + 1}\left[\lambda - (\lambda^2 - 1)\cot^{-1}(\lambda)\right]} \text{ and } \lambda = \frac{b}{\sqrt{a^2 - b^2}}.$$

Using Newton's law

$$6\pi\mu a U K = \frac{4}{3}\pi a^2 b \rho_{\text{fluid}} g - \frac{4}{3}\pi a^2 b \rho_m g,$$

the terminal velocity U is

$$U = \frac{\frac{4}{3}\pi a^2 b \rho_{\text{fluid}} g - \frac{4}{3}\pi a^2 b \rho_m g}{6\pi\mu a K} = \frac{2}{9}\frac{ab\left(\rho_{\text{fluid}} - \rho_m\right)g}{\mu K} = \frac{2}{9}\frac{\left(\rho_{\text{fluid}} - \rho_m\right)g}{\mu}f_0(a,b), \quad \text{(G.5)}$$

and $f_0(a,b) = \frac{3}{4}\frac{a^2 b}{\sqrt{a^2 - b^2}}\left(\frac{b}{\sqrt{a^2 - b^2}} - \left(\frac{b^2}{a^2 - b^2} - 1\right)\operatorname{arccot}\left(\frac{b}{\sqrt{a^2 - b^2}}\right)\right)$

The terminal velocity for a prolate and oblate spheroid falling in a fluid can also be derived from the exact velocity field and the force on the object in [67].

G.3   Terminal velocity of a slender body

When a cylindrical slender rod with radius r and length 2ℓ falls in a viscous flow, the hydrodynamics force acting on the body is computed based on the slender body theory. By the slender body theory, Stokeslets are uniformly distributed on the centerline, and the strength is determined by the no-slip boundary condition to construct the velocity. Once the strength is known, the hydrodynamic force can be computed based on the strength. When the slender rod reaches its terminal velocity U, the body can fall horizontally (perpendicular to its axis) or fall vertically (along it axis), which is an

unstable case.

If the density of rod is ρ_m, the volume of the cylindrical slender rod is $\text{Vol}_{\text{rod}} = 2\pi r^2 \ell$. The weight of the body is

$$F_g = mg = \rho_m V g = 2\rho_m \pi r^2 \ell g,$$

and the buoyant force is

$$F_b = \rho_{\text{fluid}} V g = 2\pi r^2 L \rho_{\text{fluid}} g.$$

Falling horizontally   If the slender rod is falling horizontally with the terminal velocity U, then the strength of the Stokeslets along its centerline is $\boldsymbol{\alpha} = (0, 0, \alpha_3)$ and

$$\alpha_3 = \frac{\epsilon U}{2}, \quad \text{where } \epsilon = \frac{1}{\log\left(\frac{2}{\delta}\right)} = \frac{1}{\log\left(\frac{2\ell}{r}\right)}.$$

The hydrodynamics force at each point of the centerline of rod is

$$f = 8\pi\mu\alpha_3\delta(x) = 4\pi\mu\epsilon U\delta(x).$$

Since the Stokeslet is uniformly distributed on the rod, the total hydrodynamic force on the rod is

$$F_h = \int_{-\ell}^{\ell} 4\pi\mu\epsilon W \, ds = 8\pi\mu\epsilon\ell U.$$

By Newton's' law, the buoyant force acting on the body and the force due to gravity are balanced with the hydrodynamic force $F_b - F_g = F_h$, i.e.,

$$2\pi r^2 \ell \rho_{\text{fluid}} g - 2\rho_m \pi r^2 \ell g = 8\pi\mu\epsilon\ell W.$$

The terminal velocity of a slender body falling horizontally is

$$W = \frac{(\rho_{\text{fluid}} - \rho_m)\, r^2 g}{4\mu\epsilon} = \frac{(\rho_{\text{fluid}} - \rho_m)\, r^2 g}{4} \log\left(\frac{2\ell}{r}\right).$$

Falling vertically   If the slender rod is falling vertically with the terminal velocity W, then the strength of the Stokeslet along its centerline is

$$\boldsymbol{\alpha} = (0, 0, \alpha_3) \quad \text{and } \alpha_3 = \frac{\epsilon W}{4}, \text{ where } \epsilon = \frac{1}{\log\left(\frac{2}{\delta}\right)} = \frac{1}{\log\left(\frac{2\ell}{r}\right)}.$$

The hydrodynamics force at each point of the centerline of rod is $f = 8\pi\mu\alpha_3\delta(x) = 2\pi\mu\epsilon W\delta(x)$. Since the Stokeslet is uniformly distributed on the rod, the total hydrodynamic force on the rod is

$$F_h = \int_{-\ell}^{\ell} 2\pi\mu\epsilon W\, ds = 4\pi\mu\epsilon\ell W.$$

By Newton's' law, the forces exerted on the body are balanced

$$2\pi\text{r}^2\ell\rho_{\text{fluid}} g - 2\rho_m\pi r^2 \ell g = 4\pi\mu\epsilon W.$$

So,
$$W = \frac{(\rho_{\text{fluid}} - \rho_m)\, r^2 g}{2\mu\epsilon} = \frac{(\rho_{\text{fluid}} - \rho_m)\, r^2 g}{2} \log\left(\frac{2\ell}{r}\right).$$

In summary,

- If the slender rod is falling horizontally, the terminal velocity is

$$U = \frac{(\rho_{\text{fluid}} - \rho_m)\, r^2 g}{4\mu} \log\left(\frac{2\ell}{r}\right). \tag{G.6}$$

305

- If the slender rod is falling vertically, the terminal velocity is

$$U = \frac{(\rho_{\text{fluid}} - \rho_m)\, r^2 g}{2\mu} \log\left(\frac{2\ell}{r}\right). \tag{G.7}$$

Notice the ratio 2 for the different orientations.

G.4 A sphere vs a spheroid

G.4.1 A sphere with half mass vs a spheroid

To compare the terminal velocity of the a sphere with a spheroid, we first check the terminal velocity of a sphere with half the mass of a spheroid. Then, the relation of the body volumes is $\frac{4}{3}\pi a^2 b = 2\frac{4}{3}\pi R^3$, or $R = \sqrt[3]{\frac{a^2 b}{2}}$. From (G.1), the terminal velocity of the sphere with radius $R = \sqrt[3]{\frac{a^2 b}{2}}$ is

$$U_\infty = \frac{2}{9} \frac{R^2 \left(\rho_{\text{fluid}} - \rho_m\right) g}{\mu} = \frac{2}{9} \frac{\left(\rho_{\text{fluid}} - \rho_m\right) g}{\mu} \left(\sqrt[3]{\frac{a^2 b}{2}}\right)^2. \tag{G.8}$$

The terminal velocity for a prolate spheroid is (G.3)-(G.4), and (G.5) for an oblate spheroid.

Figure G.1 shows the terminal velocity of horizontal oblate spheroid and half mass sphere R in terms of a and b, when $a = 1$ is fixed.

G.4.2 A sphere vs an oblate spheroid

Comparison of a sphere with a horizontal oblate spheroid

If the sphere has half mass of the horizontal oblate spheroid, then $\frac{4}{3}\pi a^2 b = 2\frac{4}{3}\pi R^3$. $R = \sqrt[3]{\frac{a^2 b}{2}}$, $b = \frac{2R^3}{a^2}$, or $a = \sqrt{\frac{2R^3}{b}}$. Under this condition, the terminal velocity of sphere
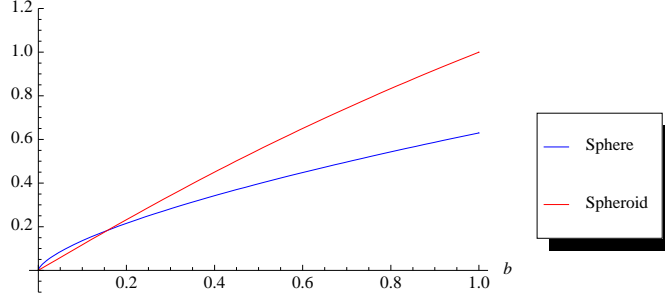
Figure G.1: Comparison of terminal velocity of a sphere in (G.8) with the terminal velocity of a horizontal oblate spheroid (G.5) when the radius of the sphere $R = \left(\sqrt[3]{\frac{a^2 b}{2}} \right)^2$ and the semimajor axis of the spheroid $a = 1$.

is

$$U_\infty = \frac{2}{9} \frac{\left(\rho_{\text{fluid}} - \rho_m \right) g}{\mu} R^2,$$

and the terminal velocity of spheroid is

$$U = \frac{2}{9} \frac{ab \left(\rho_{\text{fluid}} - \rho_m \right) g}{\mu K} = \frac{2}{9} \frac{\left(\rho_{\text{fluid}} - \rho_m \right) g}{\mu} \frac{\sqrt{2R^3 b}}{K},$$

where $K = \frac{1}{\frac{3}{4}\sqrt{\lambda^2+1}[\lambda-(\lambda^2-1)\cot^{-1}(\lambda)]}$ and $\lambda = \frac{b}{\sqrt{a^2-b^2}}$. The ratio the terminal velocity of

$$\frac{\text{the terminal velocity of the spheroid}}{\text{the terminal velocity of a sphere}} = \frac{2R}{aK} = \frac{\sqrt{2Rb}}{KR}.$$

Ratio in terms of R and b Substitute $a = \sqrt{\frac{2R^3}{b}} > b$ ($b < \sqrt[3]{2}$) into the terminal velocity and define the ratio as a function $f_b(R, b)$,

$$f_b(R, b) \equiv \frac{\sqrt{2Rb}}{RK} \tag{G.9}$$

$$= \frac{3}{4} \sqrt{\frac{2b}{R}} \sqrt{\frac{b^2}{\frac{2R^3}{b} - b^2} + 1} \left(\frac{b}{\sqrt{\frac{2R^3}{b} - b^2}} - \left(\frac{b^2}{\frac{2R^3}{b} - b^2} - 1 \right) \operatorname{arccot} \left(\frac{b}{\sqrt{\frac{2R^3}{b} - b^2}} \right) \right),$$

307
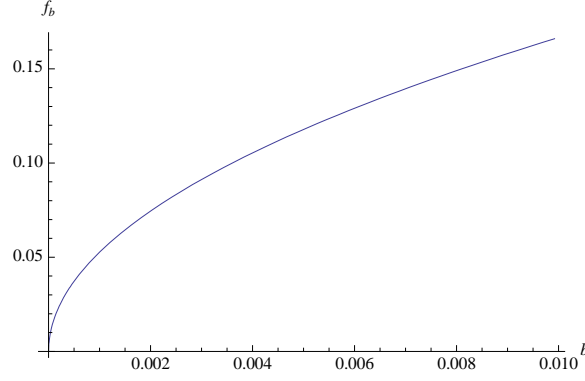
Figure G.2: The ratio of terminal velocities $f_b(1, b)$ in (G.9) with $a = \sqrt{\frac{2R^3}{b}}$ and $R = 1$.

where

$$K = \cfrac{1}{\left(\frac{3}{4} \sqrt{\frac{b^2}{\frac{2R^3}{b} - b^2} + 1} \left(\frac{b}{\sqrt{\frac{2R^3}{b} - b^2}} - \left(\frac{b^2}{\frac{2R^3}{b} - b^2} - 1 \right) \operatorname{arccot} \left(\frac{b}{\sqrt{\frac{2R^3}{b} - b^2}} \right) \right) \right)}.$$

Figure G.2 shows the coefficient $f_b(R, b)$ where $R = 1$ $(0 < b < \sqrt[3]{2})$. When $f_b(R, b) = 1$, the sphere and the horizontal oblate spheroid fall with the same terminal velocities.

Ratio in terms of R and a   Define the ratio of the terminal velocities as $f_a(R, a)$, a function of R and a. Since $b = \frac{2R^3}{a^2} < a$, the range of a is $a > \sqrt[3]{2}$,

$$
\begin{aligned}
K &= \frac{1}{\frac{3}{4}\sqrt{\lambda^2 + 1}\left[\lambda - (\lambda^2 - 1)\cot^{-1}(\lambda)\right]}, \quad \text{and } \lambda = \frac{2R^3}{\sqrt{a^6 - 4R^6}}, \\
f_a(R, a) &= \frac{2R}{aK} \\
&= \frac{3R^3}{2a}\sqrt{\frac{a^6}{a^6 - 4R^6}}\left(\frac{2R^3}{\sqrt{a^6 - 4R^6}} - \left(\frac{4R^6}{a^6 - 4R^6} - 1\right)\operatorname{arccot}\left(\frac{2R^3}{\sqrt{a^6 - 4R^6}}\right)\right)
\end{aligned}
\tag{G.10}
$$

Figure G.3 shows the ratio $f_a(R, a)$ with $R = 1$ as $a > \sqrt[3]{2}$.

308
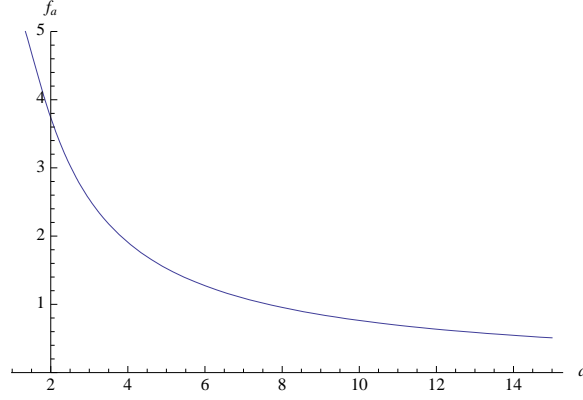
Figure G.3: Ratio $f_a(1, a)$ in (G.10) with $b = \frac{2R^3}{a^2}$ and $R = 1$.

Horizontal n-body oblate spheroid vs a sphere

If the polar radius of the oblate spheroid b ($b < a$) is fixed as the radius of the sphere R, and the mass of the spheroid is n times the mass of the sphere, then $\frac{4}{3}\pi a^2 b = \frac{4}{3}\pi a^2 R = n\frac{4}{3}\pi R^3$. So,

$$a^2 = nR^2, R = \frac{a}{\sqrt{n}} \text{ and } a = \sqrt{n}R.$$

Substitute $b = R$ and $a = \sqrt{n}R$ into the terminal velocity formula. Since $K = \frac{1}{\frac{3}{4}\sqrt{\lambda^2+1}[\lambda-(\lambda^2-1)\cot^{-1}(\lambda)]}$ and $\lambda = \frac{b}{\sqrt{a^2-b^2}}$,

$$K = \frac{4}{3\sqrt{\frac{n}{n-1}}\left(\frac{1}{\sqrt{n-1}} + \frac{(n-2)\text{arccot}\left(\frac{1}{\sqrt{n-1}}\right)}{n-1}\right)} \text{ and } \lambda = \frac{1}{\sqrt{n-1}}.$$

Thus,

$$\begin{aligned}
U &= \frac{2}{9}\frac{ab(\rho_{\text{fluid}} - \rho_m)g}{\mu K} & \text{(G.11)} \\
&= \frac{2}{9}\frac{\sqrt{n}R^2(\rho_{\text{fluid}} - \rho_m)g}{\mu}\frac{3}{4}\sqrt{\frac{n}{n-1}}\left(\frac{1}{\sqrt{n-1}} + \frac{(n-2)\text{arccot}\left(\frac{1}{\sqrt{n-1}}\right)}{n-1}\right)
\end{aligned}$$

The terminal velocity of the sphere is $U_\infty = \frac{2}{9}\frac{(\rho_{\text{fluid}} - \rho_m)g}{\mu}R^2$.

309

To compare the terminal velocities, we check the ratio of U_∞ of the sphere over the terminal velocity in (G.11).

$$f_{\rm ns}(n) = \frac{\frac{2}{9}\frac{\sqrt{n}R^2(\rho_{\rm fluid}-\rho_m)g}{\mu}\frac{3}{4}\sqrt{\frac{n}{n-1}}\left(\frac{1}{\sqrt{n-1}}+\frac{n-2}{n-1}\operatorname{arccot}\left(\frac{1}{\sqrt{n-1}}\right)\right)}{\frac{2}{9}\frac{(\rho_{\rm fluid}-\rho_m)g}{\mu}R^2}$$

$$= \frac{3\sqrt{n}}{4}\sqrt{\frac{n}{n-1}}\left(\frac{1}{\sqrt{n-1}}+\frac{n-2}{n-1}\operatorname{arccot}\left(\frac{1}{\sqrt{n-1}}\right)\right).$$

As $n \to \infty$,

$$f_{\rm ns}(n) \sim \frac{3\pi}{8}\sqrt{n} - \frac{3}{16}\pi\frac{1}{\sqrt{n}} + \frac{1}{n} - \frac{27}{64}\pi\left(\frac{1}{n}\right)^{3/2} + \frac{8}{5}\left(\frac{1}{n}\right)^2 + O\left(\left(\frac{1}{n}\right)^{5/2}\right).$$

G.4.3   A sphere vs a prolate spheroid

If the sphere has the same equatorial radius b of a prolate spheroid, the terminal velocity of sphere is

$$U_\infty = \frac{2}{9}\frac{b^2\left(\rho_{\rm fluid}-\rho_m\right)g}{\mu}.$$

The terminal velocity for a horizontally falling prolate spheroid is

$$U_h = \frac{1}{24}\frac{b^2\left(\rho_{\rm fluid}-\rho_m\right)g}{\mu}\frac{\left[2e+(3e^2-1)\ln\left(\frac{1+e}{1-e}\right)\right]}{e^3}. \tag{G.12}$$

The terminal velocity for a vertically falling prolate spheroid is

$$U_v = \frac{1}{12}\frac{b^2\left(\rho_{\rm fluid}-\rho_m\right)g}{\mu}\frac{\left[-2e+(e^2+1)\ln\left(\frac{1+e}{1-e}\right)\right]}{e^3}. \tag{G.13}$$

N-body   If the prolate spheroid $\frac{x^2}{a^2} + \frac{y^2+z^2}{b^2} = 1$ weights n times of the sphere and $b = R$ is the radius of the sphere,

$$\frac{4}{3}\pi ab^2 = \frac{4}{3}\pi aR^2 = n\frac{4}{3}\pi R^3, a = nR.$$

The eccentricity of the spheroid is

$$e = \frac{c}{a} = \frac{\sqrt{a^2 - b^2}}{a} = \frac{\sqrt{a^2 - R^2}}{a} = \sqrt{1 - \frac{1}{n^2}}.$$

We call such a spheroid a n-body spheroid.

For a horizontally falling n-body spheroid, the terminal velocity is

$$U_h = \frac{2}{9} \frac{R^2 \left(\rho_{\text{fluid}} - \rho_m\right) g}{\mu} \frac{3}{8} \frac{\sqrt{1 - \frac{1}{n^2}} + \left(2 - \frac{3}{n^2}\right) \log\left(n + \sqrt{-1 + n^2}\right)}{\left(1 - \frac{1}{n^2}\right)^{3/2}}.$$

For a vertically falling n-body spheroid, the terminal velocity is

$$U_v = \frac{2}{9} \frac{R^2 \left(\rho_{\text{fluid}} - \rho_m\right) g}{\mu} \frac{3}{4} \frac{-\sqrt{1 - \frac{1}{n^2}} + \left(2 - \frac{1}{n^2}\right) \log\left(n + \sqrt{n^2 - 1}\right)}{\left(1 - \frac{1}{n^2}\right)^{3/2}}.$$

The ratio of terminal velocity of the n-body spheroid over the terminal velocity of the sphere are

$$\frac{U_h}{U_s} = \frac{3}{8} \frac{\sqrt{1 - \frac{1}{n^2}} + \left(2 - \frac{3}{n^2}\right) \log\left(n + \sqrt{-1 + n^2}\right)}{\left(1 - \frac{1}{n^2}\right)^{3/2}}, \tag{G.14}$$

$$\frac{U_v}{U_s} = \frac{3}{4} \frac{-\sqrt{1 - \frac{1}{n^2}} + \left(2 - \frac{1}{n^2}\right) \log\left(n + \sqrt{n^2 - 1}\right)}{\left(1 - \frac{1}{n^2}\right)^{3/2}}. \tag{G.15}$$

As $n \to \infty$,

$$\frac{U_h}{U_s} \sim \frac{3}{8} (2\log(n) + 1 + 2\log(2)) + \frac{3}{16} \left(\frac{1}{n}\right)^2 + O\left(\left(\frac{1}{n}\right)^{1/3}\right),$$

$$\frac{U_v}{U_s} \sim \frac{3}{4} (2\log(n) - 1 + 2\log(2)) + \frac{3}{8} (-3 + 4\log(2) + 4\log(n)) \left(\frac{1}{n}\right)^2 + O\left(\left(\frac{1}{n}\right)^{1/3}\right).$$
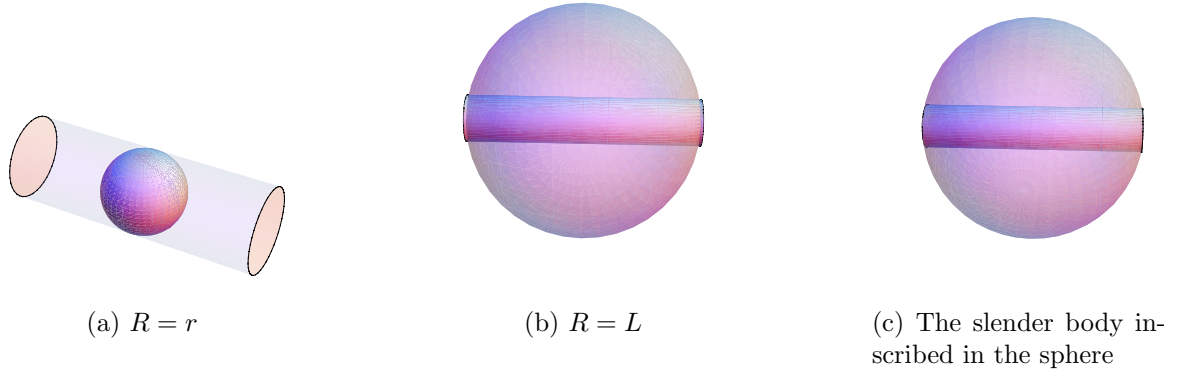
(a) $R = r$ (b) $R = L$ (c) The slender body inscribed in the sphere

Figure G.4: A sphere vs a slender body.

G.5   A sphere vs a cylindrical slender rod

The terminal velocity for a sphere with radius R is (G.1), and the terminal velocity of a slender body with length 2ℓ and radius r is (G.6) or (G.7). If the slender body is falling horizontally, the terminal velocity is $W = \frac{(\rho_{\text{fluid}} - \rho_m) r^2 g}{4\mu} \log\left(\frac{2\ell}{r}\right)$. If the slender rod is falling vertically, the terminal velocity is $W = \frac{(\rho_{\text{fluid}} - \rho_m) r^2 g}{2\mu} \log\left(\frac{2\ell}{r}\right)$.

If the density of the body keeps the same value ρ_m and the fluid is the same, then

$$\frac{\text{terminal velocity of a sphere}}{\text{terminal velocity of a horizontal slender body}} = \frac{\frac{2}{9} \frac{R^2 (\rho_{\text{fluid}} - \rho_m) g}{\mu}}{\frac{(\rho_{\text{fluid}} - \rho_m) r^2 g}{4\mu} \log\left(\frac{2\ell}{r}\right)} = \frac{8R^2}{9 r^2 \log\left(\frac{2\ell}{r}\right)},$$

$$\frac{\text{terminal velocity of a sphere}}{\text{terminal velocity of a vertical slender body}} = \frac{\frac{2}{9} \frac{R^2 (\rho_{\text{fluid}} - \rho_m) g}{\mu}}{\frac{(\rho_{\text{fluid}} - \rho_m) r^2 g}{42\mu} \log\left(\frac{2\ell}{r}\right)} = \frac{4R^2}{9 r^2 \log\left(\frac{2\ell}{r}\right)}.$$

When the terminal velocities are comparable, $R^2 \sim r^2 \log\left(\frac{2\ell}{r}\right)$.

Figure G.4 shows different case of the sphere compare to the slender body. If the sphere and the slender rod have the same radius $R = r$ shown in Figure G.4a. For a sphere with radius r, the terminal velocity is

$$U_\infty = \frac{2}{9} \frac{r^2 \left(\rho_{\text{fluid}} - \rho_m\right) g}{\mu}.$$

312

When the radius of the sphere equals to the half length of the slender body $R = \ell$ as shown in Figure G.4b, the terminal velocity of the sphere is

$$U_\infty = \frac{2}{9} \frac{\ell^2 \left(\rho_{\text{fluid}} - \rho_m\right) g}{\mu}.$$

When the slender body is inscribed in the sphere, $R^2 = \ell^2 + r^2$ see Figure G.4c. The terminal velocity of the sphere in terms of the dimensions of the slender body is

$$U_\infty = \frac{2}{9} \frac{\left(\rho_{\text{fluid}} - \rho_m\right) g}{\mu} \left(\ell^2 + r^2\right).$$

G.6 Terminal velocity of two spheres

Stimson and Jeffery [71] first derived the stream function for axisymmetric flow past two two solid spheres (equal or unequal) moving with equal small constant velocities parallel to their line of centers, and calculated the forces acting on the spheres as an infinite sum. Here we summarize the result using singularity method and method of reflections from [41].

G.6.1 Two widely separated spheres

We take two non-rotating spheres' centered at x_1 and x_2, with radii a and b and translational velocity U_1 and U_2, respectively [41]. The zeroth order solution is simply the Stokes solution for the disturbance caused by an isolated, translating sphere in a uniform stream. Thus, we have the velocity for both spheres

$$v_1 = -F_1^{(0)} \cdot \left\{1 + \frac{a^2}{6}\Delta\right\} \frac{G\left(x - x_1\right)}{8\pi\mu},$$
$$v_2 = -F_2^{(0)} \cdot \left\{1 + \frac{b^2}{6}\Delta\right\} \frac{G\left(x - x_2\right)}{8\pi\mu}$$

with $F_1^{(0)} = 6\pi\mu a \left(U^\infty - U_1\right)$, $T_1^{(0)} = 0$, and $S_1^{(0)} = 0$. A similar set of results for sphere 2, $F_2^{(0)} = 6\pi\mu b \left(U^\infty - U_2\right)$, $T_2^{(0)} = 0$, $S_2^{(0)} = 0$.

By the method of reflections, the force exerted on sphere with radius a at x_1 is

$$
\begin{aligned}
F_1 \;=\; & F_1^{(0)} \cdot \left[\left(1 + \frac{9}{4}\beta \left(\frac{a}{R}\right)^2 - \left(\frac{3\beta}{2} + \frac{81\beta^2}{16} + \frac{3\beta^3}{4} \right) \left(\frac{a}{R}\right)^4 \right) \mathbf{dd} \right. \\
& \left. + \left(1 + \frac{9}{4}\beta \left(\frac{a}{R}\right)^2 + \left(\frac{3\beta}{8} - \frac{81\beta^2}{256} + \frac{3\beta^3}{16} \right) \left(\frac{a}{R}\right)^4 \right) (\delta - \mathbf{dd}) \right] \\
& + F_2^{(0)} \cdot \left[\left(-\frac{3}{2}\frac{a}{R} + \frac{1}{2} \left(1 - \frac{27\beta}{4} + \beta^2 \right) \left(\frac{a}{R}\right)^3 \right) \mathbf{dd} \right. \\
& \left. + \left(\frac{3}{4}\frac{a}{R} + \frac{1}{4} \left(1 + \frac{27\beta}{16} + \beta^2 \right) \left(\frac{a}{R}\right)^3 \right) (\delta - \mathbf{dd}) \right],
\end{aligned}
$$

where d denotes the unit vector $\frac{(x_2 - x_1)}{|x_2 - x_1|}$ and $\beta = \frac{b}{a}$ is the ratio of sphere radii. The force is accurate to $O\left(R^4\right)$.

The force on the other sphere with radius b at x_2 is

$$
\begin{aligned}
F_2 \;=\; & F_2^{(0)} \cdot \left[\left(1 + \frac{9}{4}\beta \left(\frac{b}{R}\right)^2 - \left(\frac{3\beta}{2} + \frac{81\beta^2}{16} + \frac{3\beta^3}{4} \right) \left(\frac{b}{R}\right)^4 \right) \mathbf{dd} \right. \\
& \left. + \left(1 + \frac{9}{4}\beta \left(\frac{b}{R}\right)^2 + \left(\frac{3\beta}{8} - \frac{81\beta^2}{256} + \frac{3\beta^3}{16} \right) \left(\frac{b}{R}\right)^4 \right) (\delta - \mathbf{dd}) \right] \\
& + F_1^{(0)} \cdot \left[\left(-\frac{3}{2}\frac{b}{R} + \frac{1}{2} \left(1 - \frac{27\beta}{4} + \beta^2 \right) \left(\frac{b}{R}\right)^3 \right) \mathbf{dd} \right. \\
& \left. + \left(\frac{3}{4}\frac{b}{R} + \frac{1}{4} \left(1 + \frac{27\beta}{16} + \beta^2 \right) \left(\frac{b}{R}\right)^3 \right) (\delta - \mathbf{dd}) \right],
\end{aligned}
$$

where d denotes the unit vector $\frac{(x_1 - x_2)}{|x_1 - x_2|}$ and $\beta = \frac{a}{b}$ is the other ratio of sphere radii.

G.6.2   Two equal spheres

For two equal spheres, $a = b$ and $\beta = 1$. If the flow at infinite is at rest

$$U^\infty = 0, \quad F_1^{(0)} = 6\pi\mu a \left(-U_1\right),$$

$$F_2^{(0)} = 6\pi\mu a \left(-U_2\right).$$

The force on sphere is

$$
\begin{aligned}
F_1 &= -6\pi\mu a U_2 \cdot \left[\left(-\frac{3}{2}\frac{a}{R} - \frac{19}{8}\left(\frac{a}{R}\right)^3\right)\mathbf{dd} - \left(\frac{3}{4}\frac{a}{R} + \frac{59}{64}\left(\frac{a}{R}\right)^3\right)(\delta - \mathbf{dd})\right] \text{(G.16)} \\
&\quad -6\pi\mu a U_1 \cdot \left[\left(1 + \frac{9}{4}\left(\frac{a}{R}\right)^2 - \frac{117}{16}\left(\frac{a}{R}\right)^4\right)\mathbf{dd} \right. \\
&\quad \left. + \left(1 + \frac{9}{4}\left(\frac{a}{R}\right)^2 + \frac{63}{256}\left(\frac{a}{R}\right)^4\right)(\delta - \mathbf{dd})\right].
\end{aligned}
$$

Parallel to each other   If the two spheres are parallel to each other as they are falling with the velocity U_1 and U_2, the unit vector $d = \frac{(x_2 - x_1)}{|x_2 - x_1|} = (1, 0, 0)$ and δ involved in F_i is δ_{ij}. From (G.16), the force on the sphere is

$$F_1 = -6\pi\mu a U_1 \cdot \left[\left(1 + \frac{9}{4}\left(\frac{a}{R}\right)^2 + \frac{63}{256}\left(\frac{a}{R}\right)^4\right)\delta\right] + 6\pi\mu a U_2 \cdot \left[\left(\frac{3}{4}\frac{a}{R} + \frac{59}{64}\left(\frac{a}{R}\right)^3\right)\delta\right].$$

Especially, the hydrodynamic force in the vertical direction to determine the terminal velocity is interested, which is

$$F_1 = -6\pi\mu a \left(1 + \frac{9}{4}\left(\frac{a}{R}\right)^2 + \frac{63}{256}\left(\frac{a}{R}\right)^4\right)U_1 + 6\pi\mu a \left(\frac{3}{4}\frac{a}{R} + \frac{59}{64}\left(\frac{a}{R}\right)^3\right)U_2.$$

For the other sphere, the force is

$$F_2 = -6\pi\mu a \left(1 + \frac{9}{4}\left(\frac{a}{R}\right)^2 + \frac{63}{256}\left(\frac{a}{R}\right)^4\right)U_2 + 6\pi\mu a \left(\frac{3}{4}\frac{a}{R} + \frac{59}{64}\left(\frac{a}{R}\right)^3\right)U_1.$$

When the spheres reach their terminal velocity, $U_1 = U_2$. Otherwise, the distance between them will change. Consequently, the force will is changed. When $U_1 = U_2$, the hydrodynamic force is balanced with the buoyant force and the force due to gravity,

$$6\pi\mu a \left(1 + \frac{9}{4}\left(\frac{a}{R}\right)^2 + \frac{63}{256}\left(\frac{a}{R}\right)^4\right) U - 6\pi\mu a \left(\frac{3}{4}\frac{a}{R} + \frac{59}{64}\left(\frac{a}{R}\right)^3\right) U$$
$$= \frac{4}{3}\pi a^3 \rho_{\text{fluid}} g - \frac{4}{3}\pi a^3 \rho_m g.$$

So, the terminal velocity of the sphere is

$$U = \frac{2}{9}\frac{a^2 g \left(\rho_{\text{fluid}} - \rho_m\right)}{\mu} \frac{256}{(256 - 192s + 576s^2 - 236s^3 + 63s^4)} = \frac{2}{9}\frac{a^2 g \left(\rho_{\text{fluid}} - \rho_m\right)}{\mu} f_1(s),$$

$$(G.17)$$

where $s = \frac{a}{R}$, a is the radius of the sphere, and R is distance between the centers of two spheres.

Two spheres as a sequence   If the two spheres are falling as a sequence, then the unit vector $d = \frac{(x_2 - x_1)}{|x_2 - x_1|} = (0, 0, 1)$. The force exerted on sphere 1 is

$$
\begin{aligned}
F_1 &= -6\pi\mu a \left(-\frac{3}{2}\frac{a}{R} - \frac{19}{8}\left(\frac{a}{R}\right)^3\right) U_2 + 6\pi\mu a U_2 \cdot \left(\frac{3}{4}\frac{a}{R} + \frac{59}{64}\left(\frac{a}{R}\right)^3\right)(\delta - \mathbf{dd}) \\
&\quad -6\pi\mu a \left(1 + \frac{9}{4}\left(\frac{a}{R}\right)^2 - \frac{117}{16}\left(\frac{a}{R}\right)^4\right) U_1 \\
&\quad -6\pi\mu a U_1 \cdot \left(1 + \frac{9}{4}\left(\frac{a}{R}\right)^2 + \frac{63}{256}\left(\frac{a}{R}\right)^4\right)(\delta - \mathbf{dd}).
\end{aligned}
$$

The force in the vertical direction to determine the terminal velocity is

$$F_1 = -6\pi\mu a \left(1 + \frac{9}{4}\left(\frac{a}{R}\right)^2 - \frac{117}{16}\left(\frac{a}{R}\right)^4\right) U_1 + 6\pi\mu a \left(\frac{3}{2}\frac{a}{R} + \frac{19}{8}\left(\frac{a}{R}\right)^3\right) U_2.$$

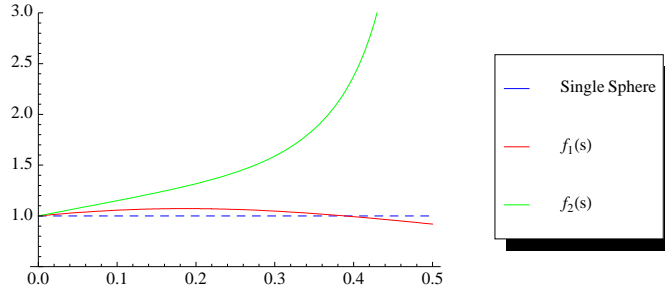Similar results are hold for the other sphere.

Figure G.5: Coefficients in the terminal velocities of one single sphere vs two spheres.

For the terminal velocity, $U_1 = U_2$. Balance the forces,

$$6\pi\mu a \left(1 + \frac{9}{4}\left(\frac{a}{R}\right)^2 - \frac{117}{16}\left(\frac{a}{R}\right)^4\right) U + 6\pi\mu a \left(-\frac{3}{2}\frac{a}{R} - \frac{19}{8}\left(\frac{a}{R}\right)^3\right) U$$
$$= \frac{4}{3}\pi a^3 \rho_{\text{fluid}} g - \frac{4}{3}\pi a^3 \rho_m g.$$

The terminal velocity of the sphere is

$$U = \frac{2}{9}\frac{a^2 g \left(\rho_{\text{fluid}} - \rho_m\right)}{\mu} \frac{16}{(16 - 24s + 36s^2 - 38s^3 - 117s^4)} = \frac{2}{9}\frac{a^2 g \left(\rho_{\text{fluid}} - \rho_m\right)}{\mu} f_2(s).$$

$$\text{(G.18)}$$

where $s = \frac{a}{R}$.

For a single rigid sphere falling in the Stokes flow, the terminal velocity is $U = \frac{2}{9}\frac{a^2 g(\rho_{\text{fluid}} - \rho_m)}{\mu}$, where a is the radius of the sphere and ρ_m is the density of the sphere. Figure G.5 shows the coefficients in the terminal velocities for a single sphere and two-sphere cases.

G.7   Two unequal spheres

When the two unequal spheres fall in the Stoke flow, we take two non-rotating spheres' centered at $\mathbf{x_1}$ and $\mathbf{x}_2$, with radii a and b and translational velocity $\mathbf{U}_1$ and $\mathbf{U}_2$ respectively.

G.7.1   Two spheres as a sequence

If the two sphere are not equal and falling as a sequence one after the other, the sphere with radius a at $x_1 = \begin{pmatrix} 0 & 0 & z_1 \end{pmatrix}^t$ with a uniform velocity $\begin{pmatrix} 0 & 0 & -U_1 \end{pmatrix}^t$, the other sphere with radius b at $x_2 = \begin{pmatrix} 0 & 0 & z_2 \end{pmatrix}^t$ with the uniform velocity $\begin{pmatrix} 0 & 0 & -U_2 \end{pmatrix}^t$

Compute the force on sphere a: $d = \frac{(x_2 - x_1)}{|x_2 - x_1|} = (0, 0, -1)$ and $\beta = \frac{b}{a}$.

$$\mathbf{dd} = \begin{pmatrix} 0 \\ 0 \\ -1 \end{pmatrix} (0, 0, -1) = \begin{pmatrix} 0 & 0 & 0 \\ 0 & 0 & 0 \\ 0 & 0 & 1 \end{pmatrix}, \quad (\delta - \mathbf{dd}) = \begin{pmatrix} 1 & 0 & 0 \\ 0 & 1 & 0 \\ 0 & 0 & 0 \end{pmatrix}$$

$$
\begin{aligned}
F_1 &= 6\pi\mu a \left(-\vec{U_1}\right) \cdot \left[\left(1 + \frac{9}{4}\frac{b}{a}\left(\frac{a}{R}\right)^2 - \left(\frac{3\frac{b}{a}}{2} + \frac{81\left(\frac{b}{a}\right)^2}{16} + \frac{3\left(\frac{b}{a}\right)^3}{4} \right)\left(\frac{a}{R}\right)^4 \right)\mathbf{dd} \right. \\
&\quad \left. + \left(1 + \frac{9}{4}\frac{b}{a}\left(\frac{a}{R}\right)^2 + \left(\frac{3\frac{b}{a}}{8} - \frac{81\left(\frac{b}{a}\right)^2}{256} + \frac{3\left(\frac{b}{a}\right)^3}{16} \right)\left(\frac{a}{R}\right)^4 \right)(\delta - \mathbf{dd}) \right] \\
&\quad + 6\pi\mu b \left(-\vec{U_2}\right) \cdot \left[\left(-\frac{3}{2}\frac{a}{R} + \frac{1}{2}\left(1 - \frac{27\frac{b}{a}}{4} + \left(\frac{b}{a}\right)^2 \right)\left(\frac{a}{R}\right)^3 \right)\mathbf{dd} \right. \\
&\quad \left. + \left(\frac{3}{4}\frac{a}{R} + \frac{1}{4}\left(1 + \frac{27\frac{b}{a}}{16} + \left(\frac{b}{a}\right)^2 \right)\left(\frac{a}{R}\right)^3 \right)(\delta - \mathbf{dd}) \right] \\
&= 6\pi\mu a \left(1 + \frac{9}{4}\frac{b}{a}\left(\frac{a}{R}\right)^2 - \left(\frac{3b}{2a} + \frac{81b^2}{16a^2} + \frac{3b^3}{4a^3} \right)\left(\frac{a}{R}\right)^4 \right)\begin{pmatrix} 0 \\ 0 \\ U_1 \end{pmatrix} \\
&\quad + 6\pi\mu b \left(-\frac{3}{2}\frac{a}{R} + \frac{1}{2}\left(1 - \frac{27b}{4a} + \left(\frac{b}{a}\right)^2 \right)\left(\frac{a}{R}\right)^3 \right)\begin{pmatrix} 0 \\ 0 \\ U_2 \end{pmatrix}.
\end{aligned}
$$

Similarly, the force on sphere with radius b and velocity U_2 is

$$
\begin{aligned}
F_2 &= 6\pi\mu b \left(1 + \frac{9}{4}\frac{a}{b} \left(\frac{b}{R}\right)^2 - \left(\frac{3a}{2b} + \frac{81a^2}{16b^2} + \frac{3a^3}{4b^3}\right)\left(\frac{b}{R}\right)^4 \right) \begin{pmatrix} 0 \\ 0 \\ U_2 \end{pmatrix} \\
&\quad + 6\pi\mu a \left(-\frac{3}{2}\frac{b}{R} + \frac{1}{2}\left(1 - \frac{27a}{4b} + \left(\frac{a}{b}\right)^2\right)\left(\frac{b}{R}\right)^3 \right) \begin{pmatrix} 0 \\ 0 \\ U_1 \end{pmatrix}.
\end{aligned}
$$

The force in vertical direction is

$$
\begin{aligned}
F_1 &= 6\pi\mu a \left(1 + \frac{9}{4}\frac{b}{a} \left(\frac{a}{R}\right)^2 - \left(\frac{3b}{2a} + \frac{81b^2}{16a^2} + \frac{3b^3}{4a^3}\right)\left(\frac{a}{R}\right)^4 \right) U_1 \\
&\quad + 6\pi\mu b \left(-\frac{3}{2}\frac{a}{R} + \frac{1}{2}\left(1 - \frac{27b}{4a} + \left(\frac{b}{a}\right)^2\right)\left(\frac{a}{R}\right)^3 \right) U_2 \\
F_2 &= 6\pi\mu b \left(1 + \frac{9}{4}\frac{a}{b} \left(\frac{b}{R}\right)^2 - \left(\frac{3a}{2b} + \frac{81a^2}{16b^2} + \frac{3a^3}{4b^3}\right)\left(\frac{b}{R}\right)^4 \right) U_2 \\
&\quad + 6\pi\mu a \left(-\frac{3}{2}\frac{b}{R} + \frac{1}{2}\left(1 - \frac{27a}{4b} + \left(\frac{a}{b}\right)^2\right)\left(\frac{b}{R}\right)^3 \right) U_1
\end{aligned}
$$

So, the velocities of the spheres satisfy the following equations,

$$
6\pi\mu a \left(1 + \frac{9}{4}\frac{b}{a} \left(\frac{a}{R}\right)^2 - \left(\frac{3b}{2a} + \frac{81b^2}{16a^2} + \frac{3b^3}{4a^3}\right)\left(\frac{a}{R}\right)^4 \right) U_1 \quad \text{(G.19)}
$$

$$
+ 6\pi\mu b \left(-\frac{3}{2}\frac{a}{R} + \frac{1}{2}\left(1 - \frac{27b}{4a} + \left(\frac{b}{a}\right)^2\right)\left(\frac{a}{R}\right)^3 \right) U_2 = \frac{4}{3}\pi a^3 \rho_{\text{fluid}} g - \frac{4}{3}\pi a^3 \rho_m g
$$

$$
6\pi\mu b \left(1 + \frac{9}{4}\frac{a}{b} \left(\frac{b}{R}\right)^2 - \left(\frac{3a}{2b} + \frac{81a^2}{16b^2} + \frac{3a^3}{4b^3}\right)\left(\frac{b}{R}\right)^4 \right) U_2 \quad \text{(G.20)}
$$

$$
+ 6\pi\mu a \left(-\frac{3}{2}\frac{b}{R} + \frac{1}{2}\left(1 - \frac{27a}{4b} + \left(\frac{a}{b}\right)^2\right)\left(\frac{b}{R}\right)^3 \right) U_1 = \frac{4}{3}\pi b^3 \rho_{\text{fluid}} g - \frac{4}{3}\pi b^3 \rho_m g
$$

If both spheres reach the terminal velocity, then $U_1 = U_2 = U$,

$$6\pi\mu\left[a\left(1+\frac{9}{4}\frac{b}{a}\left(\frac{a}{R}\right)^2-\left(\frac{3b}{2a}+\frac{81b^2}{16a^2}+\frac{3b^3}{4a^3}\right)\left(\frac{a}{R}\right)^4\right)+\right.$$

$$\left.b\left(-\frac{3}{2}\frac{a}{R}+\frac{1}{2}\left(1-\frac{27b}{4a}+\left(\frac{b}{a}\right)^2\right)\left(\frac{a}{R}\right)^3\right)\right]U$$

$$=\frac{4}{3}\pi a^3\rho_{\text{fluid}}g-\frac{4}{3}\pi a^3\rho_m g,$$

$$6\pi\mu\left[b\left(1+\frac{9}{4}\frac{a}{b}\left(\frac{b}{R}\right)^2-\left(\frac{3a}{2b}+\frac{81a^2}{16b^2}+\frac{3a^3}{4b^3}\right)\left(\frac{b}{R}\right)^4\right)+\right.$$

$$\left.a\left(-\frac{3}{2}\frac{b}{R}+\frac{1}{2}\left(1-\frac{27a}{4b}+\left(\frac{a}{b}\right)^2\right)\left(\frac{b}{R}\right)^3\right)\right]U$$

$$=\frac{4}{3}\pi b^3\rho_{\text{fluid}}g-\frac{4}{3}\pi b^3\rho_m g$$

The terminal velocity

$$U=\frac{2}{9}\frac{g\left(\rho_{\text{fluid}}-\rho_m\right)}{\mu}$$

$$\frac{a^3}{a\left(1+\frac{9}{4}\frac{b}{a}\left(\frac{a}{R}\right)^2-\left(\frac{3b}{2a}+\frac{81b^2}{16a^2}+\frac{3b^3}{4a^3}\right)\left(\frac{a}{R}\right)^4\right)+b\left(-\frac{3}{2}\frac{a}{R}+\frac{1}{2}\left(1-\frac{27b}{4a}+\left(\frac{b}{a}\right)^2\right)\left(\frac{a}{R}\right)^3\right)}$$

$$U=\frac{2}{9}\frac{g\left(\rho_{\text{fluid}}-\rho_m\right)}{\mu}$$

$$\frac{b^3}{b\left(1+\frac{9}{4}\frac{a}{b}\left(\frac{b}{R}\right)^2-\left(\frac{3a}{2b}+\frac{81a^2}{16b^2}+\frac{3a^3}{4b^3}\right)\left(\frac{b}{R}\right)^4\right)+a\left(-\frac{3}{2}\frac{b}{R}+\frac{1}{2}\left(1-\frac{27a}{4b}+\left(\frac{a}{b}\right)^2\right)\left(\frac{b}{R}\right)^3\right)}$$

To reach the terminal velocity, the following condition need to be satisfied

$$\frac{a^3}{a\left(1+\frac{9}{4}\frac{b}{a}\left(\frac{a}{R}\right)^2-\left(\frac{3b}{2a}+\frac{81b^2}{16a^2}+\frac{3b^3}{4a^3}\right)\left(\frac{a}{R}\right)^4\right)+b\left(-\frac{3}{2}\frac{a}{R}+\frac{1}{2}\left(1-\frac{27b}{4a}+\left(\frac{b}{a}\right)^2\right)\left(\frac{a}{R}\right)^3\right)}\tag{G.21}$$

$$=\frac{b^3}{b\left(1+\frac{9}{4}\frac{a}{b}\left(\frac{b}{R}\right)^2-\left(\frac{3a}{2b}+\frac{81a^2}{16b^2}+\frac{3a^3}{4b^3}\right)\left(\frac{b}{R}\right)^4\right)+a\left(-\frac{3}{2}\frac{b}{R}+\frac{1}{2}\left(1-\frac{27a}{4b}+\left(\frac{a}{b}\right)^2\right)\left(\frac{b}{R}\right)^3\right)}.$$

G.7.2 Numerical results for two spheres falling one after the other

Both spheres are released from rest and have same density. For all numerical results, the viscosity is chosen as 9.29 Pa·s. The density of fluid is 1 g/ml and the density of sphere is 1.2 g/ml. The velocities of the spheres are computed from the coupled velocity field equation (G.19)-(G.20).

For two equal spheres, take the radius $r = a = b = 0.25$. One sphere is located at $(0, 0, 0)$, the other at $(0, 0, -1)$. The distance between the centers of spheres over time t is a constant as the initial value.

For two unequal sphere, the small sphere with radius $a = 0.2$ is located at $(0, 0, 0)$ above the large one, whose radius is $b = 0.5$ and initially at $(0, 0, -1)$. The distance between centers of two spheres d is shown in figure G.6, which monotonically increases over time. From (G.21), the equilibrium distance for two sphere with radius $a = 0.5$ and $b = 0.2$ is $d = 0.84133$. If the initial distance between the two spheres is smaller than the equilibrium distance, the smaller sphere will catch the larger one, which invalidates the velocity equations (G.19)-(G.20) beyond a certain distance. More information about the hydrodynamic force on the small sphere is documented at the end of this appendix.

If the small sphere with radius $a = 0.2$ is located at $(0, 0, -1)$ below the other large sphere with radius $b = 0.5$ at $(0, 0, 0)$, the distance between centers of two spheres d is shown in figure G.7. From this numerical result, we see the distance decreases and converges to a finite value with a small gap between the spheres.

Figure G.8 shows the result for the same spheres but the initial distance is smaller than the equilibrium distance, we see that the distance still converges.
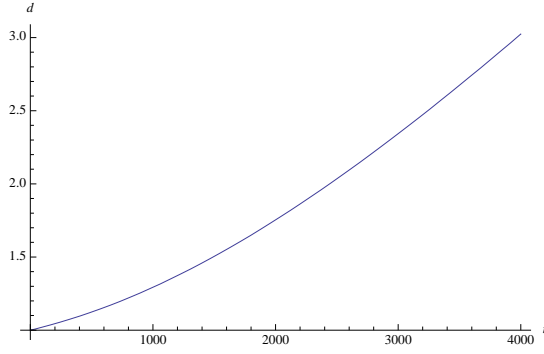
Figure G.6: The distance between centers of two unequal spheres while the small sphere above the large sphere.
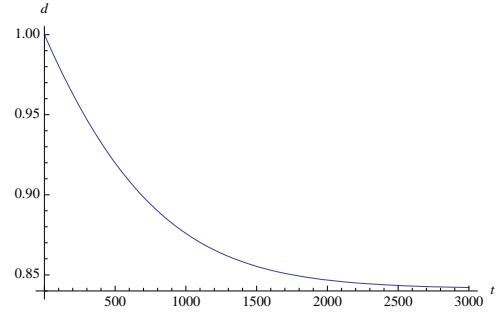

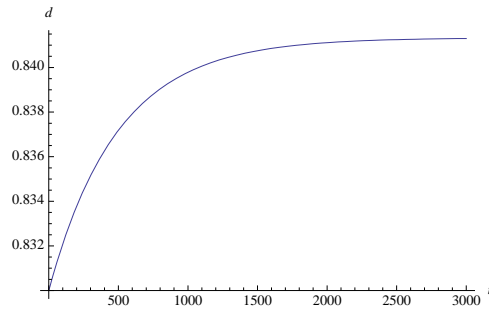Figure G.7: The distance between centers of two unequal spheres while the small sphere below the large sphere.

Figure G.8: Similar to Figure G.7 with a different initial distance.

G.7.3 Hydrodynamic force on a small sphere in flow induced by a sphere moving uniformly

For a rigid sphere moving in Stokes flow, the induced velocity field is [4]

$$u = U \left(\frac{1}{r} \frac{df}{dr} \right) + \mathbf{x} \frac{\mathbf{x} \cdot U}{r^2} \left(2 \frac{f}{r^2} - \frac{1}{r} \frac{df}{dr} \right),$$

where $f = r^2 \left(\frac{3}{4} \frac{a}{r} - \frac{1}{4} \frac{a^3}{r^3} \right)$. In the moving frame [19], the velocity field is

$$u = U\mathbf{e}_x - \frac{3a}{4} \left(\frac{U}{r} + \mathbf{x} \frac{\mathbf{x} \cdot U}{r^3} \right) + \frac{a^3}{4} \mathbf{x} \frac{\mathbf{x} \cdot U}{r^2} \nabla \left(\nabla \cdot \frac{U}{r} \right).$$

Rewrite the velocity vector in components format

$$
\begin{aligned}
u(x,y,z,a,U) &= U + \frac{a^3 U \left(2x^2 - y^2 - z^2 \right)}{4 \left(x^2 + y^2 + z^2 \right)^{5/2}} - \frac{3}{4} a \left(\frac{U x^2}{\left(x^2 + y^2 + z^2 \right)^{3/2}} + \frac{U}{\sqrt{x^2 + y^2 + z^2}} \right), \\
v(x,y,z,a,U) &= \frac{3a^3 U xy}{4 \left(x^2 + y^2 + z^2 \right)^{5/2}} - \frac{3a U xy}{4 \left(x^2 + y^2 + z^2 \right)^{3/2}}, \\
w(x,y,z,a,U) &= \frac{3a^3 U xz}{4 \left(x^2 + y^2 + z^2 \right)^{5/2}} - \frac{3a U xz}{4 \left(x^2 + y^2 + z^2 \right)^{3/2}}.
\end{aligned}
$$

Faxen correction of the drag on a small sphere with radius b on the center line (the x-axis) is

$$F = 6\pi\mu b \left(u + \frac{1}{6} b^2 \Delta u \right).$$

$$F_x = 6\pi\mu b \left(U + \frac{a^3 U}{2 \left(x^2 \right)^{3/2}} - \frac{3}{2} \frac{aU}{\sqrt{x^2}} + \frac{1}{6} b^2 \frac{3aU}{\left(x^2 \right)^{3/2}} \right)$$

$$u(x, 0, 0, a, U) = U + \frac{a^3 U}{2 \left(x^2\right)^{3/2}} - \frac{3}{2} \frac{aU}{\sqrt{x^2}}$$

$$\Delta u(x, 0, 0, a, U) = \frac{3aU}{\left(x^2\right)^{3/2}} > 0, \text{ for any } x.$$

Drag in the x-direction is

$$F_x = 6\pi\mu b \left(u(x, 0, 0, a, U) + \frac{1}{6} b^2 \Delta u(x, 0, 0, a, U) \right)$$

$$= 6\pi\mu b \left(U + \frac{a^3 U}{2 \left(x^2\right)^{3/2}} - \frac{3}{2} \frac{aU}{\sqrt{x^2}} + \frac{b^2}{6} \frac{3aU}{\left(x^2\right)^{3/2}} \right).$$

Without Faxen correction,

$$F_x = 6\pi\mu b \, u(x, 0, 0, a, U) = \frac{3b\pi U \left(a^3 + 2\left(x^2\right)^{3/2} - 3ax^2\right)\mu}{\left(x^2\right)^{3/2}}.$$

The conclusion is the drag on a sphere falling behind another one never change sign and it will try to catch the other one. This does not explain all the phenomena in the numerical results for two spheres falling one after the other, but sheds light on part of the mechanics.

Bibliography

[1] A. Acrivos. Heat transfer at high Péclet number from a small sphere freely rotating in a simple shear field. *J. Fluid Mech.*, 46:233–240, 1971.

[2] K. Bajer and H. K. Moffatt. On a class of steady confined Stokes flows with chaotic streamlines. *J. Fluid Mech.*, 212:337–363, 1990.

[3] G. K. Batchelor. Slender-body theory for particles of arbitrary cross-section in Stokes flow. *J. Fluid Mech.*, 44:419–440, 1970.

[4] G. K. Batchelor. *Introduction to Fluid Mechanics*. Cambridge University Press, 1999.

[5] J. R. Blake. A note on the image system for a stokelet in a no-slip boundary. *Proceedings of the cambridge philosophical society*, 70:303–310, 1971.

[6] J. R. Blake and A. T. Chwang. Fundamental singularities of viscous-flow. part 1. image systems in vicinity of a stationary no-slip boundary. *J. Eng. Math.*, 8:2329, 1974.

[7] S. Blaser. Forces on the surface of small ellipsoidal particles immersed in a linear flow field. *Chemical Engineering Science*, 57:515–526, 2002.

[8] J. Bouguet. *Complete Camera Calibration Toolbox for Matlab*.

[9] E. L. Bouzarth, A. Brooks, R. Camassa, H. Jing, T. J. Leiterman, R. M. Mclaughlin, R. Superfine, J. Toledo, and L. Vicci. Epicyclic orbits in a viscous fluid about a precessing rod: Theory and experiments at the micro- and macro-scales. *Physical Review E*, 76(1), 2007.

[10] F. P. Bretherton. The motion of rigid particles in a shear flow at low reynolds number. *J. Fluid Mech.*, 14(2):284–304, 1962.

[11] F. P. Bretherton. Slow viscous motion round a cylinder in a simple shear. *J. Fluid Mech.*, 12:591–613, 1962.

[12] J. Buceta, M. Ibañes, D. Rasskin-Gutman, Y. Okada, N. Hirokawa, and J. C. Izpisúa-Belmonte. Nodal cilia dynamics and the specification of the left/right axis in early vertebrate embryo development. *Biophys J. 2005 Oct;89(4):2199-209. Epub 2005 Jul 22.*, 89:2199–209, 2005.

[13] J. M. Burgers. *On the motion of small particles of elongated form, suspended in a viscous fluid*. Nordemann Publishing, New York, 1938.

[14] R. Camassa, T. J. Leiterman, and R. M. McLaughlin. Trajectory and flow properties for a rod spinning in a viscous fluid. Part 1. An exact solution. *J. Fluid Mech.*, 612:153–200, 2008.

[15] R. Camassa, R. M. McLaughlin, L. Vicci, L. Zhao, and etc. Feeding by symmetry breaking: The role of bend in spinning cilia. *Inpreparing*, 2009.

[16] J. H. E. Cartwright, O. Piro, and I. Tuval. Fluid-dynamical basis of the embryonic development of left-right asymmetry in vertebrates. *Proc. Natl. Acad. Sci. USA*, 101(19):7234–7239, May 2004.

[17] A. T. Chan and A. T. Chwang. The unsteady stokeslet and oseenlet. *Proceedings of the Institution of Mechanical Engineers. Part C, Journal of mechanical engineering science*, 214:175–179, 2000.

[18] A. T. Chwang and T. Y. Wu. A note on the helical movement of microorganisms. *Proceedings of the Royal Society of London. Series B, Biological Sciences*, 178(1052):327–346, Auguest 1971.

[19] A. T. Chwang and T. Y. Wu. Hydromechanics of low-Reynolds-number flow. Part 2. Singularity method for Stokes flows. *J. Fluid Mech.*, 67:787–815, 1975.

[20] B. Clipp, D. Gallup, H. Towles, R. Kumar, and P. Lincoln. The synchronized multi-camera digital recorder (ladybugrecord). Private communications.

[21] R. G. Cox. The motion of long slender bodies in a viscous fluid Part1: General theory. *J. Fluid Mech.*, 44:791–810, 1970.

[22] R. G. Cox. The motion of long slender bodies in a viscous fluid. Part 2. shear flow. *J. Fluid Mech.*, 45(4):625–657, 1971.

[23] R. G. Cox, Y. Z. Zia, and S. G. Mason. Particle motion in sheared suspensions. XXV. Streamline around cylinders and spheres. *Journal of Colloid and Interface Science*, 27:7–18, 1968.

[24] M. Van Dyke. *Perturbation methods in fluid mechanics*. Parabolic Press, annotated ed edition, 1975.

[25] B. A. Evans, A. R. Shields, R. Lloyd Carroll, S. Washburn, M. R. Falvo, and R. Superfine. Magnetically actuated nanorod arrays as biomimetic cilia. *Nano Letters*, 7(5):1428–1435, 2007.

[26] L. J. Fauci and R. Dillon. Biofluidmechanics of reproduction. *Annual Review of Fluid Mechanics*, 38:371–394, January 2006.

[27] D. L. Feke and W. R. Schowalter. The effect of brownian diffusion on shear-induced coagulation of colloidal dispersions. *Journal of Fluid Mechanics*, 133:17–35, 1983.

[28] G. R. Fulford and J. R. Blake. Muco-ciliary transport in the lung. *Journal of Theoretical Biology*, 121(4):381–402, August 1986.

[29] Hiroshi Hamada. Breakthroughs and future challenges in leftright patterning. *Develop. Growth Differ.*, 50:S71S78, 2008.

[30] G. J. Hancock. The self-propulsion of microscopic organisms through liquids. *Proc. R. Soc. Lond. A*, 217(1128):96–121, March 1953.

[31] J. Happel and H. Brenner. *Low Reynolds Number Hydrodynamics: with special applications to particulate media.* The Hague; Boston: M. Nijhoff; Hingham, MA, USA, 1991.

[32] Masakazu Hashimoto, Kyosuke Shinohara, Jianbo Wang, Shingo Ikeuchi, Satoko Yoshiba, Chikara Meno, Shigenori Nonaka, Shinji Takada, Kohei Hatta, Anthony Wynshaw-Boris, and Hiroshi Hamada. Planar polarization of node cells determines the rotational axis of node cilia. *Nature Cell Biology*, 12:170 – 176, 2010.

[33] N. Hirokawa, Y. Tanaka, and Y. Okada. Left-right determination: Involvement of molecular motor kif3, cilia, and nodal flow. *Cold Spring Harbor Perspectives in Biology*, 1:1:a000802, 2009.

[34] N. Hirokawa, Y. Tanaka, Y. Okada, and S. Takeda. Nodal flow and the generation of left-right asymmetry. *Cell*, 125(1):33–45, 7 April 2006.

[35] D. Holz. Body tracking program. Private communications, 2009.

[36] G. B. Jeffery. The motion of ellipsoidal particles immersed in a viscous fluid. *Proceedings of the Royal Society of London. Series A, Containing Papers of a Mathematical and Physical Character*, 102(715):161–179, 1922.

[37] D. J. Jeffrey and J. D. Sherwood. Streamline patterns and eddies in low Reynolds number flow. *J. Fluid Mech.*, 96:315334, 1980.

[38] R. E. Johnson. An improved slender-body theory for Stokes flow. *J. Fluid Mech*, 99:411–431, 1980.

[39] J. B. Keller and S. I. Rubinow. Slender-body theory for slow viscous flow. *J. Fluid Mech.*, 75(4):705–714, 1976.

[40] S. Kim. Singularity solutions for ellipsoids in Low-Reynolds-Number flows: with applications to the calculation of hydrodynamic interactions in suspensions of ellipsoids. *International journal of multiphase flow*, 12(3):469–491, 1986.

[41] S. Kim and S. J. Karrila. *Microhydrodynamics: Principles and Selected Applications.* Dover Publications, 2005.

[42] C. A. Kossack and A. Acrivos. Steady simple shear flow past a circular cylinder at moderate Reynolds numbers: A numerical solution. *J. Fluid Mech.*, 66:353–376, 1974.

[43] H. K. Kuiken. H.A. Lorentz: Sketches of his work on slow viscous flow and some other areas in fluid mechanics and the background against which it arose. *Journal of Engineering Mathematics*, 30:1–18, 1996.

[44] S. H. Lamb. *Hydrodynamic.* Dover publications, 1945.

[45] L. G. Leal. Particle motions in a viscous fluid. *Ann. Rev. Fluid Mech.*, 12:435–476, 1980.

[46] L. G. Leal. *Laminar Flow and Convective Transport Processes: Scaling Principles and Asymptotic Analysis.* Butterworth-Heinemann, June 1992.

[47] L. G. Leal. *Advanced Transport Phenomena: Fluid Mechanics and Convective Transport Processes.* Cambridge University Press, 2007.

[48] T. J. Leiterman. *Mixing properties of exact and asymptotic low Reynolds, time-varying solutions for spinning nano-rods and biological applications to ciliary function.* PhD thesis, the University of North Carolina at Chapel Hill, 2007.

[49] M. J. Lighthill. Contributions o the theory of the Pitot-tube displacement effect. *J. Fluid Mech.*, 2:493–512, 1957.

[50] N. Liron. The LGL (Lighthill-Gueron-Liron) Theorem–historical perspective and critique. *Mathematical methods in the applied science*, 24:1533–1540, 2001.

[51] H. A. Lorentz. Eene algemeene stelling omtrent de beweging eener vloeistof met wrijving en eenige daaruit afgeleide gevolgen. *Zittingsverslag van de Koninklijke Akademie van Wetenschappen te Amsterdam*, 5:168–175, 1896.

[52] T. Ma and S. Wang. A generalized Poincaré-Hopf index formula and its applications to 2-D incompressible flows. *Nonlinear Analysis:Real World Applications*, 1:467–482, 2001.

[53] F. O. Marques, R. Taborda, S. Bose, and J. Antunes. Effects of confinement on matrix flow around a rigid inclusion in viscous simple shear: insights from analogue and numerical modelling. *Journal of structural geology*, 27:379–396, 2005.

[54] A. Mashayek and C. Pozrikidis. Motion of a spherical particle inside a liquid film. *Acta Mech*, 210:27–46, 2010.

[55] H. Matsui, S. H. Randell, S. W. Peretti, C. W. Davis, and R. C. Boucher. Coordinated clearance of periciliary liquid and mucus from airway surfaces. *J Clin Invest.*, 102(6):1125–1131, September 15 1998.

[56] W. J. McKiver and D. G. Dritschel. The motion of a fluid ellipsoid in a general linear background flow. *J. Fluid Mech.*, 474:147–173, 2003.

[57] D. R. Mikulencak and J. F. Morris. Stationary shear flow around fixed and free bodies at finite Reynolds number. *J. Fluid Mech.*, 520:215–242, 2004.

[58] S. Nonaka, Y. Tanaka, Y. Okada, S. Takeda, A. Harada, Y. Kanai, M. Kido, and N. Hirokawa. Randomization of left-right asymmetry due to loss of nodal cilia generating leftward flow of extraembryonic fluid in mice lacking KIF3B motor protein. *Cell*, 95(6):829–837, December 1998.

[59] S. Nonaka, Y. Tanaka, Y. Okada, S. Takeda, A. Harada, Y. Kanai, M. Kido, and N. Hirokawa. Erratum: Randomization of left-right asymmetry due to loss of nodal cilia generating leftward flow of extraembryonic fluid in mice lacking KIF3B motor protein. *Cell*, 99(1):116, October 1 1999.

[60] C. W. Oseen. Neure methoden und ergebnisse in der hydrodynamik. in akad. verlagsgesellschaft. *Leipzig:Akad. Verlagsgesellschaft*, page 337, 1927.

[61] R. L. Panton. Incompressible flow. John Wiley & Sons, 1984.

[62] G. G. Poe and A. Acrivos. Closed streamline flows past rotating single cylinders and spheres: Inertia effects. *J. Fluid Mech.*, 72:605, 1975.

[63] C. Pozrikidis. *Introduction to theoretical and computational fluid dynamics*. New York : Oxford University Press, 1997.

[64] T. C. Price. Slow linear shear flow past a hemispherical bump in a plane wall. *Q. J. Mech. Appl. Math.*, 38(1):93–104, 1985.

[65] C. R. Robertson and A. Acrivos. Low Reynolds number shear flow past a rotating circular cylinder. Part 1. momentum transfer. *J. Fluid Mech.*, 40:685, 1970.

[66] P. G. Saffman. The lift on a small sphere in a slow shear flow. *J. Fluid Mech.*, 22:385–400, 1965.

[67] L. F. Shatz. Singularity method for oblate and prolate spheroids in Stokes and linearized oscillatory flow. *Phys. Fluids*, 16(3):664–677, 2004.

[68] K. Shintani, A. Umenura, and A. Takano. Low-reynolds-number flow past an elliptic cylinder. *J . Fluid Mech.*, 136:277–289, 1983.

[69] D. J. Smith, J. R. Blake, and E. A. Gaffney. Fluid mechanics of nodal flow due to embryonic primary cilia. *Journal of The Royal Society Interface*, 5:567–573, 2008.

[70] L. A. Spielman. Particle capture from low-speed laminar flows. *Annual Review of Fluid Mechanics*, 9:297–319, January 1977.

[71] M. Stimson and G. B. Jeffery. The motion of two spheres in a viscous fluid. *Proceedings of the Royal Society of London. Series A*, 111(757):110–116, May 1 1926.

[72] G. Subramanian and D. L. Koch. Inertial effects on the transfer of heat or mass from neutrally buoyant spheres in a steady linear velocity field. *Phys. Fluids*, 18(7):73302, 2006.

[73] R. M. Taylor. http://cismm.cs.unc.edu/downloads/. 2005.

[74] J. P. K. Tillett. Axial and transverse Stokes flow past slender axisymmetric bodies. *J. Fluid Mech.*, 44(3):401–417, 1970.

[75] E. O. Tuck. Some methods for flows past blunt slender bodies. *J. Fluid Mech.*, 18(4):619–635, 1964.

[76] K. C. Wang, H. C. Zhou, C. H. Hu, and S. Harrington. Three-dimensional separated flow structure over prolate spheroids. *Proceedings of the Royal Society of London. Series A, Mathematical and Physical Sciences*, 421:73–91, 1990.

[77] M. C. T. Wilson, P. H. Gaskell, and M. D. Savage. Nested separatrices in simple shear flows: The effect of localized disturbances on stagnation lines. *Physics of Fluids*, 17:093601, 2005.